Hybrid Asymptotic-Numerical Analysis of Pattern Formation Problems

by

Iain Moyles

B.Sc., The University of Ontario Institute of Technology, 2009
M.Sc., The University of British Columbia, 2011

A THESIS SUBMITTED IN PARTIAL FULFILLMENT OF
THE REQUIREMENTS FOR THE DEGREE OF

DOCTOR OF PHILOSOPHY

in

The Faculty of Graduate and Postdoctoral Studies

(Mathematics)

THE UNIVERSITY OF BRITISH COLUMBIA

(Vancouver)

June 2015

Abstract

In this thesis we present an analysis of the Gierer-Meinhardt model with saturation (GMS) on various curve geometries in $\mathbb{R}^2$. We derive a boundary fitted coordinate framework which translates an asymptotic two-component differential equation into a single component reaction diffusion equation with singular interface conditions. We create a numerical method that generalizes the solution of such a system to arbitrary two-dimensional curves and show how it extends to other models with singularity properties that are related to the Laplace operator. This numerical method is based on integrating logarithmic singularities which we handle by the method of product integration where logarithmic singularities are handled analytically with numerically interpolated densities. In parallel with the generalized numerical method, we present some analytical solutions to the GMS model on a circular and slightly perturbed circular curve geometry. We see that for the regular circle, saturation leads to a hysteresis effect for two dynamically stable branches of equilibrium radii. For the near circle we show that there are two distinct perturbations, one resulting from the introduction of a angular dependent radius, and one caused by Fourier mode interactions which causes a vertical shift to the solution. We perform a linear stability analysis to the true circle solution and show that there are two classes of eigenvalues leading to breakup

or zigzag instabilities. For the breakup instabilities we show that the saturation parameter can completely stabilize perturbations that we show are always unstable without saturation and for the zigzag instabilities we show that the eigenvalues are given by the near circle curve normal velocity. The breakup analysis is based on the reduction of an implicit non-local eigenvalue problem (NLEP) to a root finding problem. We derive conditions for which this eigenvalue problem can be made explicit and use it to analyze a stripe and ring geometry. This formulation allows us to classify certain technical properties of NLEPs such as instability bands and a Hopf bifurcation condition analytically.

Preface

The work in Chapter 4 has been submitted for application in [53] along with my supervisor Dr. Michael Ward and my colleague Wang Hung Tse. The major contribution of Wang Hung Tse in [53] is on the modelling of urban crime which is not presented in this thesis. Dr. Ward was the supervising author and was primarily responsible for conceptualizing the generalized explicit NLEP formulation as outlined in section 4.1 of Chapter 4 which was motivated from his work in [57]. My main contribution of this work was in the extension of this framework to the models presented in sections 4.2 and 4.3 of Chapter 4. All numerical simulations presented in [53] were performed by me and also appear in Chapter 5 Figures 5.1, 5.2, 5.3, 5.4, 5.5, and 5.6.

The work in Chapter 6 has been submitted for application in [54] along with my supervisor Dr. Brian Wetton. I was the lead investigator of this project, responsible for deriving the numerical method, performing all of the analysis, and conducting the numerical experiments. Dr. Wetton was the supervisory author and was involved in project design, conception, and manuscript revision.

The remaining work in Chapter 2 and Chapter 3, of which I was the lead

investigator, was original and is in preparation for a manuscript. I am responsible for the thesis manuscript composition with revision support from Dr. Ward and Dr. Wetton.

Table of Contents

Appendix

List of Tables

List of Figures

Acknowledgements

The completion of a thesis, particularly for a PhD, is at least as much a trial in endurance as it is an intelectual pusuit. Therefore, it is impossible to achieve any success without a vartiey of support in a number of places. I want to take the time to acknowledge the important support I have received for which I am eternally grateful.

First and foremost, I need to thank my supervisors, Brian Wetton and Michael Ward for their patience and support while completing this thesis. Each has provided technical and moral support in their own ways throughout the entire process. I am particularly grateful for the support they offered through encouraging and funding my participation at a variety of conferences where I could present my work and network with the mathematical community.

I am extremely grateful to the financial support I received through the Vanier Canada Graduate Scholarship program. This relieved a lot of financial burden and allowed me to engage fully in my project. I was also supported by a four-year fellowship which activated at the completion of the Vanier award and am grateful for the UBC tuition waiver applied during my studies.

In terms of moral support, I could not say enough to appropriately capture the love and understanding I have received from my wonderful fiancée, Sonia, to whom this thesis is dedicated. Through every long night and missed event, her patience and belief in me has helped me get through this entire process. She encourages me to pursue my dreams, but also keeps me grounded and reminds me of the truly important things in life.

I am grateful for the support of my mom, grandma, and family back home, as well as to Aida, Joe, and my new family in Vancouver. In particular, I'd like to acknowledge my mom for her unwaivering support throughout my entire life. From a young age, I had a scientific curiosity brewing inside of me, and she did everything she could to nurture my insatiable appetite for knowledge. I owe all of my commitment to making the world a better place through community engagement to the example she set in our community growing up.

There are too many friends that have provided support of various amounts to mention them all here, but I will isolate a few very significant people. Firstly, I need to thank Kai, Fred, and Chen for our numerous pub outings during my time at UBC. They were the perfect relaxation needed after long period of stress. In particular I'm grateful to Kai for our lengthy discussions, commiserating together through the stressful and frustrating moments, of which there are many, while completing my PhD. Thanks to Mike, Bernhard, Carmen, Kyle, and more for, among other things, great conversation, great sushi, and great laughs! Thank you to Devin and Devon for friendship

and support. The ferry ride to visit them on Vancouver island, always clears my mind and relaxes me. I will always be grateful to the continued support from my physics company at UOIT: Mike, Ryan, and Matt, who still inspire me to great things. In particular, I owe a lot of thanks to Matt for being an academic role model. His success in Europe gave me the self-confidence to start the next phase of my career there.

Finally, I need to thank the little ones in my life, my nieces and nephews: Addison, Zackary, Emma, and Max for continuing to sharpen what may be the most important tool for any scientist, my imagination.

for Sonia

Chapter 1

Introduction

Pattern formation is the observation of orderly outcomes arising from common attributes in a particular system. Patterns exist across all branches of science and occurs on many magnitudes of scale from cell division at the microscopic level to dune formations in the desert. The history of pattern formation is rich and was developed by groups of scientists with interdisciplinary knowledge in mathematics, chemistry, biology, and physics. The origins of pattern formation in science are traced to the study of oscillation in chemical reactions [69]. One of the earliest papers to address this issue mathematically is credited to Lotka [48] in which he solved differential equations that could represent a chemical system and showed that damped oscillation solutions occur. However, he conceded that, as of the time of writing (1910), he was unaware of any real chemical reactions which could be explained by such models. Lotka's work was eventually extended to what became known as the Lotka-Voltera equations (cf. [49],[16]), a general competition model which has most frequently been used to study predator-prey relationships. One significant criticism of this type of model to general pattern formation was that it was more representative of a mechanical equation, such as that of a pendulum, where the final solutions were heavily dependent on initial data [69]. Later, a theoretical framework was presented which allowed for this

required structural stability through limit cycle oscillations. These models became referred to as Brusselator models (cf. [75],[16]), although at the time there was still little evidence of actual chemical reactions that had any sort of oscillatory behaviour. In the many years that followed however, chemical reactions were discovered such as the Briggs-Rauscher (cf. [10], [61]) and perhaps most famously, the Belousov-Zhabotinsky reaction (cf. [8], [83], [19]), which can be described with the Brusselator framework. In the context of limit cycles, Schnakenberg (cf. [71], [16]) refined the general ideas of the Brusselator model into a set of required conditions for limit cycles to form. Tangent to the study of chemical reactions was the study of patterns in the context of fluid dynamics, such as the Rayleigh-Bénard convection patterns (cf. [21], [13]). Unlike the difficulty in experimentally confirming theoretical models of patterns in chemical reactions, the Rayleigh-Bénard instability was, experimentally, very well described [69].

Modern understanding of biological pattern formation is mostly attributed to the seminal paper by Turing [74] in which he showed that diffusion, a mechanism typically associated with stability, could be a destabilizing mechanism in a two-compartment system. His paper showcases several types of solutions including oscillations and travelling waves. The breadth of patterns discussed from this work was a catalyst in the rediscovery and correlation of literature in pattern formation which stimulated the research field [69]. In particular, many of Turing's spatiotemporal patterns were found in papers in population dynamics (cf. [17], [37]). In the context of this thesis, which is a hybrid analytical and numerical analysis of pattern formation, Turing's paper

demonstrates extra significance because it was the first paper to incorporate numerically computed solutions of reaction-diffusion equations alongside analytical results with Turing himself contributing heavily to the building of the computer used [69].

Since Turing's pioneering work, pattern formation problems have been studied in a variety of contexts including animal spotting [63], sea-shell formation [67], urban crime analysis [41], and animal aggregation [12]. A common attribute of most pattern formation problems is that pattern initiation is generally attributed to very complex dynamical systems involving positive feedback loops, self-reinforcing conditions, and antagonistic tendencies [67]. The particular focus on pattern formation in a biological context has interested scientists because of the large scale where cascades of chemical reactions and biological processes, often beginning with a single cell, eventually develop into complex structures that are necessary to support life in organisms. While it may seem a near impossible endeavour to understand the formation of these complex structures, many of them, as a first approximation, can be taken to be independent from one another. For example, the legs of most amphibians develop regularly even when placed in ectopic positions indicating that the growth is primarily due to the influence of local variables (with respect to the larger organism as a whole) [67].

Following the work of Turing, it was postulated that more complex biological pattern formation requires two conditions in order to persist: local self-enhancement and long-range inhibition (cf. [20], [72]). One such model,

presented in [20], is called the Gierer and Meinhardt (GM) model. The authors postulated a coupled partial differential equation model to describe morphogen activation and inhibition as it related to head formation in hydra. However, this model later proved to be useful in describing patterns in such things as the formation of embryonic axes, leaf formation at the tip of a growing shoot, and shell patterns on mollusks [67]. It is of interest to note that, when postulating their model, Gierer and Meinhardt were unfamiliar with the work of Turing and only became aware of it when it was mentioned by one of their article reviewers [51]. This model has a rich history of analysis (cf. [39], [80], [33], [46], [32], [15], [79] among many others) and will be the focus of this thesis. A general non-dimensional GM model can be written down as

$$v_t = D_v \Delta v - v + \frac{v^p}{u^q} \tag{1.1a}$$

$$\tau u_t = D_u \Delta u - u + \frac{v^o}{u^s} \tag{1.1b}$$

with v an activator and u an inhibitor. The coefficients D_i are the respective diffusivities, τ is the inhibitor time constant, and the exponents (p, q, o, s) satisfy [20],

$$p > 1, \quad q > 0, \quad o > 0, \quad s \geq 0, \quad \frac{p-1}{q} < \frac{o}{s+1}. \tag{1.2}$$

We refer to the activator as autocatalytic because it encourages its own growth, satisfying the local-self enhancement for pattern formation. However the activator also induces production of the inhibitor which ultimately limits the destabilizing autocatalytic behaviour, satisfying the long-range in-

hibition requirement.

Typically the onset of pattern formation is initiated by a Turing instability of a spatially homogeneous steady-state [74]. For the GM model, this was conducted in [24] where it was concluded that these types of solutions are unstable when $D_u \gg D_v$. In modern nomenclature, this is known as the semi-strong regime of the GM model which is the focus of the work in this thesis. Final patterns that ultimately form from perturbations to spatially homogeneous initial data are strongly localized and qualitatively very different from the initial structure (cf. [38], [29]). Therefore there is vast interest in understanding these patterns far from the Turing regime. For the semi-strong description, we take $D_v = \epsilon^2 \ll 1$ and $D_u = D = \mathcal{O}(1)$ and make the following scalings which are uniquely determined by appropriate order one behaviour of the system (cf. [33]),

$$v = \epsilon^{\frac{Nq}{(p-1)(s+1)-qo}}\hat{v}, \quad u = \epsilon^{\frac{N(p-1)}{(p-1)(s+1)-qo}}\hat{u}; \qquad (p-1)(s+1) - qo < 0,$$

where N is the dimension of the localized domain. Substituting these scaled variables into (1.1) simplifies to (dropping the hats),

$$v_t = \epsilon^2 \Delta v - v + \frac{v^p}{u^q} \tag{1.3a}$$

$$\tau u_t = D\Delta u - u + \frac{1}{\epsilon^N}\frac{v^o}{u^s}. \tag{1.3b}$$

We remark that the scaling is chosen so that the localized activator is of order unity as ϵ tends to zero. We will also consider a weakly saturated variant of

(1.3) where we replace

$$\frac{v^p}{u^q} \to \frac{v^p}{u^q(1+\sigma v^p)},$$

where the term *weak saturation* is denoted when $\sigma = \mathcal{O}(1)$, specifically that $\sigma \ll \epsilon^{\frac{Npq}{(p-1)(s+1)-qo}}$.

1.1 Main Contribution and Summary of Previous Work

Most of the early mathematical work of the GM model was done in the limit $D \to \infty$, known as the shadow regime (cf. [59], [26]). In this scenario, the inhibitor is spatially constant and (1.3) resolves to a single parabolic PDE for the activator. The solution to this problem concentrates on a finite number of points in a way that is related to a ball-packing problem. Moving from the shadow regime and taking D finite, multiple spike solutions were considered in a one dimensional variant of (1.3) for which $\tau = 0$ (cf. [33], [32]). It was concluded that an N spike pattern is stable if $D < D_N$, some critical diffusivity related to the properties of Green's functions. The analysis of this work was based upon the time constant τ being zero. As τ increases the inhibitor takes longer to notice changes in the activator concentration and it was postulated that this should destabilize the pattern. Indeed the extension for $\tau \neq 0$ in [79] showed this unstable behaviour for τ large and included the conditions for which a Hopf bifurcation occurs on a quasi-equilibrium spike pattern.

One extension of the study of (1.3) to two dimensions involved analyzing a stripe solution centered at the mid-line of a rectangular domain (cf. [15], [39]). The construction of this solution was such that the cross-section was a 1-spike pattern constructed in the one dimensional analysis. The stability of this stripe solution was analyzed in [39] in terms of both breakup and zigzag instabilities which are generated by a class of even and odd eigenfunctions respectively. This work also shows that the addition of saturation can stabilize a stripe from equilibrium. Unlike the one dimensional case however, studies in two-dimensional domains are not as abundant, particularly for non-stripe geometries. Steady-state ring solutions to N-D radially symmetric domains with $N \geq 2$ was investigated in [58] but with no accompanying stability analysis information. The stability of homoclinic stripes and rings has been considered for other models with the Grey-Scott model ([52], [40]), the Schnakenberg model [11], and the Swift-Hohenberg model [22], but less work is available for the GM model. Many of these models share similar characteristics but the presence of a saturation parameter in the GM model introduces unique aspects from previously studied models.

Through the use of matched asymptotic analysis (cf. [9]), we analyze the existence and stability of ring solutions to breakup and zigzag instabilities for the saturated Gierer-Meinhardt model. The analysis of breakup instabilities has a similar structure to that of a stripe and leads to the same conclusions but relies on a different Green's function formulation. Specifically, the ring geometry involves modified Bessel functions which are less analytically tractable than the exponential Green's functions that are generated on

a rectangular domain. As such we require numerical computations of key monotonicity properties to show regions of stability and instability for the breakup. The analysis of zig-zag eigenvalues associated with the odd eigenfunctions for the ring geometry shows a significant difference in derivation as compared to the stripe in [39] or [33]. The latter analysis relies on differentiating the global problem for the activator for which the Laplacian coefficients for a stripe are constant. In contrast, the polar form of the Laplace operator has non-constant coefficients arising from the $1/r$ curvature term and therefore we present a more natural formulation relying on the inner region asymptotic analysis of (1.3).

Unlike the stripe, there is no equivalent universal mid-line with which to place a ring equilibrium. Instead, the equilibrium values depend on the parameters of the problem and, when there is no saturation, undergo a saddle-node bifurcation with which equilibrium radii only exist on $D > D_c$ for some critical diffusivity that depends on the outer disk radius and exponent set. In the presence of saturation a ring equilibrium does exist for all diffusivity values and initiates a hysteresis effect with an unstable branch of equilibrium between two stable branches. This is a phenomena that has not been observed in previous steady-state analysis of the GM or related models. Away from the equilibria values, the dynamics of the ring radii follow a differential equation which persists on an $\mathcal{O}(\epsilon^{-2})$ time scale. As such, in contrast to the stripe problem, the steady-state is quasi time dependent and therefore the linear stability analysis formulation involves an application of the WKB method (or alternatively the multiple time scales method) [9] for handling

the eigenvalue problems. Typically, this slow-time evolution analysis arises with the dynamic evolution of a critical bifurcation parameter [76], but is rarely needed for a linear stability formulation.

Using a boundary fitted coordinate system, we are able to pose the GM model in an arbitrary two-dimensional framework. We use this model to find the existence of saturated near-ring solutions. We believe this is one of the first attempts to analytically treat a non-standard, non-symmetric geometry with this model. The generalization of the model to the boundary fitted coordinates, makes it non-self-adjoint and, as such, intractable to analysis in general geometries. However, it is easily recast as a singular interface problem which can be analyzed and computed numerically using the method of layer potentials. We formulate a numerical method to solve generalized singular interface problems, one of which is the saturated GM model. These singular interface problems are in contrast to pattern formation models developed in [23] which reduce to non-singular curve evolution equations which are more tractable for computation than the models we present. Aside from solving the GM model, we show the generality of our numerical method by applying it to the well studied Mullins-Sekerka problem [55]. The method involves singular properties of the Laplace operator and related operators, such as the modified Helmholtz operator in the GM model. Recent work (cf. [68]) has studied the modified Helmholtz operator using a layer potential formulation as well. However, the focus of that work was for solutions in all of space based on a set of static singular interfaces. Since we are generally interested solely on the evolution of curves, we have designed our method

to focus only on the tracking of curves subject to a set of dynamic conditions.

Finally, for both stripes and rings using general exponent sets for (1.3), the stability analysis involves understanding a non-self-adjoint, non local eigenvalue problem (NLEP). The complex structure of the eigenvalue problem generally leads to bounding arguments for eigenvalues such as the results in [39] and what we present in Chapter 3. However, for specific choices of exponent sets, the eigenvalue problems can be formed in an *explicitly solvable* way. These results were first discovered in [57] and we generalize the conditions for which an NLEP can be explicitly solvable, leading to a new stability classification for a previously unreported exponent set.

1.2 Thesis Outline

We present the material of this thesis as follows. In Chapter 2 we formulate the general boundary fitted coordinate Laplace operator for use in solving the Gierer-Meinhardt model and reduce it to a singular interface problem involving a flux jump condition across some (possibly disconnected) curve Γ and a normal velocity condition. We then restrict this problem to two geometries. In 2.3.1, we first consider the asymptotic construction of a ring solution on some circular domain Ω_{ring} including the extension of the normal velocity condition to a dynamic differential equation for the ring radius. We use this to analyze the ring radii equilibrium and conclude that the equilibrium structure is drastically different with and without saturation where a saddle node bifurcation occurs for the former and a hysteresis effect for the

latter. We also show the existence of ring solutions for which the inhibitor is non-radially symmetric. The determination of these solutions relies on studying a root finding problem of a Fourier transform decomposition and is extremely preferential to the radially symmetric solution root. However, this root finding problem can be used to verify non-radially symmetric solutions that are found with the numerical study of Chapter 6. Next in 2.3.2, we utilize the boundary fitted coordinate framework to analyze the quasi-steady solutions of a near circular solution where the ring radius $r = r(\theta)$. The same model could be derived from a polar coordinate framework but the jump and velocity conditions would be less natural to implement. The boundary-fitted framework extracts both of these conditions regardless of the underlying geometry. We show, using a Fourier analysis, that the first order corrections introduce sinusoidal perturbations to both the curve inhibitor value and radial velocity but that a second order correction is required to account for vertical shifts that may occur. This shifting is due to the interaction of Fourier modes at higher order. Furthermore, we show that when the base radius of a slightly perturbed ring radius is small enough, the velocity corrections are in phase with the curve perturbation and therefore act to stabilize the curve toward a circle. This is due to the curvature being a stabilizing term in the normal velocity equation.

In Chapter 3 we return to the pure radially symmetric ring problem, and perform a linear stability analysis for arbitrary initial ring radius r_0, not necessarily in equilibrium. Because of this, the problem is not separable in time and we rely on a multiple scales argument through the WKB method

to formulate the stability problem. We then derive an NLEP that exists for a certain class of even functions as activator perturbations. We show that without saturation there is, for all τ, an unstable branch of real eigenvalues that leads to breakup instabilities. However, with the inclusion of saturation, we show that breakup patterns can be stabilized. We verify all of these stability bands in 3.2.10, where we discretize the eigenvalue problem and solve it numerically. This requires a robust Newton solve due to the high nonlinearity in the eigenvalue. We perform several numerical experiments to compare asymptotic and numeric computations of upper and lower stability bounds. In 3.3 we consider a second class of instabilities where the activator perturbation is odd. These eigenvalues are perturbations of $\lambda = 0$ and, as we show, are of order ϵ^2. The analysis of these eigenvalues is intimately related to the asymptotic construction of the activator and inhibitor solutions in the inner region near the ring.

In Chapter 4 we introduce the notion of an explicitly solvable NLEP and provide a general framework to classify an NLEP as such. We then apply this framework to a specific exponent set for the GM model in 4.2 for a rectangular domain and in 4.3 for a circular domain. This exponent set yields the same conclusions as the non-explicit case in Chapter 3 but in a way that is more tractable to analysis. Furthermore, in the case of a stripe, the simplicity of the Green's function allows us to determine the stability boundary, dominant mode, and Hopf bifurcation analytically which is generally not obtainable in the classic NLEP formulation. For the ring in which the Green's function involves modified Bessel functions, we can recast the

problem in a way that is amendable to the framework for general NLEPs on a ring in Chapter 3. In this decomposition, we see that the explicit formulation has the effect of extracting the singular behaviour of the eigenvalue pole, a crucial component of the NLEP analysis. Chapter 5 is devoted to full numerical computations of (1.3) in order to verify the existence of stripe and ring solutions, as well as to verify stability results. This includes performing a number of numerical experiments which verify predicted dominant wavemodes for breakup instabilities, the stabilizing effect of saturation, and the stability effects of a circle to zig-zag instabilities.

Finally, in Chapter 6 we derive a numerical scheme to solve the singular interface limit of (1.3) derived in Chapter 2 for any curve geometry in $\mathbb{R}^2$. This involves the use of a layer potential formulation to handle the curve singularities and normal interface velocity. We formulate the problem over M possibly disjoint curves using a scaled arclength formulation in 6.1.2. In 6.1.5, we discuss methods of handling the singular logarithmic integrals and discretize them using a combined Lagrange interpolation, trapezoid method in 6.2.1. In order to validate our method we solve a different, but related problem known as the Mullins-Sekerka problem in 6.2.2. We show that the error converges in the standard way with chosen finite difference and time stepping schemes. In 6.3 we solve the saturated GM model for a variety of initial curves including circles, perturbed circles, ellipses in concentric and non-concentric initializations. We use the analytical results of Chapter 2 to confirm the numerical errors are consistent with the chosen discretizing schemes.

Chapter 2

General Curve Formulation and Quasi-Steady Solutions

Consider a general reaction diffusion equation for an activator v and inhibitor u of the form

$$v_t = \epsilon^2 \Delta v - v + g(u, v) \tag{2.1a}$$

$$\tau u_t = D\Delta u - u + \frac{1}{\epsilon} f(u, v) \tag{2.1b}$$

on a domain $\Omega \subset \mathbb{R}^2$ subject to Neumann boundary conditions on $\partial\Omega$. τ is an effective time scale delay between the activator and inhibitor while D and ϵ^2 are the diffusivities of the inhibitor and activator respectively. As was discussed in Chapter 1, we consider $D = \mathcal{O}(1)$ while $\epsilon \ll 1$ which defines the semi-strong regime.

2.1 Choosing a Coordinate System

Before proceeding to specific geometries, we will derive a general global problem for the inhibitor based on activator localization on arbitrary curves Γ. To do this, we will consider a boundary fitted coordinate system (cf. Figure

2.1, [22], [35], [27]) where

$$x \equiv \gamma_1(s) + \eta\hat{n}_x, \qquad y \equiv \gamma_2(s) + \eta\hat{n}_y.$$

Here s is the arclength of the curve with $\langle\gamma_1(s), \gamma_2(s)\rangle$ being the parametrization of Γ and η is the signed normal distance from the curve with normal $\hat{\mathbf{n}} = \langle\hat{n}_x, \hat{n}_y\rangle$. We consider the normal to be the inward pointing normal relative to Γ and so $\eta > 0$ denotes inside the curve for a single curve.

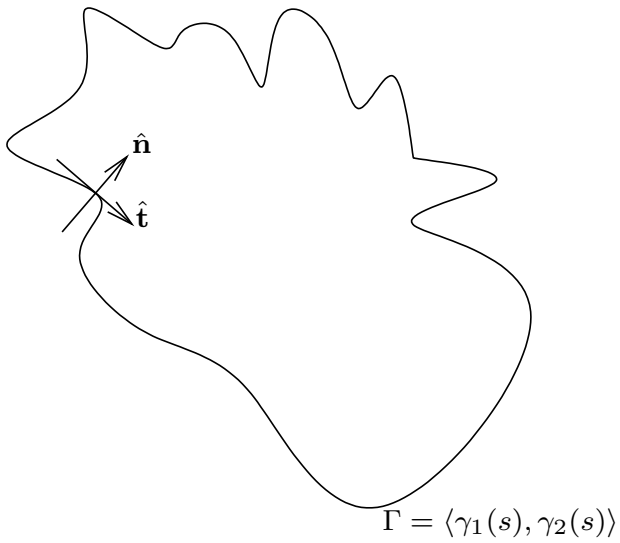

Figure 2.1: The boundary fitted coordinate system for some curve in $\mathbb{R}^2$. The normal points inward relative to the moving curve which is parametrized by unit arclength.

We need to determine the Laplace operator using these boundary fitted coordinates. If we keep in mind that the curve is being parametrized by arclength

then the unit tangent and normal vectors satisfy

$$\hat{\mathbf{t}} \equiv \langle \gamma_1', \gamma_2' \rangle, \qquad \hat{\mathbf{n}} \equiv \langle -\gamma_2', \gamma_1' \rangle;$$
$$\hat{\mathbf{t}}' = \kappa \hat{\mathbf{n}}, \qquad \hat{\mathbf{n}}' = -\kappa \hat{\mathbf{t}}$$

where prime denotes differentiation with respect to s and κ is the signed curvature (positive for convex curves). Using this information we can compute the (s, η) derivatives for (x, y) to get the Jacobian,

$$J = \begin{bmatrix} x_s & x_\eta \\ y_s & y_\eta \end{bmatrix} = \begin{bmatrix} (1-\kappa\eta)\gamma_1' & -\gamma_2' \\ (1-\kappa\eta)\gamma_2' & \gamma_1' \end{bmatrix}; \qquad \det J = 1 - \kappa\eta$$

by noting that $|\hat{\mathbf{t}}| = \sqrt{\gamma_1'^2 + \gamma_2'^2} = 1$. Therefore, by the inverse function theorem,

$$\begin{bmatrix} s_x & s_y \\ \eta_x & \eta_y \end{bmatrix} = \begin{bmatrix} \frac{\gamma_1'}{(1-\kappa\eta)} & \frac{\gamma_2'}{(1-\kappa\eta)} \\ -\gamma_2' & \gamma_1'. \end{bmatrix} \tag{2.2}$$

Taking higher order derivatives and using the chain rule we can ascertain that the Laplace operator in the new coordinate system can be written as

$$\Delta = \partial_{xx} + \partial_{yy} = \partial_{\eta\eta} - \frac{\kappa}{(1-\kappa\eta)}\partial_\eta + \frac{1}{(1-\kappa\eta)}\partial_s \left(\frac{\partial_s}{(1-\kappa\eta)} \right). \tag{2.3}$$

It is worth noting that there is a slight issue with this formulation and that is the singularity $(1 - \kappa\eta)$ in the Laplace operator. The curvature at a point s is the inverse of the radius of the osculating circle tangent to the curve at s which is centered at some $\mathbf{x} \in \mathbb{R}^2$. The singularity arises if the

normal distance from the curve is equal to this osculating radius. Since points infinitesimally close to s will also lie on the osculating circle then they would be the same distance η away from the centre of the circle $\mathbf{x}$. Therefore $\mathbf{x}$ is no longer uniquely defined by a single (s, η) coordinate which means it cannot be a coordinate system for all of $\mathbb{R}^2$. However, the specific use of this coordinate transformation will be in analysis of the activator problem where $\eta \ll 1$ in which case the coordinate system is uniquely defined as long as the curvature is not sufficiently large.

2.2 Asymptotic Expansion of Steady-State

We begin by determining a quasi steady-state solution to (2.1) in the boundary fitted coordinates. We define quasi-steady solutions such that the only time dependence should come from a potential motion of the curve Γ, i.e. for some slow time scale $T = a(\epsilon)t$, we have that the boundary fitted coordinates satisfy $(\eta, s) = (\eta(T), s(T))$. Quasi-steady solutions are typical when considering front motion problems (cf. [65], [31], [11]). We rescale our time derivative,

$$\frac{\partial}{\partial t} \to a\dot{\eta}\frac{\partial}{\partial \eta} + a\dot{s}\frac{\partial}{\partial s}$$

where the dot indicates differentiation with respect to T. We will begin by considering an inner region near the front where v is localized. Having defined the boundary fitted coordinate system, it is easy to see that an $\mathcal{O}(\epsilon)$ region near Γ can be defined with the local distance coordinate $\hat{\eta} = \frac{\eta}{\epsilon}$. We

will also define the activator and inhibitor variable near the front,

$$\tilde{u}(\hat{\eta}, s) = u(\epsilon\hat{\eta}, s), \qquad \tilde{v}(\hat{\eta}, s) = v(\epsilon\hat{\eta}, s).$$

In the local coordinate frame, the system (2.1) becomes,

$$\begin{aligned}
\frac{a}{\epsilon}\dot{\eta}\tilde{v}_{\hat{\eta}} + a\dot{s}\tilde{v}_s =& \tilde{v}_{\hat{\eta}\hat{\eta}} - \frac{\epsilon\kappa}{(1-\epsilon\kappa\hat{\eta})}\tilde{v}_{\hat{\eta}} \\
&+ \frac{\epsilon^2}{(1-\epsilon\kappa\hat{\eta})}\frac{\partial}{\partial s}\left(\frac{\tilde{v}_s}{(1-\epsilon\kappa\hat{\eta})}\right) - \tilde{v} + g(\tilde{u}, \tilde{v}) \qquad (2.4a) \\
\epsilon a\tau\dot{\eta}\tilde{u}_{\hat{\eta}} + \epsilon^2 a\tau\dot{s}\tilde{u}_s =& D\tilde{u}_{\hat{\eta}\hat{\eta}} - \frac{\epsilon D\kappa}{(1-\epsilon\kappa\hat{\eta})}\tilde{u}_{\hat{\eta}} \\
&+ \frac{\epsilon^2 D}{(1-\epsilon\kappa\hat{\eta})}\frac{\partial}{\partial s}\left(\frac{\tilde{u}_s}{(1-\epsilon\kappa\hat{\eta})}\right) - \epsilon^2\tilde{u} + \epsilon f(\tilde{u}, \tilde{v}). \qquad (2.4b)
\end{aligned}$$

We expand the inner solutions as follows:

$$\tilde{v} \sim \tilde{v}_0 + \epsilon\tilde{v}_1 + \ldots \quad \tilde{u} \sim \tilde{u}_0 + \epsilon\tilde{u}_1 + \ldots, \quad \kappa \sim \kappa_0 + \epsilon\kappa_1 + \ldots, \quad \dot{\eta} \sim \dot{\eta}_0 + \epsilon\dot{\eta}_1 + \ldots$$

and note that since we want the curve motion to be on a sub-order one time scale, it is most natural to take $a = \epsilon^2$. To first order we get,

$$\tilde{v}_{0\hat{\eta}\hat{\eta}} - \tilde{v}_0 + g(\tilde{u}_0, \tilde{v}_0) = 0 \qquad (2.5a)$$

$$\tilde{u}_{0\hat{\eta}\hat{\eta}} = 0. \qquad (2.5b)$$

We can solve (2.5b) to get,

$$\tilde{u}_0 = A\hat{\eta} + B$$

but since we expect the global solution for the inhibitor to be $\mathcal{O}(1)$, matching would required that $A = 0$. Therefore we have that

$$\tilde{u}_0 = U_0(s, T)$$

where we explicitly note the possible dependence on the arclength and timescale T. We now draw our attention to (2.5a) which is supplemented by far-field conditions decaying to zero so that the solution is entirely localized. Since the problem exhibits translational invariance, we will impose that $\tilde{v}_{0\hat{\eta}}(0) = 0$ as a front centering condition. We consider the following Lemma for the existence of a homoclinic orbit solution,

Lemma 2.2.0.1 *Consider the problem*

$$\begin{aligned} w_{yy} - w + f(w) = 0, \quad -\infty < y < \infty, \qquad w \to 0 \text{ as } |y| \to \infty, \\ w'(0) = 0, \quad w_m = w(0) > 0 \end{aligned} \tag{2.6}$$

and assume $f(w)$ is C^2 smooth on $w > 0$ with $f(0) = 0$ and $f'(0) < -1$. If we define $Q(w) \equiv f(w) - w$ then a unique, positive, homoclinic orbit solution exists when

1. $Q(0) = 0, \quad Q'(0) < 0$
2. *For $s > 0$ $Q(s) = 0$, $Q'(s) > 0$;* $\qquad Q(w) < 0$, *for $0 < w < s$*
3. $Q(w) > 0$ *for $s < w < w_m$ with w_m satisfying $\int_0^{w_m} Q(w)\,\mathrm{d}w = 0$.*

The requirements on $f(w)$ are needed so that w decays exponentially in the far-field. When $f'(0)$ is finite (such as the case when $f(w) = w^p$) then it

is easy to see the exponential decay condition holds. In an example where $f'(0)$ is not finite such as $f(w) = w \log w$ we can solve (2.6) exactly and show that $w \to \exp(-y^2)$ as y tends to infinity which has an even faster decay than the finite case. The conditions on $Q(w)$ can be proven by taking a first integral of (2.6) and using the front centering condition $w'(0) = 0$. If we take $w = \tilde{v}_0$ and $f(w) = g(U_0, \tilde{v}_0)$ then Lemma 2.2.0.1 gives the conditions for (2.5a) to have homoclinic orbit solutions. See [39], [33], and [43] as examples of where this formulation is used to form homoclinic orbit solutions.

Completely separate from the homoclinic orbit solution, we note that $g(u, v)$ does not depend explicitly on the space parameter and so the solutions to (2.5a) can be written as a superposition of an even and odd function [30]. Since the homoclinic orbit satisfies positivity, this must be the even solution and so formally we say that $\tilde{v}_0$ is the even homoclinic orbit solution to (2.5a). A corollary to the even homoclinic orbit solution is that the odd solution to (2.5a) necessarily blows up as $|\hat{\eta}| \to \infty$.

Continuing the expansion of (2.4) we have at $\mathcal{O}(\epsilon)$,

$$L\tilde{v}_1 = \kappa_0 \tilde{v}_{0\hat{\eta}} - g_u(U_0, \tilde{v}_0)\tilde{u}_1 + \tilde{v}_{0\hat{\eta}}\dot{\eta}_0 \tag{2.7a}$$

$$\tilde{u}_{1\hat{\eta}\hat{\eta}} = -\frac{1}{D} f(U_0, \tilde{v}_0) \tag{2.7b}$$

where

$$L\tilde{v}_1 = \tilde{v}_{1\hat{\eta}\hat{\eta}} - \tilde{v}_1 + g_v(U_0, \tilde{v}_0)\tilde{v}_1.$$

Consider the problem for the homoclinic orbit (2.5a) and differentiate,

$$(\tilde{v}_{0\hat{\eta}})_{\hat{\eta}\hat{\eta}} - \tilde{v}_{0\hat{\eta}} + g_v(U_0, \tilde{v}_0)\tilde{v}_{0\hat{\eta}} = L\tilde{v}_{0\hat{\eta}} = 0. \tag{2.8}$$

Here we see that $\tilde{v}_{0\hat{\eta}}$ is a homogeneous solution to (2.7a) and therefore we will require an orthogonality condition with the source terms. This condition is

$$\kappa_0 \int_{-\infty}^{\infty} \tilde{v}_{0\hat{\eta}}^2 \,\mathrm{d}\hat{\eta} + \dot{\eta}_0 \int_{-\infty}^{\infty} \tilde{v}_{0\hat{\eta}}^2 \,\mathrm{d}\hat{\eta} - \underbrace{\int_{-\infty}^{\infty} g_u(U_0, \tilde{v}_0)\tilde{v}_{0\hat{\eta}}\tilde{u}_1 \,\mathrm{d}\hat{\eta}}_{I} = 0. \tag{2.9}$$

If we define

$$\mathcal{G} \equiv \int_0^{\tilde{v}_0} g_u(U_0, x) \,\mathrm{d}x \tag{2.10}$$

then we can simplify the final integral and use integration by parts to get

$$I = -\int_{-\infty}^{\infty} \mathcal{G}\tilde{u}_{1\hat{\eta}} \,\mathrm{d}\hat{\eta}$$

by noting that since $\tilde{v}_0$ is even then $\mathcal{G}(-\infty) = \mathcal{G}(\infty) = 0$. We now define a new function,

$$\hat{\mathcal{G}}(\hat{\eta}) \equiv \int_0^{\hat{\eta}} \mathcal{G}(x) \,\mathrm{d}x \tag{2.11}$$

so that integrating I by parts once more, we have

$$I = -\tilde{u}_{1\hat{\eta}}\hat{\mathcal{G}}\Big|_{-\infty}^{\infty} + \int_{-\infty}^{\infty} \hat{\mathcal{G}}\tilde{u}_{1\hat{\eta}\hat{\eta}} \,\mathrm{d}\hat{\eta}.$$

Again, since $\tilde{v}_0$ is even then $\mathcal{G}$ is as well, which ensures $\hat{\mathcal{G}}$ is an odd function, so that

$$I = -\hat{\mathcal{G}}(\infty)\left(\tilde{u}_{1\hat{\eta}}(\infty) + \tilde{u}_{1\hat{\eta}}(-\infty)\right) - \frac{1}{D}\int_{-\infty}^{\infty} \hat{\mathcal{G}} f(U_0, \tilde{v}_0)\,\mathrm{d}\hat{\eta}, \tag{2.12}$$

where we have simplified the last integral by using (2.7b). However, since $\tilde{v}_0$ is even then so to is $f(U_0, \tilde{v}_0)$ so the final integrand is odd and hence vanishes over the domain. Finally then we can write the solvability condition (2.9) as

$$\dot{\eta}_0 = -\kappa_0 - \frac{\hat{\mathcal{G}}(\infty)}{\int_{-\infty}^{\infty} \tilde{v}_{0\hat{\eta}}^2\,\mathrm{d}\hat{\eta}}\left(\tilde{u}_{1\hat{\eta}}(\infty) + \tilde{u}_{1\hat{\eta}}(-\infty)\right) \tag{2.13}$$

which prescribes the leading order velocity of the curve. We can also relate the difference in $\tilde{u}_{1\hat{\eta}}$ by integrating (2.7b),

$$\left(\tilde{u}_{1\hat{\eta}}(\infty) - \tilde{u}_{1\hat{\eta}}(-\infty)\right) = -\frac{1}{D}\int_{-\infty}^{\infty} f(U_0, \tilde{v}_0)\,\mathrm{d}\hat{\eta}. \tag{2.14}$$

Finally, we will consider the expansion at $\mathcal{O}(\epsilon^2)$ as this will be needed when analyzing the spectrum of the linearization for a radial geometry,

$$\begin{aligned} L\tilde{v}_2 =& \kappa_0\tilde{v}_{1\hat{\eta}} + \kappa_1\tilde{v}_{0\hat{\eta}} + \kappa_0^2\hat{\eta}\tilde{v}_{0\hat{\eta}} + \dot{\eta}_0\tilde{v}_{1\hat{\eta}} + \dot{\eta}_1\tilde{v}_{0\hat{\eta}} + \dot{s}_0\tilde{v}_{0s} - \tilde{v}_{0ss} \\ & - \frac{1}{2}g_{uu}(U_0, \tilde{v}_0)\tilde{u}_1^2 - g_{uv}(U_0, \tilde{v}_0)\tilde{u}_1\tilde{v}_1 - \frac{1}{2}g_{vv}(U_0, \tilde{v}_0)\tilde{v}_1^2 - g_u(U_0, \tilde{v}_0)\tilde{u}_2, \end{aligned} \tag{2.15a}$$

$$\tilde{u}_{2\hat{\eta}\hat{\eta}} = \frac{1}{D}U_0 + \kappa_0\tilde{u}_{1\hat{\eta}} - \frac{1}{D}f_u(U_0, \tilde{v}_0)\tilde{u}_1 - \frac{1}{D}f_v(U_0, \tilde{v}_0)\tilde{v}_1. \tag{2.15b}$$

Once again, this will have an orthogonality relationship with $\tilde{v}_{0\hat{\eta}}$ producing a condition for the velocity correction $\dot{\eta}_1$ but we do not derive this here as

we will consider a singularity limit where we take ϵ to zero and hence this correction will occur at higher order.

2.2.1 Global Inhibitor Sharp Interface Limit

Turning our attention to the global region where $\eta = \mathcal{O}(1)$, we have that $v \equiv 0$ (to within exponential order) and so we only need to consider the problem for the inhibitor u:

$$D\Delta u - u + \frac{1}{\epsilon} f(u, v) = 0 \tag{2.16}$$

where we assume that $f(u, 0) = 0$ so that the inhibitor solution does not experience global blowup as $\epsilon \to 0$. Therefore then, the only contribution to the reaction term is very close to the curve. In fact, since $f(u, 0) = 0$ and v decays super-linearly to zero we have that,

$$\frac{f(u,v)}{\epsilon} = \frac{f(u, \tilde{v}\left(\frac{\eta}{\epsilon}\right))}{\epsilon} \underset{\epsilon\to 0}{=} \begin{cases} \infty, & \eta = 0 \\ 0, & \text{else} \end{cases}$$

and so (cf. [33])

$$\lim_{\epsilon\to 0} \frac{f(u,v)}{\epsilon} = A\delta(\eta)$$

with $\delta(\eta)$ the Dirac mass centered at $\eta = 0$. To find A, we integrate over a small domain including zero and scale to the inner coordinate,

$$\lim_{\epsilon\to 0} \int_{0^-}^{0^+} \frac{f(u(\eta), v(\eta))}{\epsilon} \, \mathrm{d}\eta = \lim_{\epsilon\to 0} \int_{0^-/\epsilon}^{0^+/\epsilon} f(\tilde{u}(\hat{\eta}), \tilde{v}(\hat{\eta})) \, \mathrm{d}\hat{\eta} = A.$$

Expanding out $f(\tilde{u}, \tilde{v})$,

$$f(\tilde{u}, \tilde{v}) = f(U_0, \tilde{v}_0) + \epsilon \left(f_u(U_0, \tilde{v}_0)\tilde{u}_1 + f_v(U_0, \tilde{v}_0)\tilde{v}_1 \right) + \ldots \underset{\epsilon \to 0}{=} f(U_0, \tilde{v}_0)$$

so that

$$A = \int_{-\infty}^{\infty} f(U_0, \tilde{v}_0)\, \mathrm{d}\hat{\eta},$$

and finally (2.16) becomes

$$D\Delta u - u = -\left(\int_{-\infty}^{\infty} f(U_0, \tilde{v}_0)\, \mathrm{d}\hat{\eta} \right) \delta(\eta). \tag{2.17}$$

We refer to this as the sharp interface limit of (2.16) since we have captured all of the asymptotic structure via a singularity at the interface. By using the sharp interface limit, we do not need to expand u in powers of ϵ as (2.17) captures the entire global problem. Upon solving u we will need to match to the inner region via

$$u(\epsilon\hat{\eta}, s) \sim u(0, s) + \epsilon\hat{\eta} \left. \frac{\partial u}{\partial \eta} \right|_{\eta = 0^{\pm}} + \cdots = \tilde{u}_0(\pm\infty) + \epsilon\tilde{u}_1(\pm\infty),$$

where the $\pm$ indicates approaching the curve from either side of $\eta = 0$. Upon performing the matching we have $u(0, s) = U_0$ and

$$\tilde{u}_{1\hat{\eta}}(\pm\infty) = \left. \frac{\partial u}{\partial \eta} \right|_{\eta = 0^{\pm}}. \tag{2.18}$$

Using this with (2.14) we have that

$$\left[\frac{\partial u}{\partial n} \right]_{\eta = 0} = -\frac{1}{D} \int_{-\infty}^{\infty} f(U_0, \tilde{v}_0)\, \mathrm{d}\hat{\eta},$$

where $[\cdot]_{\eta=a}$ indicates a jump from $\eta = a^+$ to $\eta = a^-$. This is the equivalent singularity structure to match the Dirac measure in (2.17). Combining everything we can write the problem for u as

$$D\Delta u - u = 0, \qquad x \in \Omega \tag{2.19a}$$

$$\frac{\partial u}{\partial n} = 0, \qquad x \in \partial\Omega \tag{2.19b}$$

$$u = U_0(s), \qquad x \in \Gamma \tag{2.19c}$$

$$\left[\frac{\partial u}{\partial n}\right]_\Gamma = -\frac{1}{D}\int_{-\infty}^{\infty} f(U_0, \tilde{v}_0)\,\mathrm{d}\hat{\eta}, \qquad x \in \Gamma. \tag{2.19d}$$

This quasi-steady problem is subject to a normal velocity V given by (2.13) which we can rewrite using the outer coordinates as

$$V_0 = \kappa_0 + \mathcal{H}\left(\left.\frac{\partial u}{\partial n}\right|_{\eta=0^+} + \left.\frac{\partial u}{\partial n}\right|_{\eta=0^-}\right) \tag{2.19e}$$

where we have defined

$$\mathcal{H} \equiv \frac{\hat{\mathcal{G}}(\infty)}{\int_{-\infty}^{\infty} \tilde{v}_{0\hat{\eta}}^2\,\mathrm{d}\hat{\eta}}. \tag{2.20}$$

Note that if V is the normal velocity measured with respect to the origin then $\dot{\eta} = -V$. This is because for a single curve, if $\dot{\eta} > 0$ then points inside the curve are increasing their distance from the curve, i.e. the curve is expanding in space. However, we have defined the inward pointing normal to be positive and so $V > 0$ means that the curve shrinks, hence $V = -\dot{\eta}$. The system (2.19) is what we will solve for quasi-steady state profiles.

2.3 Quasi-Steady State Profiles for the Gierer-Meinhardt Model

Moving forward, we will consider the saturated Gierer-Meinhardt (GMS) model (cf. [20], [39], [82]),

$$g(u,v) = \frac{v^2}{u^q(1+\sigma v^2)}, \qquad f(u,v) = \frac{v^o}{u^s} \tag{2.21}$$

for some exponent set $(2, q, o, s)$ and saturation parameter $\sigma > 0$. Notice that these functions obey the required properties of $f(u,v)$ and $g(u,v)$ outlined above. With this formulation then we can write $\tilde{v}_0 = U_0^q w$ and recast (2.5a) for w with

$$w_{\hat{\eta}\hat{\eta}} - w + \frac{w^2}{1+bw^2} = 0, \qquad w'(0) = 0, \quad \lim_{|\hat{\eta}|\to\infty} w = 0, \tag{2.22}$$

where

$$b = U_0^{2q}\sigma > 0 \tag{2.23}$$

is a modified saturation parameter. Notice if $\sigma = b = 0$ then we can analytically satisfy the conditions of Lemma 2.2.0.1 and get that the positive even homoclinic orbit solution to (2.22) is

$$w(\hat{\eta}) = \frac{3}{2}\,\mathrm{sech}^{\,2}\left(\frac{\hat{\eta}}{2}\right). \tag{2.24}$$

If $b \neq 0$ we can no longer obtain an analytic solution but we can investigate the criteria on b for which a homoclinic solution exists via Lemma 2.2.0.1 and compute it numerically. This was considered in [39] for a stripe and we reproduce the analysis here. Let

$$Q(w) = \frac{w^2}{1 + bw^2} - w$$

and look for rest-points of the differential equation when $Q(w) = 0$. We see that $w = 0$ is a root for all b and the other two roots are given by,

$$w^{\pm} = \frac{1 \pm \sqrt{1 - 4b}}{2b} \tag{2.25}$$

where we notice that real roots fail to exist if $b > 1/4$. If $b = 1/4$ then we have that the two roots degenerate to a single root $w^{\dagger} = 2$. If we classify the roots of (2.25) by linear theory, we have that $Q'(0) < 0$ for all b which classifies it as a saddle point as was required via condition 1 in Lemma 2.2.0.1. Aside from $w^* = 0$, we have

$$Q'(w^*) = \frac{2 - w^*}{w^*}$$

which is zero when $w^* = w^{\dagger}$ owing to the degeneracy of the root. Therefore this root cannot be classified by linear theory but we have that $Q''(w^{\dagger}) = -1/2$ and therefore for $b = 1/4$ since $w = 0$ and $w = w^{\dagger}$ are the only roots then $Q(w) < 0$ for all w. Therefore we cannot satisfy condition 2 or 3 in Lemma 2.2.0.1 and no homoclinic orbit exists at this value. For $0 \leq b < 1/4$, since $w^+ > w^{\dagger}$ ($w^- < w^{\dagger}$) then $Q'(w^+) < 0$ ($Q'(w^-) > 0$) and therefore $w = w^-$ is a center while $w = w^+$ is another saddle point. Therefore, in

terms of condition 2 in Lemma 2.2.0.1, $s = w^-$. To satisfy condition 3, we require

$$\int_0^{w(0)} Q(u)\,\mathrm{d}u = 0. \tag{2.26}$$

We already concluded that no homoclinic orbit exists when $b = 1/4$ but as b decreases from this value, causing $w = w^\dagger$ to degenerate into w^+ and w^- then by condition 3 of Lemma 2.2.0.1, a homoclinic orbit will begin to exist at the moment when $w(0) = w^+$. We can determine this critical $b = b_c$ value by numerically solving (2.26) with w^+ given by (2.25). We conclude that

$$b_c = 0.2113763204, \qquad w^+(b_c) = 3.295208658. \tag{2.27}$$

Notice that at this point exactly, the maximum value $w(0) = w^+$ is also a saddle point of the phase space and therefore we actually have a heteroclinic orbit here connecting $w = 0$ to $w = w^+$. However for $b < b_c$ then $w(0) < w^+$ and therefore, the homoclinic orbit exists on $0 \leq b < b_c$. Having chosen a b value in the acceptable range then we can compute solutions to (2.22) using a standard finite difference solver on a truncated domain $[0, \hat{L}]$ (see section 6.3). Examples of homoclinic orbits for different b values are in Figure 2.2.

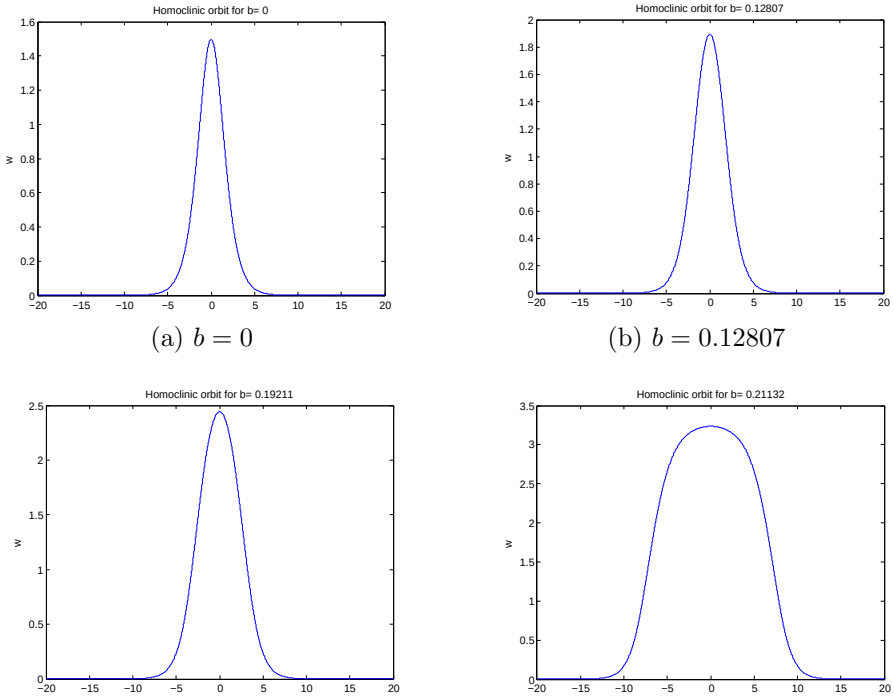

(a) $b = 0$ (b) $b = 0.12807$

(c) $b = 0.19211$ (d) $b = 0.21132$

Figure 2.2: Solutions to (2.22) for different values of b. Here we choose $\hat{L} = 20$ as a sufficient representation of infinity. Note we can solve the equation on $[0, \hat{L}]$ and use symmetry because the functions are even.

The homoclinic orbit problem holds for any curve Γ and hence the only effect of the geometry of the curve is in the inhibitor problem u. Separating the homoclinic, we can write (2.19) in a more tractable way. Firstly we have that

$$\int_{-\infty}^{\infty} f(U_0, \tilde{v}_0)\,\mathrm{d}\hat{\eta} = U_0^{\beta}\int_{-\infty}^{\infty} w^o\,\mathrm{d}\hat{\eta}, \quad \int_{-\infty}^{\infty} \tilde{v}_{0\hat{\eta}}^2\,\mathrm{d}\hat{\eta} = U_0^{2q}\int_{-\infty}^{\infty} w_{\hat{\eta}}^2\,\mathrm{d}\hat{\eta}; \quad (2.28a)$$

$$\beta = qo - s. \quad (2.28b)$$

Furthermore, we can actually simplify $\hat{\mathcal{G}}$ in (2.11) which we first write using

the homoclinic as

$$\hat{\mathcal{G}}(\infty) = -qU_0^{2q-1}\int_0^\infty \int_0^{w(\hat{\eta})} \frac{v^2}{1+bv^2}\,\mathrm{d}v\,\mathrm{d}\hat{\eta} = qU_0^{2q-1}\int_0^\infty \mathcal{W}(w)\,\mathrm{d}\hat{\eta}$$

where $\mathcal{W}$ is defined by

$$\mathcal{W} \equiv \int_0^w \frac{v^2}{(1+bv^2)}\,\mathrm{d}v. \tag{2.29}$$

To simplify this, consider the homoclinic orbit problem (2.22), multiply by $w_{\hat{\eta}}$, and integrate to get

$$w_{\hat{\eta}}^2 - w^2 + 2\mathcal{W}(w) = 0.$$

If we integrate again, we get

$$\int_0^\infty \mathcal{W}(w)\,\mathrm{d}\hat{\eta} = \frac{1}{4}\left(\int_{-\infty}^\infty w^2\,\mathrm{d}\hat{\eta} - \int_{-\infty}^\infty w_{\hat{\eta}}^2\,\mathrm{d}\hat{\eta}\right) \tag{2.30}$$

where we have exploited that $\mathcal{W}(w)$ is an even function. Finally then we can use this expression for $\hat{\mathcal{G}}$ with (2.28a) in $\mathcal{H}$ to write (2.20) as

$$\mathcal{H} = -\frac{q}{4U_0}\left(\frac{\int_{-\infty}^\infty w^2\,\mathrm{d}\hat{\eta}}{\int_{-\infty}^\infty w_{\hat{\eta}}^2\,\mathrm{d}\hat{\eta}} - 1\right) \equiv -\frac{q}{4U_0}\hat{\mathcal{H}}. \tag{2.31}$$

This form is convenient because we avoid the integral with respect to w and the spatial integrals can easily be computed from an analytic or numerically computed homoclinic. This form is also useful because it holds for any function $g(u,v)$ with perhaps slightly different leading constants which makes it more universal. Furthermore, as long as $g(u,v)$ is such that U_0 can easily be

extracted from $\tilde{v}_0$ then we explicitly remove the U_0 dependence in a tractable way. With this simplification we now have the inhibitor problem is

$$D\Delta u - u = 0, \qquad x \in \Omega \tag{2.32a}$$

$$\frac{\partial u}{\partial n} = 0, \qquad x \in \partial\Omega \tag{2.32b}$$

$$u = U_0(s), \qquad x \in \Gamma \tag{2.32c}$$

$$\left[\frac{\partial u}{\partial n}\right]_\Gamma = -\frac{1}{D}U_0^\beta \mathcal{A}, \tag{2.32d}$$

$$V_0 = \kappa_0 - \frac{q}{4U_0}\hat{\mathcal{H}}\left(\left.\frac{\partial u}{\partial n}\right|_{\eta=0^+} + \left.\frac{\partial u}{\partial n}\right|_{\eta=0^-}\right), \tag{2.32e}$$

where we have defined

$$\mathcal{A} = \int_{-\infty}^{\infty} w^o \,\mathrm{d}\hat{\eta}. \tag{2.33}$$

2.3.1 Inhibitor Problem on a Circular Curve

We start by considering the curve Γ to be a circle of radius r_0 inside a circular domain $0 \le r \le R$. In this case, the inward normal is $\hat{\mathbf{n}} = -\hat{\mathbf{r}}$ and

$$\left.\frac{\mathrm{d}u}{\mathrm{d}n}\right|_{\hat{\eta}=0^\pm} = -u_r(r_0^\mp)$$

where we note that $\hat{\eta}^+$ is slightly on the inside of the curve which from the radial coordinate perspective is r_0^- and the opposite is true for $\hat{\eta}^-$. Using a polar coordinate system, we have, for this geometry, that the inhibitor

problem (2.32) reduces to

$$\frac{1}{r}\frac{\partial}{\partial r}\left(r\frac{\partial u}{\partial r}\right)+\frac{1}{Dr^2}\frac{\partial^2 u}{\partial \theta^2}-\frac{1}{D}u=0, \qquad 0\le r\le R, \quad r\neq r_0, \tag{2.34a}$$

$$\frac{\partial u}{\partial r}=0, \qquad r=R \tag{2.34b}$$

$$u=U_0(\theta), \qquad r=r_0 \tag{2.34c}$$

$$\left[\frac{\partial u}{\partial r}\right]_{r_0}=-\frac{1}{D}U_0^{\beta}\mathcal{A}, \tag{2.34d}$$

$$\frac{\mathrm{d}r_0}{\mathrm{d}t}=-\frac{1}{r_0}-\frac{q}{4U_0}\hat{\mathcal{H}}\left(\left.\frac{\partial u}{\partial r}\right|_{r=r_0^+}+\left.\frac{\partial u}{\partial r}\right|_{\eta=r_0^-}\right). \tag{2.34e}$$

Here we have noted that the curvature κ_0 and normal velocity V are, $\kappa_0=\frac{1}{r_0}$, $\frac{\mathrm{d}r_0}{\mathrm{d}t}=-V$ respectively.

Radially Symmetric Solution

We will begin by considering U_0 a constant and denote this as the radially symmetric ring solution, the details of which are similar to [45]. We can immediately write the bounded solution to (2.34a) satisfying $u_r=0$ on $r=R$ and u bounded as $r\to 0^+$ as

$$u(r)=\begin{cases} AI_0\left(\frac{r}{\sqrt{D}}\right), & 0\le r\le r_0 \\ E\left(\alpha_0 I_0\left(\frac{r}{\sqrt{D}}\right)+K_0\left(\frac{r}{\sqrt{D}}\right)\right), & r_0\le r\le R \end{cases}, \qquad \alpha_0=-\frac{K_0\left(\frac{R}{\sqrt{D}}\right)'}{I_0\left(\frac{R}{\sqrt{D}}\right)'}$$

where I_0 and K_0 are the zeroth order modified Bessel functions and prime indicates differentiation with respect to r. To avoid certain chain rule expressions, we will adopt the following notation for the location of the prime

throughout:

$$f'(u(r)) = \left.\frac{\mathrm{d}f}{\mathrm{d}u}\right|_{u=u(r)}, \qquad f(u(r))' = \frac{\mathrm{d}f(u(r))}{\mathrm{d}r} = f'(u(r))\frac{\mathrm{d}u}{\mathrm{d}r}. \tag{2.35}$$

Enforcing continuity and the jump condition (2.34d) at r_0 we have

$$u(r) = \frac{r_0}{D}U_0^{\beta}\mathcal{A}G_0(r;r_0) \tag{2.36}$$

where we have used the Wronskian relationship,

$$W(r) = I_0\left(\frac{r}{\sqrt{D}}\right)K_0\left(\frac{r}{\sqrt{D}}\right)' - K_0\left(\frac{r}{\sqrt{D}}\right)I_0\left(\frac{r}{\sqrt{D}}\right)' = -\frac{1}{r}. \tag{2.37}$$

Here $G_0(r;r_0)$ is the Green's function

$$G_0(r;r_0) = \begin{cases} \mathcal{J}_{0,1}(r)\mathcal{J}_{0,2}(r_0), & 0 \le r \le r_0 \\ \mathcal{J}_{0,1}(r_0)\mathcal{J}_{0,2}(r), & r_0 \le r \le R \end{cases} \tag{2.38}$$

where

$$\mathcal{J}_{0,1}(r) = I_0\left(\frac{r}{\sqrt{D}}\right), \qquad \mathcal{J}_{0,2}(r) = \alpha_0 I_0\left(\frac{r}{\sqrt{D}}\right) + K_0\left(\frac{r}{\sqrt{D}}\right). \tag{2.39}$$

We can determine the value of U_0 by solving $u(r_0) = U_0$ to get

$$U_0 = \left(\frac{D}{r_0\mathcal{A}G_0(r_0;r_0)}\right)^{1/(\beta-1)}. \tag{2.40}$$

For $b = 0$, this is an explicit expression for U_0, However, for $b \neq 0$ then $\mathcal{A}$ depends on b and hence U_0 as well. However, this can be solved with an

iterative technique such as Newton's Method. Regardless we can use (2.23) to define (cf. [39])

$$\tilde{G}(b) \equiv b\mathcal{A}^{\frac{2q}{\beta-1}} = \left(\frac{D}{r_0 G_0(r_0; r_0)}\right)^{\frac{2q}{\beta-1}} \sigma \tag{2.41}$$

and numerically (Figure 2.3) we see that $\frac{\mathrm{d}\mathcal{A}}{\mathrm{d}b} > 0$. Therefore, $\frac{\mathrm{d}\tilde{G}}{\mathrm{d}b} > 0$ and so for each σ there is a unique b and vice-versa. An elegant proof in appendix B of [82] shows analytically that $\frac{\mathrm{d}\tilde{G}}{\mathrm{d}b} > 0$ when $o = 2$. The monotonicity of $\tilde{G}$ guarantees that there is a unique root U_0 to find with the Newton solve of (2.40).

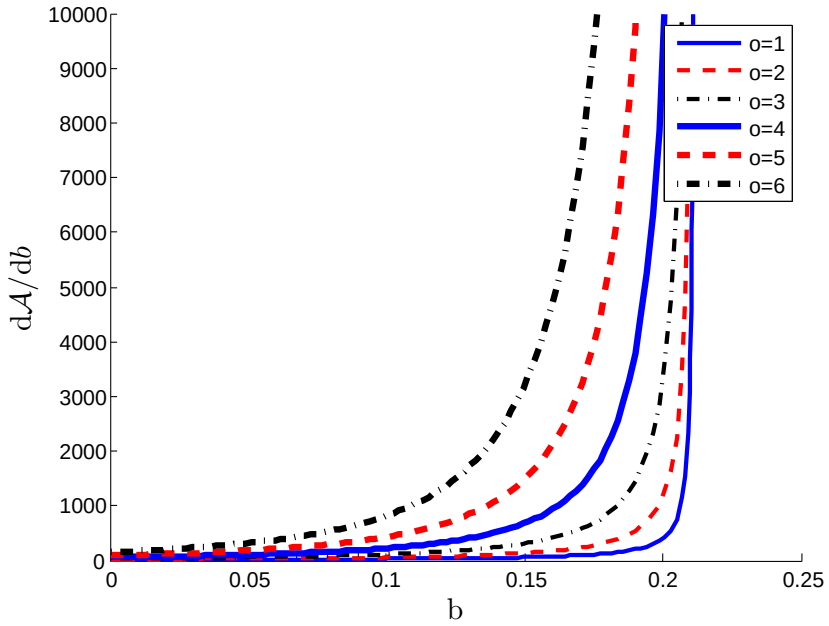

Figure 2.3: Numerical computation of the b derivative of $\mathcal{A}$ for $o = 1$ to $o = 6$. Here we see that the derivative is always positive and each value of o is bounded from below by the previous values. The integral diverges as b approaches b_c from the left.

Finally, we can determine the normal velocity of the ring solution. We can re-write (2.36) as

$$u(r) = \frac{U_0}{G_0(r_0; r_0)} G_0(r; r_0) \tag{2.42}$$

which we substitute into (2.34e) to get

$$\frac{\mathrm{d}r_0}{\mathrm{d}T} = -\frac{1}{r_0} - \frac{q}{4}\hat{\mathcal{H}}\left(\frac{\mathcal{J}'_{0,1}(r_0)}{\mathcal{J}_{0,1}(r_0)} + \frac{\mathcal{J}'_{0,2}(r_0)}{\mathcal{J}_{0,2}(r_0)}\right). \tag{2.43}$$

Rather than consider varying R and D separately, typically (cf. [39]) the outer radius is set to $R = 1$ in an absolute geometry frame and then it is rescaled to an effective domain with a unit diffusion coefficient. We note that this can be achieved in the current formulation by setting $D = 1$ everywhere and then replacing

$$R = \frac{1}{\sqrt{D}} = \ell$$

where this D or ℓ is to be varied. Unless otherwise stated, we will adopt this formulation moving forward. It is worth noting that when the saturation is not zero, the problems are not entirely equivalent as the diffusivity does not properly scale in (2.41). We begin by considering no saturation ($\sigma = b = 0$) where Figure 2.4 shows (2.43) versus r_0 for exponent set $(2, 1, 2, 0)$ and various values of $R = \ell$.

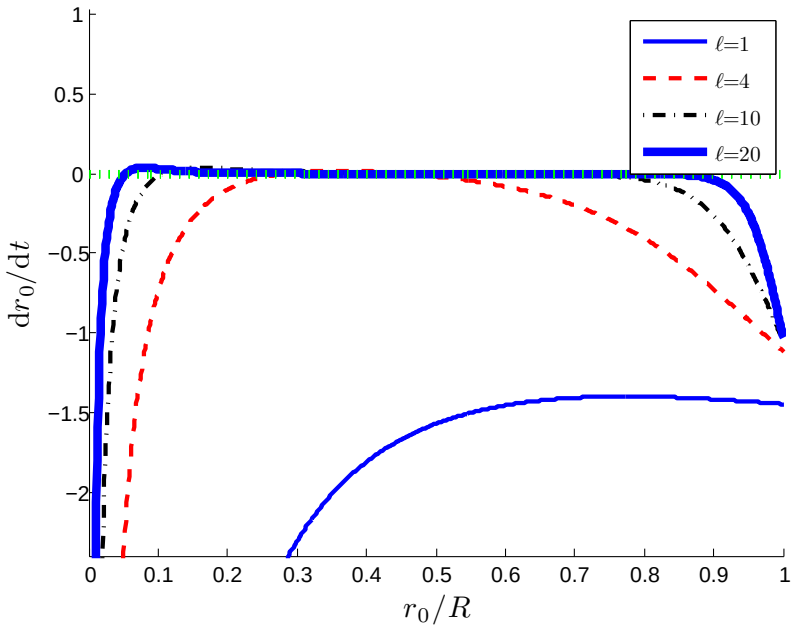

Figure 2.4: Phase portrait of (2.43) for $D = 1$, $b = 0$, exponent set $(2, 1, 2, 0)$, and various values of R.

Notice that (2.43) does not depend on the exponents o or s and so only varying q can make a difference. The plot for $q = 2$ is shown in Figure 2.5 which overall does not show any qualitative difference to $q = 1$.

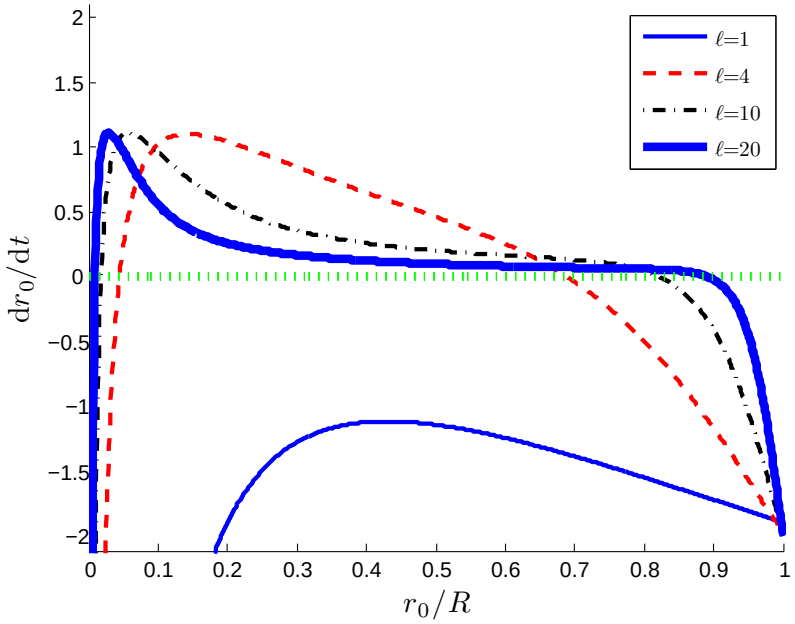

Figure 2.5: Phase portrait of (2.43) for $D = 1$, $b = 0$, exponent set $(2, 2, 2, 0)$, and various values of R.

In both Figure 2.4 and 2.5, we have that for small values of $R = \ell$ there are no equilibrium values to (2.43) and that transitions to a stable and unstable equilibrium as ℓ increases. Therefore, (2.43) undergoes a saddle-node bifurcation. We compute this bifurcation curve numerically by using a Newton's method continuation on r_0 starting from the smallest root r_{0s}. We can approximate these roots asymptotically by defining

$$F(r) = \left(\frac{\mathcal{J}'_{0,1}(r)}{\mathcal{J}_{0,1}(r)} + \frac{\mathcal{J}'_{0,2}(r)}{\mathcal{J}_{0,2}(r)}\right) = \frac{I_1(r)}{I_0(r)} + \frac{\alpha_0 I_1(r) - K_1(r)}{\alpha_0 I_0(r) + K_0(r)} \tag{2.44}$$

and then for $r \ll 1$ we have

$$F(r) \sim -\frac{1}{(\alpha_0 + \log(2) - \log(r) - \gamma)r}$$

with $\gamma \approx 0.5772156649$ the Euler-Mascheroni constant. Therefore from (2.43),

$$\frac{\mathrm{d}r_0}{\mathrm{d}T} \sim \left(\frac{q\hat{\mathcal{H}}}{4(\alpha_0 + \log(2) - \log(r) - \gamma)} - 1 \right) \frac{1}{r_0} + \mathcal{O}(r_0). \tag{2.45}$$

and we can approximate r_{0s} by setting the expression in brackets to zero,

$$r_{0s} \approx \exp\left(\alpha_0 + \log(2) - \gamma - \frac{q\hat{\mathcal{H}}}{4} \right). \tag{2.46}$$

As R tends to infinity, α_0 tends to zero and so there is a limiting small radius,

$$r_{0s} \approx 1.1229 \exp(-q) \tag{2.47}$$

where we have noted that when $\sigma = 0$ then $\hat{\mathcal{H}} = 4$. In Figures 2.4 and 2.5 we can see this limiting small stationary point radius being approached as ℓ increases. For the continuation method then we take R sufficiently large (here we choose $R = 10$) and take as an initial guess $r_0 = r_{0s}$ and iterate until convergence. We then increase r_0 and find the corresponding R that creates an equilibrium value. We plot the $\sigma = 0$ bifurcation diagram in Figure 2.6. Notice that for $q = 1$ the asymptotic approximation is not very accurate for the lower root but from Figure 2.4 we see that at $R = 10$ the small equilibrium radius is $r_{0s} \approx 1$ which is sufficiently far from the small r_0 asymptotic regime

that terms of $\mathcal{O}(r_0)$ can no longer be neglected in (2.45). However, since we are mostly interested using the asymptotic approximation for initializing the numerical algorithm, the accuracy is not of critical importance.

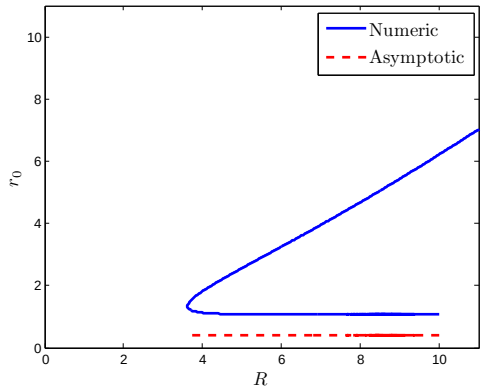

(a) $q = 1$

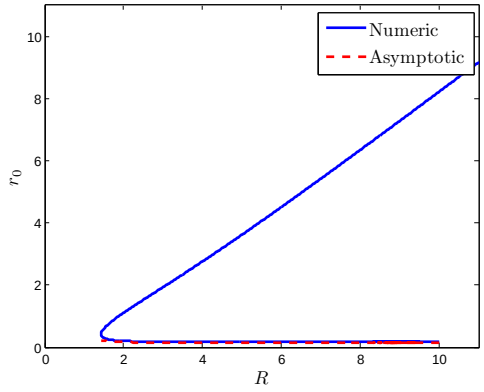

(b) $q = 2$

Figure 2.6: Bifurcation diagram to (2.43) for different values of the exponent q and $b = 0$. The differential equation undergoes a saddle node bifurcation when $R = 3.6220$ (for $q = 1$) and $R = 1.4296$ (for $q = 2$). The larger of the equilibrium r_0 values belong to the stable branch. The red dashed curve represents an asymptotic approximation to the lower radius.

The case with no saturation was mentioned as an extension of work for

ring solutions with the Grey-Scott model [45]. However, the analysis did not consider saturation which we now present. The addition of saturation requires a more delicate approach since the saturation value σ is the static parameter and not b which varies as U_0 varies. Therefore, $\hat{\mathcal{H}}$ in (2.43) is no longer static when $b \neq 0$ and to solve (2.43) we must first solve (2.40) for a given r_0 and then compute b (and hence $\hat{\mathcal{H}}$) with (2.23). We solve the problem (2.40) for U_0 numerically using Newton's method. However, we do so in a special way that stabilizes b. The details of this are presented in 6.3.2 and are omitted here but we indicate that the reason is to prevent b from exceeding its maximum value artificially (i.e. as in the intermediate Newton's method steps). Something we notice immediately from (2.41) is that the denominator tends to zero as r_0 tends to zero and thus for any $\sigma > 0$ we have that $\mathcal{A}$ diverges or that b tends to the critical value as r_0 tends to 0. This is demonstrated numerically in Figure 2.7.

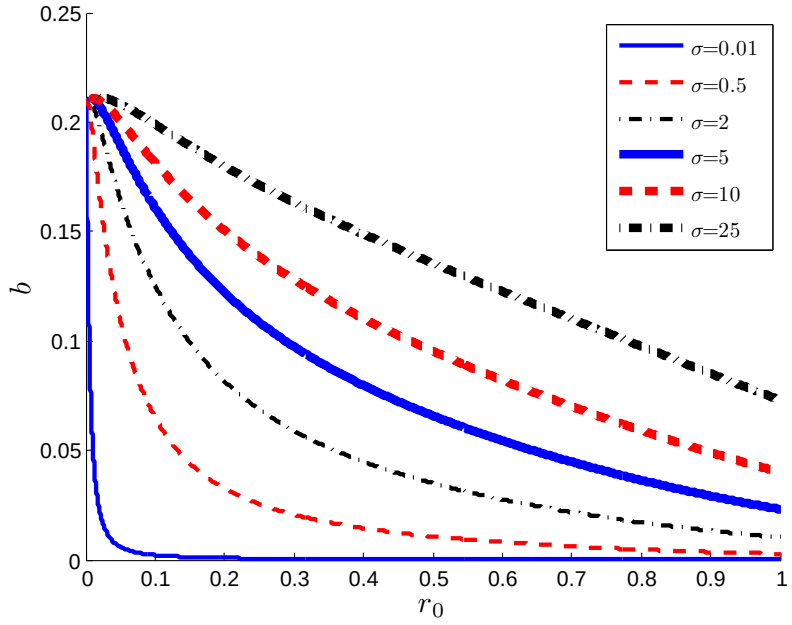

Figure 2.7: Modified saturation parameter b as a function of r_0 for various saturation values σ. Here we take $D = 1$, $R = 1$ and exponent set $(2, 1, 2, 0)$.

When $\sigma = 0$ we had that as r_0 tended to zero then $F(r_0)$ from (2.44) tended to zero as well since $\hat{\mathcal{H}}$ was fixed. Therefore $\mathrm{d}r_0/\mathrm{d}t$ tended to negative infinity as evidenced by Figures 2.4 and 2.5. However, when $\sigma \neq 0$ then since b tends to the critical value as r_0 tends to zero then $\hat{\mathcal{H}}$ tends to infinity. While it can be hard to analyze the growth of $\hat{\mathcal{H}}$ analytically, from Figure 2.8, we can conjecture that it grows faster than $\log r_0$ and so therefore we actually have that $F(r_0)$ (and hence $\mathrm{d}r_0/\mathrm{d}t$) tends to positive infinity as r_0 tends to zero.

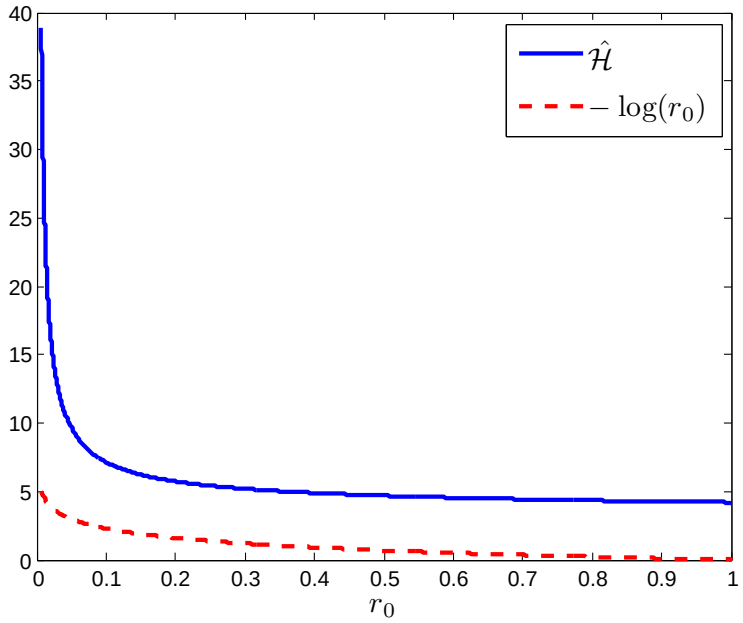

Figure 2.8: Growth of $\hat{\mathcal{H}}$ versus $-\log(r_0)$ for $R = 1$ and when $\sigma = 5$.

We plot (2.43) in Figure 2.9 for saturation values $\sigma = 0.5$, 5, 10, and 25 for exponent set $(2, 1, 2, 0)$ and various values of $R = \ell$ (with $D = 1$). Figure (2.10) repeats the experiment but with the exponent set $(2, 2, 2, 0)$ and excludes $\sigma = 25$ since the single root is so close to $r_0 = R$ for R large that it is difficult to compute.

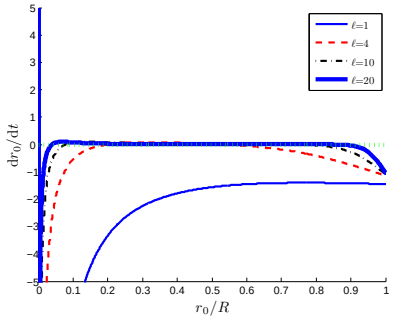

(a) $\sigma = 0.5$

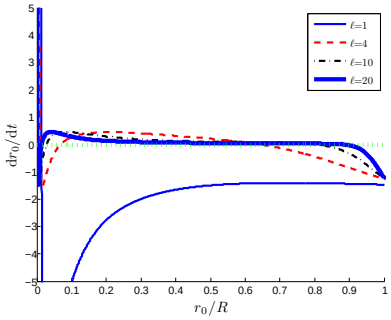

(b) $\sigma = 5$

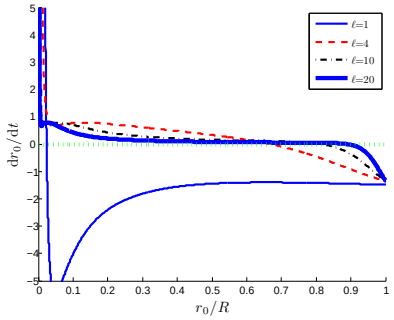

(c) $\sigma = 10$

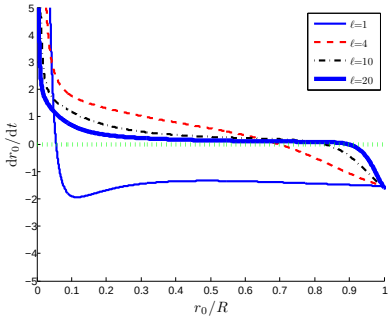

(d) $\sigma = 25$

Figure 2.9: Right-hand side to (2.43) for various saturation values, σ and boundary values R. The exponent set here is $(2, 1, 2, 0)$ and $D = 1$.

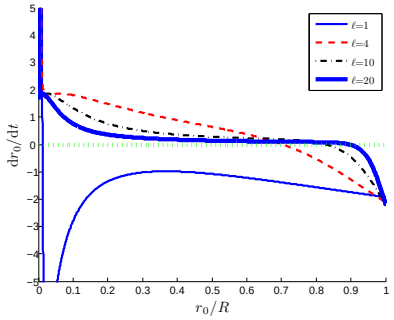

(a) $\sigma = 0.5$

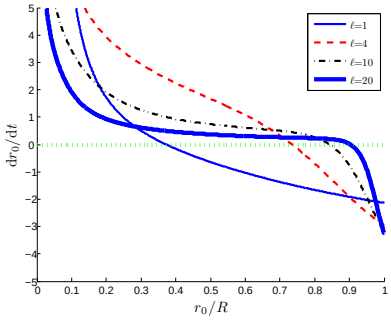

(b) $\sigma = 5$

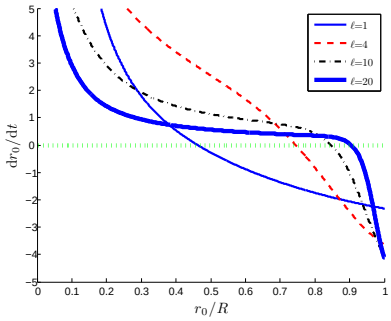

(c) $\sigma = 10$

Figure 2.10: Right-hand side to (2.43) for various saturation values, σ and boundary values R. The exponent set here is $(2, 2, 2, 0)$ and $D = 1$.

The addition of saturation drastically alters the root structure to (2.43). If $\sigma \ll 1$ then the behaviour should be similar to $\sigma = 0$ since, from Figure 2.7, b very quickly tends to zero. This means that very quickly, for R not too large, $\mathrm{d}r_0/\mathrm{d}t$ goes negative and there must be a root very close to $r_0 = 0$ as is evidenced in Figure 2.9a when $\sigma = 0.5$. Since $\mathrm{d}r_0/\mathrm{d}t$ starts positive, this root is necessarily stable and exists prior to $R = R_c$, the saddle-node bifurcation point when $\sigma = 0$. Therefore, the effect of the saturation is to add an extra stability branch emanating from $r_0 = 0$. Since these stable roots are very

small, they can quickly cause instability in Newton algorithms where b is near the critical value. Furthermore, since $\mathrm{d}r_0/\mathrm{d}t$ starts at positive infinity, we can no longer guarantee the existence of a small root for $R \gg 1$ and therefore cannot initialize around something analogous to (2.47). However, as r_0 tends to R we have that b tends to zero and so we still expect the larger stable root near $r_0 = R$. As such, we begin the bifurcation solver by numerically searching for a root near $r_0 = R$ and follow a downward continuation in r_0. Figure 2.11 shows the bifurcation diagram for $\sigma = 10$ and $\sigma = 8$ with exponent set $(2, 1, 2, 0)$ along with the small r_0 asymptotic expression computed from (2.46) where now this has to also be handled with a Newton solve since $\hat{\mathcal{H}} = \hat{\mathcal{H}}(r_0)$.

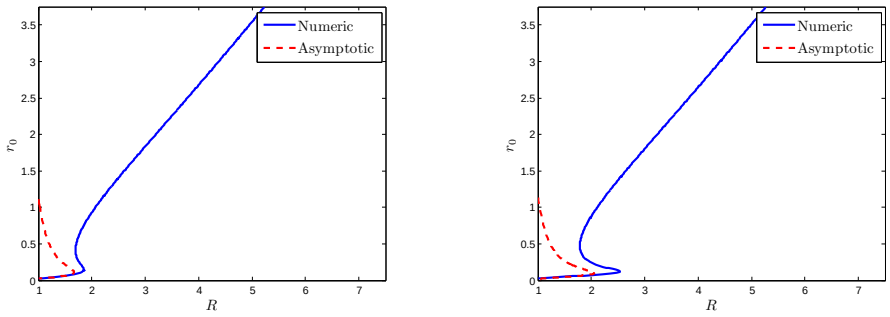

(a) $\sigma = 10$ (b) $\sigma = 8$

Figure 2.11: Bifurcation diagram to (2.43) for exponent set $(2, 1, 2, 0)$ and different values of σ. The dashed curve represents an asymptotic approximation for $r_0 \ll 1$. The smallest and highest equilibrium values are stable while there is an unstable transition branch in the middle.

Non-Radially Symmetric Solutions

Standard techniques guarantee that solutions to the modified Helmholtz problem are unique for prescribed Dirichlet or Neumann boundary data (cf.

[68]) and thus one would expect that the radially symmetric solution to (2.34) is unique. However, since the boundary data U_0 is an unknown of the problem, we can no longer prescribe uniqueness and we briefly demonstrate that by finding solutions for which U_0 is a periodic, non-constant, function. Even while removing the restriction that U_0 be constant, (2.34a) is still separable and therefore we can perform a Fourier eigenfunction expansion,

$$u(r,\theta) = \sum_{n=-\infty}^{\infty} \mathcal{U}_n(r)\exp(in\theta), \quad U_0 = \sum_{n=-\infty}^{\infty} a_n \exp(in\theta),$$
$$U_0^\beta = \sum_{n=-\infty}^{\infty} f_n \exp(in\theta)$$

where we treat the U_0^β term separately just for simplicity. Using this expansion in (2.34) we get for each eigenmode n,

$$\frac{1}{r}\frac{\mathrm{d}}{\mathrm{d}r}\left(r\frac{\mathrm{d}\mathcal{U}_n}{\mathrm{d}r}\right) - \frac{n^2\mathcal{U}_n}{r^2} - \frac{\mathcal{U}_n}{D} = 0, \tag{2.48a}$$
$$\left.\frac{\mathrm{d}\mathcal{U}_n}{\mathrm{d}r}\right|_{r=R} = 0, \tag{2.48b}$$
$$\mathcal{U}_n(r_0) = a_n, \tag{2.48c}$$
$$\left[\frac{\mathrm{d}\mathcal{U}_n}{\mathrm{d}r}\right]_{r=r_0} = -\frac{1}{D}f_n\mathcal{A}. \tag{2.48d}$$

This is the $n > 0$ analogue of the radially symmetric case and so if we define the functions

$$\mathcal{J}_{n,1}(r) = I_n\left(\frac{r}{\sqrt{D}}\right), \quad \mathcal{J}_{n,2}(r) = \alpha_n I_n\left(\frac{r}{\sqrt{D}}\right) + K_n\left(\frac{r}{\sqrt{D}}\right) \tag{2.49a}$$

where

$$\alpha_n = -\frac{K_n\left(\frac{R}{\sqrt{D}}\right)'}{I_n\left(\frac{R}{\sqrt{D}}\right)'} = \left(\frac{K_{n+1}\left(\frac{R}{\sqrt{D}}\right) - \frac{n\sqrt{D}}{R}K_n\left(\frac{R}{\sqrt{D}}\right)}{\frac{n\sqrt{D}}{R}I_n\left(\frac{R}{\sqrt{D}}\right) + I_{n+1}\left(\frac{R}{\sqrt{D}}\right)}\right) \tag{2.49b}$$

then the solution can be written as

$$\mathcal{U}_n(r) = \frac{r_0}{D} f_n \mathcal{A} G_{0,n}(r; r_0)$$

with $G_{0,n}(r; r_0)$, the Green's function

$$G_{0,n}(r; r_0) = \begin{cases} \mathcal{J}_{n,1}(r)\mathcal{J}_{n,2}(r_0), & 0 \le r \le r_0 \\ \mathcal{J}_{n,1}(r_0)\mathcal{J}_{n,2}(r), & r_0 \le r \le R \end{cases}. \tag{2.50}$$

Using the Dirichlet value at r_0 we have a condition to solve for U_0,

$$a_n = \frac{r_0}{D}\mathcal{A} G_{0,n}(r_0; r_0) f_n.$$

Notice that for radial symmetry, $a_n = f_n = 0$ for $n \neq 0$ and $f_0 = a_0^\beta$ leading to the form for U_0 in (2.40). We can approximate the Fourier coefficients c_n of a discrete vector g using the discrete Fourier transform,

$$c_n \approx \frac{1}{N}\sum_{j=1}^{N} \exp\left(\frac{-2\pi i n(j-1)}{N}\right) g_j,$$

where here N is the number of discrete wavemodes to consider. We can write this as

$$c = \frac{1}{N}\mathcal{F} g,$$

for a Fourier transform matrix $\mathcal{F}$ where

$$\mathcal{F}_{n,j} = \exp\left(\frac{-2\pi i n(j-1)}{N}\right).$$

Using this, we can get the Fourier coefficients we desire by numerically solving,

$$\mathcal{F}U_0 = \text{diag}(\mathcal{Y})\mathcal{F}U_0^{\beta}, \tag{2.51}$$

for fixed r_0 where $\mathcal{Y}$ is a vector with entries,

$$\mathcal{Y}_n = \frac{r_0}{D}\mathcal{A}G_{0,n}(r_0; r_0).$$

Computing solutions to (2.51) using Newton iterations starting at arbitrary initial data tends to converge to the radially symmetric solution which is not surprising since the decay of Fourier coefficients for increasing n will always have the constant term dominate regardless. We will therefore return to this formulation in 6.3.2 when we compute solutions on arbitrary domains to use this as a verification of non-radially symmetric solutions.

2.3.2 Inhibitor Problem on a Near Circular Curve

Now consider the curve Γ to be a perturbed circle given by

$$r = r_0 + \varepsilon h(\theta), \qquad \varepsilon \ll 1 \tag{2.52}$$

still inside a global circular domain $0 \leq r \leq R$. We will not consider the equilibria of such a geometry because dynamics may distort it beyond a near-circle and we will therefore consider the inhibitor and velocity perturbation for any initial base ring radius $0 < r_0 < R$. Recall that in deriving the singular limit inhibitor problem (2.32), we took the limit as ϵ tends to zero and so for our machinery to work with this perturbed circle geometry, we require $\epsilon \ll \varepsilon \ll 1$. We can write the inner normal to Γ as

$$\hat{\mathbf{n}} = \frac{\langle -1, \frac{\varepsilon h'(\theta)}{r_0+\varepsilon h(\theta)} \rangle}{\sqrt{1+\frac{\varepsilon^2 h'(\theta)^2}{(r_0+\varepsilon h(\theta))^2}}},$$

where prime here indicates differentiation with respect to θ. We can use this normal vector to write

$$\frac{\partial u}{\partial n} = \frac{-u_r + \frac{\varepsilon h'(\theta)}{(r_0+\varepsilon h(\theta))^2} u_\theta}{\sqrt{1+\frac{\varepsilon^2 h'(\theta)^2}{(r_0+\varepsilon h(\theta))^2}}}.$$

We consider solving (2.32) with a formal expansion

$$u(r,\theta) = u_0(r) + \varepsilon u_1(r,\theta) + \varepsilon^2 u_2(r,\theta) + \dots$$

where we explicitly note that we want to consider a perturbation from the radially symmetric inhibitor solution hence why u_0 is independent of θ. Using

the condition (2.32c) we have

$$\begin{aligned} U_0 = u(r_0 + \varepsilon h(\theta)) \sim u_0(r_0) + \varepsilon(u_{0r}(r)h(\theta) + u_1(r))_{r_0} \\ + \varepsilon^2 \left(\frac{1}{2} u_{0rr}(r)h(\theta)^2 + u_{1r}(r)h(\theta) + u_2(r) \right)_{r_0} \\ = U_{00} + \varepsilon U_{01}(\theta) + \varepsilon^2 U_{02}(\theta). \end{aligned} \tag{2.53}$$

Here we have put the evaluation at $r = r_0$ outside the brackets since individually, each term may be discontinuous but together, they must be continuous since U_0 has a fixed value. Using our asymptotic expansion we can write the normal derivative as

$$\begin{aligned} \left. \frac{\mathrm{d}u}{\mathrm{d}n} \right|_{\hat{\eta}=0^{\pm}} \sim & -u_{0r}(r_0^{\mp}) + \varepsilon \left(-u_{0rr}(r_0^{\mp})h(\theta) - u_{1r}(r_0^{\mp}) \right) \\ & + \varepsilon^2 \left(-\frac{1}{2} u_{0rrr}(r_0^{\mp})h(\theta)^2 - u_{1rr}(r_0^{\mp})h(\theta) + \frac{u_{1\theta}(r_0^{\mp})h'(\theta)}{r_0^2} \right. \\ & \left. + \frac{u_{0r}(r_0^{\mp})h'(\theta)^2}{2r_0^2} - u_{2r}(r_0^{\mp}) \right) \end{aligned} \tag{2.54}$$

where we recall that because we are using the inner normal, $\hat{\eta} = 0^{\pm}$ corresponds to $r = r_0^{\mp}$. Finally we use (2.53) to write

$$U_0^{\beta} \sim U_{00}^{\beta} + \varepsilon\beta U_{00}^{\beta-1} U_{01} + \varepsilon^2 \beta \frac{U_{00}^{\beta-2}}{2} \left((\beta - 1)U_{01}^2 + 2U_{00}U_{02} \right). \tag{2.55}$$

In the presence of saturation, both $\mathcal{A}$ and $\hat{\mathcal{H}}$ depend on the curve inhibitor value U_0 and so we will also need to consider an expansion of the effective

saturation parameter b,

$$\begin{aligned} b = U_0^{2q}\sigma &\sim U_{00}^{2q}\sigma + \varepsilon 2qU_{00}^{2q-1}U_{01}\sigma + \varepsilon^2 qU_{00}^{2q-2}\left((2q-1)U_{01}^2 + 2U_{00}U_{02}\right)\sigma \\ &= b_0 + \varepsilon b_1 + \varepsilon^2 b_2, \end{aligned} \tag{2.56}$$

and then write

$$\mathcal{A} \sim \mathcal{A}_0 + \varepsilon\frac{\mathrm{d}\mathcal{A}_0}{\mathrm{d}b}b_1 + \varepsilon^2\left(\frac{\mathrm{d}\mathcal{A}_0}{\mathrm{d}b}b_2 + \frac{1}{2}\frac{\mathrm{d}^2\mathcal{A}_0}{\mathrm{d}b^2}b_1^2\right), \tag{2.57a}$$

$$\hat{\mathcal{H}} \sim \hat{\mathcal{H}}_0 + \varepsilon\frac{\mathrm{d}\hat{\mathcal{H}}_0}{\mathrm{d}b}b_1 + \varepsilon^2\left(\frac{\mathrm{d}\hat{\mathcal{H}}_0}{\mathrm{d}b}b_2 + \frac{1}{2}\frac{\mathrm{d}^2\hat{\mathcal{H}}_0}{\mathrm{d}b^2}b_1^2\right), \tag{2.57b}$$

where the zero subscript indicates evaluation at $b = b_0$, the unperturbed saturation parameter. We will begin by looking at corrections to the inhibitor value before analyzing the corrections to the curve front velocity. The leading order problem for u_0 is given precisely by the radially symmetric version of (2.34) in section 2.3.1 with solution (2.36) and curve value U_{00} given by (2.40) and as such we continue directly to the problem at $\mathcal{O}(\varepsilon)$:

$$\frac{1}{r}\frac{\partial}{\partial r}\left(r\frac{\partial u_1}{\partial r}\right) + \frac{1}{r^2}\frac{\partial^2 u_1}{\partial\theta^2} - \frac{1}{D}u_1 = 0, \qquad r \neq r_0, \tag{2.58a}$$

$$\left.\frac{\partial u_1}{\partial r}\right|_{r=R} = 0, \tag{2.58b}$$

$$[u_1]_{r_0} = -h(\theta)\left[\frac{\mathrm{d}u_0}{\mathrm{d}r}\right]_{r_0}, \tag{2.58c}$$

$$\left[\frac{\partial u_1}{\partial r}\right]_{r_0} = -h(\theta)\left[\frac{\mathrm{d}^2 u_0}{\mathrm{d}r^2}\right]_{r_0} - \frac{\mathcal{A}_0}{D}U_{00}^{\beta-1}\bar{\bar{A}}_0 U_{01}, \tag{2.58d}$$

where we have defined

$$\bar{\bar{A}}_0 = \beta + \frac{2qb_0}{\mathcal{A}_0}\frac{\mathrm{d}\mathcal{A}_0}{\mathrm{d}b}. \tag{2.59}$$

The continuity condition (2.58c) comes from utilizing (2.53) and that globally, the inhibitor value U_0 must be continuous across the front. The derivative condition (2.58d) comes from (2.54), (2.55), and (2.56) where we have expressed b_1 in terms of b_0. We can rewrite (2.58d) by noticing that

$$\begin{aligned}\left[\frac{\mathrm{d}^2u_0}{\mathrm{d}r^2}\right]_{r_0} =& \bar{A}_0 r_0 \left[\frac{\mathrm{d}^2G_0}{\mathrm{d}r^2}\right]_{r_0} = \bar{A}_0 r_0 \left(\mathcal{J}_{0,1}(r_0)\mathcal{J}_{0,2}(r_0)'' - \mathcal{J}_{0,1}(r_0)''\mathcal{J}_{0,2}(r_0)\right) \\ =& \bar{A}_0 r_0 \left(K_0\left(\frac{r_0}{\sqrt{D}}\right)'' I_0\left(\frac{r_0}{\sqrt{D}}\right) - K_0\left(\frac{r_0}{\sqrt{D}}\right) I_0\left(\frac{r_0}{\sqrt{D}}\right)''\right)\end{aligned}$$

where we define

$$\bar{A}_0 = \frac{\mathcal{A}_0}{D}U_{00}^{\beta}, \tag{2.60}$$

$G_0(r;r_0)$ by (2.38) and $\mathcal{J}_{0,1}$ and $\mathcal{J}_{0,2}$ by (2.39). If we use the Wronskian (2.37) and differentiate we get,

$$W'(r) = K_0\left(\frac{r}{\sqrt{D}}\right)'' I_0\left(\frac{r}{\sqrt{D}}\right) - K_0\left(\frac{r}{\sqrt{D}}\right) I_0\left(\frac{r}{\sqrt{D}}\right)'' = \frac{1}{r^2}.$$

Therefore,

$$\left[\frac{\mathrm{d}^2u_0}{\mathrm{d}r^2}\right]_{r_0} = \frac{\bar{A}_0}{r_0} \tag{2.61}$$

and the derivative jump condition (2.58d) becomes

$$\left[\frac{\partial u_1}{\partial r}\right]_{r_0} = -h(\theta)\frac{\bar{A}_0}{r_0} - \frac{\bar{A}_0}{U_{00}}\bar{\bar{A}}_0 U_{01}. \tag{2.62}$$

Since the problem (2.58) is linear in the θ dependence, we can perform an eigenfunction expansion,

$$u_1(r,\theta) = \sum_{n=-\infty}^{\infty} \mathcal{V}_{1n}(r)\exp(in\theta), \quad U_{01}(\theta) = \sum_{n=-\infty}^{\infty} \mathcal{U}_{1n}\exp(in\theta),$$
$$h(\theta) = \sum_{n=-\infty}^{\infty} H_n \exp(in\theta)$$

for integer eigenmodes, n. Upon this expansion, (2.58) becomes

$$\frac{1}{r}\frac{\mathrm{d}}{\mathrm{d}r}\left(r\frac{\mathrm{d}\mathcal{V}_{1n}}{\mathrm{d}r}\right) - \frac{n^2}{r^2}\mathcal{V}_{1n} - \frac{1}{D}\mathcal{V}_{1n} = 0, \qquad r \neq r_0, \tag{2.63a}$$
$$\left.\frac{\mathrm{d}\mathcal{V}_{1n}}{\mathrm{d}r}\right|_{r=R} = 0, \tag{2.63b}$$
$$[\mathcal{V}_{1n}]_{r_0} = H_n\bar{A}_0, \tag{2.63c}$$
$$\left[\frac{\mathrm{d}\mathcal{V}_{1n}}{\mathrm{d}r}\right]_{r_0} = -\frac{H_n\bar{A}_0}{r_0} - \frac{\bar{A}_0}{U_{00}}\bar{\bar{A}}_0\mathcal{U}_{1n}. \tag{2.63d}$$

This problem is very similar to the non-radially symmetric case for the pure circle geometry and so if we define $\mathcal{J}_{n,1}$, $\mathcal{J}_{n,2}$, and α_n by (2.49) then we can write

$$\mathcal{V}_{1n} = \begin{cases} A\mathcal{J}_{n,1}(r), & 0 \leq r < r_0 \\ B\mathcal{J}_{n,2}(r), & r_0 < r \leq R \end{cases}$$

where the boundary derivative condition (2.63b) has been used. Using (2.63c) and (2.63d) we have

$$\underbrace{\begin{bmatrix} -\mathcal{J}_{n,1}(r_0) & \mathcal{J}_{n,2}(r_0) \\ -\mathcal{J}'_{n,1}(r_0) & \mathcal{J}'_{n,2}(r_0) \end{bmatrix}}_{=M} \begin{bmatrix} A \\ B \end{bmatrix} = \begin{bmatrix} H_n \bar{A}_0 \\ -\frac{H_n \bar{A}_0}{r_0} - \frac{\bar{A}_0}{U_{00}} \bar{\bar{A}}_0 \mathcal{U}_{1n} \end{bmatrix} = \begin{bmatrix} \bar{A}_{1n} \\ \bar{B}_{1n} \end{bmatrix}.$$

Using the Wronskian relationship (2.37), which holds for any n, we have that $\det M = 1/r_0$ and therefore

$$\begin{bmatrix} A \\ B \end{bmatrix} = \begin{bmatrix} \bar{A}_{1n} r_0 \mathcal{J}'_{n,2}(r_0) - \bar{B}_{1n} r_0 \mathcal{J}_{n,2}(r_0) \\ \bar{A}_{1n} r_0 \mathcal{J}'_{n,1}(r_0) - \bar{B}_{1n} r_0 \mathcal{J}_{n,1}(r_0) \end{bmatrix}.$$

If we define $G_{0,n}(r; r_0)$ as in (2.50) and $G_{1,n}$ via

$$G_{1,n}(r; r_0) = \begin{cases} \mathcal{J}_{n,1}(r) \mathcal{J}'_{n,2}(r_0), & 0 \le r < r_0 \\ \mathcal{J}'_{n,1}(r_0) \mathcal{J}_{n,2}(r), & r_0 < r \le R \end{cases}. \tag{2.64}$$

then we can write

$$\mathcal{V}_{1n}(r) = \bar{A}_{1n} r_0 G_{1,n}(r; r_0) - \bar{B}_{1n} r_0 G_{0,n}(r; r_0). \tag{2.65}$$

Now we can determine $\mathcal{U}_{1n}$ via (2.53),

$$\mathcal{U}_{1n} = \mathcal{V}_{1n} + H_n \frac{\mathrm{d}u_0}{\mathrm{d}r},$$

evaluated from either side of $r = r_0$. However, since this must be continuous across r_0 we can actually compute it using the average value,

$$\begin{aligned}\mathcal{U}_{1n} =& \bar{A}_{1n} r_0 \left(\langle G_{1,n}(r; r_0) \rangle_{r_0} + \left\langle \frac{\mathrm{d}G_0}{\mathrm{d}r} \right\rangle_{r_0} \right) \\ &+ \left(\bar{A}_{1n} + \frac{\bar{A}_0 r_0}{U_{00}} \bar{\bar{A}}_0 \mathcal{U}_{1n} \right) G_{0;n}(r_0, r_0),\end{aligned}$$

where $\langle \cdot \rangle_a$ indicates the average value across $r = a$. If we notice that

$$\bar{A}_0 r_0 = \frac{U_{00}}{G_0(r_0; r_0)},$$

then we can solve for $\mathcal{U}_{1n}$ and get

$$\begin{aligned}\mathcal{U}_{1n} =& \frac{H_n U_{00}}{G_0(r_0; r_0)} \\ & \left(1 - \bar{\bar{A}}_0 \frac{G_{0;n}(r_0; r_0)}{G_0(r_0; r_0)} \right)^{-1} \left(\frac{G_{0,n}(r_0; r_0)}{r_0} + \left\langle G_{1,n}(r, r_0) + \frac{\mathrm{d}G_0}{\mathrm{d}r} \right\rangle_{r_0} \right).\end{aligned} \tag{2.66}$$

Typically, we consider the perturbation $h(\theta)$ to be a finite combination of sinusoidal modes and if this is the case then the correction at $\mathcal{O}(\varepsilon)$ will add components in each of those modes. However, unless an $n = 0$ mode is explicitly part of $h(\theta)$, the perturbation at this order can not describe vertical shifting as there is no cross-mode influence. Therefore, we will consider the expansion at $\mathcal{O}(\varepsilon^2)$ to account for this shifting since mode interactions occur

at this level through quadratic terms. The problem at $\mathcal{O}(\varepsilon^2)$ is

$$\frac{1}{r}\frac{\partial}{\partial r}\left(r\frac{\partial u_2}{\partial r}\right)+\frac{1}{r^2}\frac{\partial^2 u_2}{\partial \theta^2}-\frac{1}{D}u_2=0, \qquad r\neq r_0 \tag{2.67a}$$

$$\left.\frac{\partial u_2}{\partial r}\right|_{r=R}=0, \tag{2.67b}$$

$$[u_2]_{r_0}=-h(\theta)\left[\frac{\partial u_1}{\partial r}\right]_{r_0}-\frac{h(\theta)^2}{2}\left[\frac{\mathrm{d}^2 u_0}{\mathrm{d}r^2}\right]_{r_0}, \tag{2.67c}$$

$$\begin{aligned}\left[\frac{\partial u_2}{\partial r}\right]_{r_0}=&\frac{1}{2}\frac{h'(\theta)^2}{r_0^2}\left[\frac{\mathrm{d}u_0}{\mathrm{d}r}\right]_{r_0}+\frac{h'(\theta)}{r_0^2}\left[\frac{\partial u_1}{\partial \theta}\right]_{r_0}\\&-h(\theta)\left[\frac{\partial^2 u_1}{\partial r^2}\right]_{r_0}-\frac{1}{2}h(\theta)^2\left[\frac{\mathrm{d}^3 u_0}{\mathrm{d}r^3}\right]_{r_0}\\&-\frac{\bar{A}_0}{U_{00}^2}\left(\bar{\bar{A}}_1U_{01}^2+\bar{\bar{A}}_0U_{00}U_{02}\right),\end{aligned} \tag{2.67d}$$

where we define

$$\bar{\bar{A}}_1=\frac{1}{2}\beta(\beta-1)+\frac{qb_0(2q-1)}{\mathcal{A}_0}\frac{\mathrm{d}\mathcal{A}_0}{\mathrm{d}b}+\frac{2q^2b_0^2}{\mathcal{A}_0}\frac{\mathrm{d}^2\mathcal{A}_0}{\mathrm{d}b^2}.$$

As with the $\mathcal{O}(\varepsilon)$ expansion, this is generated by appropriately substituting the expansions from (2.53), (2.54), (2.55), and the corrections to b have been expressed using (2.56). We can rewrite the continuity condition (2.67c) using (2.61) and (2.62) to get

$$[u_2]_{r_0}=h(\theta)^2\frac{\bar{A}_0}{2r_0}+h(\theta)\frac{\bar{A}_0\bar{\bar{A}}_0}{U_{00}}U_{01}. \tag{2.68}$$

Next we turn our attention to the jump condition (2.67d). First we notice using (2.63c) that

$$\left[\frac{\partial u_1}{\partial \theta}\right]_{r_0} = \sum_{n=-\infty}^{\infty} in \left[\mathcal{V}_{1n}\right]_{r_0} \exp(in\theta) = \bar{A}_0 \sum_{n=-\infty}^{\infty} inH_n \exp(in\theta) = \bar{A}_0 h'(\theta).$$

Next, we need to determine

$$\left[\frac{\partial^2 u_1}{\partial r^2}\right]_{r_0} = \sum_{n=-\infty}^{\infty} \left(\bar{A}_{1n} r_0 \left[\frac{\mathrm{d}^2 G_{1,n}}{\mathrm{d}r^2}\right]_{r_0} - \bar{B}_{1n} r_0 \left[\frac{\mathrm{d}^2 G_{0,n}}{\mathrm{d}r^2}\right]_{r_0}\right) \exp(in\theta)$$
$$\left[\frac{\mathrm{d}^3 u_0}{\mathrm{d}r^3}\right]_{r_0} = \bar{A}_0 r_0 \left[\frac{\mathrm{d}^3 G_0}{\mathrm{d}r^3}\right]_{r_0}.$$

Since the Wronskian relationship (2.37) also holds for $n \neq 0$ we have

$$W_{0,n}(r) = I_n\left(\frac{r}{\sqrt{D}}\right) K_n\left(\frac{r}{\sqrt{D}}\right)' - K_n\left(\frac{r}{\sqrt{D}}\right) I_n\left(\frac{r}{\sqrt{D}}\right)' = -\frac{1}{r} \quad (2.69)$$

which we can differentiate to get

$$\begin{aligned} W'_{0,n}(r) =& I_n\left(\frac{r}{\sqrt{D}}\right) K_n\left(\frac{r}{\sqrt{D}}\right)'' - K_n\left(\frac{r}{\sqrt{D}}\right) I_n\left(\frac{r}{\sqrt{D}}\right)'' \\ =& \left[\frac{\mathrm{d}^2 G_{0,n}}{\mathrm{d}r^2}\right]_r = \frac{1}{r_0^2}, \end{aligned}$$

just as in the $n = 0$ case. If we differentiate this again,

$$\begin{aligned} W''_{0,n}(r) &= I_n\left(\frac{r}{\sqrt{D}}\right)K_n\left(\frac{r}{\sqrt{D}}\right)''' - K_n\left(\frac{r}{\sqrt{D}}\right)I_n\left(\frac{r}{\sqrt{D}}\right)''' \\ &\quad + I_n\left(\frac{r}{\sqrt{D}}\right)'K_n\left(\frac{r}{\sqrt{D}}\right)'' - K_n\left(\frac{r}{\sqrt{D}}\right)'I_n\left(\frac{r}{\sqrt{D}}\right)'' \\ &= \left[\frac{\mathrm{d}^3 G_{0,n}}{\mathrm{d}r^3}\right]_r + I_n\left(\frac{r}{\sqrt{D}}\right)'K_n\left(\frac{r}{\sqrt{D}}\right)'' - K_n\left(\frac{r}{\sqrt{D}}\right)'I_n\left(\frac{r}{\sqrt{D}}\right)'' \\ &= -\frac{2}{r_0^3} + W_{1,n}(r_0), \end{aligned}$$

where we define the new Wronskian,

$$W_{1,n}(r) = I_n\left(\frac{r}{\sqrt{D}}\right)'K_n\left(\frac{r}{\sqrt{D}}\right)'' - K_n\left(\frac{r}{\sqrt{D}}\right)'I_n\left(\frac{r}{\sqrt{D}}\right)''. \tag{2.70}$$

Furthermore,

$$\left[\frac{\mathrm{d}^2 G_{1,n}}{\mathrm{d}r^2}\right]_{r_0} = I_n\left(\frac{r_0}{\sqrt{D}}\right)'K_n\left(\frac{r_0}{\sqrt{D}}\right)'' - K_n\left(\frac{r_0}{\sqrt{D}}\right)'I_n\left(\frac{r_0}{\sqrt{D}}\right)'',$$

and therefore

$$\left[\frac{\mathrm{d}^3 G_0}{\mathrm{d}r^3}\right]_{r_0} = -\frac{2}{r_0^3} - W_{1,0}(r_0), \qquad \left[\frac{\mathrm{d}^2 G_{1,n}}{\mathrm{d}r^2}\right]_{r_0} = W_{1,n}(r_0).$$

To determine the Wronskian (2.70), consider that $y = u_0 = I_n\left(\frac{r}{\sqrt{D}}\right)$ and $y = v_0 = K_n\left(\frac{r}{\sqrt{D}}\right)$ satisfy

$$\frac{\mathrm{d}^2 y}{\mathrm{d}r^2} + \frac{1}{r}\frac{\mathrm{d}y}{\mathrm{d}r} - \left(\frac{n^2}{r^2} + \frac{1}{D}\right)y = 0$$

and differentiate this expression. Therefore $u = I_n\left(\frac{r}{\sqrt{D}}\right)'$ and $v = K_n\left(\frac{r}{\sqrt{D}}\right)'$ satisfy

$$\frac{\mathrm{d}^2u}{\mathrm{d}r^2} + \frac{1}{r}\frac{\mathrm{d}u}{\mathrm{d}r} - \left(\frac{n^2+1}{r^2} + \frac{1}{D}\right)u + \frac{2}{n^2}r^3u_0 = 0,$$
$$\frac{\mathrm{d}^2v}{\mathrm{d}r^2} + \frac{1}{r}\frac{\mathrm{d}v}{\mathrm{d}r} - \left(\frac{n^2+1}{r^2} + \frac{1}{D}\right)v + \frac{2}{n^2}r^3v_0 = 0$$

respectively. We define $W_{1,n}(r) = u'v - uv'$ and so multiplying the first expression by v and the second by u we have

$$\frac{\mathrm{d}W_{1,n}}{\mathrm{d}r} + \frac{W_{1,n}}{r} - \frac{2n^2}{r^3}W_{0,n}(r) = \frac{\mathrm{d}W_{1,n}}{\mathrm{d}r} + \frac{W_{1,n}}{r} + \frac{2n^2}{r^4} = 0.$$

Solving for this Wronskian, we get

$$W_{1,n}(r) = \frac{n^2}{r^3} + \frac{1}{Dr}, \tag{2.71}$$

where the $1/Dr$ term is determined by looking at the small r asymptotics of $W_{1,n}(r)$ for $n = 0$ (since the expression must hold for all n). We therefore have that

$$\left[\frac{\partial^2 u_1}{\partial r^2}\right]_{r_0} = \sum_{n=-\infty}^{\infty}\left(\bar{A}_{1n}\left(\frac{n^2}{r^2} + \frac{1}{D}\right) - \frac{\bar{B}_{1n}}{r_0}\right)\exp(in\theta),$$
$$\left[\frac{\mathrm{d}^3u_0}{\mathrm{d}r^3}\right]_{r_0} = -\bar{A}_0\left(\frac{2}{r_0^2} + \frac{1}{D}\right).$$

We can simplify the first expression,

$$\left[\frac{\partial^2 u_1}{\partial r^2}\right]_{r_0} = \frac{\bar{A}_0}{r_0^2}\left(h(\theta) - h''(\theta)\right) + \frac{\bar{A}_0}{D}h(\theta) + \frac{\bar{A}_0\bar{\bar{A}}_0}{U_{00}r_0}U_{01}$$

and finally write

$$\left[\frac{\partial u_2}{\partial r}\right]_{r_0} = \frac{\bar{A}_0 h'(\theta)^2}{2r_0^2} + \frac{\bar{A}_0}{r_0^2}h(\theta)h''(\theta) - \frac{\bar{A}_0}{2D}h(\theta)^2 - \frac{\bar{A}_0\bar{\bar{A}}_0}{U_{00}r_0}h(\theta)U_{01} - \frac{\bar{A}_0}{U_{00}^2}\left(\bar{\bar{A}}_1 U_{01}^2 + \bar{\bar{A}}_0 U_{00}U_{02}\right). \tag{2.72}$$

We wish to perform an eigenfunction expansion on this problem but we must delicately handle the product of infinite sums that occurs. We will define the product in the following way,

Definition 2.3.2.1 *Assume two functions $f(\theta)$ and $g(\theta)$ have a fourier series given by*

$$f(\theta) \sim \sum_{n=-\infty}^{\infty} a_n \exp(in\theta), \qquad g(\theta) \sim \sum_{m=-\infty}^{\infty} b_m \exp(im\theta)$$

and that there exists some N and M such that $|a_n| = 0$ when $|n| > N$ and $|b_m| = 0$ when $|m| > M$. If this is the case then we can define the product of these functions as

$$f(\theta)g(\theta) = \sum_{m=-\infty}^{\infty}\sum_{n=-\infty}^{\infty} a_n b_m \exp(i(n+m)\theta).$$

This definition states that when a Fourier series terminates then we can use the finite series product. This is in contrast to the Cauchy-product typically used for infinite sums. Since we expect the perturbation $h(\theta)$ is composed of finite sinusoidal modes, the Fourier series will terminate. This allows us to use Definition 2.3.2.1 for quadratic products of $h(\theta)$ at $\mathcal{O}(\varepsilon^2)$. Using definition 2.3.2.1 for handling series products, we can perform the

eigenfunction expansion as

$$u_2(r,\theta) = \sum_{k=-\infty}^{\infty} \mathcal{V}_{2k}(r)\exp(ik\theta), \quad U_{02}(\theta) = \sum_{k=-\infty}^{\infty} \mathcal{U}_{2k}\exp(ik\theta),$$

and the base problem is identical to (2.63) so we can immediately write

$$\mathcal{V}_{2k} = \begin{cases} A\mathcal{J}_{k,1}(r), & 0 \le r < r_0 \\ B\mathcal{J}_{k,2}(r), & r_0 < r \le R \end{cases}.$$

The continuity and derivative jump conditions for each mode k become

$$[\mathcal{V}_{2k}]_{r_0} = \frac{\bar{A}_0}{2r_0}\sum_{n\in N} H_n H_{k-n} + \frac{\bar{A}_0\bar{\bar{A}}_0}{U_{00}}\sum_{n\in N} H_n\mathcal{U}_{1k-n} = \bar{A}_{2k}, \tag{2.73a}$$

$$\begin{aligned}\left[\frac{\mathrm{d}\mathcal{V}_{2k}}{\mathrm{d}r}\right]_{r_0} =& -\frac{\bar{A}_0}{2r_0^2}\sum_{n\in N} n(k-n)H_nH_{k-n} - \frac{\bar{A}_0}{r_0^2}\sum_{n\in N}(k-n)^2 H_nH_{k-n} \\ &- \frac{\bar{A}_0}{2D}\sum_{n\in N} H_nH_{k-n} - \frac{\bar{A}_0\bar{\bar{A}}_0}{U_{00}r_0}\sum_{n\in N} H_n\mathcal{U}_{1k-n} \\ &- \frac{\bar{A}_0}{U_{00}^2}\left(\bar{\bar{A}}_1\sum_{n\in N}\mathcal{U}_{1n}\mathcal{U}_{1k-n} + \bar{\bar{A}}_0U_{00}\mathcal{U}_{2k}\right) = \bar{B}_{2k}.\end{aligned} \tag{2.73b}$$

Here the sum is over a set N which contains the integer modes n that produce valid integer k modes. For example, if $h(\theta) = \cos(6\theta)$ then there are two modes at $\mathcal{O}(\varepsilon)$ of $n = -6$ and $n = 6$. Various quadratic combinations of these modes leads to $k = -12$, $k = 0$, and $k = 12$ as the only possible modes that can occur at $\mathcal{O}(\varepsilon^2)$. Therefore, if $k = -12$ then $N = \{-6\}$ since it is only through this mode that frequencies $\exp(-12i\theta)$ can occur but for $k = 0$ then the set $N = \{-6, 6\}$ since these two modes lead to terms of frequency 1.

As another example, consider $h(\theta) = \cos(3\theta) + \cos(6\theta)$ which has admissible modes at $\mathcal{O}(\varepsilon^2)$ of $k = 0, \pm 3, \pm 6, \pm 9, \pm 12$ and here for $k = 0$, the set is $N = \{\pm 3, \pm 6\}$ while for $k = 9$, the set is $N = \{3, 6\}$. In similar fashion to (2.63) at $\mathcal{O}(\varepsilon)$, we can use (2.73) to write,

$$\mathcal{V}_{2k}(r) = \bar{A}_{2k} r_0 G_{1,k}(r; r_0) - \bar{B}_{2k} r_0 G_{0,k}(r; r_0). \tag{2.74}$$

As with $\mathcal{U}_{1n}$, we can solve $\mathcal{U}_{2k}$ by taking the average value of (2.53) at $\mathcal{O}(\varepsilon^2)$

$$\begin{aligned}\mathcal{U}_{2k} =& \frac{\bar{A}_0 r_0}{2} \frac{\mathrm{d}^2 G_0}{\mathrm{d}r^2} \sum_{n \in N} H_n H_{k-n} + r_0 \sum_{n \in N} H_n \left(\bar{A}_{1k-n} \frac{\mathrm{d}G_{1,k-n}}{\mathrm{d}r} - \bar{B}_{1k-n} \frac{\mathrm{d}G_{0,k-n}}{\mathrm{d}r} \right) \\ &+ r_0 \bar{A}_{2k} G_{1,k} - r_0 \bar{B}_{2k} G_{0,k}.\end{aligned}$$

If we define

$$\tilde{B}_{2k} = \bar{B}_{2k} + \frac{\bar{A}_0 \bar{\bar{A}}_0}{U_{00}} \mathcal{U}_{2k}$$

then we can solve

$$\begin{aligned}\mathcal{U}_{2k} = \left(1 - \bar{\bar{A}}_0 \frac{G_{0,k}(r_0; r_0)}{G_0(r_0; r_0)}\right)^{-1} \Bigg(& \frac{\bar{A}_0 r_0}{2} \left\langle \frac{\mathrm{d}^2 G_0}{\mathrm{d}r^2} \right\rangle_{r_0} \sum_{n \in N} H_n H_{k-n} \\ & + r_0 \sum_{n \in N} H_n \left(\bar{A}_{1k-n} \left\langle \frac{\mathrm{d}G_{1,k-n}}{\mathrm{d}r} \right\rangle_{r_0} - \bar{B}_{1k-n} \left\langle \frac{\mathrm{d}G_{0,k-n}}{\mathrm{d}r} \right\rangle_{r_0} \right) \\ & + r_0 \bar{A}_{2k} \left\langle G_{1,k} \right\rangle_{r_0} - r_0 \tilde{B}_{2k} G_{0,k}(r_0; r_0) \Bigg).\end{aligned} \tag{2.75}$$

Thus we have completely solved the inhibitor problem up to $\mathcal{O}(\varepsilon^2)$. We will present an example verifying the asymptotic calculations in section 2.3.2 but first will consider velocity corrections.

Velocity Correction

We will now furnish corrections to the velocity magnitude (2.32e) which we rewrite as

$$V_0 = \kappa_0 - \frac{q}{2U_0}\hat{\mathcal{H}}\left\langle \frac{\mathrm{d}u}{\mathrm{d}n} \right\rangle_{\eta=0}.$$

The process of determining this asymptotically is much simpler than determining the inhibitor value because it can be computed explicitly in terms of already known quantities. First we note that in polar coordinates we can write the curvature as (cf [25]),

$$\kappa_0 = \left| \frac{\mathrm{d}\hat{\mathbf{t}}}{\mathrm{d}s} \right| = \frac{r^2 + 2r'^2 - rr''}{(r^2 + r'^2)^{3/2}}$$

where $\hat{\mathbf{t}}$ is the unit tangent vector and once again prime is differentiation with respect to s. Using the near-circle radius (2.52) we have that

$$\kappa_0 \sim \frac{1}{r_0} - \varepsilon\left(\frac{h''(\theta) + h(\theta)}{r_0^2}\right) + \varepsilon^2\left(\frac{4h(\theta)h''(\theta) + h'(\theta)^2 + 2h(\theta)^2}{2r_0^3}\right). \quad (2.76)$$

We can make a velocity expansion as follows

$$V_0 \sim V_{00} + \varepsilon V_{01} + \varepsilon^2 V_{02}$$

and to leading order, the velocity is exactly that which was derived for the radially symmetric case (2.43). Using (2.53), (2.54), (2.76), and (2.57b) we

can get the velocity correction at $\mathcal{O}(\varepsilon)$ is

$$V_{01} = -\left(\frac{h''(\theta)+h(\theta)}{r_0^2}\right) - \frac{q\hat{\mathcal{H}}_0}{2U_{00}^2}\left(1 - \frac{2qb_0}{\hat{\mathcal{H}}_0}\frac{\mathrm{d}\hat{\mathcal{H}}_0}{\mathrm{d}b}\right)\left\langle \frac{\mathrm{d}u_0}{\mathrm{d}r}\right\rangle_{r_0} U_{01} + \frac{q\hat{\mathcal{H}}_0}{2U_{00}}\left(h(\theta)\left\langle \frac{\mathrm{d}^2u_0}{\mathrm{d}r^2}\right\rangle_{r_0} + \left\langle \frac{\partial u_1}{\partial r}\right\rangle_{r_0}\right) \tag{2.77}$$

All of the necessary values to compute V_1 have been obtained and can therefore be directly substituted. Notice that if $r_0 \ll 1$ then to leading order

$$V_{01} \sim -\left(\frac{h''(\theta)+h(\theta)}{r_0^2}\right),$$

and for typical $h(\theta) = \cos(m\theta)$ then

$$V_{01} \sim \left(\frac{m^2-1}{r_0^2}\right)\cos(m\theta),$$

which is in phase with $h(\theta)$ and so the velocity is positive where the perturbed radius is larger than the base radius r_0 and negative where the radius is smaller. Therefore, since the inward normal is positive, this has the effect of circularizing the curve. If $r_0 \gg 1$ then it is possible for the curve velocity to be negative allowing the perturbation to grow but this does not necessarily mean that the pattern destabilizes. Continuing in the expansion, we can get

that the velocity at $\mathcal{O}(\varepsilon^2)$ is

$$V_{02} = \left(\frac{4h(\theta)h''(\theta) + h'(\theta)^2 + 2h(\theta)^2}{2r_0^3}\right) + \frac{q}{2}\left(\left(\frac{U_{01}^2}{U_{00}^2} - \frac{U_{02}}{U_{00}^2}\right)\hat{\mathcal{H}}_0 - \frac{U_{01}}{U_{00}^2}\frac{\mathrm{d}\hat{\mathcal{H}}_0}{\mathrm{d}b}b_1 + \frac{1}{U_{00}}\left(\frac{1}{2}\frac{\mathrm{d}^2\hat{\mathcal{H}}_0}{\mathrm{d}b^2}b_1^2 + \frac{\mathrm{d}\hat{\mathcal{H}}_0}{\mathrm{d}b}b_2\right)\right)\left\langle\frac{\mathrm{d}u_0}{\mathrm{d}r}\right\rangle_{r_0} + \frac{q}{2U_{00}^2}\left(U_{00}\frac{\mathrm{d}\hat{\mathcal{H}}_0}{\mathrm{d}b}b_1 - U_{01}\hat{\mathcal{H}}_0\right)\left(h(\theta)\left\langle\frac{\mathrm{d}^2u_0}{\mathrm{d}r^2}\right\rangle_{r_0} + \left\langle\frac{\partial u_1}{\partial r}\right\rangle_{r_0}\right) - \frac{q\hat{\mathcal{H}}_0}{2U_{00}}\left(-\frac{1}{2}h(\theta)^2\left\langle\frac{\mathrm{d}^3u_0}{\mathrm{d}r^3}\right\rangle_{r_0} - h(\theta)\left\langle\frac{\partial^2u_1}{\partial r^2}\right\rangle_{r_0} + \frac{h'(\theta)}{r_0^2}\left\langle\frac{\partial u_1}{\partial\theta}\right\rangle_{r_0} + \frac{h'(\theta)^2}{2r_0^2}\left\langle\frac{\mathrm{d}u_0}{\mathrm{d}r}\right\rangle_{r_0} - \left\langle\frac{\partial^2u_2}{\partial r^2}\right\rangle_{r_0}\right) \tag{2.78}$$

which is also explicitly known in terms of previously computed values.

Numerical Validation of the Asymptotic Theory

In Chapter 6, we discuss and derive a method for solving the full problem (2.32) for arbitrary curves of which a near circle could be chosen. Therefore, while we omit the numerical details here, we can compare our asymptotic corrections to the full numerically computed simulations. To ensure that the errors we make are asymptotic and not numeric, we choose a proper computational resolution that is significantly smaller than our choice of ε (taken here to be 0.01). In all of our simulations we take $\sigma = 10$, $R = 1$, $D = 1$, exponent set $(2, 1, 2, 0)$, and $r_0 = 0.5$ and we consider the near circle perturbation $h(\theta) = \cos(6\theta)$. Figure 2.12 shows the corrections at each order of ε for U_0 and b.

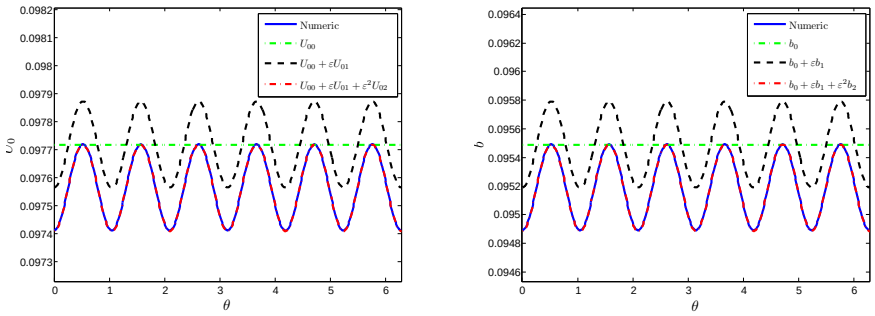

(a) U_0 corrections (b) b corrections

Figure 2.12: Asymptotic corrections compared to numeric simulations of the curve inhibitor value U_0 and the corresponding saturation value b from solving (2.32) for a perturbed circle with radius (2.52) and $h(\theta) = \cos(6\theta)$. Here we take exponent set $(2, 1, 2, 0)$, $R = 1$, $D = 1$, $r_0 = 0.5$, $\sigma = 10$, and $\varepsilon = 0.01$.

We see that indeed the correction at $\mathcal{O}(\varepsilon)$ introduces the sinusoidal perturbation only whereas the correction at $\mathcal{O}(\varepsilon^2)$ allows for the vertical shift correction. Figure 2.13 shows the corrections at each order of ε for the velocity V_0. In Figure 2.13b we zoom in to better show the asymptotic alignment.

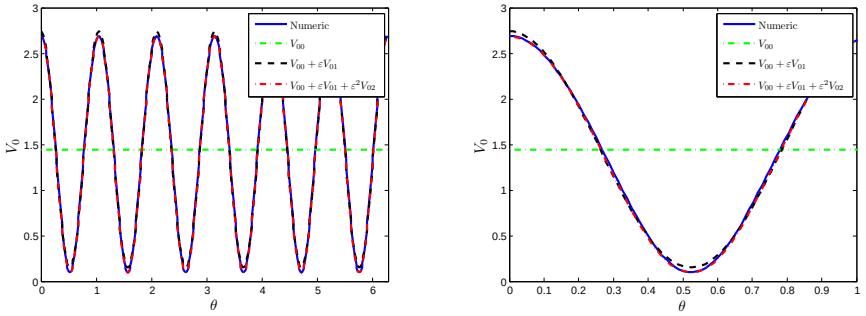

(a) Velocity corrections (b) Velocity corrections (zoom)

Figure 2.13: Asymptotic corrections compared to numeric simulations of the curve velocity V_0 from solving (2.32) for a perturbed circle with radius (2.52) and $h(\theta) = \cos(6\theta)$. Here we take exponent set $(2, 1, 2, 0)$, $R = 1$, $D = 1$, $r_0 = 0.5$, $\sigma = 10$, and $\varepsilon = 0.01$.

Chapter 3

Linear Stability of Ring Solutions to Breakup and Zigzag Modes

We will now consider the linear stability analysis to the problem of the radially symmetric inhibitor value produce by the activator localized on a ring of radius r_0. The base problem for this is

$$v_t = \epsilon^2 \frac{1}{r}\frac{\partial}{\partial r}\left(r\frac{\partial v}{\partial r}\right) + \frac{\epsilon^2}{r^2}\frac{\partial^2 v}{\partial \theta^2} - v + \frac{v^2}{u^q(1+\sigma v^2)} \tag{3.1a}$$

$$\tau u_t = D\frac{1}{r}\frac{\partial}{\partial r}\left(r\frac{\partial u}{\partial r}\right) + \frac{D}{r^2}\frac{\partial^2 u}{\partial \theta^2} - u + \frac{1}{\epsilon}\frac{v^o}{u^s} \tag{3.1b}$$

which leads to a quasi-steady state for the activator $v = U_0^q w$ where w is a homoclinic orbit obtained by solving (2.22) and U_0 is given by (2.40). The quasi-steady state for the inhibitor u is then given by (2.36).

3.1 Linear Stability Formulation

To perform a linear stability analysis of this steady state we first note that since the activator is locally confined to a ring of radius r_0 then we can define

an inner radius

$$\rho = \frac{r - r_0(T)}{\epsilon}$$

and we expect that the perturbation will also be localized entirely around this radius. Secondly, we note that the linearization of the full equation (3.1) is linear in θ and so we can perform a Fourier expansion as follows:

$$v \sim \tilde{v}_e \left(\frac{r - r_0}{\epsilon}, T \right) + \phi \left(\frac{r - r_0}{\epsilon}, t \right) \exp(im\theta) \tag{3.2a}$$

$$u \sim u_e(r, T) + M\,(r, t) \exp(im\theta) \tag{3.2b}$$

where v_e is the radial geometry form of the homoclinic orbit discussed in section 2.3 and u_e is the steady-state from section 2.3.1. Continuity in θ dictates that m is an integer on $(-\infty, \infty)$, but in what follows we will consider m to be a continuous parameter bearing in mind that all results will need to be rounded down to the nearest integer mode. Furthermore, we will consider it to be a positive parameter since the eigenfunctions for $m < 0$ are the same as for $m > 0$ and so we just need to be aware that all results need to accompany the complex conjugate mode. Note that in our expansion (3.2), we do not perform a standard Laplace expansion in time because the base state is actually dependent on the slow time $T = \epsilon^2 t$. Substituting our

expansion (3.2) into (3.1) we get

$$\epsilon^2\phi_T - \epsilon\phi_\rho \frac{\mathrm{d}r_0}{\mathrm{d}T} = \frac{1}{r_0+\epsilon\rho}\frac{\partial}{\partial\rho}\left((r_0+\epsilon\rho)\phi_\rho\right) \tag{3.3a}$$

$$- \frac{\epsilon^2 m^2}{(r_0+\epsilon\rho)^2}\phi - \phi - \frac{q\tilde{v}_e^2}{\tilde{u}_e^{q+1}(1+\sigma\tilde{v}_e^2)}M(r_0+\epsilon\rho)$$

$$+ \frac{2\tilde{v}_e}{\tilde{u}_e(1+\sigma\tilde{v}_e^2)^2}\phi, \tag{3.3b}$$

$$\epsilon^2\tau M_T = \frac{D}{r}\frac{\partial}{\partial r}(rM_r) - \frac{Dm^2}{r^2}M - M + \frac{1}{\epsilon}\frac{ov_e^{o-1}}{u_e^s}\phi\left(\frac{r-r_0}{\epsilon}\right)$$

$$- \frac{1}{\epsilon}\frac{sv_e^o}{u_e^{s+1}}M \tag{3.3c}$$

where we have scaled to the inner coordinate for the activator problem and have explicitly removed the slow-time dependence on r_0. Furthermore, we have rewritten the time dependence on ϕ and M using the long time scale. We now consider a WKB ansatz (cf. [9]) for each eigenfunction,

$$\phi(\rho,T) = \Phi(\rho,T)\exp\left(\frac{\varphi(T)}{\epsilon^2}\right), \quad M(r,T) = N(r,T)\exp\left(\frac{\varphi(T)}{\epsilon^2}\right). \tag{3.4}$$

Here we assume that the amplitude can vary with the radial coordinate but not the phase and we choose the phase function to be the same for each eigenfunction. The derivation of (3.4) can also be done via an application of multiple time scales (cf. [27]). We use this formulation in (3.3) to get

(dividing out the exponential function)

$$\begin{aligned}\epsilon^2\Phi_T + \Phi\varphi_T - \epsilon\Phi_\rho\frac{\mathrm{d}r_0}{\mathrm{d}T} =& \frac{1}{r_0+\epsilon\rho}\frac{\partial}{\partial\rho}\left((r_0+\epsilon\rho)\Phi_\rho\right) \\ &- \frac{\epsilon^2 m^2}{(r_0+\epsilon\rho)^2}\Phi - \Phi - \frac{q\tilde{v}_e^2}{\tilde{u}_e^{q+1}(1+\sigma\tilde{v}_e^2)}N(r_0+\epsilon\rho) \\ &+ \frac{2\tilde{v}_e}{\tilde{u}_e(1+\sigma\tilde{v}_e^2)^2}\Phi, \qquad (3.5a)\end{aligned}$$

$$\begin{aligned}\epsilon^2\tau N_T + \tau N\varphi_T =& \frac{D}{r}(rN_r)_r - \frac{Dm^2}{r^2}N - N + \frac{1}{\epsilon}\frac{ov_e^{o-1}}{u_e^s}\Phi\left(\frac{r-r_0}{\epsilon}\right) \\ &- \frac{1}{\epsilon}\frac{sv_e^o}{u_e^{s+1}}N. \qquad (3.5b)\end{aligned}$$

Since N is $\mathcal{O}(1)$ to leading order, we seek a natural asymptotic expansion of the inner activator function and phase,

$$\Phi \sim \Phi_0 + \epsilon\Phi_1 + \ldots \qquad \varphi \sim \varphi_0 + \epsilon\varphi_1 + \ldots$$

to finally get the leading order problem

$$\Phi_0\varphi_{0T} = \Phi_{0\rho\rho} - \frac{\epsilon^2 m^2}{r_0^2}\Phi_0 - \Phi_0 + \frac{2w}{(1+bw^2)^2}\Phi_0 - \frac{qU_0^{q-1}w^2}{(1+bw^2)}N(r_0), \qquad (3.6a)$$

$$\tau N\varphi_{0T} = \frac{D}{r}(rN_r)_r - \frac{Dm^2}{r^2}N - N + \frac{1}{\epsilon}\frac{ov_e^{o-1}}{u_e^s}\Phi_0\left(\frac{r-r_0}{\epsilon}\right) - \frac{1}{\epsilon}\frac{sv_e^o}{u_e^{s+1}}N, \qquad (3.6b)$$

where we have used in (3.6a) that to leading order $\tilde{u}_e \sim U_0$ and $\tilde{v}_e \sim U_0^q w$. Note that this formulation assumes that $N(r_0)$ is $\mathcal{O}(1)$ to leading order and we will analyze when this is so. We also include terms that are $\mathcal{O}(\epsilon^2 m^2)$

because if $m \gg 1$ then this can be an $\mathcal{O}(1)$ term. If we define,

$$L_{0b}\Phi_0 = \Phi_{0\rho\rho} - \Phi_0 + \frac{2w}{(1+bw^2)^2}\Phi_0, \tag{3.7}$$

then we can write (3.6a) as

$$L_{0b}\Phi_0 - qU_0^{q-1}\frac{w^2}{(1+bw^2)}N(r_0) = \left(\varphi_{0T} + \frac{\epsilon^2 m^2}{r_0^2}\right)\Phi_0, \quad \lim_{|\rho|\to\infty}\Phi = 0, \tag{3.8}$$

and so we can think of $\varphi_{0T} = \lambda$ as the eigenvalues of (3.8). In (3.8) we don't define the normalization of the eigenfunctions but rather leave this discussion to section 3.2.11 where we compute them numerically. If we solved the eigenvalues of (3.8) we would have

$$\phi(\rho, T) \sim \Phi_0 \exp\left(\int_0^T \lambda(s)\,\mathrm{d}s/\epsilon^2\right), \tag{3.9}$$

where we have assumed that $\varphi_0(0) = 0$ without loss of generality. Notice that if the eigenvalues were not time-dependent we would get the standard $\exp(\lambda t)$ from the Laplace expansion in a linear stability analysis. This slight difference can actually lead to delays in stability or instability if an eigenvalue changes sign over the long-time domain. This behaviour is similar to what is responsible for parameter delayed bifurcations in certain dynamical systems models (cf. [76], [50], [28]). We will now turn our attention to actually determining the eigenvalues of (3.8). To analyze this eigenvalue problem we need to first solve (3.6b) which requires looking at the apparent singular term,

$$\frac{1}{\epsilon}\frac{o v_e^{o-1}}{u_e^s}\Phi\left(\frac{r-r_0}{\epsilon}\right) = \frac{o\tilde{v}_e\left(\frac{r-r_0}{\epsilon}\right)^{o-1}}{\tilde{u_e}\left(\frac{r-r_0}{\epsilon}\right)^{s}}\Phi \underset{\epsilon\to 0}{=} A\delta(r-r_0).$$

To find A, we follow a procedure similar to section 2.2.1 and integrate this expression around the singularity r_0 to get

$$A = oU_0^{\beta-q} \int_{-\infty}^{\infty} w^{o-1} \Phi_0 \, \mathrm{d}\rho.$$

In a similar fashion we have that

$$\frac{1}{\epsilon} \frac{s v_e^o}{u_e^{s+1}} N(r) \underset{\epsilon \to 0}{=} s U_0^{\beta-1} N(r_0) \mathcal{A} \delta(r - r_0), \quad \mathcal{A} = \int_{-\infty}^{\infty} w^o \, \mathrm{d}\rho,$$

and so we can write (3.6b) as

$$\begin{aligned} &\frac{1}{r}(rN_r)_r - \frac{m^2}{r^2} N - \theta_\lambda^2 N \\ &= \left(\frac{s U_0^{\beta-1}}{D} N(r_0) \mathcal{A} - \frac{o U_0^{\beta-q}}{D} \int_{-\infty}^{\infty} w^{o-1} \Phi_0 \, \mathrm{d}\rho \right) \delta(r - r_0), \end{aligned} \tag{3.10}$$

where

$$\theta_\lambda = \sqrt{\frac{1 + \tau\lambda}{D}}. \tag{3.11}$$

Like for the non-radially symmetric ring solution (2.48) or the near circular ring solution (2.63) from section 2.3.1, (3.10) is the $n > 0$ analogue to the radially symmetric problem (eqn:circprob) and the solution technique immediately mimics that of section sec:radialsym. As such, we omit the details here but simply write down

$$N(r) = r_0 \left(\frac{o U_0^{\beta-q}}{D} \int_{-\infty}^{\infty} w^{o-1} \Phi_0 \, \mathrm{d}\rho - \frac{s U_0^{\beta-1}}{D} N(r_0) \mathcal{A} \right) \bar{G}_{0,m}(r; r_0), \tag{3.12}$$

where

$$\bar{G}_{0,m}(r;r_0) = \begin{cases} \bar{\mathcal{J}}_{m,1}(\theta_\lambda r)\bar{\mathcal{J}}_{m,2}(\theta_\lambda r_0), & 0 \le r \le r_0 \\ \bar{\mathcal{J}}_{m,1}(\theta_\lambda r_0)\bar{\mathcal{J}}_{m,2}(\theta_\lambda r), & r_0 \le r \le R \end{cases},$$

with

$$\bar{\mathcal{J}}_{m,1}(\theta_\lambda r) = I_m\left(\theta_\lambda r\right), \tag{3.13a}$$

$$\bar{\mathcal{J}}_{m,2}(\theta_\lambda r) = \bar{\alpha}_m I_m\left(\theta_\lambda r\right) + K_m\left(\theta_\lambda r\right), \tag{3.13b}$$

and $\bar{\alpha}_m$ given by

$$\bar{\alpha}_m = -\frac{K_m\left(\theta_\lambda R\right)'}{I_m\left(\theta_\lambda R\right)'} = \left(\frac{K_{m+1}\left(\theta_\lambda R\right) - \frac{m}{\theta_\lambda R}K_m\left(\theta_\lambda R\right)}{\frac{m}{\theta_\lambda R}I_m\left(\theta_\lambda R\right) + I_{m+1}\left(\theta_\lambda R\right)}\right). \tag{3.13c}$$

If we notice that

$$\frac{\mathcal{A}U_0^{\beta-1}r_0}{D} = \frac{1}{G_0(r_0;r_0)},$$

with G_0 defined by (2.38) then we can write (3.12) as

$$N(r) = \left(\frac{oU_0^{1-q}}{G_0(r_0;r_0)\mathcal{A}}\int_{-\infty}^{\infty} w^{o-1}\Phi_0\,\mathrm{d}\rho - \frac{s}{G_0(r_0;r_0)}N(r_0)\right)\bar{G}_{0,m}(r;r_0). \tag{3.14}$$

By evaluating this expression at $r = r_0$, we solve for $N(r_0)$ to get

$$N(r_0) = oU_0^{1-q}\left(s + \frac{\mathcal{J}_{0,1}(r_0)\mathcal{J}_{0,2}(r_0)}{\bar{\mathcal{J}}_{m,1}(\theta_\lambda r_0)\bar{\mathcal{J}}_{m,2}(\theta_\lambda r_0)}\right)^{-1}\frac{\int_{-\infty}^{\infty} w^{o-1}\Phi_0\,\mathrm{d}\rho}{\mathcal{A}} \tag{3.15}$$

with $\mathcal{J}_{0,1}$ and $\mathcal{J}_{0,2}$ defined by (2.39). There is something significant to note about $N(r_0)$ and that is the integral involving Φ_0. The structure of (3.8) dictates that Φ_0 will admit both an even and an odd solution (cf. [30]). Since w is even then if Φ_0 is odd, $N(r_0)$ vanishes and the assumption that it is $\mathcal{O}(1)$ to leading order fails. If Φ_0 is even and has multiple nodal points then $N(r_0)$ may still vanish. In this case, the eigenvalue of (3.8) is part of the spectrum of (3.7) for which we adapt the following Lemma of [7]:

Lemma 3.1.0.1 *Consider the problem*

$$w_{yy} - w + f(w) = 0, \qquad w_y(0) = 0, \quad w \to 0 \text{ as } |y| \to \infty, \quad w(0) > 0$$

and assume this has a homoclinic orbit solution via Lemma 2.2.0.1. The associated linearized operator

$$\mathcal{L}\Phi = \Phi_{yy} - \Phi + f'(w)\Phi = \lambda\Phi$$

has a discrete simple positive eigenvalue $\lambda_0 > 0$ associated to a positive eigenfunction Φ_0. There is also a discrete eigenvalue $\lambda_1 = 0$ with the eigenfunction $\Phi_1 = w'$. Furthermore when $f'(0)$ is finite, a continuous spectrum exists on $Re(\lambda) \leq -1 + f'(0) < 0$ with $Im(\lambda) = 0$.

A corollary to Lemma 3.1.0.1 is that if other discrete eigenvalues λ_j, $j > 1$ exist then $-1 + f'(0) < \lambda_j < 0$. See [14] for other discretely computed eigenvalues with $f(w) = w^p$. Since the principal eigenvalue is the only one for which $\mathrm{Re}(\lambda) > 0$ and its eigenfunction is even and of one sign, instability can only occur for even eigenfunctions where $N(r_0)$ does not vanish.

3.2 Eigenvalues Associated with Φ_0 Even

Since the curve is defined as the point where the activator reaches its maximum (defined to be at $r = r_0$ for the steady-state) then if the eigenfunction is even, this will affect the amplitude of the maximal value but not the location (the derivative at r_0 still vanishes). Therefore, we consider even eigenfunctions to correspond with amplitude or break-up instabilities. Using the expression (3.15), we define

$$\chi_m = qo\left(s + \frac{\mathcal{J}_{0,1}(r_0)\mathcal{J}_{0,2}(r_0)}{\bar{\mathcal{J}}_{m,1}(\theta_\lambda r_0)\bar{\mathcal{J}}_{m,2}(\theta_\lambda r_0)}\right)^{-1},$$

so that we can write (3.8) as

$$L_{0b}\Phi_0 - \frac{\chi_m}{\mathcal{A}}\frac{w^2}{(1+bw^2)}\int_{-\infty}^{\infty} w^{o-1}\Phi_0\,\mathrm{d}\rho = \left(\lambda + \frac{\epsilon^2 m^2}{r_0^2}\right)\Phi_0, \tag{3.16}$$

subject to far-field decay conditions. We call (3.16) the non-local eigenvalue problem (NLEP) for λ and the study of NLEPs has a rich history of study (cf. [39], [45], [46], [81]). The non-local feature of the eigenvalue problem is common in pattern formation problems as a measure of the long-range inhibitor effect in the semi-strong regime. Aside from being non-local, NLEPs such as (3.16) are also non-self-adjoint and as such are notoriously difficult for finding conditions for which the eigenvalues satisfy $\mathrm{Re}(\lambda) < 0$. If we define the quantities

$$\mu = \lambda + \frac{\epsilon^2 m^2}{r_0^2}, \quad A(\Phi_0) = \int_{-\infty}^{\infty} w^{o-1}\Phi_0\,\mathrm{d}\rho \tag{3.17}$$

then we can write (3.16) as

$$L_{0b}\Phi_0 - \frac{\chi_m}{\mathcal{A}}\frac{w^2}{(1+bw^2)}A(\Phi_0) = \mu\Phi_0.$$

We notice that L_{0b} is a self-adjoint operator and with this in mind, multiply the eigenvalue problem with a function ψ, satisfying the same boundary conditions as Φ_0, and integrate

$$\int_{-\infty}^{\infty}(L_{0b}\Phi - \mu\Phi_0)\psi\,\mathrm{d}\rho = \frac{\chi_m}{\mathcal{A}}\int_{-\infty}^{\infty}\frac{w^2}{(1+bw^2)}A(\Phi_0)\psi\,\mathrm{d}\rho.$$

Since L_{0b} is self-adjoint,

$$\int_{-\infty}^{\infty}(L_{0b}\Phi_0 - \mu\Phi_0)\psi\,\mathrm{d}\rho = \int_{-\infty}^{\infty}(L_{0b}\psi - \mu\psi)\Phi_0\,\mathrm{d}\rho,$$

and so

$$\int_{-\infty}^{\infty}(L_{0b}\psi - \mu\psi)\Phi_0 - \frac{\chi_m}{\mathcal{A}}\frac{w^2}{(1+bw^2)}A(\Phi_0)\psi\,\mathrm{d}\rho = 0.$$

Define ψ such that

$$(L_{0b} - \mu)\psi = \frac{w^2}{(1+bw^2)}, \tag{3.18}$$

so that

$$\int_{-\infty}^{\infty}\frac{w^2}{(1+bw^2)}\left(\Phi_0 - \frac{\chi_m}{\mathcal{A}}A(\Phi_0)\psi\right)\mathrm{d}\rho = 0.$$

Since everything outside the brackets in the integrand is positive, the integral can only vanish if

$$\Phi_0 = \frac{\chi_m}{\mathcal{A}}A(\Phi_0)\psi.$$

We can use this to write (3.16) as

$$\frac{\chi_m}{\mathcal{A}}A(\Phi_0)L_{0b}\psi - \frac{\chi_m}{\mathcal{A}}A(\Phi_0)\frac{\chi_m}{\mathcal{A}}\frac{w^2}{(1+bw^2)}\int_{-\infty}^{\infty} w^{o-1}\psi\,\mathrm{d}\rho = \frac{\chi_m}{\mathcal{A}}A(\Phi_0)\mu\psi.$$

Dividing through by $\frac{\chi_m}{\mathcal{A}}A(\Phi)$ and using (3.18) we get,

$$\frac{1}{\chi_m} - \frac{\int_{-\infty}^{\infty} w^{o-1}\psi\,\mathrm{d}\rho}{\mathcal{A}} = 0.$$

We define $C_m(\lambda)$ and $f(\mu)$ by,

$$C_m(\lambda) \equiv \frac{1}{\chi_m} = \frac{1}{qo}\left(s + \frac{\mathcal{J}_{0,1}(r_0)\mathcal{J}_{0,2}(r_0)}{\bar{\mathcal{J}}_{m,1}(\theta_\lambda r_0)\bar{\mathcal{J}}_{m,2}(\theta_\lambda r_0)}\right), \tag{3.19a}$$

$$f(\mu) \equiv \frac{\int_{-\infty}^{\infty} w^{o-1}\psi\,\mathrm{d}\rho}{\mathcal{A}}, \tag{3.19b}$$

and so the eigenvalue problem (3.16) becomes a root finding problem

$$g_m(\lambda) \equiv C_m(\lambda) - f(\mu) = 0, \tag{3.20}$$

subject to (3.18) where μ is given by (3.17). Note that we are only interested in roots satisfying $\mathrm{Re}(\lambda) > 0$ which correspond to unstable eigenvalues.

3.2.1 Removing Saturation: The case $b = 0$

We begin by considering $\sigma = 0$ (hence $b = 0$) as this will allow us to recover some analytic properties for the even eigenfunctions for which the nonlocal

term in (3.16) does not vanish. First when $b = 0$, we write (3.7) as

$$L_0\Phi_0 = L_{00}\Phi_0 = \Phi_{0\rho\rho} - \Phi_0 + 2w\Phi_0, \tag{3.21}$$

so that the NLEP (3.16) simplifies to

$$L_0\Phi_0 - \frac{\chi_m}{\mathcal{A}} w^2 \int_{-\infty}^{\infty} w^{o-1}\Phi_0 \,\mathrm{d}\rho = \mu\Phi_0. \tag{3.22}$$

For this limiting case, the root finding problem (3.20) remains unchanged except that now the function ψ from (3.19b) satisfies

$$(L_0 - \mu)\psi = w^2, \tag{3.23}$$

instead of (3.18). We will decompose the process of determining unstable eigenvalues by considering real and complex eigenvalues separately.

3.2.2 Real Eigenvalues

If λ is purely real then the root finding problem remains completely unchanged. When $b = 0$ then we can determine the discrete eigenvalues $L_0\Psi = \nu\Psi$ using Lemma 3.1.0.1 explicitly (cf. [14], [47]). The continuous spectrum exists on $\mathrm{Re}(\nu) < -1$ and the discrete eigenvalues and eigenfunctions satisfy,

$$\nu_0 = \frac{5}{4}, \quad \Psi_0 = w^{3/2}; \quad \nu_1 = 0, \quad \Psi_1 = w'; \quad \nu_2 = -\frac{3}{4}, \quad \Psi_2 = \left(1 - \frac{5}{6}w\right) w^{1/2}. \tag{3.24}$$

The principal eigenfunction Ψ_0, is a solution to the homogeneous problem (3.23) when $\mu = \nu_0$ and since the operator is self-adjoint, there will only be a solution ψ if the compatibility condition,

$$\int_{-\infty}^{\infty} w^2 \Psi \, \mathrm{d}\rho = 0,$$

is satisfied which is impossible because both functions are even and hence their product is as well. Therefore we immediately understand that f, as defined in (3.19b), will have a vertical asymptote at $\mu = \nu_0$. Properties of $f(\mu)$ in (3.19b) have been analyzed in [79] where the asymptotic structure of $f(\mu)$ for $\mu \ll 1$ is given by

$$f(\mu) \sim 1 + \left(1 - \frac{1}{2o}\right) \mu + \kappa_c \mu^2 + \ldots \tag{3.25}$$

with

$$\kappa_c = \frac{\int_{-\infty}^{\infty} w^{o-1} \psi_c \, \mathrm{d}\rho}{\mathcal{A}}, \qquad \psi_c = L_0^{-3}(w^2). \tag{3.26}$$

In general, ψ_c needs to be computed numerically. However, in Proposition 3.1 of [79], an explicit analytic representation is given for the case $o = 2$ and $o = 3$ (based on the exponent 2 in $(2, q, o, s)$). With these same cases, the following global properties of $f(\mu)$ are also provided in Proposition 3.5:

$$f'(\mu) > 0, \qquad \mu \in [0, \nu_0) \tag{3.27a}$$

$$f''(\mu) > 0, \qquad \mu \in [0, \nu_0) \tag{3.27b}$$

$$f(\mu) < 0, \qquad \mu \in (\nu_0, \infty). \tag{3.27c}$$

These properties rely on easily being able to compute or bound the integrals in (3.19b) and solve (3.23) along with derivatives of eigenfunctions. However, in the absence of analytic solutions, we can solve (3.23) and (3.19b) numerically and we conjecture that (3.27) holds for any exponent o. In Figure 3.1, we plot $f(\mu)$ for $o = 1, 4$, and 5.

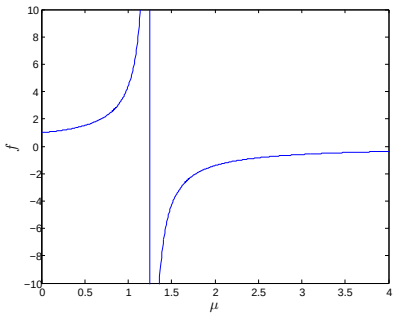

(a) $o = 1$

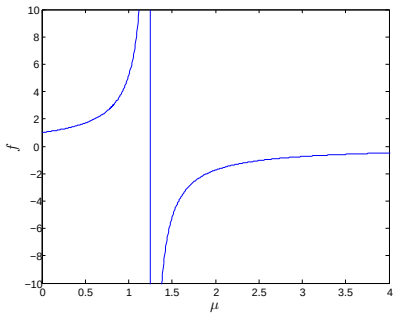

(b) $o = 4$

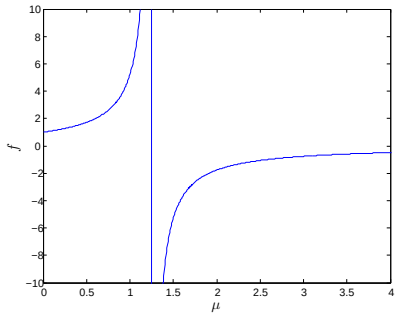

(c) $o = 5$

Figure 3.1: Computation of $f(\mu)$ from (3.19b) for various o with $m = 0$, $r_0 = 0.5$, and $\epsilon = 0.025$. We set $m = 0$ solely to satisfy $\mu = \lambda$ and deal with a single variable. The properties (3.27) derived analytically from $o = 2$ or $o = 3$ still hold for various exponents.

To understand the singularity properties of the asymptote to (3.19b) at $\mu =$

ν_0 we consider a small parameter δ such that

$$\mu = \nu_0 + \delta\mu_1, \qquad \psi = \omega(\delta)(\psi_0 + \delta\psi_1),$$

with $\omega(\delta)$ to be determined and substitute this into (3.23). The source of this asymptote, as previously stated, is that the homogeneous solution is incompatible with the non-homogeneous term. Near ν_0, we can only achieve solution compatibility if the right hand-side of (3.23) is subdominant to ψ_0. If we expand our substitution,

$$L_0\psi_0 - \nu_0\psi_0 + \delta(L_0\psi_1 - \nu_0\psi_1 - \nu_1\psi_0) + \mathcal{O}(\delta^2) = \frac{w^2}{\omega},$$

then a reasonable balance is to take $\omega = 1/\delta$. The leading order problem then results in $\psi_0 = \Psi_0$, the eigenfunction for ν_0. At next order the problem is,

$$L_0\psi_1 - \nu_0\psi_1 = w^2 + \mu_1\psi_0.$$

We notice that $\psi_1 = \Psi_0$ is a solution to the homogeneous problem and so, in order for a solution to exist, we must have that the compatibility condition,

$$\int_{-\infty}^{\infty} w^2\Psi_0 \,\mathrm{d}\rho + \mu_1 \int_{-\infty}^{\infty} \Psi_0^2 \,\mathrm{d}\rho = 0,$$

is satisfied. This yields that

$$\mu_1 = -\frac{\int_{-\infty}^{\infty} w^2\Psi_0 \,\mathrm{d}\rho}{\int_{-\infty}^{\infty} \Psi_0^2 \,\mathrm{d}\rho}.$$

If we rewrite

$$\delta = \frac{\mu - \nu_0}{\mu_1},$$

then we have that to leading order,

$$\psi \sim \frac{\mu_1}{\mu - \nu_0}\Psi_0,$$

for μ near ν_0. With this we can compute,

$$f(\mu) \sim \frac{\mu_1}{\mu - \nu_0}\frac{\int_{-\infty}^{\infty} w^{o-1}\Psi_0 \,\mathrm{d}\rho}{\int_{-\infty}^{\infty} w^o \,\mathrm{d}\rho}, \qquad \mu \approx \nu_0. \tag{3.28}$$

Therefore we have that there is a simple pole to $f(\mu)$ at $\mu = \nu_0$ satisfying $f \to \infty$ as $\mu \to \nu_0^-$ and $f \to -\infty$ as $\mu \to \nu_0^+$. In Figure 3.2 we show $f(\mu)$ computed numerically for $m = 0$, $r_0 = 0.5$, $\epsilon = 0.025$, and $o = 2$ and overlay the asymptotic approximation (3.28). The asymptotic agreement extends quite well beyond the asymptote and generally describes the entire function.

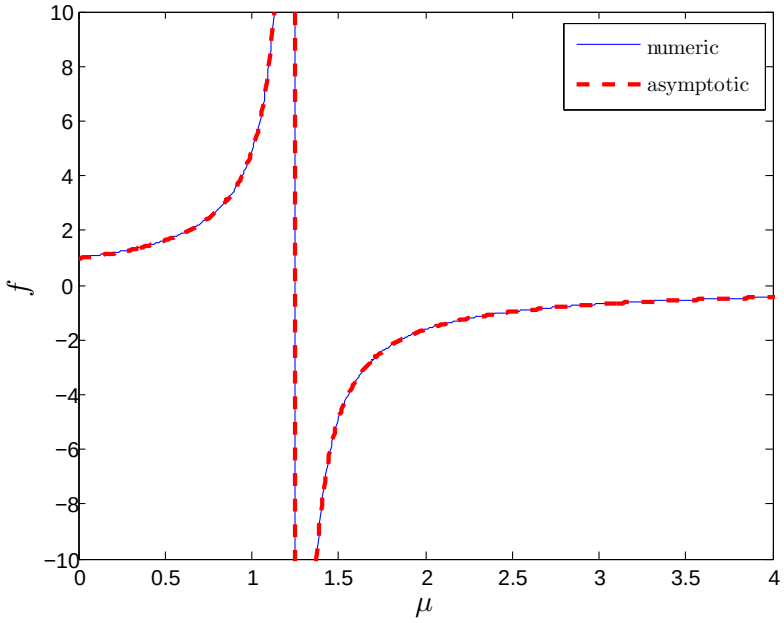

Figure 3.2: Numerical computation of $f(\mu)$ when $m = 0$, $r_0 = 0.5$, $\epsilon = 0.025$, and $o = 2$ along with the asymptotic expression (3.28) demonstrating the simple pole at $\mu = \nu_0$.

Returning to the root problem g given by (3.20), the structure can depend significantly on the magnitude of m and specifically centers around the term $\epsilon^2 m^2/r_0^2$ being significant or not. As such we will independently investigate these cases.

3.2.3 Real Eigenvalues: $m = \mathcal{O}(1)$

Consider $m = \mathcal{O}(1)$ so that for $\epsilon \ll 1$,

$$\mu = \lambda + \frac{\epsilon^2 m^2}{r_0^2} \approx \lambda.$$

First note that if $\lambda > \nu_0$ then since $C_m(\lambda) > 0$ and $f(\lambda) < 0$ from (3.27) then we conclude that $g_m(\lambda) > 0$ when $\lambda > \nu_0$. Therefore, to leading order, all eigenvalues to (3.22) satisfy $\lambda < \nu_0$. We begin by finding the neutral stability point $\lambda = 0$. From the asymptotic expansion of $f(\mu)$ given by (3.25), we have that $f(0) = 1$ and so

$$g_m(0) = C_m(0) - 1.$$

Furthermore, when $\lambda = 0$ then $\theta_\lambda = 1/\sqrt{D}$ and when $m = 0$ we have that $\bar{\mathcal{J}}_{m,i}(\theta_\lambda r) = \mathcal{J}_{0,i}(r)$ so from (3.19a), $C_0(0) = s/qo$ and so since $s + 1 < qo$, $g_0(0) < 0$. To understand the existence of roots we must look at the C_m function in (3.19a) and differentiate it with respect to order,

$$\frac{\partial C_m}{\partial m} = -\frac{\bar{C}_0}{(\bar{\mathcal{J}}_{m,1}(\theta_\lambda r_0)\bar{\mathcal{J}}_{m,2}(\theta_\lambda r_0))^2}\frac{\partial}{\partial m}\left(\bar{\mathcal{J}}_{m,1}(\theta_\lambda r_0)\bar{\mathcal{J}}_{m,2}(\theta_\lambda r_0)\right),$$

where

$$\bar{C}_0 = \frac{\mathcal{J}_{0,1}(r_0)\mathcal{J}_{0,2}(r_0)}{qo} > 0.$$

Order derivative expressions have been formulated (cf. [1]) but are relatively intractable for general m in terms of obtaining sign estimates. However, they do simplify for $m = 0$ to,

$$\frac{\partial}{\partial m} I_m(z)\Big|_{m=0} = -K_0(z), \quad \frac{\partial}{\partial m} K_m(z)\Big|_{m=0} = 0,$$

and so in this case

$$\frac{\partial J_m}{\partial m}\Big|_{m=0} = -2\bar{\alpha}_0 I_0(\theta_\lambda r_0) K_0(\theta_\lambda r_0) - K_0(\theta_\lambda r_0)^2 + I_0(\theta_\lambda r_0)^2 \frac{\partial \bar{\alpha}_m}{\partial m}\Big|_{m=0}, \tag{3.29}$$

where

$$J_m(r_0) = \bar{\mathcal{J}}_{m,1}(\theta_\lambda r_0)\bar{\mathcal{J}}_{m,2}(\theta_\lambda r_0). \tag{3.30}$$

To understand this better we require the order derivative of $\bar{\alpha}_0$,

$$\begin{aligned}\left.\frac{\mathrm{d}\bar{\alpha}_m}{\mathrm{d}m}\right|_{m=0} =& \frac{\left.\frac{\partial K_m(\theta_\lambda R)}{\partial m}\right|_{m=1} - K_0(\theta_\lambda R)}{I_1(\theta_\lambda R)} \\ & - \frac{K_1(\theta_\lambda R)\left(\left.\frac{\partial I_m(\theta_\lambda R)}{\partial m}\right|_{m=1} + I_0(\theta_\lambda R)\right)}{I_1(\theta_\lambda R)^2}.\end{aligned}$$

Once again from [1] we can compute that

$$\left.\frac{\partial I_m(z)}{\partial m}\right|_{m=1} = K_1(z) - \frac{I_0(z)}{z}, \quad \left.\frac{\partial K_m(z)}{\partial m}\right|_{m=1} = \frac{K_1(z)}{z},$$

and using the Wronskian relationship (2.37) we can finally write that

$$\left.\frac{\mathrm{d}\bar{\alpha}_m}{\mathrm{d}m}\right|_{m=0} = \frac{1}{(\theta_\lambda R)^2 I_1(\theta_\lambda R)^2}(1 - \theta_\lambda R) - \bar{\alpha}_0^2.$$

For $\theta_\lambda R > 1$, this expression is negative and for $\theta_\lambda R < 1$, if we use the small argument asymptotics for the modified Bessel functions [1], we have

$$\left.\frac{\mathrm{d}\bar{\alpha}_m}{\mathrm{d}m}\right|_{m=0} \sim -\frac{1}{4(\theta_\lambda R)^3},$$

and therefore the order derivative of $\bar{\alpha}_0$ is always negative so (3.29) is always negative and therefore

$$\left.\frac{\partial C_m}{\partial m}\right|_{m=0} > 0.$$

We expect this still to hold for m near zero and in fact, numerically, we can confirm positivity on C_m holds for all m with $r_0 \in [0, R]$ via Figure 3.3 which plots the maximum of the order derivative of (3.30) for $r_0 \in [0, R]$ versus θ_λ for various values of R. This derivative is always negative and tending to zero so therefore we have that $\frac{\partial C_m}{\partial m} > 0$ for all m.

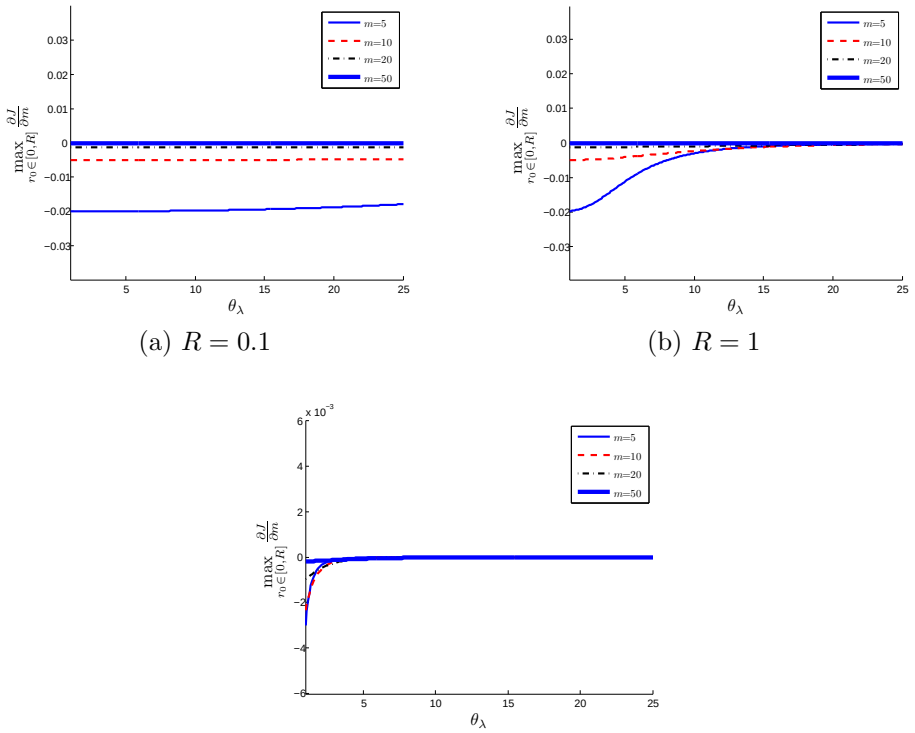

(a) $R = 0.1$

(b) $R = 1$

(c) $R = 10$

Figure 3.3: Numerical computation of the derivative of (3.30) with respect to m. For a given value of m, R, and θ_λ, we compute the order derivative of (3.30) over $r_0 \in [0, R]$ and then take the maximum value over that interval. The figure shows each maximal value of the derivative as a function of θ_λ for various values of R.

Since the derivative is always positive, we can have at most one root to C_m.

If we consider m large then we can use the small argument asymptotics for $I_m(x)$ and $K_m(x)$ which are valid for $x \ll \sqrt{m+1}$ [1]. These expansions are,

$$I_m(x) \sim \frac{1}{\Gamma(m+1)}\left(\frac{x}{2}\right)^m, \quad K_m(x) \sim \frac{\Gamma(m)}{2}\left(\frac{2}{x}\right)^m \tag{3.31}$$

and so therefore

$$C_m(\lambda) \underset{m\gg 1}{\approx} \frac{\bar{C}_0}{J_m(r_0)} \sim \bar{C}_0 \frac{2m}{1+\left(\frac{r_0}{R}\right)^{2m}} \gg 1. \tag{3.32}$$

This in combination with $C_0(0) < 0$ and $\frac{\mathrm{d}C_m}{\mathrm{d}m} > 0$ shows there exists exactly one point where $C_m(0) = 1$ and hence a single value $m = m_{b^-}$ such that

$$g_{m_{b^-}}(0) = 0. \tag{3.33}$$

Now, just because there is a value of m for which a neutral stability point occurs, this does not mean that $\lambda = 0$ is the largest eigenvalue when $m = m_{b^-}$. To investigate this, we need to consider the λ derivative and second derivative for C_m. In a similar fashion to what we did with the order derivative, we can conclude numerically that

$$\frac{\partial C_m}{\partial \lambda} > 0, \quad \frac{\partial^2 C_m}{\partial \lambda^2} < 0, \tag{3.34}$$

when $\tau \neq 0$. When $\tau = 0$ then $C_m(\lambda) = C_m(0)$ since the eigenvalue only occurs in a product with τ and therefore $\frac{\mathrm{d}C_m}{\mathrm{d}\lambda} = 0$ when $\tau = 0$. Using these

expressions along with (3.27) we have that

$$\frac{\partial^2 g_m}{\partial \lambda^2} = \frac{\partial^2 C_m}{\partial \lambda^2} - \frac{\partial^2 f}{\partial \lambda^2} < 0. \tag{3.35}$$

Since this expression holds for all m, it must hold at $m = m_{b^-}$ and so $g_{m_{b^-}}$ can have at most 2 roots of which we already know $\lambda = 0$ is one. As λ tends to ν_0 from the left then $g_{m_{b^-}}$ tends to negative infinity. If $\frac{\mathrm{d}g_{m_{b^-}}}{\mathrm{d}\lambda} < 0$ when $\lambda = 0$ then the only possible way there can exist a second root and have the far-field behaviour be satisfied is if there are at least three roots to $g_{m_{b^-}}$ which violates the maximal root condition. Conversely, if the derivative is positive when $\lambda = 0$ then there must be a second crossing to achieve the far-field behaviour and therefore a second, larger, root must exist. When $\tau = 0$, we know that $\frac{\mathrm{d}C_m}{\mathrm{d}\lambda} = 0$ and so by (3.27)

$$\left.\frac{\mathrm{d}g_{m_{b^-}}}{\mathrm{d}\lambda}\right|_{\tau=0} < 0, \tag{3.36}$$

always. If $\tau \gg 1$ then $\theta_\lambda \gg 1$ and we can use the large argument asymptotic expansions for the Bessel functions [1],

$$I_m(x) \sim \frac{\exp(x)}{\sqrt{2\pi x}}, \quad K_m(x) \sim \sqrt{\frac{\pi}{2x}}\exp(-x)$$

to write

$$C_m(\lambda) \sim 2\bar{C}_0 r_0 \theta_\lambda \frac{1}{(1+\exp(-2\theta_\lambda(R-r_0)))} \approx 2\bar{C}_0 r_0 \theta_\lambda \gg 1 \qquad \tau \gg 1. \tag{3.37}$$

Consider λ small such that $f \sim 1$ via (3.25) but large enough (i.e. $\lambda > \mathcal{O}(1/\tau)$) so that for $\tau \gg 1$

$$g_m \sim C_m \gg 1.$$

Specifically then, when $m = m_{b^-}$, and if τ is large, we have

$$\left.\frac{\mathrm{d}g_{m_{b^-}}}{\mathrm{d}\lambda}\right|_{\tau\gg 1} > 0$$

for some range of λ and therefore this must be true when $\lambda = 0$ otherwise the two-root condition will be violated. Therefore, there must exist some critical value $\tau = \tau^*_{m_{b^-}}$ which satisfies

$$\left.\frac{\mathrm{d}g_{m_{b^-}}}{\mathrm{d}\lambda}(0)\right|_{\tau=\tau^*_{m_{b^-}}} = 0 \tag{3.38}$$

such that a new root $\lambda_{\tau^*_{m_{b^-}}} > 0$ is created and persists for $\tau > \tau^*_{m_{b^-}}$. We can find this point by using a numerical root-finding algorithm to solve (3.33) and (3.38). For example using Newton's method with $r_0 = 0.5$, $R = 1$, $D = 1$, and exponent set $(2, 1, 2, 0)$, we get,

$$m_{b^-} \approx 0.4003 \qquad \tau^*_{m_{b^-}} \approx 1.8376. \tag{3.39}$$

While we solve this problem numerically, it is still an asymptotic approximation as we are ignoring the terms $\epsilon^2 m^2/r_0^2$.

Now that we have investigated the neutral stability point, we will turn our attention to the intervals that $m = m_{b^-}$ creates. Firstly, we will look at

$m \in [0, m_{b^-})$. When $m = m_{b^-}$ we have that $C_{m_{b^-}} = 1$ and since $\frac{\mathrm{d}C_m}{\mathrm{d}m} > 0$ for all m then for $0 \leq m < m_{b^-}$ we must have $C_m(0) < 1$. Since $f(0) = 1$ then $g_m(0) < 0$. When $\tau = 0$ then recall $C_m(\lambda) = C_m(0)$ and therefore via (3.36), there are no positive λ for $m \in [0, m_{b^-})$ when $\tau = 0$. When τ is really large then (3.37) holds for C_m and by a similar logic as when $m = m_{b^-}$ there is a range of λ for which $g_m(\lambda) > 0$. Furthermore, we still have that $g_m \to -\infty$ as $\lambda \to \nu_0^-$, and so combining this information there are at least two roots to g_m for $\tau \gg 1$ for $m \in [0, m_{b^-})$. Using (3.35) we can restrict this further and conclude that there are exactly two roots when $\tau \gg 1$. Of course, this means there must exist some $\tau = \tau_m^*$ such that there is exactly one positive root $\lambda_{\tau_m^*}$ which will occur when

$$g_m(\lambda_{\tau_m^*}) = \left.\frac{\partial g_m}{\partial \lambda}\right|_{\lambda_{\tau_m^*}} = 0.$$

Note that since the only neutral stability point occurs at $m = m_{b^-}$, these positive roots cannot transition through $\lambda = 0$ and must become real via the complex plane.

Finally, we consider $m \in (m_{b^-}, \infty)$, bearing in mind that we are only asymptotically considering $m = \mathcal{O}(1)$. On this region, $C_m(0) > C_{m_{b^-}}(0) = 1$ and so $g_m(0) > 1$. When $\tau = 0$, then once again (3.36) holds and by the far-field behaviour of g_m, there must be exactly one root to g_m. When $\tau \neq 0$ then (3.35) states that there can be at most one critical point to g_m. Regardless of the sign of $\frac{\mathrm{d}g_m}{\mathrm{d}\lambda}(0)$, there will be exactly one root to g_m as otherwise the far-field behaviour dictates the single critical point condition will be violated.

3.2.4 Real Eigenvalues: $m \gg \mathcal{O}(1)$

We now turn our attention to the case when m is large enough that $\mu \approx \lambda$ is no longer valid as an approximation to (3.17). This approximation ceases to be valid when $m = \mathcal{O}(\epsilon^{-1})$ and so we define

$$\tilde{m} = \epsilon m.$$

Since $m \gg 1$, we can use (3.32) as an approximation to C_m which means that $\chi_m = \mathcal{O}(\epsilon^{-1}) \ll 1$, and so to leading order (3.22) becomes

$$L_0\Phi_0 = \left(\lambda + \frac{\tilde{m}^2}{r_0^2}\right)\Phi_0. \tag{3.40}$$

We once again start by looking for a neutral stability point and so setting $\lambda = 0$, we know from Lemma 3.1.0.1 that ν_0 in (3.24) is the only eigenvalue, eigenfunction pair with $\mathrm{Re}(\lambda) > 0$ to L_0, and so we have a neutral stability point $\tilde{m} = \tilde{m}_{b^+}$ which satisfies

$$\tilde{m}_{b^+} = r_0\sqrt{\nu_0}. \tag{3.41}$$

We can find a correction to this by expanding

$$\tilde{m}_{b^+}^2 \sim r_0^2\nu_0 + \epsilon\tilde{m}_1, \qquad \Phi_0 \sim \Psi_0 + \epsilon\Phi_{01},$$

and after substituting into (3.22), Φ_{01} and $\tilde{m}_1$ satisfy

$$L_0\Phi_{01} - \nu_0\Phi_{01} = \frac{w^2}{2\bar{C}_0 r_0\sqrt{\nu_0}\mathcal{A}}\int_{-\infty}^{\infty} w^{o-1}\Psi_0\,\mathrm{d}\rho + \frac{\tilde{m}_1}{r_0^2}\Psi_0. \tag{3.42}$$

Here we have used (3.32) for large m asymptotics to C_m (and hence χ_m) and have taken that since $r_0 < R$, $\left(\frac{r_0}{R}\right)^{2m}$ tends to zero as $m \to \infty$. The solution $\Phi_{01} = \Psi_0$ is a homogeneous solution to (3.42) and so we require a solvability condition for the right-hand side. From this we get $\tilde{m}_1$ satisfies

$$\tilde{m}_1 = -\frac{r_0}{2\bar{C}_0\sqrt{\nu_0}}\mathcal{B},$$

where

$$\mathcal{B} = \frac{\int_{-\infty}^{\infty} w^2\Psi_0\,\mathrm{d}\rho \int_{-\infty}^{\infty} w^{o-1}\Psi_0\,\mathrm{d}\rho}{\mathcal{A}\int_{-\infty}^{\infty}\Psi_0^2\,\mathrm{d}\rho}.$$

Therefore, overall we have,

$$m_{b^+} \sim \frac{1}{\epsilon}\sqrt{r_0^2\nu_0 + \epsilon\tilde{m}_1} = \frac{r_0\sqrt{\nu_0}}{\epsilon} - \frac{\mathcal{B}}{4\bar{C}_0\nu_0}. \tag{3.43}$$

Now, unlike the case when $m = m_{b^-}$, $\lambda = 0$ is the only eigenvalue when $m = m_{b^+}$. This is because if $\lambda > 0$ then $\mu > \nu_0$ and there is no solution to (3.40). In fact, this conclusion holds on the interval $m > m_{b^+}$ because for all $\lambda \geq 0$, $\mu > \nu_0$ always. Now we consider $\tilde{m} < \tilde{m}_{b^+}$ and first note that by the same logic just discussed, if $\lambda > \nu_0 - \tilde{m}$ then there are no solutions to (3.40). We therefore restrict our attention to $\lambda < \nu_0 - \tilde{m}$. From (3.27) we have $f(0) = 1$, and from (3.32) we have $C_m(0) \gg 1$ so $g_m(0) \gg 1$. Once again via (3.35), we have that g_m can have at most one critical point and since $g_m \to -\infty$ as $\lambda \to \nu_0^-$ then there is exactly one root to g_m on $\tilde{m} \in [0, \tilde{m}_{b^+})$. Asymptotically, this root is given by,

$$\lambda = \nu_0 - \frac{\tilde{m}^2}{r_0^2}. \tag{3.44}$$

3.2.5 Real Eigenvalue Summary

We have now analyzed all the possible cases for real eigenvalues and we summarize them here. For $0 \leq m < m_{b^-}$ with m_{b^-} given asymptotically by the numerical solution of (3.33) and (3.38), we have that there are no real, positive eigenvalues when τ is sufficiently small and two positive real eigenvalues when τ is sufficiently large. Furthermore, there exists some $\tau = \tau_m^*$ where there is exactly one real eigenvalue on this interval. When $m = m_{b^-}$ then $\lambda = 0$ is the largest eigenvalue for $0 \leq \tau < \tau^*_{m_{b^-}}$ with $\tau^*_{m_{b^-}}$ satisfying (3.38). When $\tau > \tau^*_{m_{b^-}}$, there exists a non-zero positive real eigenvalue as the largest eigenvalue. When $m_{b^-} < m < m_{b^+}$ with m_{b^+} given asymptotically by (3.43) then there is exactly one real eigenvalue for all values of τ. When $m = m_{b^+}$, $\lambda = 0$ is the largest eigenvalue and when $m > m_{b^+}$ all the real eigenvalues are strictly negative.

3.2.6 Complex Eigenvalues

We now consider the possibility that λ is complex. Note that the possibility of complex eigenvalues is due to the full operator in (3.22) being non self-adjoint. We start by letting

$$\lambda = \lambda_R + i\lambda_I, \quad \psi = \psi_R + i\psi_I \tag{3.45}$$

which we substitute into (3.23) to get

$$L_0\psi_R = \left(\lambda_R + \frac{\epsilon^2 m^2}{r_0^2}\right)\psi_R - \lambda_I\psi_I + w^2, \tag{3.46a}$$

$$L_0\psi_I = \left(\lambda_R + \frac{\epsilon^2 m^2}{r_0^2}\right)\psi_I + \lambda_I\psi_R. \tag{3.46b}$$

We then define

$$f_R = \frac{\int_{-\infty}^{\infty} w^{o-1}\psi_R \,\mathrm{d}\rho}{\mathcal{A}}, \quad f_I = \frac{\int_{-\infty}^{\infty} w^{o-1}\psi_I \,\mathrm{d}\rho}{\mathcal{A}}, \tag{3.47}$$

and $g_m = g_{mR} + ig_{mI}$ with

$$g_{mR} = \mathrm{Re}(C_m(\lambda)) - f_R, \quad g_{mI} = \mathrm{Im}(C_m(\lambda)) - f_I, \tag{3.48}$$

and $C_m(\lambda)$ still defined by (3.19a). To determine the number of roots to g_m, we will use the Nyquist criteria [70] which says that the change in argument of a function is related to the number of zeros, N_0, and the number of poles, N_p, inside a given closed contour, Γ, via

$$[\arg f(x)]_\Gamma = 2\pi(N_0(f) - N_p(f)). \tag{3.49}$$

We take as a contour $\Gamma = \Gamma_I \cup \Gamma_K$ with

$$\Gamma_K : \left\{\lambda = K\exp(it) | t \in \left[-\frac{\pi}{2}, \frac{\pi}{2}\right]\right\}, \quad \Gamma_I : -Ki \le \lambda \le Ki,$$

traversed counter-clockwise and we consider what happens as K tends to infinity while assuming that τ is chosen so that g_m has no roots on the

imaginary axis. As K tends to infinity, so does μ, and from (3.23) we have that ψ tends to zero. Therefore f_R and f_I tend to zero as well as $\mu \to \infty$. Also since $|\lambda| \gg 1$ then (3.37) holds and

$$C_m(\lambda) \sim 2\bar{C}_0 r_0 \sqrt{\frac{K\tau}{D}} \exp\left(\frac{it}{2}\right) \tag{3.50}$$

where we have chosen the principal value for the square root by taking the branch cut along the negative real axis. We are interested in the change in argument of g_m as we traverse Γ_K in the counter clockwise direction. When $t = -\pi/2$ then from (3.50),

$$\arg g_m = \arg C_m = -\frac{\pi}{4},$$

and conversely when $t = \pi/2$,

$$\arg g_m = \arg C_m = \frac{\pi}{4},$$

and so

$$[\arg g_m]_{\Gamma_R} = \frac{\pi}{2}.$$

For the change in argument along Γ_I, since $C_m(\lambda)$ is holomorphic and real valued when λ is real then $C_m(\bar{\lambda}) = \overline{C_m(\lambda)}$. This similarly holds for f and so we can write

$$[\arg g_m]_{\Gamma_I} = 2[\arg g_m]_{\Gamma_I^+}$$

where Γ_I^+ is the positive imaginary axis traversed from infinity to zero. We therefore have from (3.49) that

$$N_0(g_m) = \frac{1}{4} + N_p(g_m) + \frac{1}{\pi}[\arg g_m]_{\Gamma_I^+}.$$

We are already aware from (3.28) that $f(\mu)$ (and hence g_m) has a simple pole when $\mu = \nu_0$. However, we also determined that if $m > m_{b^+}$ then $\mu > \nu_0$, and so the pole only exists inside the contour on $m \in [0, m_{b^+})$. Therefore, we have the number of roots to g_m is given by

$$N_0(g_m) = \begin{cases} \frac{5}{4} + \frac{1}{\pi}[\arg g_m]_{\Gamma_I^+}, & m < m_{b^+} \\ \frac{1}{4} + \frac{1}{\pi}[\arg g_m]_{\Gamma_I^+}, & m > m_{b^+} \end{cases}. \tag{3.51}$$

At the start of Γ_I^+, coming in from infinity, where $K \gg 1$, we can once again use (3.37) and write

$$C_m(\lambda) \sim 2\bar{C}_0 r_0 \sqrt{\frac{iK\tau}{D}},$$

where

$$\mathrm{Re}(C_m) = \mathrm{Im}(C_m) \sim \sqrt{2}\bar{C}_0 r_0 \sqrt{\frac{K\tau}{D}}. \tag{3.52}$$

As we already discussed, $\psi \to 0$ as $\lambda \to \infty$ and so for $K \gg 1$,

$$\arg g_m = \arg C_m = \arctan\left(\frac{\mathrm{Im}(C_m)}{\mathrm{Re}(C_m)}\right) = \frac{\pi}{4}.$$

Near the end of Γ_I^+, traversing towards the origin, we have $K \ll 1$ and so we can use (3.32) which, even though derived for $m \gg 1$, was based off of

small argument asymptotics and so will be valid for all m with $K \ll 1$. In this case we have

$$\mathrm{Re}(C_m) = \frac{2\bar{C}_0 m}{1 + \left(\frac{r_0}{R}\right)^m}, \quad \mathrm{Im}(C_m) = 0.$$

From Proposition 3.1 and 3.2 of [79], we have that for $\lambda_I \ll 1$ and $m = \mathcal{O}(1)$,

$$f_R(\lambda_I) \sim 1 - \kappa_c \lambda_I^2 + \mathcal{O}(\lambda_I^4), \tag{3.53a}$$

$$f_I(\lambda_I) \sim \left(1 - \frac{1}{2o}\right)\lambda_I + \mathcal{O}(\lambda_I^3) \tag{3.53b}$$

where κ_c is defined by (3.26). If $m \gg \mathcal{O}(1)$ then for $\lambda_I \ll 1$ (3.46b) simplifies to

$$L_0 \psi_I = \frac{\epsilon^2 m^2}{r_0^2} \psi_I$$

which only has a non-trivial solution at $m = m_{b^+}$ but we are not considering this point since it places the pole on the contour. Therefore, regardless of m, we have $f_I = 0$ for $\lambda_I \ll 1$ and $g_{mI} = 0$. For g_{mR}, recall that we already determined $g_m(0) < 0$ on $0 \leq m < m_{b^-}$ and $g_m(0) > 0$ on $m > m_{b^-}$ so therefore,

$$\arg g_m = \arctan\left(\frac{g_{mI}}{g_{mR}}\right) = \begin{cases} \pi, & m \in [0, m_{b^-}) \\ 0, & m \in (m_{b^-}, \infty) \setminus m_{b^+} \end{cases},$$

near $\lambda_I = 0$ of Γ_I^+. All that we are left to do now is determine the path of g_m as it changes its global argument and to do that, we will need a new

set of properties for f_R and f_I. Particularly we require that for $\lambda_I > 0$ and $m = \mathcal{O}(1)$,

$$\frac{\partial f_R}{\partial \lambda_I} < 0, \quad f_I(\lambda_I) > 0, \tag{3.54}$$

which for $o = 2$ has been proven explicitly in Proposition 3.1 and 3.2 of [79]. However, as we did for (3.27), we can conjecture numerically that these properties hold for any o. In Figure 3.4, we verify (3.27) for $o = 1, 4$, and 5.

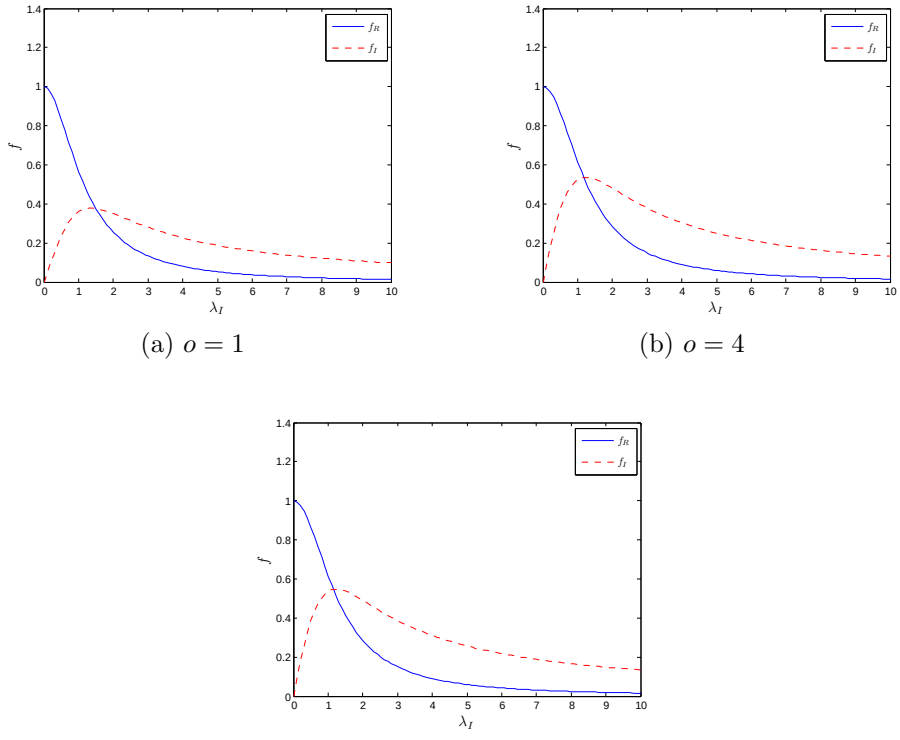

(a) $o = 1$ (b) $o = 4$

(c) $o = 5$

Figure 3.4: Computation of f_R and f_I from (3.47) for various o with $m = 0$, $r_0 = 0.5$, and $\epsilon = 0.025$. We set $m = 0$ solely to satisfy dealing with a single variable λ_I. The properties (3.54) derived analytically from $o = 2$ or $o = 3$ in Proposition 3.1 and 3.2 of [79] still hold for various exponents.

3.2.7 Complex Eigenvalues: $0 \leq m < m_{b^-}$

On this range we know that the argument must transition from $\pi/4$ to π and so we will determine the path to get here by looking at crossings along the imaginary axis where $g_{mR} = 0$ of which at least one must exist. From (3.34) and (3.54) we have

$$\frac{\mathrm{d}g_{mR}}{\mathrm{d}\lambda_I} = \frac{\mathrm{d}}{\mathrm{d}\lambda_I}\mathrm{Re}(C_m) - \frac{\mathrm{d}f_R}{\mathrm{d}\lambda_I} > 0 \tag{3.55}$$

for all λ_I and so by the mean value theorem there is a unique crossing of the imaginary axis. To determine which branch gets crossed, we need to consider the sign of g_{mI} at the crossing. Recall, if $\tau = 0$ then $C_m(\lambda) = C_m(0)$ and so for $\tau = 0$,

$$\mathrm{Re}(C_m) = C_m(0), \quad \mathrm{Im}(C_m) = 0,$$

and so from (3.54),

$$g_{mI} = \mathrm{Im}(C_m) - f_I = -f_I < 0,$$

and so the negative imaginary axis is crossed. Therefore,

$$[\arg g_m]_{\Gamma_I^+} = -\frac{5\pi}{4}, \quad \tau \ll 1.$$

When $\tau \gg 1$ then from (3.37), we can use (3.52) for the real and imaginary parts of C_m. Furthermore, since f_I does not have a vertical asymptote then

$$g_{mI} \approx \mathrm{Im}(C_m) \gg 1$$

and so for $\tau \gg 1$, the positive imaginary axis is crossed and

$$[\arg g_m]_{\Gamma_I^+} = \frac{3\pi}{4}, \quad \tau \gg 1.$$

Therefore on $0 \leq m \leq m_{b^-}$ we have from (3.51)

$$N_0(g_m) = \begin{cases} 0, & \tau \ll 1 \\ & \\ 2, & \tau \gg 1 \end{cases}.$$

Therefore, for τ small, there are no complex eigenvalues with positive real part which eventually transition to two complex eigenvalues with positive real part. These eigenvalues cannot transition through $\lambda = 0$ since, if $\lambda = 0$ for one value of τ, it is an eigenvalue for all values of τ and therefore, the eigenvalues must cross through the imaginary axis at some value $\tau = \tau_m^H$ where a Hopf bifurcation occurs. We know from analyzing the real eigenvalues that, eventually for τ large enough, these two complex eigenvalues must become purely real and therefore $\tau_m^H < \tau_m^*$.

3.2.8 Complex Eigenvalues: $m > m_{b^-}$

On this region, the argument transitions from $\pi/4$ to 0 and so there must be zero or an even number of crossings through the imaginary axis. With

$m = \mathcal{O}(1)$, we concluded in the previous section that via (3.55), there can exist at most one crossing through the imaginary axis and therefore, on $m > m_{b^-}$ with $m = \mathcal{O}(1)$, we must have zero crossings. This tells us that

$$[\arg g_m]_{\Gamma_I^+} = -\frac{\pi}{4}. \tag{3.56}$$

For $m = \mathcal{O}(\epsilon^{-1})$, we have that (3.32) holds for $C_m \gg 1$ and since, unlike the case for purely real eigenvalues, f_R does not have a vertical asymptote for $m \neq m_{b^+}$ then

$$g_{mR} \approx \mathrm{Re}(C_m) \sim \mathcal{O}(m) \gg 1.$$

Therefore $g_{mR} > 0$ always and cannot cross the imaginary axis so (3.56) holds as well. Therefore, via (3.51), we have

$$N_0(g_m) = \begin{cases} 1, & m_{b^-} < m < m_{b^+} \\ 0, & m > m_{b^+} \end{cases}.$$

Since we have already determined that a real eigenvalue exists on $m \in (m_{b^-}, m_{b^+})$, this must be the only positive eigenvalue for this range.

3.2.9 Eigenvalue Summary

We are now finally in a position to classify the entire spectrum of eigenvalues to (3.16) for Φ_0 even and $\sigma = 0$ via the following principal result:

Principal Result 3.2.9.1 *Eigenvalue Classification:*
On $0 < m < m_{b^-}$*:*
There are no eigenvalues with positive real part when τ *is sufficiently small*

and two complex eigenvalues with positive real part when τ is sufficiently large. These eigenvalues undergo a Hopf bifurcation when $\tau = \tau_m^H$ and as τ increases further, these eigenvalues coincide as a single real eigenvalue when $\tau = \tau_m^*$ before splitting on the real axis for $\tau > \tau_m^*$.

If $m = m_{b^-}$:
The eigenvalue $\lambda = 0$ persists for all τ and when $\tau < \tau^*_{m_{b^-}}$ then $\lambda = 0$ is the largest eigenvalue. If $\tau > \tau^*_{m_{b^-}}$ then there exists some $\lambda_\tau > 0$ that is purely real and positive.

On $m_{b^-} < m < m_{b^+}$:
There is exactly one real positive eigenvalue on this interval for all τ.

On $m > m_{b^+}$:
There are no eigenvalues with positive real part on this interval for all τ.

The condition that there is always at least one unstable eigenvalue for all r_0 and all values of τ allows us to classify these eigenvalues as being an instability on an $\mathcal{O}(1)$ time scale. This is because if $m_{b^-} < m < m_{b^+}$ then $\lambda(0) > 0$ so when we use condition (3.9), the integral diverges immediately. For an initial radius r_0, unstable modes near the neutral stability points could be delayed or prevented. Specifically, for m_{b^+} satisfied by (3.41) asymptotically, the mode decreases with increasing radius. Therefore modes that are initially unstable may stabilize depending if secondary bifurcations occur before the pattern can stabilize or not. This is irrelevant however, since there will always be a band of unstable modes for random perturbations to amplify. However, if

the ring radius decreases then the upper instability mode increases and this would lead to previously stable modes becoming unstable.

3.2.10 Numerical Computation of Eigenvalues

We will now verify some of our analytic conclusions by numerically computing the full non-local eigenvalue problem (3.16) for any b or τ as desired. To do this, we can discretize L_{0b} with a standard second order finite difference scheme and in order to discretize the non-local part involving the integral of Φ_0, we first truncate to a finite domain

$$\int_{-\infty}^{\infty} w^{o-1}\Phi \,\mathrm{d}\rho \approx \int_{-L}^{L} w^{o-1}\Phi \,\mathrm{d}\rho.$$

for some L to be chosen so that as L increases the change in the integral is below some tolerance. We disretize over $N+1$ points with

$$x_k = -L + kh, \qquad k = 0 \ldots N, \quad h = \frac{2L}{N}.$$

With this in mind we write the integral as

$$\int_{-L}^{L} w^{o-1}\Phi \,\mathrm{d}\rho = \sum_{k=0}^{N-1} \int_{-L+kh}^{-L+(k+1)h} w^{o-1}\Phi \,\mathrm{d}\rho$$

and discretize each integral with the trapezoid method [6]. Finally, we supplement far-field conditions that $\Phi_0 = 0$ at $x = \pm L$.

We will begin computations by setting $\sigma = b = 0$ since this is what we have previously analyzed analytically. Furthermore, when $\tau = 0$, χ_m is in-

dependent of λ and the eigenvalue problem becomes completely linear. As such eigenvalues can easily be computed with a standard eigenvalue package such as `eigs` in Matlab. Figure 3.5 plots $\max\{\mathrm{Re}(\lambda)\}$ as a function of m when $\tau = 0$ for various parameters computed in Matlab.

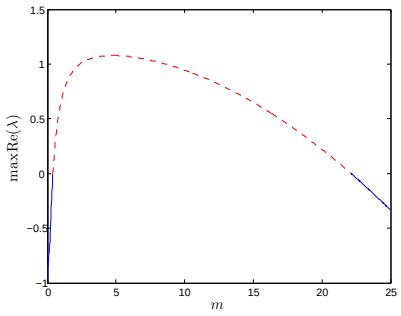

(a) $(2, q, o, s) = (2, 1, 2, 0)$, $\epsilon = 0.025$, $R = 1$, $r_0 = 0.5$

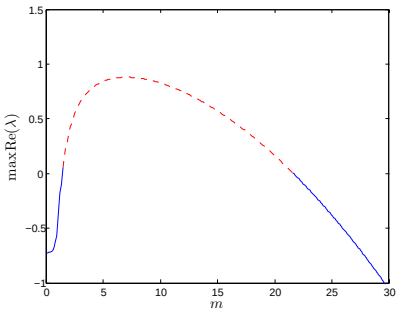

(b) $(2, q, o, s) = (2, 2, 3, 0)$, $\epsilon = 0.025$, $R = 1$, $r_0 = 0.5$

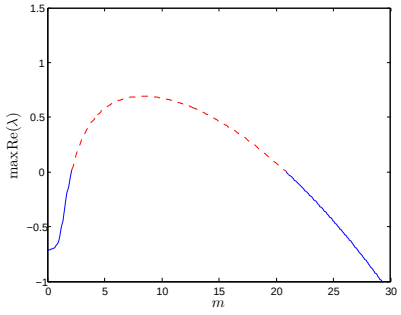

(c) $(2, q, o, s) = (2, 4, 3, 3)$, $\epsilon = 0.025$, $R = 1$, $r_0 = 0.5$

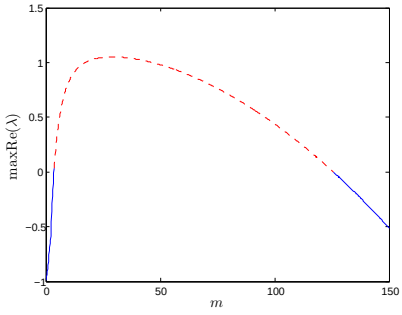

(d) $(2, q, o, s) = (2, 1, 2, 0)$, $\epsilon = 0.025$, $R = \sqrt{10}$, $r_0 = 9/\sqrt{10}$

Figure 3.5: Numerical computation of the largest real part of the eigenvalue λ in (3.16) for the case $\tau = 0$ and $b = 0$ using `eigs` in Matlab. The blue solid curves are where the largest eigenvalue is negative while the red dashed curves are where it is positive. In all experiments $D = 1$.

In all cases, Principal Result 3.2.9.1 holds and there is a spectrum of real positive eigenvalues. Using the eigenvalue solver we can also numerically

obtain m_{b^-} and m_{b^+} and compare them to the asymptotic approximations (3.33) for m_{b^-} and (3.43) for m_{b^+}. This is presented in Table 3.1 for a variety of cases, and shows an excellent agreement with the analytical theory. Many of the experimental cases have been chosen to mimic a similar eigenvalue discussion for stripe solutions considered in [39].

$(2,q,r,s)$	ϵ	$R=\ell$	r_0	m_{b^-}(n)	m_{b^-}(a)	m_{b^+}(n)	m_{b^+}(a1)	m_{b^+}(a2)
(2,1,2,0)	0.1	1	0.5	0.4033	0.4003	5.3542	5.5902	5.3671
(2,1,2,0)	0.05	1	0.5	0.4008	0.4003	10.9528	11.1803	10.9573
(2,1,2,0)	0.025	1	0.5	0.3996	0.4003	22.1389	22.3607	22.1376
(2,1,2,0)	0.025	$1/\sqrt{10}$	$1/2\sqrt{10}$	0.0485	0.0485	7.0482	7.0711	7.0469
(2,1,2,0)	0.025	$\sqrt{10}$	$\sqrt{10}/2$	2.3362	2.3373	69.3076	70.7107	69.3350
(2,1,2,0)	0.025	$\sqrt{10}$	$2/\sqrt{10}$	0.9756	0.9745	27.6761	28.2843	27.6900
(2,1,2,0)	0.025	$\sqrt{10}$	$9/\sqrt{10}$	3.4737	3.4771	125.7202	127.2792	125.7232
(2,1,3,0)	0.025	1	0.5	0.6974	0.6986	22.0085	22.3607	22.0122
(2,2,3,0)	0.025	1	0.5	1.4307	1.4251	21.6334	22.3607	21.6637
(2,4,3,3)	0.025	1	0.5	2.1107	2.0866	20.8712	22.3607	20.9667

Table 3.1: Comparison for $\tau = 0$ and $b = 0$ of numerical and asymptotic computations of m_{b^-} and m_{b^+} for a variety of exponent sets, ϵ, R, and r_0 with $D = 1$ for all. The (n) refers to numeric computations of (3.16) using `eigs` in Matlab. m_{b^-}(a) is computed via Newton's method on (3.33), m_{b^+}(a1) is computed via (3.41) while m_{b^+}(a2) is computed via (3.43).

3.2.11 Computing Eigenvalues, $\tau \neq 0$

When $\tau \neq 0$ then χ_m in (3.16) is a function of λ and the eigenvalue problem is more intricate as χ_m depends nonlinearly on the product $\tau\lambda$. For this case, we must solve

$$T(\lambda)\mathbf{\Phi} = 0,$$

where $\mathbf{\Phi}$ is the discrete eigenvector and $T(\lambda)$ are the discretized coefficients for (3.16). In order to enforce uniqueness of eigenvector solutions, we require

some normalizing constraint,

$$\mathbf{v}^T\mathbf{\Phi} = 1.$$

We can write the problem as a block system

$$\mathbf{F}(\lambda, \Phi) = \begin{bmatrix} T(\lambda)\mathbf{\Phi} \\ \mathbf{v}^T\mathbf{\Phi} - 1 \end{bmatrix} = \mathbf{0}$$

and hence our eigenvalues and eigenvectors are roots to $\mathbf{F}$ which we can solve with Newton's Method. We can write the Jacobian to the problem as,

$$J(\lambda, \mathbf{\Phi}) = \begin{bmatrix} T_\lambda(\lambda)\mathbf{\Phi} & T(\lambda) \\ 0 & \mathbf{v}^T \end{bmatrix}$$

and so the Newton problem is,

$$J(\lambda_k, \mathbf{\Phi}_k) \begin{bmatrix} \lambda_{k+1} - \lambda_k \\ \mathbf{\Phi}_{k+1} - \mathbf{\Phi}_k \end{bmatrix} = -F(\lambda_k, \mathbf{\Phi}_k), \tag{3.57}$$

where k indicates the iteration count. We note that the normalizing vector can also change with each iterate and so $\mathbf{v} = \mathbf{v}_k$. If we write out the first equation from the matrix multiplication we get

$$(\lambda_{k+1} - \lambda_k)T_\lambda(\lambda_k)\mathbf{\Phi}_k + T(\lambda_k)\mathbf{\Phi}_{k+1} - T(\lambda_k)\mathbf{\Phi}_k = -T(\lambda_k)\mathbf{\Phi}_k,$$

which can simplify to

$$\mathbf{\Phi}_{k+1} = -\mathbf{u}_k(\lambda_{k+1} - \lambda_k), \tag{3.58}$$

where we define

$$\mathbf{u}_k = T(\lambda_k)^{-1} T_\lambda(\lambda_k)\mathbf{\Phi}_k.$$

If we left-multiply by $\mathbf{v}_k^T$ then

$$\lambda_{k+1} = \lambda_k - \frac{\mathbf{v}_k^T \mathbf{\Phi}_{k+1}}{\mathbf{v}_k^T \mathbf{u}_k},$$

which still appears to depend on the solution Φ_{k+1}. However, if we expand out the second equation in (3.57) then we get

$$\mathbf{v}_k^T \mathbf{\Phi}_{k+1} = 1$$

and so

$$\lambda_{k+1} = \lambda_k - \frac{1}{\mathbf{v}_k^T \mathbf{u}_k}. \tag{3.59}$$

This determines λ_{k+1} and we could use (3.58) to determine $\mathbf{\Phi}_{k+1}$ but since it is just $\mathbf{u}_k$ up to a constant we instead renormalize via,

$$\mathbf{\Phi}_{k+1} = \frac{\mathbf{u}_k}{\mathbf{v}_k^T \mathbf{u}_k},$$

which completes the problem. For simplicity we take,

$$\mathbf{v}_k = \frac{\mathbf{u}_{k-1}}{|\mathbf{u}_{k-1}|^2}$$

to normalize. There are several practical issues to deal with when implementing Newton's method for this problem because there are several eigenvalues that exist (including the continuous spectrum that exists below $\lambda = 1$). We are only interested in capturing the eigenvalues at each m for a given τ that have the largest positive real part. To accomplish this we take as initial data the $\tau = 0$ case where the problem is linear and the largest eigenvalues are easily computed. We choose an $m = m^*$ value in the interval $m_{b^-} < m < m_{b^+}$ (typically the average point) because from Principal Result 3.2.9.1, when $b = 0$ there is only one positive root in this interval and therefore, the Newton solve will be more robust in this region. Having chosen m^*, we compute the Newton solve by slowly varying τ and finding eigenvalues at $m = m^*$ until a desired final τ value is reached. At this point, we begin another Newton solve, fixing τ, for $m < m^*$ and $m > m^*$ until we have traversed the entire spectrum of m, or until we enter the continuous spectrum. We allow the stepsize on m to vary dynamically, getting smaller when there are convergence issues and getting larger when roots are found in relatively few iterations. On $m > m^*$, there is very little trouble because once $m > m_{b^+}$ we know that there are no eigenvalues with positive real part for all τ and so we can terminate the Newton iteration quickly after this point. However, on $m < m^*$, if τ satisfies $\tau_m^H < \tau < \tau_m^*$, the Newton iteration has some stability issues. This is due to the existence of complex eigenvalues with positive real part on this interval of τ. On this region, there are still real eigenvalues for

$m \geq m_{b^-}$ and so there is a point where eigenvalues transition from being real to complex. Since the Newton algorithm at this stage is based on using the previous m values as initial data, the stability issues arise from trying to find complex solutions with real initial data. Therefore, if the number of attempted iterations exceeds a certain threshold within this region of m, the code modifies the initial guess to include an imaginary component of magnitude on order with the selected tolerance and the algorithm continues. One last issue of practicality that occurs when solving the problem is when the eigenvalues get close to zero ($m = m_{b^-}$ and $m = m_{b^+}$). The problem is that $\lambda = 0$ is always an eigenvalue of (3.16) with eigenfunction $\Phi = w'$ (see Lemma 3.1.0.1). Notice this eigenfunction is odd and so this zero eigenvalue is ignored in the present analysis of even eigenfunctions but it still exists and can be captured by the algorithm. Therefore, we have a checking criterion that the solved eigenfunction at some $m = m_1$ is not orthogonal to the eigenfunction of the previous $m = m_0$ value. If $\Phi_{m_1}^T \Phi_{m_0}$ is less than some preset threshold then we discard the solution, reduce the step size in m, and reinitialize the algorithm with the values at m_0. In Figure 3.6 we plot the numerically computed eigenvalues using Newton's method as outlined above for various values of τ with $(p, q, o, s) = (2, 1, 2, 0)$, $\epsilon = 0.025$, $D = 1$, $R = 1$, and $r_0 = 0.5$.

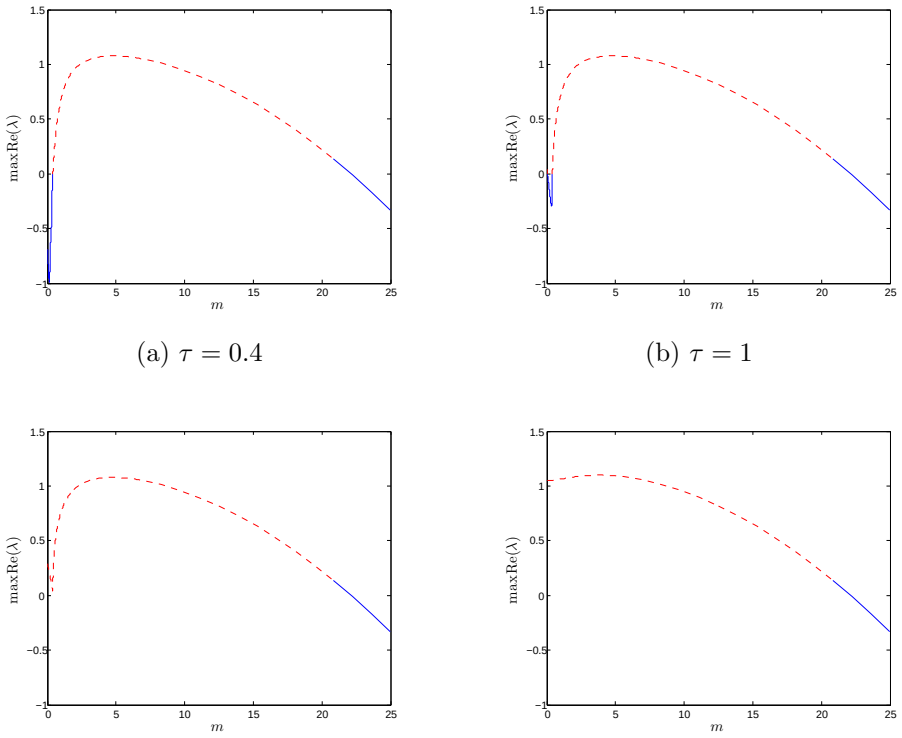

(a) $\tau = 0.4$ (b) $\tau = 1$

(c) $\tau = 2$ (d) $\tau = 30$

Figure 3.6: Numerical computation for $b = 0$ of the largest real part of the eigenvalue λ in (3.16) using Newton's method on (3.59). The solid curves are where the largest eigenvalue has negative real part while the dashed curves are where it has positive real part. In all experiments $(2, q, o, s) = (2, 1, 2, 0)$, $\epsilon = 0.025$, $D = 1$, $R = 1$, and $r_0 = 0.5$.

When $\tau \ll 1$ as in Figure 3.6a then the plot is almost indistinguishable from the linear case of $\tau = 0$ (Figure 3.5a) as should be expected. This helps verify that the Newton algorithm is working properly. In Figure 3.6c when $\tau = 2$ we see that at $m = m_{b^-}$ the zero eigenvalue is no longer the largest eigenvalue. In (3.39) we estimated that $\tau^*_{m_{b^-}} = 1.8376$ and in this case $\tau > \tau^*_{m_{b^-}}$. Figure 3.7 verifies our predicted $\tau^*_{m_{b^-}}$ value as in Figure 3.7a-3.7b $\tau = 1.82 < \tau^*_{m_{b^-}}$

and we indeed still see at $m = m_{b^-}$ that $\lambda = 0$ as the largest eigenvalue. In Figure 3.7c-3.7d, $\tau = 1.84 > \tau^*_{m_{b^-}}$ and at $m = m_{b^-}$ there is an eigenvalue larger than 0.

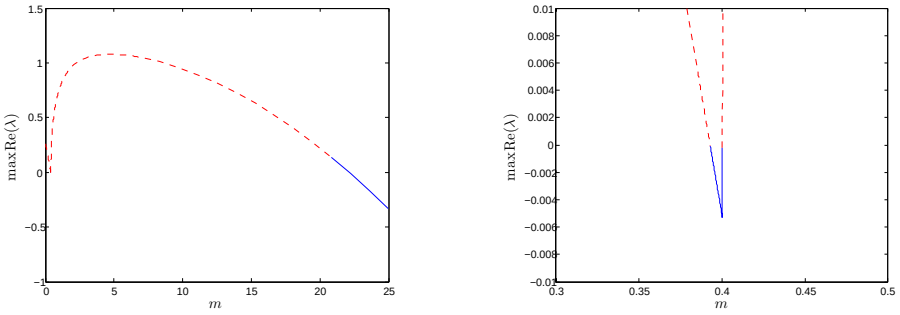

(a) $\tau = 1.82$ (b) $\tau = 1.82$ (zoom)

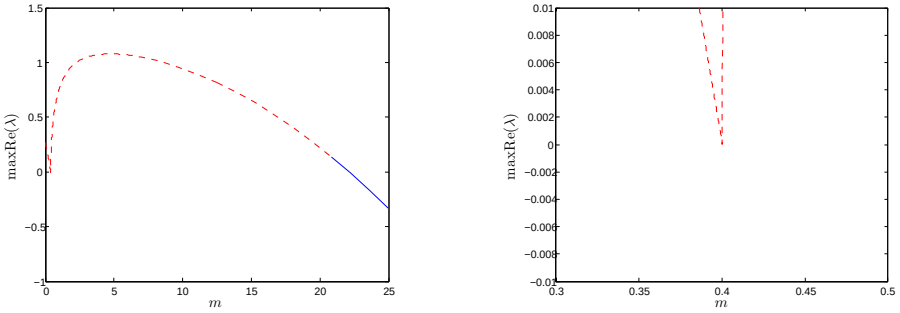

(c) $\tau = 1.84$ (d) $\tau = 1.84$ (zoom)

Figure 3.7: Numerical computation of eigenvalues near $m = m_{b^-}$ for $\tau > \tau^*_{m_{b^-}}$ and $\tau < \tau^*_{m_{b^-}}$. In all experiments $(2, q, o, s) = (2, 1, 2, 0)$, $\epsilon = 0.025$, $D = 1$, $R = 1$, and $r_0 = 0.5$.

In Figure 3.7b it may appear that there is a second neutral eigenvalue near $m = m_{b^-}$ as there is certainly another eigenvalue where $\mathrm{Re}(\lambda) = 0$. However, as we mentioned in doing the analytical analysis, there should only be one truly neutral stability point. To emphasize this, we plot the imaginary part

of the eigenvalues for a range of τ in Figure 3.8. For $\tau = 1.83$, we see that indeed the second eigenvalue with $\mathrm{Re}(\lambda) = 0$ has a non-zero imaginary part and thus there is a Hopf bifurcation at this m value for this particular value of τ. We see that when $\tau = 1.84 > \tau^*_{m_{b^-}}$ and $\lambda = 0$ is no longer the biggest eigenvalue that the eigenvalues on $m < m_{b^-}$ are complex and therefore $\tau^*_m > 1.84$. However, when $\tau = 30$ we that all of the eigenvalue are purely real so $\tau^*_m < 30$.

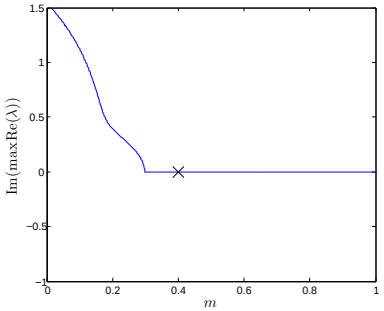

(a) $\tau = 0.4$

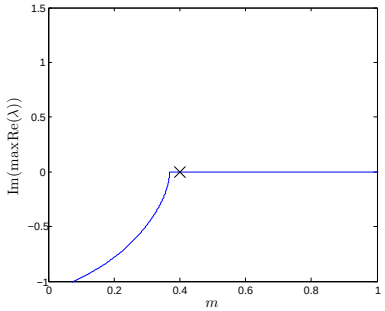

(b) $\tau = 1$

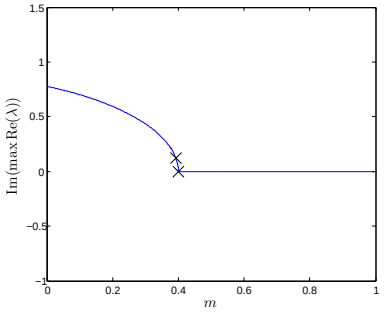

(c) $\tau = 1.82$

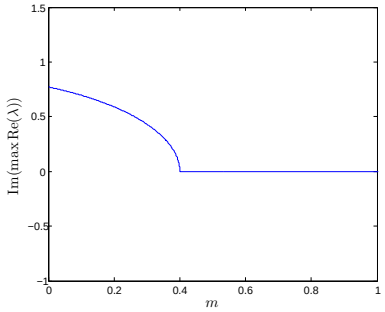

(d) $\tau = 1.84$

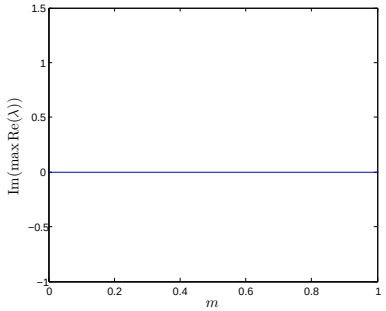

(e) $\tau = 30$

Figure 3.8: Imaginary part of the eigenvalues with largest real part computed using Newton's method on (3.59). The black x mark points where $\mathrm{Re}(\lambda) = 0$. In all experiments $(2, q, o, s) = (2, 1, 2, 0)$, $\epsilon = 0.025$, $D = 1$, $R = 1$, and $r_0 = 0.5$.

3.2.12 Adding Saturation

We now turn our attention to the case when there is saturation and $b \neq 0$. Fortunately, the Newton algorithm for (3.59) holds for any value of b and so we can easily consider this case numerically. One thing that does hold true analytically for $b \neq 0$ is the leading result on m_{b^+} of section 3.2.4 when $m \gg 1$. There we have that the non-local part in (3.16) is negligible to leading order and therefore the only contribution with saturation is through the operator L_{0b} (3.7). This operator is still classified by Lemma 3.1.0.1 and so there must still be a single positive eigenvalue with an eigenfunction that has no nodal lines when a homoclinic orbit exists. If we let $\nu_0(b)$ be this largest discrete eigenvalue to $b \neq 0$ then the upper bound neutral stability wave mode is given by,

$$m_{b^+} \sim \frac{r_0\sqrt{\nu_0(b)}}{\epsilon}.$$

In section 2.3 we have that the homoclinic orbit solution $w(\hat{\eta})$ only exists up to a critical value $b < b_c$ with b_c given by (2.27). When $b = b_c$ we saw that w became a heteroclinic orbit and therefore in this instance w' is even and has no nodal lines. Therefore when $b = b_c$, we must have that the largest eigenvalue is the zero eigenvalue and therefore

$$\lim_{b \to b_c^-} m_{b^+} = 0.$$

We can compute the eigenvalues of L_{0b} numerically using `eigs` which we plot in Figure 3.9 and we indeed notice that the largest eigenvalue goes to zero as b approaches the critical value.

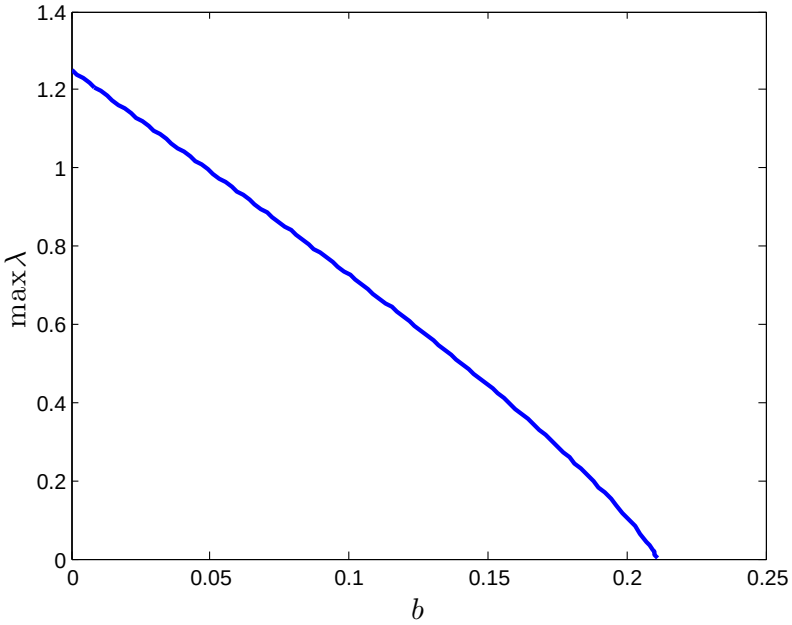

Figure 3.9: Computation of b dependent eigenvalues to L_{0b} given by (3.7).

We demonstrate the spectrum of the NLEP (3.16) becoming entirely negative in Figure 3.10 where we take $(2, q, o, s) = (2, 1, 2, 0)$, $\epsilon = 0.025$, $R = 1$, $r_0 = 0.5$, and $D = 1$. In this figure, we have plotted the numerically computed eigenvalues to (3.16) for $\tau = 0$ and various values of b. It can be seen that by the time $b = 0.2$ all of the eigenvalues satisfy $\mathrm{Re}(\lambda) < 0$.

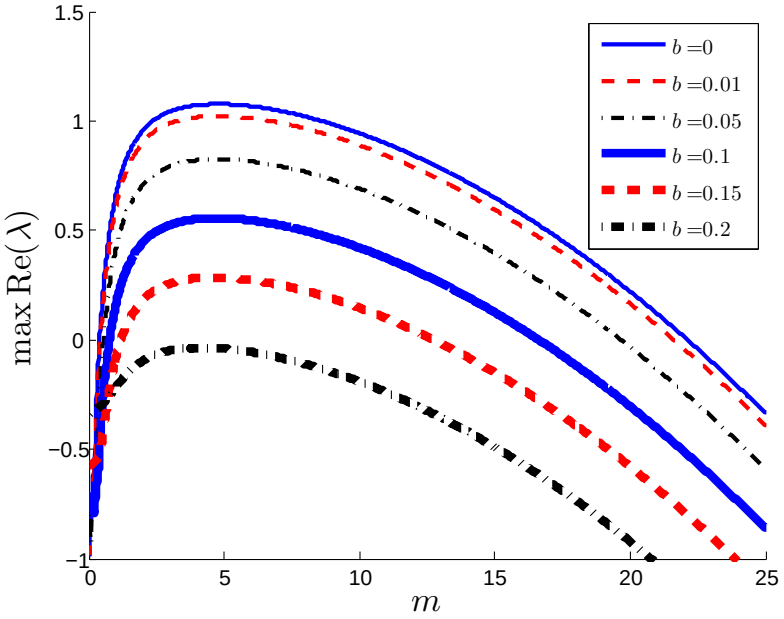

Figure 3.10: Computation of eigenvalues for $b \neq 0$ and $\tau = 0$. In all cases $(2, q, o, s) = (2, 1, 2, 0)$, $\epsilon = 0.025$, $R = 1$, $r_0 = 0.5$, and $D = 1$

Finally, in Figure 3.11 we plot the eigenvalues for $b = 0.2$, $(2, q, o, s) = (2, 1, 2, 0)$, $\epsilon = 0.025$, $R = 1$, $r_0 = 0.5$, and $D = 1$ for various values of τ.

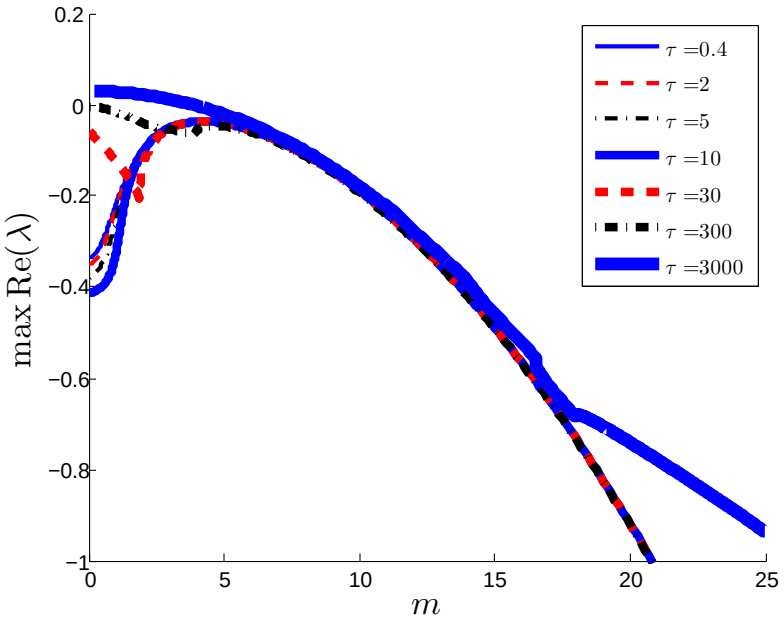

Figure 3.11: Computation of eigenvalues for $b = 0.2$ and $\tau \neq 0$. In all cases $(2, q, o, s) = (2, 1, 2, 0)$, $\epsilon = 0.025$, $R = 1$, $r_0 = 0.5$, and $D = 1$

Unsurprisingly, since we saw $g_m \gg 1$ for $\tau \gg 1$, we have that there is a threshold of τ where eigenvalues begin to enter $\mathrm{Re}(\lambda) > 0$. However, unlike r_0, and b, τ is a static parameter and so for a fixed τ, there will exist a range of b for which all of the eigenvalues satisfy $\mathrm{Re}(\lambda) < 0$. There is some delicacy required here since as we saw in section 2.3.1, b depends intimately on r_0 and generally decreases as r_0 increases. Therefore, in the dynamic transition of circle radii, bands of instability can arise. Fortunately due to the delay effect from (3.9), as long as these instability bands are transient, it is possible to stabilize everything. As is noted in Figure 2.7, the rate at which b decreases as r_0 increases gets slower as a function of saturation and so it is possible to

find a saturation value σ^* such that for $\sigma > \sigma^*$, the spectrum of the NLEP (3.16) satisfies $\mathrm{Re}(\lambda) < 0$ for most values of r_0.

3.3 Eigenvalues Associated with Φ_0 Odd

We will now consider the second class of eigenfunctions for which Φ_0 is odd. Odd functions do not obtain their maximum values at $r = r_0$ and so this class of functions will affect the position of the curve where maximal activator occurs. Therefore, we consider odd eigenfunctions to correspond with translation or zig-zag instabilities. As we already discussed, when Φ_0 is odd then from (3.15), we have $N(r_0) = 0$ to leading order, and so for Φ_0 the leading order problem from (3.8) is

$$L_{0b}\Phi_0 = \left(\lambda + \frac{\epsilon^2 m^2}{r_0^2}\right)\Phi_0 = \mu\Phi_0.$$

For $\lambda \geq 0$ then $\mu \geq 0$ and from [14] and section 3.2.12, we have that the only possibility for Φ_0 to be odd is if $\mu = 0$ and $\Phi_0 = w'$ where w is the homoclinic orbit solution (2.22) and prime indicates differentiation with respect to ρ. We could once again analyze for $m = \mathcal{O}(1)$ and $m \gg \mathcal{O}(1)$ but for the latter case note that $\mu = 0$ implies

$$\lambda = -\frac{\epsilon^2 m^2}{r_0^2} < 0$$

and so there are no unstable roots for $m \gg 1$ with an odd eigenfunction. As such we will strictly consider $m = \mathcal{O}(1)$ moving forward. If we consider the expansion (3.5), the most natural scaling for the inhibitor function is ϵ and

therefore, to leading order,

$$\Phi_0 \sim w', \quad \lambda = \omega(\epsilon)\hat{\lambda}, \quad N(r) = \epsilon\hat{N}$$

with $\omega \ll 1$ to be determined. We let $\tilde{N}(\rho) = \hat{N}(r_0 + \epsilon\rho)$ and make the following expansions,

$$\Phi \sim w' + \epsilon\Phi_1 + \epsilon^2\Phi_2 + \ldots, \quad \tilde{N}(\rho) \sim \tilde{N}_0 + \epsilon\tilde{N}_1 + \ldots.$$

We also consider the asymptotic expansion of the equilibrium solution from sections 2.2 and 2.3,

$$\tilde{v}_e \sim U_0^q w + \epsilon\tilde{v}_1 + \epsilon^2\tilde{v}_2 + \ldots, \quad \tilde{u}_e \sim U_0 + \epsilon\tilde{u}_1 + \epsilon^2\tilde{u}_2 + \ldots.$$

We have already satisfied the leading order problem and so we consider the problem at $\mathcal{O}(\epsilon)$ for Φ_1 (by expanding (3.5a)) which becomes,

$$L_{0b}\Phi_1 = -\frac{\Phi_{0\rho}}{r_0} - \Phi_{0\rho}\frac{\mathrm{d}r_0}{\mathrm{d}T} - a_1\Phi_0 + \frac{qU_0^{q-1}}{(1+bw^2)}w^2\tilde{N}_0 + \hat{\lambda}\Phi_0, \tag{3.60}$$

where we have defined

$$a_1 \equiv \frac{2}{U_0(1+bw^2)^2}\left(\frac{(1-3bw^2)}{U_0^{q-1}(1+bw^2)}\tilde{v}_1 - qw\tilde{u}_1\right), \tag{3.61}$$

and, at least temporarily, consider $\omega(\epsilon) = \epsilon$. Next, consider the problem for $\tilde{v}_1$ and $\tilde{u}_1$ given by (2.7) which, in radial coordinates, is

$$L_{0b}\tilde{v}_1 = -\frac{U_0^q}{r_0}w' + qU_0^{q-1}\frac{w^2}{(1+bw^2)}\tilde{u}_1 - U_0^q\frac{\mathrm{d}r_0}{\mathrm{d}T}w', \tag{3.62a}$$

$$\tilde{u}_1'' = -\frac{1}{D}U_0^\beta w^o. \tag{3.62b}$$

Upon differentiating (3.62a), we obtain

$$\begin{aligned} L_{0b}\tilde{v}_1' + 2\frac{(1-3bw^2)}{(1+bw^2)^3}w'\tilde{v}_1 = &-\frac{U_0^q}{r_0}w'' + qU_0^{q-1}\frac{2w}{(1+bw^2)^2}w'\tilde{u}_1 \\ &+ qU_0^{q-1}\frac{w^2}{(1+bw^2)}\tilde{u}_1' - U_0^q\frac{\mathrm{d}r_0}{\mathrm{d}T}w'', \end{aligned} \tag{3.63}$$

where we note that

$$(L_{0b}y)' = L_{0b}y' + 2\frac{(1-3bw^2)}{(1+bw^2)^3}w'y. \tag{3.64}$$

We can rearrange (3.63) to get

$$a_1 w' = -\frac{1}{U_0^q}L_{0b}\tilde{v}_1' - \frac{w''}{r_0} + \frac{q}{U_0}\frac{w^2}{(1+bw^2)}\tilde{u}_1' - \frac{\mathrm{d}r_0}{\mathrm{d}T}w'', \tag{3.65}$$

so that (3.60) becomes

$$L_{0b}\Phi_1 = \frac{1}{U_0^q}L_{0b}\tilde{v}_1' + \frac{q}{U_0}\frac{w^2}{(1+bw^2)}(U_0^q\tilde{N}_0 - \tilde{u}_1') + \hat{\lambda}w', \tag{3.66}$$

where we have used that $\Phi_0 = w'$. We know $\Phi_1 = w'$ is a homogeneous solution to (3.66) and so we must satisfy the following compatibility condition:

$$\frac{1}{U_0^q}\int_{-\infty}^{\infty} w' L_{0b}\tilde{v}_1' \,\mathrm{d}\rho + \frac{q}{U_0}\int_{-\infty}^{\infty} \frac{w^2}{(1+bw^2)}(U_0^q\tilde{N}_0 - \tilde{u}_1')w' \,\mathrm{d}\rho + \hat{\lambda}\int_{-\infty}^{\infty} w'^2 \,\mathrm{d}\rho = 0. \tag{3.67}$$

Now since L_{0b} is self-adjoint and w' a homogeneous solution then,

$$\int_{-\infty}^{\infty} w' L_{0b}\tilde{v}_1' \,\mathrm{d}\rho = \int_{-\infty}^{\infty} \tilde{v}_1 L_{0b} w' \,\mathrm{d}\rho = 0. \tag{3.68}$$

In this way, (3.67) reduces to

$$-\frac{q}{U_0}\int_{-\infty}^{\infty} \frac{w^2}{(1+bw^2)}(U_0^q\tilde{N}_0 - \tilde{u}_1')w' \,\mathrm{d}\rho = \hat{\lambda}\int_{-\infty}^{\infty} w'^2 \,\mathrm{d}\rho. \tag{3.69}$$

We now wish to understand the behaviour of the function $\tilde{\mathcal{F}}$ defined by,

$$\tilde{\mathcal{F}}_0 \equiv U_0^q\tilde{N}_0 - \tilde{u}_1',$$

which is easier to obtain if we differentiate,

$$\tilde{\mathcal{F}}_0' = U_0^q\tilde{N}_0' - \tilde{u}_1''.$$

First from (3.62b) we have that

$$\tilde{u}_1'' = -\frac{U_0^\beta}{D}w^o,$$

and for $\tilde{N}_0$ we turn to the expansion (3.5b) in inner coordinates:

$$\begin{aligned}\epsilon^4\tau\tilde{N}_T + \epsilon^2\tau\tilde{N}\omega(\epsilon)\hat{\lambda} =& \frac{D}{(r_0+\epsilon\rho)}((r_0+\epsilon\rho)\tilde{N}')' - \epsilon^2\frac{Dm^2}{(r_0+\epsilon\rho)^2}\tilde{N} - \epsilon^2\tilde{N} \\ &+ \frac{o\tilde{v}_e^{o-1}}{\tilde{u_e}^s}\Phi - \epsilon\frac{s\tilde{v}_e^o}{\tilde{u}_e^{s+1}}\tilde{N},\end{aligned} \tag{3.70}$$

which to leading order satisfies,

$$\tilde{N}_0'' = -\frac{oU_0^{\beta-q}}{D}w^{o-1}w'.$$

If we multiply this by U_0^q and integrate we have

$$U_0^q\tilde{N}_0' = -\frac{U_0^\beta}{D}w^o,$$

and therefore $\tilde{\mathcal{F}}_0' = 0$ so $\tilde{\mathcal{F}}_0$ is a constant. We already know that the derivative of u_e in the global region is discontinuous and therefore $\tilde{\mathcal{F}}_0$ being constant implies that $\hat{N}$ must be discontinuous as well but in such a way that the appropriate sum is continuous and $\tilde{\mathcal{F}}_0$ is defined. Having $\tilde{\mathcal{F}}_0$ be constant makes the integrand on the left-hand side of (3.69) an odd function and so the integral vanishes. Therefore we conclude that $\omega(\epsilon) \ll \epsilon$. Next we consider $\omega(\epsilon) = \epsilon^2$ and by expanding (3.5a) to the proper order we get the problem for Φ_2:

$$\begin{aligned}L_{0b}\Phi_2 =& qU_0^{q-1}\frac{w^2}{(1+bw^2)}\tilde{N}_1 + \bar{a}_2U_0^q\tilde{N}_0 - a_1\Phi_1 - a_2w' - \frac{\Phi_1'}{r_0} + \frac{\rho w''}{r_0^2} \\ &- \frac{\mathrm{d}r_{01}}{\mathrm{d}T}w'' - \frac{\mathrm{d}r_{00}}{\mathrm{d}T}\Phi_1' + \left(\hat{\lambda} + \frac{m^2}{r_0^2}\right)w',\end{aligned} \tag{3.71}$$

where we define a_2 and $\bar{a}_2$ by,

$$a_2 \equiv \frac{2}{U_0(1+bw^2)^2}\left(\frac{(1-3bw^2)}{U_0^{q-1}(1+bw^2)}\tilde{v}_2 - qw\tilde{u}_2\right) + \frac{q(q+1)}{U_0^2}\frac{w}{(1+bw^2)^2}\tilde{u}_1^2 - \frac{2q}{U_0^{q+1}}\frac{(1-3bw^2)}{(1+bw^2)^3}\tilde{u}_1\tilde{v}_1 - \frac{12bw}{U_0^{2q}}\frac{(1-bw^2)}{(1+bw^2)^4}\tilde{v}_1^2 \tag{3.72a}$$

$$\bar{a}_2 \equiv \frac{2q}{U_0^{q+1}}\frac{w}{(1+bw^2)^2}\tilde{v}_1 - \frac{q(q+1)}{U_0^2}\frac{w^2}{(1+bw^2)}\tilde{u}_1. \tag{3.72b}$$

In (3.71) we replace $r_0 = r_{00} + \epsilon r_{01}$ where r_{00} is the value previously used for r_0 (i.e. it satisfies (2.43)) and r_{01} is added as a correction to satisfy an orthogonality condition of the base-state at $\mathcal{O}(\epsilon^2)$. It may seem erroneous to introduce a radial correction, r_{01}, without any consideration to matching conditions from previous quasi steady-state analysis. However, for the outer problem, we are interested in the singular limit solution where all variables are $\mathcal{O}(1)$ and matching terms generated by radial corrections furnish conditions smaller than this order. Therefore, whenever global matching is concerned, we will consider $r_0 + \epsilon\rho \approx r_{00} + \epsilon\rho$. As we did with the $\mathcal{O}(\epsilon)$ problem, we consider the problem for $\tilde{v}_2$ and $\tilde{u}_2$ given by (2.15a) and (2.15b) respectively which, in radial coordinates, is

$$L_{0b}\tilde{v}_2 = -\frac{\tilde{v}_1'}{r_{00}} + \frac{\rho U_0^q}{r_{00}^2}w' - \frac{\mathrm{d}r_{00}}{\mathrm{d}T}\tilde{v}_1' - \frac{\mathrm{d}r_{01}}{\mathrm{d}T}U_0^q w' - \frac{U_0^{q-2}q(q+1)}{2}\frac{w^2}{(1+bw^2)}\tilde{u}_1^2 + \frac{2q}{U_0}\frac{w}{(1+bw^2)^2}\tilde{u}_1\tilde{v}_1 - \frac{1}{U_0^q}\frac{(1-3bw^2)}{(1+bw^2)^3}\tilde{v}_1^2 + U_0^{q-1}q\frac{w^2}{(1+bw^2)}\tilde{u}_2, \tag{3.73a}$$

$$\tilde{u}_2'' = \frac{U_0}{D} - \frac{\tilde{u}_1'}{r_{00}} + \frac{1}{D}U_0^{\beta-1}sw^o\tilde{u}_1 - \frac{1}{D}U_0^{\beta-q}ow^{o-1}\tilde{v}_1. \tag{3.73b}$$

As before, we differentiate (3.73a) and use (3.64) to get

$$\begin{aligned} a_2 w' = &-\frac{1}{U_0^q} L_{0b}\tilde{v}_2' - \frac{\tilde{v}_1''}{U_0^q r_{00}} + \frac{w'}{r_{00}^2} + \frac{\rho w''}{r_{00}^2} - \frac{1}{U_0^q}\frac{\mathrm{d}r_{00}}{\mathrm{d}T}\tilde{v}_1'' \\ &- \frac{\mathrm{d}r_{01}}{\mathrm{d}T} w'' + \bar{a}_2 \tilde{u}_1' - \frac{a_1}{U_0^q}\tilde{v}_1' + \frac{q}{U_0}\frac{w^2}{(1+bw^2)}\tilde{u}_2'. \end{aligned} \tag{3.74}$$

Upon substituting (3.74) into (3.71) and simplifying we get

$$\begin{aligned} L_{0b}\Phi_2 = &\frac{q}{U_0}\frac{w^2}{(1+bw^2)}\tilde{\mathcal{F}}_1 + \bar{a}_2\tilde{\mathcal{F}}_0 - a_1\Phi_1 + \frac{1}{U_0^q}L_{0b}\tilde{v}_2' + \frac{\tilde{v}_1''}{U_0^q r_{00}} - \frac{w'}{r_{00}^2} \\ &+ \frac{1}{U_0^q}\frac{\mathrm{d}r_{00}}{\mathrm{d}T}\tilde{v}_1'' + \frac{a_1}{U_0^q}\tilde{v}_1' - \frac{\Phi_1'}{r_{00}} - \frac{\mathrm{d}r_{00}}{\mathrm{d}T}\Phi_1' + \left(\hat{\lambda} + \frac{m^2}{r_{00}^2}\right) w', \end{aligned} \tag{3.75}$$

where we define,

$$\tilde{\mathcal{F}}_1 = U_0^q \tilde{N}_1 - \tilde{u}_2'. \tag{3.76}$$

To simplify further we return to the problem for Φ_1 given by (3.66), which we can simplify as

$$L_{0b}\left(\Phi_1 - \frac{1}{U_0^q}\tilde{v}_1'\right) = \frac{q\tilde{\mathcal{F}}_0}{U_0}\frac{w^2}{(1+bw^2)}. \tag{3.77}$$

Now, considering the even eigenfunction problem discussed in section 3.2, when $\mu = 0$ there is a function ψ in (3.18) which satisfies

$$L_{0b}\psi = \frac{w^2}{(1+bw^2)}, \tag{3.78}$$

and so we can write (3.77) as

$$L_{0b}\left(\Phi_1 - \frac{1}{U_0^q}\tilde{v}_1' - \frac{q\tilde{\mathcal{F}}_0}{U_0}\psi\right) = 0.$$

Therefore, the function being operated on must be some multiple of the null eigenfunction w' which we can take to be zero without loss of generality, and we have that,

$$\Phi_1 = \frac{1}{U_0^q}\tilde{v}_1' + \frac{q\tilde{\mathcal{F}}_0}{U_0}\psi. \tag{3.79}$$

We can actually determine ψ analytically by first noticing that when $b = 0$, we can directly verify that $\psi = w$. With this in mind, we consider how the L_{0b} operator acts on w even with saturation:

$$L_{0b}w = w'' - w + 2\frac{w^2}{(1+bw^2)^2} = \frac{w^2}{(1+bw^2)^2} - b\frac{w^4}{(1+bw^2)^2} \tag{3.80}$$

where we have used (2.22) to simplify the second derivative term. We can get a better understanding of the last term in this expression by differentiating the homoclinic orbit problem (2.22) with respect to the saturation parameter b,

$$w_b'' - w_b + 2\frac{ww_b}{(1+bw^2)^2} - \frac{w^4}{(1+bw^2)^2} = 0$$

which implies

$$L_{0b}w_b = \frac{w^4}{(1+bw^2)^2}$$

and this is precisely the last term in (3.80). With this in mind we attempt a solution for ψ of the form,

$$\psi = w + cw_b,$$

with c to be determined. Substituting this into (3.78) we have,

$$\begin{aligned}\frac{w^2}{(1+bw^2)} = L_{0b}(w+cw_b) =& \frac{w^2}{(1+bw^2)^2} + (c-b)\frac{w^4}{(1+bw^2)^2} \\ =& \frac{w^2}{(1+bw^2)}\frac{(1+(c-b)w^2)}{(1+bw^2)}\end{aligned}$$

which will hold if $c = 2b$ and thus we have

$$\psi = w + 2bw_b. \tag{3.81}$$

Substituting (3.79) into (3.75) we get

$$\begin{aligned}L_{0b}\Phi_2 =& \frac{q}{U_0}\frac{w^2}{(1+bw^2)}\tilde{\mathcal{F}}_1 + \left(\bar{a}_2 - \frac{q}{U_0}\left(a_1\psi + \frac{1}{r_{00}}\psi' + \frac{\mathrm{d}r_{00}}{\mathrm{d}T}\psi'\right)\right)\tilde{\mathcal{F}}_0 \\ &+ \frac{1}{U_0^q}L_{0b}\tilde{v}_2' - \frac{w'}{r_{00}^2} + \left(\hat{\lambda} + \frac{m^2}{r_{00}^2}\right)w'.\end{aligned}$$

Once again, $\Phi_2 = w'$ is a homogeneous solution to this and so we need to satisfy the solvability condition,

$$\begin{aligned}
&\frac{q}{U_0}\underbrace{\int_{-\infty}^{\infty}\frac{w^2}{(1+bw^2)}w'\tilde{\mathcal{F}}_1\,\mathrm{d}\rho}_{I_1}\\
&+\tilde{\mathcal{F}}_0\underbrace{\int_{-\infty}^{\infty}\bar{a}_2w'-\frac{q}{U_0}\left(a_1\psi w'+\frac{1}{r_{00}}\psi'w'+\frac{\mathrm{d}r_{00}}{\mathrm{d}T}\psi'w'\right)\mathrm{d}\rho}_{I_2}\\
&+\left(\hat{\lambda}+\frac{m^2-1}{r_{00}^2}\right)\int_{-\infty}^{\infty}w'^2\,\mathrm{d}\rho=0,
\end{aligned}\tag{3.82}$$

where we have once again used (3.68) to remove the $L_{0b}\tilde{v}_2'$ term. First consider the integral I_2 in (3.82). We can use (3.65) to write,

$$\begin{aligned}
\int_{-\infty}^{\infty}a_1\psi w'\,\mathrm{d}\rho&=\int_{-\infty}^{\infty}-\frac{1}{U_0^q}\psi L_{0b}\tilde{v}_1'-\frac{w''\psi}{r_{00}}+\frac{q}{U_0}\psi\tilde{u}_1'\frac{w^2}{(1+bw^2)}-\frac{\mathrm{d}r_{00}}{\mathrm{d}T}w''\psi\,\mathrm{d}\rho\\
&=\int_{-\infty}^{\infty}-\frac{1}{U_0^q}\psi L_{0b}\tilde{v}_1'+\frac{w'\psi'}{r_{00}}+\frac{q}{U_0}\psi\tilde{u}_1'\frac{w^2}{(1+bw^2)}+\frac{\mathrm{d}r_{00}}{\mathrm{d}T}w'\psi'\,\mathrm{d}\rho,
\end{aligned}\tag{3.83}$$

where we have integrated by parts on the second and last term. We also have

$$\begin{aligned}
\int_{-\infty}^{\infty}\bar{a}_2w'\,\mathrm{d}\rho&=\frac{2q}{U_0^{q+1}}\int_{-\infty}^{\infty}\frac{ww'}{(1+bw^2)^2}\tilde{v}_1\,\mathrm{d}\rho-\frac{q(q+1)}{U_0^2}\int_{-\infty}^{\infty}\frac{w^2w'}{(1+bw^2)}\tilde{u}_1\,\mathrm{d}\rho\\
&=\frac{q}{U_0^{q+1}}\int_{-\infty}^{\infty}\tilde{v}_1(L_{0b}\psi)'\,\mathrm{d}\rho-\frac{q(q+1)}{U_0^2}\int_{-\infty}^{\infty}\mathcal{W}'\tilde{u}_1\,\mathrm{d}\rho,
\end{aligned}$$

where we have differentiated (3.18) to get the simplification in the first integral and $\mathcal{W}$ is given by (2.29). Integrating each term by parts

$$\int_{-\infty}^{\infty} \bar{a}_2 w' \,\mathrm{d}\rho = -\frac{q}{U_0^{q+1}} \int_{-\infty}^{\infty} \tilde{v}_1' L_{0b} \psi \,\mathrm{d}\rho + \frac{q(q+1)}{2U_0^2} \hat{\mathcal{H}} \left\langle \frac{\mathrm{d}u_e}{\mathrm{d}r} \right\rangle_{r_{00}} \int_{-\infty}^{\infty} w'^2 \,\mathrm{d}\rho$$

where the last term was simplified using (2.12), (2.18), and that

$$\frac{\int_0^{\infty} \mathcal{W} \,\mathrm{d}\rho}{\int_{-\infty}^{\infty} w'^2 \,\mathrm{d}\rho} = \frac{\hat{\mathcal{H}}}{4}. \tag{3.84}$$

Using the self-adjoint property of L_{0b} we can finalize once more to obtain

$$\int_{-\infty}^{\infty} \bar{a}_2 w' \,\mathrm{d}\rho = -\frac{q}{U_0^{q+1}} \int_{-\infty}^{\infty} \psi L_{0b} \tilde{v}_1' \,\mathrm{d}\rho + \frac{q(q+1)}{2U_0^2} \hat{\mathcal{H}} \left\langle \frac{\mathrm{d}u_e}{\mathrm{d}r} \right\rangle_{r_{00}} \int_{-\infty}^{\infty} w'^2 \,\mathrm{d}\rho. \tag{3.85}$$

Combining (3.83) and (3.85) we can simplify I_2 in (3.82) as

$$\begin{aligned} I_2 =& \frac{q(q+1)}{2U_0^2} \hat{\mathcal{H}} \left\langle \frac{\mathrm{d}u_e}{\mathrm{d}r} \right\rangle_{r_{00}} \int_{-\infty}^{\infty} w'^2 \,\mathrm{d}\rho - \frac{q^2}{U_0^2} \int_{-\infty}^{\infty} \psi \tilde{u}_1' \frac{w^2}{(1+bw^2)} \,\mathrm{d}\rho \\ & - \frac{2q}{U_0} \left(\frac{1}{r_{00}} + \frac{\mathrm{d}r_{00}}{\mathrm{d}T} \right) \int_{-\infty}^{\infty} w' \psi' \,\mathrm{d}\rho. \end{aligned}$$

Using (2.34e) we can re-write the last term and we have

$$\begin{aligned} I_2 =& \frac{q(q+1)}{2U_0^2} \hat{\mathcal{H}} \left\langle \frac{\mathrm{d}u_e}{\mathrm{d}r} \right\rangle_{r_{00}} \int_{-\infty}^{\infty} w'^2 \,\mathrm{d}\rho - \frac{q^2}{U_0^2} \int_{-\infty}^{\infty} \psi \tilde{u}_1' \frac{w^2}{(1+bw^2)} \,\mathrm{d}\rho \\ & + \frac{q^2}{U_0^2} \hat{\mathcal{H}} \left\langle \frac{\mathrm{d}u_e}{\mathrm{d}r} \right\rangle_{r_{00}} \int_{-\infty}^{\infty} w' \psi' \,\mathrm{d}\rho. \end{aligned}$$

Finally we substitute ψ from (3.81) to get

$$\begin{aligned} I_2 =& \frac{q}{2U_0^2}\hat{\mathcal{H}}\left\langle \frac{\mathrm{d}u_e}{\mathrm{d}r}\right\rangle_{r_{00}} \int_{-\infty}^{\infty} w'^2\,\mathrm{d}\rho + \frac{3q^2}{2U_0^2}\hat{\mathcal{H}}\left\langle \frac{\mathrm{d}u_e}{\mathrm{d}r}\right\rangle_{r_{00}} \int_{-\infty}^{\infty} w'^2\,\mathrm{d}\rho \\ &+ \frac{q^2}{U_0^2}\left(2b\hat{\mathcal{H}}\left\langle \frac{\mathrm{d}u_e}{\mathrm{d}r}\right\rangle \int_{-\infty}^{\infty} w'w_b'\,\mathrm{d}\rho - \underbrace{\int_{-\infty}^{\infty} \frac{w^3}{(1+bw^2)}\tilde{u}_1'\,\mathrm{d}\rho}_{I_3} \right. \\ &\left. -2b\underbrace{\int_{-\infty}^{\infty} \frac{w^2 w_b}{(1+bw^2)}\tilde{u}_1'\,\mathrm{d}\rho}_{I_4} \right). \end{aligned}$$

Integrate I_4 by parts to get

$$I_4 = 2\int_0^{\infty} \frac{w^2 w_b}{(1+bw^2)}\,\mathrm{d}\rho \left\langle \frac{\mathrm{d}u_e}{\mathrm{d}r}\right\rangle_{r_{00}} - \int_{-\infty}^{\infty}\left(\int_0^{\rho} \frac{w^2 w_b}{(1+bw^2)}\,\mathrm{d}x\right)\tilde{u}_1''\,\mathrm{d}\rho,$$

but the last integral vanishes since $\tilde{u}_1''$ is an even function. For the integral I_3, we also integrate by parts to split the integral,

$$I_3 = -3\int_{-\infty}^{\infty} \frac{w^2 w'}{(1+bw^2)}\tilde{u}_1\,\mathrm{d}\rho + 2b\int_{-\infty}^{\infty} \frac{w^4 w'}{(1+bw^2)^2}\tilde{u}_1\,\mathrm{d}\rho,$$

but then integrate by parts on each separate integral again, twice, transferring the derivative back to the $\tilde{u}_1$ term. After doing this, and once again removing integrals involving $\tilde{u}_1''$, we get

$$\begin{aligned} I_3 &= \left(6\int_0^{\infty}\mathcal{W}\,\mathrm{d}\rho - 4b\int_0^{\infty}\int_0^{w}\frac{v^4}{(1+bv^2)^2}\,\mathrm{d}v\,\mathrm{d}\rho\right)\left\langle \frac{\mathrm{d}u_e}{\mathrm{d}r}\right\rangle_{r_{00}} \\ &= \left(\frac{3}{2}\hat{\mathcal{H}}\int_{-\infty}^{\infty} w'^2\,\mathrm{d}\rho - 4b\int_0^{\infty}\int_0^{w}\frac{v^4}{(1+bv^2)^2}\,\mathrm{d}v\,\mathrm{d}\rho\right)\left\langle \frac{\mathrm{d}u_e}{\mathrm{d}r}\right\rangle_{r_{00}}, \end{aligned}$$

where we have used (3.84) to simplify. Transferring everything together back into I_2 we have

$$I_2 = \frac{q}{2U_0^2}\hat{\mathcal{H}}\left\langle \frac{\mathrm{d}u_e}{\mathrm{d}r}\right\rangle_{r_{00}} \int_{-\infty}^{\infty} w'^2\,\mathrm{d}\rho - \frac{bq^2}{U_0^2}\left\langle \frac{\mathrm{d}u_e}{\mathrm{d}r}\right\rangle_{r_{00}} \left(4\int_0^{\infty}\frac{w^2 w_b}{(1+bw^2)}\,\mathrm{d}\rho \right.$$
$$\left. +4\int_0^{\infty}\int_0^{w}\frac{v^4}{(1+bv^2)^2}\,\mathrm{d}v\,\mathrm{d}\rho - 2\hat{\mathcal{H}}\int_{-\infty}^{\infty} w' w_b'\,\mathrm{d}\rho\right).$$

We can actually simplify this if we differentiate $\hat{\mathcal{H}}$ in (3.84) with respect to b and notice that this is exactly the last term in the expression. Therefore we have,

$$I_2 = \frac{q}{2U_0^2}\hat{\mathcal{H}}\left\langle \frac{\mathrm{d}u_e}{\mathrm{d}r}\right\rangle_{r_{00}} \int_{-\infty}^{\infty} w'^2\,\mathrm{d}\rho\left(1 - \frac{2bq}{\hat{\mathcal{H}}}\frac{\mathrm{d}\hat{\mathcal{H}}}{\mathrm{d}b}\right). \tag{3.86}$$

Finally, we consider I_1 in (3.82) which we integrate by parts to get

$$I_1 = -\frac{\hat{\mathcal{H}}}{4}\int_{-\infty}^{\infty} w'^2\,\mathrm{d}\rho\left(\tilde{\mathcal{F}}_1'(\infty)+\tilde{\mathcal{F}}_1'(-\infty)\right) + \int_{-\infty}^{\infty}\int_0^{\rho}\left(\mathcal{W}(x)\,\mathrm{d}x\right)\tilde{\mathcal{F}}_1''\,\mathrm{d}\rho. \tag{3.87}$$

To simplify this we need to understand the behaviour of $\tilde{\mathcal{F}}_1$ given by (3.76) and specifically, its second derivative,

$$\tilde{\mathcal{F}}_1'' = U_0^q\tilde{N}_1'' - \tilde{u}_2'''.$$

Therefore, we need to consider the problem for $\tilde{N}_1$ which we obtain by expanding (3.70) to $\mathcal{O}(\epsilon^2)$,

$$\begin{aligned}\tilde{N}_1'' = &-\frac{\tilde{N}_0'}{r_{00}} + \frac{sU_0^{\beta-1}}{D}w^o\tilde{N}_0 - \frac{oU_0^{\beta-q}}{D}w^{o-1}\left(\frac{\tilde{v}_1'}{U_0^q} + \frac{q\tilde{\mathcal{F}}_0}{U_0}\psi\right)\\ &+ \frac{osU_0^{\beta-q-1}}{D}w^{o-1}w'\tilde{u}_1 - \frac{o(o-1)U_0^{\beta-2q}}{D}w^{o-2}w'\tilde{v}_1. \end{aligned} \tag{3.88}$$

If we multiply this by U_0^q and subtract $\tilde{u}_2'''$ by differentiating (3.73b) we get

$$\tilde{\mathcal{F}}_1'' = \frac{U_0^{\beta-1}}{D}w^{o-1}\tilde{\mathcal{F}}_0\left(sw - o\psi\right) \tag{3.89}$$

which is even and so, since $\mathcal{W}$ is also even, the integrand in the second integral in (3.87), is odd and hence, the integral vanishes. Rather than attempt and use $\tilde{\mathcal{F}}_1'$ to simplify I_1 we will instead consider the global $\mathcal{F}$ problem and relate them via

$$\mathcal{F}(r_{00}+\epsilon\rho) \sim \mathcal{F}(r_{00}) + \epsilon\rho\frac{\mathrm{d}\mathcal{F}}{\mathrm{d}r}\bigg|_{r_{00}} + \cdots = \tilde{\mathcal{F}}_0 + \epsilon\tilde{\mathcal{F}}_1, \tag{3.90}$$

where we note that sided limits apply when functions are not continuous. Using (3.90), we can write (3.87) as

$$I_1 = -\frac{\hat{\mathcal{H}}}{2}\int_{-\infty}^{\infty} w'^2\,\mathrm{d}\rho\left(U_0^q\left\langle\frac{\mathrm{d}\hat{N}}{\mathrm{d}r}\right\rangle_{r_{00}} - \left\langle\frac{\mathrm{d}^2u_e}{\mathrm{d}r^2}\right\rangle_{r_{00}}\right). \tag{3.91}$$

Finally, returning to (3.82) and substituting I_1 and I_2, we see that everything does not vanish, and so we require eigenvalues at this order to satisfy the orthogonality condition. Hence $\omega(\epsilon) = \epsilon^2$ and the eigenvalues, to leading

order, are given by

$$\hat{\lambda} = \frac{1-m^2}{r_{00}^2} - \frac{q}{2U_0^2}\hat{\mathcal{H}}\left(1 - \frac{2bq}{\hat{\mathcal{H}}}\frac{\mathrm{d}\hat{\mathcal{H}}}{\mathrm{d}b}\right)\left\langle \frac{\mathrm{d}u_e}{\mathrm{d}r}\right\rangle_{r_{00}} \mathcal{F}(r_{00}) + \frac{q\hat{\mathcal{H}}}{2U_0}\left(U_0^q\left\langle \frac{\mathrm{d}\hat{N}}{\mathrm{d}r}\right\rangle_{r_{00}} - \left\langle \frac{\mathrm{d}^2u_e}{\mathrm{d}r^2}\right\rangle_{r_{00}}\right). \tag{3.92}$$

The fact that the eigenvalues exist to leading order at $\mathcal{O}(\epsilon^2)$ is why we can classify them as long-time instabilities because even positive values will only begin to cause relative instability in (3.9) when $T = \mathcal{O}(1)$ which corresponds to regular time $t = \mathcal{O}(\epsilon^{-2})$. Since $\hat{N}$ is not continuous, but $\mathcal{F}(r_{00}) = \tilde{\mathcal{F}}_0$ is, we will define $\mathcal{F}(r_{00})$ by the average value as we did when discussing the perturbed circle problem in section (2.3.2) and therefore,

$$\mathcal{F}(r_{00}) = U_0^q\left\langle \hat{N}\right\rangle_{r_{00}} - \left\langle \frac{\mathrm{d}u_e}{\mathrm{d}r}\right\rangle_{r_{00}}.$$

We now need to consider the global problem for $\hat{N}$.

3.3.1 Global Inhibitor Eigenvalue Problem

Substitute $N = \epsilon\hat{N}$ into (3.6b) and simplify to get the base problem for $\hat{N}$ is

$$\frac{1}{r}(r\hat{N}_r)_r - \frac{m^2}{r^2}\hat{N} - \frac{1}{D}\hat{N} + \underbrace{\frac{1}{\epsilon^2}\frac{o}{D}\frac{v_e^{o-1}}{u_e^s}\Phi\left(\frac{r-r_0}{\epsilon}\right) - \frac{1}{\epsilon}\frac{s}{D}\frac{v_e^o}{u_e^{s+1}}\hat{N}}_{S_1} = 0, \tag{3.93}$$

where we do not use θ_λ here as we did for even eigenfunctions because $\lambda = \mathcal{O}(\epsilon^2)$. Focusing solely on the singular terms S_1 and expanding to all singular

powers of ϵ, we have,

$$\begin{aligned} S_1 =& \frac{oU_0^{\beta-q}}{D\epsilon^2} w^{o-1}(\cdot)w'(\cdot) + \frac{oU_0^{\beta-q}}{D\epsilon} w^{o-1}(\cdot)\Phi_1(\cdot) - \frac{osU_0^{\beta-q-1}}{D\epsilon} w^{o-1}(\cdot)\tilde{u}_1(\cdot)w'(\cdot) \\ &+ \frac{o(o-1)U_0^{\beta-2q}}{D\epsilon} w^{o-2}(\cdot)\tilde{v}_1(\cdot)w'(\cdot) - \frac{sU_0^{\beta-1}}{D\epsilon} w^{o}(\cdot)\tilde{N}_0(\cdot), \end{aligned} \tag{3.94}$$

where the dot indicates evaluation at $(r - r_0)\epsilon^{-1}$, i.e. the inner functions evaluated in the outer region. In a manner similar to that as we discussed in section 3.1, when deriving the singularity behaviour for the even eigenfunctions functions, we have

$$\frac{w^o\left(\frac{r-r_0}{\epsilon}\right)}{\epsilon} \underset{\epsilon\to 0}{=} \mathcal{A}\delta(r - r_0),$$

where δ is the Dirac measure and $\mathcal{A}$ is again given by (2.33). Differentiating this expression we get

$$\frac{o}{\epsilon^2} w^{o-1}\left(\frac{r-r_0}{\epsilon}\right) w'\left(\frac{r-r_0}{\epsilon}\right) = \mathcal{A}\delta'(r - r_0),$$

and the first term of S_1 in (3.94) is precisely a multiple of this. If we associate inverse powers of ϵ as leading to Dirac singularities then we expect this behaviour for the remaining terms in (3.94) and so

$$S_1 = \frac{U_0^{\beta-q}}{D}\mathcal{A}\delta'(r - r_0) + A\delta(r - r_0),$$

where we can determine A by integrating all but the first term in (3.94) over the entire inner domain. This yields that

$$A = \int_{-\infty}^{\infty} \frac{oU_0^{\beta-2q}}{D} w^{o-1}\tilde{v}_1 + \frac{oU_0^{\beta-q-1}}{D} q\mathcal{F}(r_0) w^{o-1}\psi - \frac{osU_0^{\beta-q-1}}{D} w^{o-1}\tilde{u}_1 w' + \frac{o(o-1)U_0^{\beta-2q}}{D} w^{o-2}\tilde{v}_1 w' - \frac{sU_0^{\beta-1}}{D} w^o \tilde{N}_0 \,\mathrm{d}\rho,$$

where we have substituted (3.79) for Φ_1. We can integrate the third and fourth term by parts and upon simplifying we have

$$A = \frac{U_0^{\beta-q-1}}{D}\mathcal{F}(r_0) \int_{-\infty}^{\infty} \left(qow^{o-1}\psi - sw^o\right) \mathrm{d}\rho.$$

Substituting ψ using (3.81) and recognizing that

$$\frac{\mathrm{d}\mathcal{A}}{\mathrm{d}b} = \int_{-\infty}^{\infty} ow^{o-1} w_b \,\mathrm{d}\rho,$$

we finally have that

$$A = \frac{U_0^{\beta-q-1}}{D}\mathcal{F}(r_0)\beta \left(\mathcal{A} + 2qb\frac{\mathrm{d}\mathcal{A}}{\mathrm{d}b}\right),$$

where β is given by (2.28b). Putting everything together we have,

$$S_1 = \frac{U_0^{\beta-q}}{D}\mathcal{A}\delta'(r-r_0) + \frac{U_0^{\beta-q-1}}{D}\mathcal{F}(r_0)\mathcal{A}\left(\beta + \frac{2qb}{\mathcal{A}}\frac{\mathrm{d}\mathcal{A}}{\mathrm{d}b}\right)\delta(r-r_0), \quad (3.95)$$

and therefore the global problem for $\hat{N}$ is (by once again taking $r_0 \approx r_{00}$),

$$\frac{1}{r}(r\hat{N}_r)_r - \frac{m^2}{r^2}\hat{N} - \frac{1}{D}\hat{N} = -\frac{U_0^{\beta-q}}{D}\mathcal{A}\delta'(r-r_{00}) - \frac{U_0^{\beta-q-1}}{D}\mathcal{F}(r_{00})\mathcal{A}\left(\beta + \frac{2qb}{\mathcal{A}}\frac{\mathrm{d}\mathcal{A}}{\mathrm{d}b}\right)\delta(r-r_{00}),$$

which we can rewrite using constants $\bar{A}_0$ (given by (2.60)) and $\bar{\bar{A}}_0$ (given by (2.59)) used in section 2.3.2 to get:

$$\frac{1}{r}(r\hat{N}_r)_r - \frac{m^2}{r^2}\hat{N} - \frac{1}{D}\hat{N} = -\frac{\bar{A}_0}{U_0^q}\delta'(r-r_{00}) - \frac{\bar{A}_0\bar{\bar{A}}_0}{U_0^{q+1}}\mathcal{F}(r_{00})\delta(r-r_{00}). \quad (3.96)$$

It is more convenient if we turn this into a problem with homogeneous sources away from the interface $r \neq r_{00}$ supplemented by jump conditions across the interface. To do this we first multiply by r and integrate over a small domain containing r_{00}. Since the differential equation has a dipole source term then $\hat{N}$ will have jump discontinuities, but otherwise will be continuous and therefore, by the integral mean value theorem, the second and third terms on the left-side of (3.96) will vanish over the integral. Therefore we have that

$$\left[\frac{\mathrm{d}\hat{N}}{\mathrm{d}r}\right]_{r_{00}} = \frac{\bar{A}_0}{U_0^q r_{00}} - \frac{\bar{A}_0\bar{\bar{A}}_0}{U_0^{q+1}}\mathcal{F}(r_{00}) = \frac{\bar{A}_0}{U_0^q r_{00}} - \frac{\bar{A}_0\bar{\bar{A}}_0}{U_0^{q+1}}U_0^q\left\langle\hat{N}\right\rangle_{r_{00}} + \frac{\bar{A}_0\bar{\bar{A}}_0}{U_0^{q+1}}\left\langle\frac{\mathrm{d}u_e}{\mathrm{d}r}\right\rangle_{r_{00}}. \quad (3.97a)$$

To get the jump in the function itself, we first compute the indefinite integral of (3.96), ignoring constants of integration,

$$r\hat{N}_r - m^2 \int \frac{1}{r}\hat{N}\,\mathrm{d}r - \frac{1}{D}\int \hat{N}\,\mathrm{d}r = -\frac{\bar{A}_0}{U_0^q} r_{00}\delta(r-r_{00}) + \frac{\bar{A}_0}{U_0^q}\mathcal{H}(r-r_{00}) - \frac{\bar{A}_0\bar{\bar{A}}_0}{U_0^{q+1}} r_{00}\mathcal{F}(r_{00})\mathcal{H}(r-r_{00})$$

with $\mathcal{H}$ the Heaviside function. We then divide by r, and integrate this expression over a small domain centered around r_{00} to get

$$[\hat{N}]_{r_{00}} = -\frac{\bar{A}_0}{U_0^q}, \tag{3.97b}$$

where once again appropriate continuous terms have been neglected as they vanish over the region of integration. We could now solve the problem for $\hat{N}$ subject to the jump conditions (3.97), but we have seen a similar problem to this in section 2.3.2 when we looked at $\mathcal{V}_{1n}$, the perturbed circle steady-state problem at $\mathcal{O}(\varepsilon)$, given by (2.63). In fact if we add the jump conditions (2.63d) to (3.97a) and (2.63c) to (3.97b), letting $n = m$, and define a function

$$\mathcal{Z} = H_n U_0^q \hat{N} + \mathcal{V}_{1n},$$

then we have the following problem for $\mathcal{Z}$,

$$\begin{aligned}\frac{1}{r}(r\mathcal{Z}_r)_r - \frac{n^2}{r^2}\mathcal{Z} - \frac{1}{D}\mathcal{Z} = 0, \qquad & r \neq r_{00} \\ \left.\frac{\mathrm{d}\mathcal{Z}}{\mathrm{d}r}\right|_{r=r_{00}} &= 0, \\ [\mathcal{Z}]_{r_{00}} &= 0, \\ \left[\frac{\mathrm{d}\mathcal{Z}}{\mathrm{d}r}\right]_{r_{00}} &= -\frac{\bar{A}_0\bar{\bar{A}}_0}{U_0}\mathcal{Z}(r_{00}).\end{aligned}$$

Solving this problem we have

$$\mathcal{Z}(r) = \frac{r_{00}\bar{A}_0\bar{\bar{A}}_0}{U_0}\mathcal{Z}(r_{00})G_{0;n}(r;r_{00})$$

with $G_{0,n}$ given by (2.50). Evaluating at $r = r_{00}$ leads to the conclusion that $\mathcal{Z}(r_{00}) = 0$ is the only possibility for arbitrary r_{00} and therefore $\mathcal{Z}$ is identically zero and thus,

$$\hat{N} = -\frac{1}{H_n U_0^q}\mathcal{V}_{1n}. \tag{3.98}$$

Therefore our perturbed inhibitor eigenfunction is already determined by the solution to $\mathcal{V}_{1n}$. This allows us to write the small eigenvalues (3.92) as

$$\begin{aligned}\hat{\lambda} =& \frac{1-m^2}{r_{00}^2} + \frac{q}{2H_m U_0^2}\hat{\mathcal{H}}\left(1 - \frac{2bq}{\hat{\mathcal{H}}}\frac{\mathrm{d}\hat{\mathcal{H}}}{\mathrm{d}b}\right)\left\langle\frac{\mathrm{d}u_e}{\mathrm{d}r}\right\rangle_{r_{00}}\left(\langle\mathcal{V}_{1m}\rangle_{r_{00}} + H_m\left\langle\frac{\mathrm{d}u_e}{\mathrm{d}r}\right\rangle_{r_{00}}\right) \\ & - \frac{q\hat{\mathcal{H}}}{2H_m U_0}\left(\left\langle\frac{\mathrm{d}\mathcal{V}_{1m}}{\mathrm{d}r}\right\rangle_{r_{00}} + H_m\left\langle\frac{\mathrm{d}^2u_e}{\mathrm{d}r^2}\right\rangle_{r_{00}}\right).\end{aligned} \tag{3.99}$$

It is rather unsurprising that there is such an intimate relationship between the problem for $\hat{N}$ and the perturbed circle since the odd eigenfunctions displace the activator curve sinusoidally and thus exactly deform the circle into a near-circle, at least initially. The problems are, in fact, even more intimately related than just through the $\hat{N}$ function. Recall that we define the concentrated activator curve at $r = r_0 + \epsilon\rho^*(\theta)$ where ρ^* is defined as the location of the maximum of the activator and hence

$$\tilde{v}(\rho^*)' = \tilde{v}_e'(\rho^*) + \Phi'(\rho^*) \exp\left(im\theta + \int_0^T \hat{\lambda}(s)\,\mathrm{d}s\right) = 0. \tag{3.100}$$

The radial velocity of the curve will be given by

$$\frac{\mathrm{d}r}{\mathrm{d}T} = \frac{\mathrm{d}r_0}{\mathrm{d}T} + \epsilon\frac{\mathrm{d}\rho^*}{\mathrm{d}T}$$

and differentiating (3.100) with respect to T, we have

$$\begin{aligned} 0 = &\left(\tilde{v}_e''(\rho^*) + \Phi''(\rho^*) \exp\left(im\theta + \int_0^T \hat{\lambda}(s)\,\mathrm{d}s\right)\right)\frac{\mathrm{d}\rho^*}{\mathrm{d}T} \\ &+ \Phi'(\rho^*) \exp\left(im\theta + \int_0^T \hat{\lambda}(s)\,\mathrm{d}s\right)\hat{\lambda}(T). \end{aligned}$$

Using (3.100) we can simplify and write

$$\frac{\mathrm{d}\rho^*}{\mathrm{d}T} = \frac{\tilde{v}_e'(\rho^*)}{\tilde{v}''(\rho^*)}\hat{\lambda}(T) \tag{3.101}$$

and therefore

$$\frac{\mathrm{d}r}{\mathrm{d}T} = \frac{\mathrm{d}r_0}{\mathrm{d}T} + \epsilon\frac{\tilde{v}_e'(\rho^*)}{\tilde{v}''(\rho^*)}\hat{\lambda}(T).$$

If we think of the coefficient on $\hat{\lambda}$ playing to role of ε in the near circle perturbation then $-\hat{\lambda}$ should be the first velocity correction we obtained. Indeed if we compare the negative of (3.99) with (2.77) then if we take

$$h(\theta) = \exp(im\theta)$$

we see perfect agreement. Notice this required choice of $h(\theta)$ to balance comes from the eigenfunction expansion of the linear stability problem (3.2). The coefficients H_m in the Fourier expansion of $h(\theta)$ were arbitrary and, if desired, could be extracted from the coefficient in front of $\hat{\lambda}$.

Chapter 4

Classification of Explicitly Solvable Non-Local Eigenvalue Problems

4.1 Explicit Non-Local Eigenvalue Formulation

In Chapter, 3 we considered the stability of the Gierer-Meinhardt model on a ring to breakup instabilities. This led to the derivation of a non-self-adjoint, non-local eigenvalue problem (3.16) which we analyzed by recasting it as a root-finding problem. This allowed us to determine regions of stability but did not lend itself well to determining eigenvalues explicitly. In this chapter we consider scenarios for which the explicit determination of these eigenvalues can be obtained. A similar analysis in what follows was done in [57] for the model,

$$v_t = \epsilon^2 v_{xx} - v + a(u)v^{2r-3},$$
$$\tau u_t = u_{xx} + (u_b - u) + \frac{1}{\epsilon} b(u)v^r,$$

for certain conditions on the constants r, u_b and the functions $a(u)$ and $b(u)$. To setup the theory, we generally consider a class of problems for which linear stability analysis produces a non-local eigenvalue problem of the form

$$\begin{aligned} L_0\Phi - \chi(\lambda)h(w)\int_{-\infty}^{\infty} g(w)\Phi \,\mathrm{d}y = \lambda\Phi, \quad -\infty < y < \infty; \\ \Phi \to 0 \text{ as } |y| \to \infty, \end{aligned} \tag{4.1}$$

where ,

$$L_0\Phi = \Phi_{yy} - \Phi + f'(w)\Phi, \tag{4.2}$$

with prime indicating differentiation with respect to w. $\chi(\lambda)$ is a transcendental function of the eigenvalue parameter λ and $w(y)$ is the unique homoclinic of

$$\begin{aligned} &w_{yy} - w + f(w) = 0, \quad -\infty < y < \infty; \\ &w \to 0 \text{ as } |y| \to \infty, \quad w_y(0) = 0, \quad w(0) > 0. \end{aligned} \tag{4.3}$$

This homoclinic orbit exists for certain functions $f(w)$ that satisfy Lemma 2.2.0.1 in section 2.2. For example, this criteria was used in section 2.3 to help establish the critical saturation parameter b for the saturated Gierer-Meinhardt model. Along with restrictions on $f(w)$ we also require in (4.1)

that

$$g(0) = 0, \quad g(w) > 0 \text{ for } w > 0, \quad g(w) \text{ is } C^1 \text{ as } w \to 0^+;$$
$$h(0) = 0, \quad h(w) \text{ is } C^1 \text{ as } w \to 0^+. \tag{4.4}$$

The conditions on $g(w)$ and $h(w)$ are such that the integral in (4.1) vanishes as $\Phi \to 0$ and that Φ has exponentially decaying solutions when y is asymptotically large and $\mathrm{Re}(\lambda) > 0$. In order to form (4.1) in an explicitly solvable way, we will exploit the eigenvalue structure of the L_0 operator which we discussed in 3.2.2 but will repeat here. Assuming $f(w)$ holds such that a homoclinic orbit solution to (4.3) exists then Lemma 3.1.0.1 provides the details of the eigenvalue spectrum to $L_0\psi = \nu\psi$. Specifically, it admits a simple discrete eigenvalue ν_0 with eigenfunction ψ_0 of one sign and an eigenvalue $\nu_1 = 0$ with $\psi_1 = w'$. Consider a choice of $g(w)$ in (4.1) which satisfies (4.4), and is such that

$$L_0 g(w) = \sigma g(w), \tag{4.5}$$

for some $\sigma > 0$. Since there can only be one positive eigenvalue to L_0, we must have that $\sigma = \nu_0$ and $g(w) = \psi_0$. If we multiply (4.1) by $g(w)$ and integrate over the entire domain then

$$\int_{-\infty}^{\infty} g(w) L_0 \Phi \, \mathrm{d}y - \chi(\lambda) \int_{-\infty}^{\infty} h(w) g(w) \, \mathrm{d}y \int_{-\infty}^{\infty} g(w) \Phi \, \mathrm{d}y = \lambda \int_{-\infty}^{\infty} g(w) \Phi \, \mathrm{d}y. \tag{4.6}$$

While the entire NLEP is not self adjoint, the operator L_0 given by (4.2) is and so we can integrate by parts the first term in (4.6) to simplify,

$$\int_{-\infty}^{\infty} g(w)\Phi\left(\sigma - \chi(\lambda)\int_{-\infty}^{\infty} h(w)g(w)\,\mathrm{d}y - \lambda\right)\mathrm{d}y = 0,$$

where we have used (4.5) to simplify. Assuming that $\int_{-\infty}^{\infty} g(w)\Phi\,\mathrm{d}y \neq 0$ then we have an explicit relationship for λ,

$$\lambda = \sigma - \chi(\lambda)\int_{-\infty}^{\infty} h(w)g(w)\,\mathrm{d}y, \tag{4.7}$$

where this integral converges because of the decay behaviour on $h(w)$ and $g(w)$. Before continuing, consider the case $\int_{-\infty}^{\infty} g(w)\Phi\,\mathrm{d}y = 0$, where (4.1) reduces to

$$L_0\Phi = \lambda\Phi,$$

i.e. Φ is an eigenfunction of the operator L_0. The only positive solution to this is for $\lambda = \nu_0$ but this would require $\Phi = g(w)$ and we would not be able to satisfy $\int_{-\infty}^{\infty} g(w)\Phi\,\mathrm{d}y = 0$. Therefore, any unstable eigenvalue to (4.1) needs to satisfy (4.7).

We now need to consider the appropriate $f(w)$ in (4.3) that produces a $g(w)$ for (4.5) and ultimately allow (4.7) to hold. If we recognize that

$$g(w)_{yy} = g''(w)w_y^2 + g'(w)w_{yy}$$

then we can write (4.5) as,

$$g''(w)w_y^2 + g'(w)w_{yy} + f'(w)g(w) = (1+\sigma)g(w). \tag{4.8}$$

To remove w_{yy} we can use (4.3) and to remove w_y^2 multiply that same equation and integrate over the entire domain to get

$$w_y^2 - w^2 + 2\mathcal{W} = 0, \quad \mathcal{W} = \int_0^w f(s)\,\mathrm{d}s.$$

Substituting into (4.8) we get,

$$g''(w)w^2 - 2g''(w)\mathcal{W} + g'(w)w - g'(w)f(w) + f'(w)g(w) = (1+\sigma)g(w).$$

If we integrate by parts and use that $g(0) = f(0) = 0$ we can simplify to get

$$(w^2 - 2\mathcal{W})g'(w) = \Sigma(w) - f(w)g(w); \tag{4.9a}$$

$$\Sigma(w) \equiv \int_0^w \xi(s)\,\mathrm{d}s, \quad \xi(s) \equiv sg'(s) + (\sigma+1)g(s). \tag{4.9b}$$

If we differentiate (4.9a) with respect to w then

$$2(w - f(w))g'(w) + (w^2 - 2\mathcal{W})g''(w) = \Sigma'(w) - (f(w)g(w))'.$$

Using (4.9a) we can simplify to

$$2wg'(w) - 2f(w)g'(w) + \frac{\Sigma(w) - f(w)g(w)}{g'(w)}g''(w) = \Sigma'(w) - (f(w)g(w))'.$$

Dividing by $g'(w)$ and rearranging this expression we have

$$\frac{f'(w)g(w)}{g'(w)} - \frac{f(w)g'(w)}{g'(w)} - \frac{f(w)g''(w)}{g'(w)^2} = \frac{\Sigma'(w)}{g'(w)} - \frac{\Sigma(w)g''(w)}{g'(w)^2} - 2w. \quad (4.10)$$

We can recognize the expression on the left of (4.10) as,

$$\frac{f'(w)g(w)}{g'(w)} - \frac{f(w)g'(w)}{g'(w)} - \frac{f(w)g''(w)}{g'(w)^2} = g^2\left(\frac{f}{gg'}\right)',$$

and the first two expressions on the right of (4.10) as,

$$\frac{\Sigma'(w)}{g'(w)} - \frac{\Sigma(w)g''(w)}{g'(w)^2} = \left(\frac{\Sigma(w)}{g'(w)}\right)',$$

so that finally, for a given $g(w)$, we can compute $f(w)$ as the solution to

$$\left(\frac{f(w)}{g(w)g'(w)}\right)' = \frac{1}{g(w)^2}\left(\left(\frac{\Sigma(w)}{g'(w)}\right)' - 2w\right). \quad (4.11)$$

It is important to note that for a given $g(w)$, while this formula provides the necessary $f(w)$, there is no guarantee that the resulting $f(w)$ will satisfy the homoclinic orbit criteria in Lemma 2.2.0.1. Many common NLEPs from reaction diffusion problems (cf. [39], [40], [45], [46], [81], [57]) involve $g(w)$ with algebraic powers in w. As such we will present two general cases $g(w) = w$ and $g(w) = w^\alpha$ for $\alpha > 1$ for which this theory can easily be used to determine $f(w)$.

First consider $g(w) = w$ so that from (4.9b),

$$\xi(w) = (\sigma + 2)w, \qquad \Sigma = \frac{(\sigma + 2)w^2}{2}.$$

From (4.11) we have

$$\left(\frac{f(w)}{w}\right)' = \frac{1}{w^2}\left(\left(\frac{(\sigma+2)w^2}{2}\right) - 2w\right) = \frac{\sigma}{w},$$

and therefore,

$$f(w) = \sigma w \log w + Aw,$$

where we can set $A = 0$ without loss of generality. Next consider $g(w) = w^\alpha$ for $\alpha > 1$. In this case,

$$\xi(w) = (\sigma + 1 + \alpha)w^\alpha, \qquad \Sigma = \frac{(\sigma+1+\alpha)w^{\alpha+1}}{\alpha+1},$$

and hence from (4.11),

$$\left(\frac{f(w)}{\alpha w^{2\alpha-1}}\right)' = \frac{1}{w^{2\alpha}}\left(\left(\frac{(\sigma+1+\alpha)w^2}{\alpha(\alpha+1)}\right)' - 2w\right) = \frac{2(\sigma+1+\alpha)}{\alpha(\alpha+1)}w^{1-2\alpha}.$$

Integrating this yields that

$$f(w) = \frac{(\sigma+1-\alpha^2)}{(1-\alpha^2)}w + Aw^{2\alpha-1},$$

for arbitrary A which we set to be one without loss of generality. Since this holds for any σ, we can avoid the term that is linear in w by choosing,

$$\sigma = \alpha^2 - 1, \tag{4.12}$$

so that $f(w) = w^{2\alpha-1}$. We will now focus the rest of this chapter on studying the unsaturated Gierer-Meinhardt model as an example using the general

explicit NLEP framework.

4.2 Explicit Stability Formulation for the Gierer-Meinhardt Model on a Stripe

In contrast to Chapter 2, we will now focus solely on the unsaturated version of the Gierer-Meinhardt model,

$$v_t = \epsilon^2 \Delta v - v + \frac{v^p}{u^q}, \tag{4.13a}$$

$$\tau u_t = \Delta u - u + \frac{v^o}{\epsilon u^s}, \tag{4.13b}$$

and for the time being consider a rectangular domain with homogeneous Neumann conditions on the boundary. The rectangular domain Ω is defined by

$$\Omega \equiv \{(x_1, x_2) | -l < x_1 < l, \quad 0 < x_2 < d\}$$

for some length l and width d. We have taken the diffusivity on (4.13b) to be unity since, as per the discussion in section 2.3.1, the diffusivity can be absorbed into the length scale. We want to use the explicitly solvable framework with $g(w) = w^\alpha$, $\alpha > 1$, and use the simplified condition on σ given by (4.12). The $f(w)$ in (4.3) is related to the exponent p in (4.13) and since we need the exponent set (p, q, o, s) to be integers, in order to use (4.12), we require p to be odd and specifically we take $p = 3$. Furthermore as we saw for the ring derivation in 3.1, $g(w) = w^\alpha$ is intimately tied to the exponent set o via $\alpha = o - 1$, and by choosing $p = 3$, this specifies that

$\alpha = 2$ and so we need $o = 3$. Therefore, by making our choice for p, we will consider the specific variant of (4.13) to be:

$$v_t = \epsilon^2 \Delta v - v + \frac{v^3}{u^q}, \tag{4.14a}$$

$$\tau u_t = \Delta u - u + \frac{v^3}{\epsilon u^s}, \tag{4.14b}$$

with $q > 0$ and $s \geq 0$. We consider the activator v localized on an $\mathcal{O}(\epsilon)$ region around the midpoint $x_1 = 0$ for all x_2 (hence the classification of a stripe) and define an inner coordinate variable $y = x/\epsilon$. The derivation of this stripe solution is very similar in approach to that of the ring in section 2.3.1 and was presented in entirety in [39]. We therefore omit the details here and summarize the results. The equilibrium activator denoted $v_e(x_1)$ and the equilibrium inhibitor denoted by $u_e(x_1)$ are given by

$$v_e(x_1) \sim U_0^{\gamma} w\left(\frac{x_1}{\epsilon}\right); \quad u_e(x_1) \sim U_0 \frac{G_l(x_1)}{G_l(0)}, \tag{4.15}$$

where $w(y) = \sqrt{2}\operatorname{sech} y$ is the unique homoclinic orbit solution that satisfies

$$\begin{aligned} &w'' - w + w^3 = 0, \quad -\infty < y < \infty; \\ &w \to 0 \text{ as } |y| \to \infty \quad , w(0) > 0, \quad w'(0) = 0. \end{aligned} \tag{4.16}$$

We define the constants U_0 and γ by

$$U_0^{\zeta} \equiv \frac{1}{\tilde{b} G_l(0)}; \quad \tilde{b} \equiv \int_{-\infty}^{\infty} w^3 \, \mathrm{d}y = \sqrt{2}\pi; \quad \zeta \equiv \frac{3q}{2} - (s+1) > 0; \quad \gamma \equiv \frac{q}{2}. \tag{4.17}$$

The Green's function $G_l(x_1)$ in (4.15) satisfies

$$G_{lx_1x_1} - G_l = -\delta(x_1), \quad |x_1| \leq l; \quad G_{lx_1}(\pm l) = 0,$$

with $\delta(\cdot)$ the Dirac measure. This has solution

$$G_l(x_1) = \frac{\cosh(l - |x_1|)}{2\sinh(l)}, \tag{4.18}$$

and therefore $G_l(0) = 1/2\coth(l)$.

We are now in a position to perform a linear stability analysis on this base state. Since, unlike the ring solution in 2.3.1, the stripe always starts in its equilibrium position, there are no long-time dynamics to consider and so we can make the appropriate usual formulation

$$v = v_e + \phi(x_1)\exp(imx_2 + \lambda t), \quad u = u_e + \eta(x_1)\exp(imx_2 + \lambda t); \quad m = \frac{k\pi}{d}, \tag{4.19}$$

where k is an integer. The restriction on m comes from the homogeneous Neumann conditions on $x_2 = 0$ and $x_2 = d$. These conditions also necessitate that we need to take the true solution as only the real part of (4.19). However, in what follows we treat m as a continuous variable and are just mindful that true unstable modes must satisfy the discrete condition. Alternatively one can think of the operator eigenvalue problem having continuous eigenvalues for which we only sample the discrete ones to capture the appropriate boundary conditions. Substituting (4.19) into (4.14), we obtain the

eigenvalue problem

$$\epsilon^2\phi_{x_1x_1} - \phi + \frac{3v_e^2}{u_e^q}\phi - \frac{qv_e^3}{u_e^{q+1}}\eta = (\lambda + \epsilon^2 m^2)\phi, \quad |x_1| \leq l; \quad \phi_{x_1}(\pm l) = 0, \tag{4.20a}$$

$$\eta_{x_1x_1} - (1 + \tau\lambda + m^2)\eta = -\frac{3ve^2}{\epsilon u_e^s}\phi + \frac{sv_e^3}{\epsilon u_e^{s+1}}\eta, \quad |x_1| \leq l; \quad \eta_{x_1}(\pm l) = 0. \tag{4.20b}$$

Once again, as in 3.2, we do not ignore the terms $\epsilon^2 m^2$ in the event that high frequency modes lead to instability behaviour. Like the base state, v_e, the activator perturbation ϕ will be entirely localized and so we take $\phi(x_1) \sim \Phi(\epsilon^{-1}x_1)$. The leading order problem for Φ from (4.20a) is

$$\begin{aligned}\Phi_{yy} - \Phi + 3w^2\Phi - qU_0^{q/2-1}w^3\eta(0) = (\lambda + \epsilon^2 m^2)\Phi, \quad -\infty < y < \infty,\\ \Phi \to 0 \text{ as } |y| \to \infty.\end{aligned} \tag{4.21}$$

Here $\eta(0)$ comes from the outer problem (4.20b) because it is not singularly perturbed. The simplification of (4.20b) involves using Dirac measures for terms of $\mathcal{O}(\epsilon^{-1})$ (see 2.2.1) and therefore,

$$\begin{aligned}\frac{3v_e^2}{\epsilon u_e^s}\phi =& 3U_0^{2\gamma-s}\int_{-\infty}^{\infty} w^2\Phi \,\mathrm{d}y\delta(x_1) = \frac{3U_0^{1-\gamma}}{\tilde{b}G_l(0)}\int_{-\infty}^{\infty} w^2\Phi \,\mathrm{d}y\delta(x_1),\\ \frac{sv_e^3}{\epsilon u_e^{s+1}}\eta =& sU_0^{\zeta}\eta(0)\int_{-\infty}^{\infty} w^3 \,\mathrm{d}y\delta(x_1) = \frac{s\eta(0)}{G_l(0)}\delta(x_1),\end{aligned}$$

where we have simplified using (4.17). Therefore, $\eta(x_1)$ satisfies

$$\eta_{x_1x_1} - \theta_\lambda^2 \eta = \left(\frac{s}{G_l(0)} \eta(0) - \frac{3U_0^{1-\gamma}}{\tilde{b} G_l(0)} \int_{-\infty}^{\infty} w^2 \Phi \, \mathrm{d}y \right) \delta(x_1),$$
$$|x_1| \leq l; \quad \eta_{x_1}(\pm l) = 0, \tag{4.22}$$

where $\theta_\lambda \equiv \sqrt{1 + m^2 + \tau\lambda}$ is the principal value of the square root. By this we mean the branch cut taken along the negative real axis such that $\mathrm{Re}(\lambda) \leq \frac{-1-m^2}{\tau}$ which implies $\eta(0)$ is analytic in $\mathrm{Re}(\lambda) \geq 0$. If we consider the Green's function problem

$$G_{\lambda x_1 x_1} - \theta_\lambda^2 G_\lambda = -\delta(x_1), \quad |x_1| \leq l, \quad G_{\lambda x_1}(\pm l) = 0,$$

which has solution,

$$G_\lambda(x_1) = \frac{\cosh(\theta_\lambda(l - |x_1|))}{2\theta_\lambda \sinh(\theta_\lambda l)} \tag{4.23}$$

then we can write

$$\eta(x_1) = \left(\frac{3U_0^{1-\gamma}}{\tilde{b} G_l(0)} \int_{-\infty}^{\infty} w^2 \Phi \, \mathrm{d}y - \frac{s}{G_l(0)} \eta(0) \right) G_\lambda(x_1).$$

Using (4.18) and (4.23) we can solve for $\eta(0)$ to yield that

$$\eta(0) = \frac{3U_0^{1-\gamma}}{\tilde{b}} \int_{-\infty}^{\infty} w^2 \Phi \, \mathrm{d}y \left[s + \frac{\theta_\lambda \tanh(\theta_\lambda l)}{\tanh(l)} \right]^{-1}. \tag{4.24}$$

This expression is non-zero as long as $\int_{-\infty}^{\infty} w^2 \Phi \, \mathrm{d}y \neq 0$ which as per the discussion in section 4.1 holds for any unstable eigenvalue $\mathrm{Re}(\lambda) > 0$. This

means that Φ is even and as with section 3.2, this corresponds to breakup or amplitude instabilities. We substitute (4.24) into (4.21) to get our NLEP for breakup instabilities of the stripe as

$$L_0\Phi - \chi w^3 \int_{-\infty}^{\infty} w^2\Phi \,\mathrm{d}y = (\lambda + \epsilon^2 m^2)\Phi, \quad -\infty < y < \infty;$$

$$\Phi \to 0 \text{ as } |y| \to \infty, \tag{4.25a}$$

$$\chi \equiv \frac{3q}{\tilde{b}}\left[s + \frac{\theta_\lambda \tanh(\theta_\lambda l)}{\tanh(l)}\right]^{-1}, \tag{4.25b}$$

with L_0 defined by (4.2). In terms of the explicit formulation discussed in section 4.1, by choosing $p = o = 3$ in (4.14), we prescribed $\alpha = 2$ ($g(w) = w^2$) and $\sigma = 3$ so that

$$L_0 w^2 = 3w^2.$$

By comparing (4.25a) to (4.7) we take

$$\lambda = \lambda + \epsilon^2 m^2, \quad h(w) = w^3$$

to get that (4.25a) becomes

$$\lambda = 3 - \epsilon^2 m^2 - \frac{9q}{2}\left[s + \frac{\theta_\lambda \tanh(\theta_\lambda l)}{\tanh(l)}\right]^{-1}, \tag{4.26}$$

where we have simplified that

$$\frac{\int_{-\infty}^{\infty} w^5 \,\mathrm{d}y}{\tilde{b}} = \frac{3}{2}.$$

We will now analyze (4.26) for $\tau = 0$ and $\tau > 0$.

4.2.1 Explicit Stripe Eigenvalues, $\tau = 0$

When $\tau = 0$, we have that (4.26) becomes

$$\lambda = 3 - \epsilon^2 m^2 - \frac{9q}{2}\left[s + \frac{\sqrt{1+m^2}\tanh(\sqrt{1+m^2}l)}{\tanh(l)}\right]^{-1}. \tag{4.27}$$

We begin by finding neutral stability points $\lambda = 0$. If m is $\mathcal{O}(1)$ then to leading order the neutral stability point (4.27) becomes

$$0 = 3 - \frac{9q}{2}\left[\frac{3q}{2} + \kappa(z)\right]^{-1},$$

where

$$z = \sqrt{m^2+1}, \quad z \geq 1; \qquad \kappa(z) = \frac{z\tanh(zl)}{\tanh(l)} - (\zeta + 1),$$

with ζ from (4.17). This expression simplifies so that the neutral stability point is a root of $\kappa(z)$. Now $\kappa(1) = -\zeta < 0$ and $\kappa(z) \to \infty$ as $z \to \infty$ so there is at least one root to $\kappa(z)$. Furthermore,

$$\kappa'(z) = \frac{\tanh(zl)}{\tanh(l)} + zl\frac{\operatorname{sech}^2(zl)}{\tanh(l)} > 0$$

and so there is a unique root $z_- > 1$ to $\kappa(z)$ and hence a unique neutral stability mode

$$m_{b^-} = \sqrt{z_-^2 - 1}. \tag{4.28}$$

If $z < z_-$ then $\lambda < 0$ and so there are no unstable eigenvalues on $0 < m < m_{b^-}$, and conversely, $\lambda > 0$ is $z > z_-$. If we now consider $m = \mathcal{O}(\epsilon)$ and define $m = \epsilon^{-1}\tilde{m}$ then (4.27) becomes

$$\lambda = 3 - \tilde{m}^2 - \frac{\epsilon 9q}{2}\left[\epsilon s + \frac{\sqrt{\tilde{m}^2+\epsilon^2}\tanh(\sqrt{\tilde{m}^2+\epsilon^2}l\epsilon^{-1})}{\tanh(l)}\right]^{-1}. \tag{4.29}$$

If we search for the neutral stability point $\tilde{m}_b^+$ and expand $\tilde{m}_b^{+2} \sim \tilde{m}_0^2 + \epsilon\tilde{m}_1^2$ then we get $\tilde{m}_0 = \sqrt{3}$ and for $\tilde{m}_1$ we have

$$\tilde{m}_1^2 = -\frac{9q}{2}\frac{\tanh(l)}{\tilde{m}_0},$$

and so the upper neutral stability point is

$$m_{b^+} \sim \frac{1}{\epsilon}\sqrt{\tilde{m}_0^2 + \epsilon\tilde{m}_1^2} = \frac{\sqrt{3}}{\epsilon} - \frac{3q}{4}\tanh(l). \tag{4.30}$$

If $m > m_{b^+}$ ($m < m_{b^+}$) then $\lambda < 0$ ($\lambda > 0$) and therefore unstable eigenvalues exist on $m_{b^-} < m < m_{b^+}$. Next we seek to estimate the dominant wave mode m_{dom} where λ achieves its maximum. When m is an $\mathcal{O}(1)$ or $\mathcal{O}(\epsilon^{-1})$ number we have that to leading order λ is monotonic and therefore the dominant mode must occur at some intermediate scaling in ϵ. Therefore we let,

$$m = \epsilon^{-a}\hat{m}, \quad 0 < a < 1,$$

and substitute into (4.27),

$$\lambda = 3 - \epsilon^{2-2a}\hat{m}^2 - \frac{\epsilon^a 9q}{2}\left[\epsilon^a s + \frac{\sqrt{\hat{m}^2+\epsilon^{2a}}\tanh(\sqrt{\hat{m}^2+\epsilon^{2a}}\epsilon^{-a}l)}{\tanh(l)}\right]^{-1}. \tag{4.31}$$

The only hope for non-monotonic λ is if there is balance in the second and third term and so we take $a = 2/3$. Differentiating (4.31) with respect to $\hat{m}$ and setting to zero we get

$$\begin{aligned}\frac{\mathrm{d}\lambda}{\mathrm{d}\hat{m}} =& -2\hat{m} + \frac{9q}{2\tanh(l)}\left[\epsilon^{2/3}s + \frac{\sqrt{\hat{m}^2+\epsilon^{4/3}}\tanh(\sqrt{\hat{m}^2+\epsilon^{4/3}}\epsilon^{-2/3}l)}{\tanh(l)}\right]^{-2} \\ & \left(\frac{\hat{m}\tanh(\sqrt{\hat{m}^2+\epsilon^{4/3}}\epsilon^{-2/3}l)}{\sqrt{\hat{m}^2+\epsilon^{4/3}}} + \epsilon^{-2/3}l\hat{m}\,\mathrm{sech}^2(\sqrt{\hat{m}^2+\epsilon^{4/3}}\epsilon^{-2/3}l)\right) \\ =& \,0. \end{aligned} \tag{4.32}$$

Substituting $\hat{m} = \hat{m}_0 + \epsilon^{2/3}\hat{m}_1$ where the $\hat{m}_1$ correction comes from s introducing terms of $\mathcal{O}(\epsilon^{2/3})$, we get that to leading order

$$-2\hat{m}_0 + \frac{9q\tanh(l)}{2\hat{m}_0^2} = 0,$$

and so

$$\hat{m}_0 = \left(\frac{9q\tanh(l)}{4}\right)^{1/3}. \tag{4.33}$$

For the $\hat{m}_1$ problem, both $\tanh(\epsilon^{-2/3})$ and $\operatorname{sech}(\epsilon^{-2/3})$ terms will remain their saturated values up to exponential order in ϵ and therefore

$$-2\hat{m}_1 - \frac{9q\tanh(l)\hat{m}_1}{\hat{m}_0} - \frac{9q\tanh(l)^2 s}{\hat{m}_0^3} \approx 0,$$

and using (4.33),

$$\hat{m}_1 \approx -\frac{2}{3}s\tanh(l).$$

Combining everything, we have,

$$m_{\text{dom}} \sim \epsilon^{-2/3}\left(\frac{9\tanh(l)}{4q}\right)^{1/3} - \frac{2s\tanh(l)}{3}. \tag{4.34}$$

If one were to consider the effect of the walls negligible (taking $l \to \infty$) then (4.27) becomes

$$\lambda = 3 - \epsilon^2 m^2 - \frac{9q}{2(s+\sqrt{1+m^2})},$$

and we have that

$$m_{b^-} = \sqrt{\zeta^2 + 2\zeta}, \tag{4.35a}$$

$$m_{b^+} = \sqrt{3}/\epsilon - 3q/4, \tag{4.35b}$$

$$m_{\text{dom}} = \epsilon^{-2/3}(9q/4)^{1/3} - 2s/3. \tag{4.35c}$$

This limit will allows us to obtain more tractable analytical results when we consider $\tau > 0$.

We now plot (4.27) in Figure 4.1 with $\epsilon = 0.05$, and $s = 0$ for $q = 1$ and $q = 2$. In each case we plot $l = 0.5$, $l = 1$, and $l = \infty$. In Table 4.1 we list

the numeric evaluation (denoted n) of m_{b^-}, m_{b^+} and m_{dom} along with the asymptotic approximations (denoted a) given by (4.28) for m_{b^-}, (4.30) for m_{b^+}, and (4.34) for m_{dom}. The agreement for both $q = 1$ and $q = 2$ for all values of l agrees favourably with the analytic results.

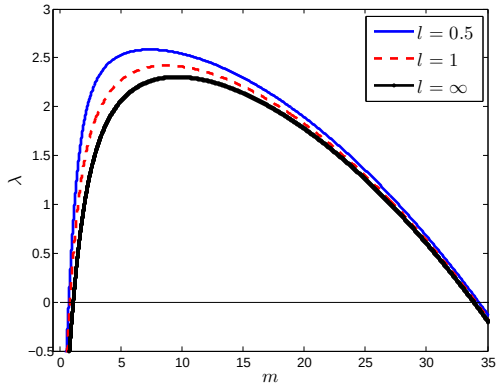

(a) $q = 1$

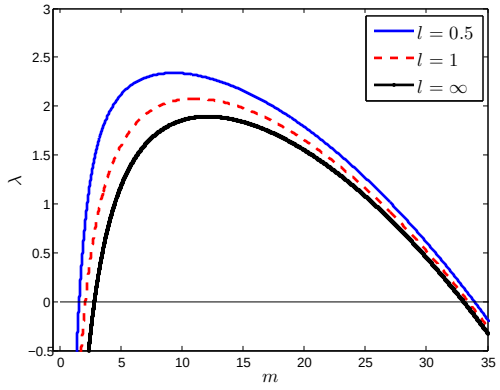

(b) $q = 2$

Figure 4.1: Eigenvalues for $\tau = 0$ computed from (4.27) versus m for $\epsilon = 0.05$, and $s = 0$ for several values of l. The curves from highest maximum to smallest maximum are $l = 0$, $l = 0.5$, and $l = \infty$ respectively.

$q = 1$						
l	$m_{b^-}(n)$	$m_{b^-}(a)$	$m_{b^+}(n)$	$m_{b^+}(a)$	$m_{\text{dom}}(n)$	$m_{\text{dom}}(a)$
0.5	0.75	0.75	34.29	34.29	7.42	7.46
1	0.86	0.86	34.06	34.07	8.76	8.82
∞	1.12	1.12	33.87	33.89	9.60	9.65
$q = 2$						
l	$m_{b^-}(n)$	$m_{b^-}(a)$	$m_{b^+}(n)$	$m_{b^+}(a)$	$m_{\text{dom}}(n)$	$m_{\text{dom}}(a)$
0.5	1.60	1.60	33.93	33.95	9.36	9.40
1	2.11	2.10	33.44	33.50	11.07	11.11
∞	2.85	2.83	33.03	33.14	12.13	12.16

Table 4.1: Asymptotic and numerical comparison of the neutral stability points m_{b^-}, m_{b^+}, and the dominant wave mode m_{dom}. The numerical values (n) are obtained from Figure 4.1 and the asymptotic approximations (a) are obtained from (4.28) for m_{b^-}, (4.30) for m_{b^+}, and (4.34) for m_{dom}

Predicting m_{dom} allows us to approximate the number of spots N_{spots} that would occur in a breakup pattern where

$$N_{\text{spots}} = \left\lfloor \frac{m_{\text{dom}} d}{2\pi} \right\rfloor$$

where $\lfloor \cdot \rfloor$ is the floor function, rounding down to the nearest integer and d is the rectangle width.

4.2.2 Explicit Stripe Eigenvalues, $\tau > 0$

We now consider (4.26) for $\tau > 0$, which becomes a transcendental equation for λ because of the presence of θ_λ. For simplicity, we consider the scenario discussed in section 4.2.1 where the sidewalls have no effect ($l = \infty$). In this

case (4.26) becomes

$$\lambda = 3 - \epsilon^2 m^2 - \frac{9q}{2(s + \sqrt{1+m^2}\sqrt{1+\hat{\tau}\lambda})}, \qquad \hat{\tau} \equiv \frac{\tau}{1+m^2}. \tag{4.36}$$

While we can make little progress analytically on prescribing values for the roots, we would like to understand the qualitative features of the roots as well as how many exist. Therefore, we attempt to isolate λ separately from (4.36) and write,

$$\lambda - 3 + \epsilon^2 m^2 = -\frac{9q}{\sqrt{1+m^2}} \left[\frac{2s}{\sqrt{1+m^2}} + 2\sqrt{1+\hat{\tau}\lambda} \right]^{-1}.$$

If we define

$$d_0 = -\frac{2s}{\sqrt{1+m^2}} \leq 0, \tag{4.37a}$$

$$d_1 = -\frac{9q}{\sqrt{1+m^2}} < 0, \tag{4.37b}$$

$$\beta \equiv 3 - \epsilon^2 m^2, \tag{4.37c}$$

then we can write (4.36) as a root finding problem

$$\mathcal{F}(\lambda) = 2\sqrt{1+\hat{\tau}\lambda} - \mathcal{G}(\lambda), \qquad \mathcal{G}(\lambda) \equiv d_0 - \frac{d_1}{\beta - \lambda}. \tag{4.38}$$

We will look for the roots to (4.38) that satisfy $\mathrm{Re}(\lambda) > 0$ by using the argument principle around the same closed contour $\Gamma = \Gamma_I \cup \Gamma_K$ from section

3.2.6 with

$$\Gamma_K : \left\{\lambda = K\exp(it) | t \in \left[-\frac{\pi}{2}, \frac{\pi}{2}\right]\right\} \quad \Gamma_I : -Ki \leq \lambda \leq Ki$$

which we traverse counter-clockwise and take the limit as K tends to infinity. When $\tau \gg 1$, $\mathcal{F}(\lambda) \sim 2\sqrt{\hat{\tau}\lambda}$ and so on Γ_K when $t = -\pi/2$, $\arg\mathcal{F} = -\pi/4$ and when $t = \pi/2$, $\arg\mathcal{F} = \pi/4$. Therefore, the change in argument of $\mathcal{F}(\lambda)$ over Γ_K is $\pi/2$. When $\beta < 0$ ($m > \sqrt{3}/\epsilon$) then for all $\mathrm{Re}(\lambda) > 0$, $\mathcal{G}(\lambda)$ is analytic but when $\beta > 0$ ($0 < m < \sqrt{3}/\epsilon$) then there is a simple pole at $\lambda = \beta$. Finally, since $\mathcal{F}$ is analytic (aside from $\lambda = \beta$) and real valued when λ is real-valued then $\overline{\mathcal{F}(\lambda)} = \mathcal{F}(\bar{\lambda})$. Combining all of this together with the argument principle in a way similar to section 3.2.6, we have that the number of roots J to $\mathcal{F}(\lambda)$ are given by

$$J = \frac{1}{4} + h(\beta) + \frac{1}{\pi}[\arg\mathcal{F}]_{\Gamma_I^+}, \qquad \text{where} \quad h(\beta) = \begin{cases} 1, & \beta > 0, \\ 0, & \beta < 0 \end{cases}, \tag{4.39}$$

and Γ_I^+ is the positive imaginary axis $i\lambda_I$ with $0 < \lambda_I < \infty$ traversed downwards and $[\arg\mathcal{F}]$ indicates the change in argument of $\mathcal{F}$ over the contour. When $\lambda = i\lambda_I$, $\lambda_I > 0$ we have

$$\mathcal{G}(i\lambda_I) = d_0 - \frac{\beta d_1}{\beta^2 + \lambda_I^2} - i\frac{\lambda_I d_1}{\beta^2 + \lambda_I^2}$$

and

$$2\sqrt{1 + i\hat{\tau}\lambda_I} = 2(1 + \hat{\tau}^2\lambda_I^2)^{1/4}\exp\left(i\frac{\arctan(\hat{\tau}\lambda_I)}{2}\right).$$

Using the trig identities

$$\cos^2\theta = \frac{1+\cos\theta}{2}, \qquad \sin^2\theta = \frac{1-\cos\theta}{2},$$

we can write

$$2\sqrt{1+i\hat{\tau}\lambda_I} = \mathcal{K}_+(\hat{\tau}\lambda_I) + i\mathcal{K}_-(\hat{\tau}\lambda_I), \qquad \mathcal{K}_\pm(z) = \sqrt{2}\left(\sqrt{1+z^2}\pm 1\right)^{1/2},$$

and therefore we can decompose $\mathcal{F}(i\lambda_I) = \mathcal{F}_R(\lambda_I) + i\mathcal{F}_I(\lambda_I)$ with

$$\mathcal{F}_R(\lambda_I) \equiv \mathcal{K}_+(\hat{\tau}\lambda_I) - d_0 + \frac{\beta d_1}{\beta^2+\lambda_I^2}, \qquad \mathcal{F}_I(\lambda_I) \equiv \mathcal{K}_-(\hat{\tau}\lambda_I) + \frac{\lambda_I d_1}{\beta^2+\lambda_I^2}. \tag{4.40}$$

For $\lambda_I \gg 1$ then since $\tau > 0$, $\mathcal{F}_R \sim \mathcal{F}_I \sim \sqrt{2\hat{\tau}\lambda_I}$ and therefore $\arg(\mathcal{F}(i\lambda_I)) \to \pi/4$ as $\lambda_I \to \infty$. At $\lambda_I = 0$, we have that $\mathcal{F}_R(0) = 2 - \mathcal{G}(0)$ and $\mathcal{F}_I(0) = 0$, so when $\lambda = 0$ is a root of $\mathcal{F}(\lambda) = 0$ which occurs at m_{b^-} and m_{b^+} defined by (4.35a) and (4.35b) respectively then $\mathcal{G}(0) = 2$. When m is $\mathcal{O}(1)$,

$$\mathcal{G}(0) = \frac{\zeta+1}{2\sqrt{1+m^2}}$$

and so $\mathrm{d}\mathcal{G}(0)/\mathrm{d}m < 0$. When m is $\mathcal{O}(\epsilon^{-1})$ then

$$\left.\frac{\mathrm{d}G(0)}{\mathrm{d}m}\right|_{m=m_{b^+}} = -\frac{2m_{b^+}}{\sqrt{1+{m_{b^+}}^2}} + \frac{18q\epsilon^2 m_{b^+}}{\sqrt{1+{m_{b^+}}^2}(3-\epsilon^2{m_{b^+}}^2)} \sim \frac{8}{3q} > 0.$$

Finally, if $m > \sqrt{3}/\epsilon$, $G(0) < 0$. Combining everything together we have that

$$\mathcal{G}(0) < 2, \qquad m_{b^-} < m < m_{b^+} \cup m > \frac{\sqrt{3}}{\epsilon} \tag{4.41a}$$

$$\mathcal{G}(0) > 2, \qquad 0 < m < m_{b^-} \cup m_{b^+} < m < \frac{\sqrt{3}}{\epsilon}. \tag{4.41b}$$

We are now in a position to classify the roots J to $\mathcal{F}(\lambda)$. If $m > \sqrt{3}/\epsilon$ then $\beta < 0$ and since $d_0 \leq 0$ and $d_1 < 0$ then by (4.40), $\mathcal{F}_R(\lambda_I) > 0$ for all λ_I. Furthermore $\mathcal{F}_R(0) > 0$ and so the argument along Γ_I^+ changes from $\pi/4$ to 0. Since $\mathcal{F}_R(\lambda_I) > 0$ always then it cannot enter the negative real plane so we must have $[\arg(\mathcal{F})]_{\Gamma_I^+} = -\pi/4$. From (4.39) this means that $J = 0$ on this region. Next consider $m_{b^+} < m < \sqrt{3}/\epsilon$. On this interval $\beta > 0$ and from (4.41), $\mathcal{F}_R(0) < 0$ so the argument changes from $\pi/4$ to π. We can calculate that

$$\frac{\mathrm{d}\mathcal{F}_R}{\mathrm{d}\lambda_I} = \hat{\tau}\mathcal{K}'(\hat{\tau}\lambda_I) - \frac{2\lambda_I\beta d_1}{(\beta^2 + \lambda_I^2)^2}, \tag{4.42}$$

which for $m_{b^+} < m < \sqrt{3}/\epsilon$ is positive and therefore since $\mathcal{F}_R(\lambda_I) \to \infty$ as $\lambda_I \to \infty$ then there is a unique root λ_I^* to $\mathcal{F}_R$. We can find this root asymptotically by letting $m = \sqrt{3}/\epsilon + m_1$ with $-3q/4 < m_1 < 0$ and therefore $\beta = 3 - \epsilon^2 m^2 \sim -2\sqrt{3}m_1\epsilon$. Substituting into (4.40) we get that to leading order $\mathcal{F}_R(\lambda_I^*) = \mathcal{K}_+(\hat{\tau}\lambda_I^*) = 0$ for which there is no solution. Therefore we let $\lambda_I^* = \epsilon\lambda_{I0}^*$ and repeat the asymptotic expansion in (4.40) to get that to leading order,

$$2 + \frac{18qm_1}{12m_1^2 + \lambda_{I0}^{*2}} = 0,$$

and so we get $\lambda_{I0}^* = \sqrt{-3m_1(4m_1+3q)}$ which exists for all m_1 since $m_1 > -3q/4$. Using this root in $\mathcal{F}_I$ from (4.40) we have that,

$$\mathcal{F}_I(\epsilon\lambda_{I0}^*) = \mathcal{K}_-(\epsilon\hat{\tau}\lambda_{I0}^*) + \frac{\epsilon d_1 \lambda_{I0}^*}{\beta^2 + \epsilon^2 \lambda_{I0}^{*2}} \sim -\frac{9q\lambda_{I0}^*}{\sqrt{3}(12m_1^2 + \lambda_{I0}^2)} < 0.$$

Since $\mathcal{F}_I(\lambda_I^*) < 0$ then $[\arg \mathcal{F}]_{\Gamma_I^+} = -5\pi/4$ and from (4.39), $J = 0$. Next we consider $m_{b^-} < m < m_{b^+}$ where from (4.41), $\mathcal{F}_R(0) > 0$ and since $\beta > 0$ and $d_1 < 0$ then by (4.42), $\mathrm{d}\mathcal{F}_R/\mathrm{d}\lambda_I > 0$. Therefore $[\arg \mathcal{F}]_{\Gamma_I^+} = -\pi/4$ and from (4.39) $J = 1$. This root is actually on the positive real axis and satisfies $0 < \lambda < \beta$. To see this we consider (4.38) with $0 < \mathcal{F}(0) < 2$ and $\mathcal{F} \to -\infty$ as $\lambda \to \beta$ and therefore $\mathcal{F}$ has at least one root on $0 < \lambda < \beta$. If $\lambda > \beta$ then $\mathcal{G}(\lambda) < 0$ and $\mathcal{F} > 0$ for all λ. We have that $\sqrt{1+\tau\lambda}$ is an increasing concave function as well as $\mathcal{G}'(\lambda) > 0$ and $\mathcal{G}''(\lambda) > 0$ so that $\mathcal{F}''(\lambda) < 0$. Therefore $\mathcal{F}(\lambda)$ can have at most one critical point and regardless of the sign of $\mathcal{F}'(0)$, this can only be satisfied if $\mathcal{F}$ has exactly one root. Therefore there is exactly one real root on $m_{b^-} < m < m_{b^+}$. Finally we consider $0 < m < m_{b^-}$, where $\mathcal{F}_R(0) < 0$ and so the argument goes from $\pi/4$ to π. Once again $\mathrm{d}\mathcal{F}_R/\mathrm{d}\lambda_I > 0$ and $\mathcal{F}_R \to \infty$ as $\lambda_I \to \infty$ so there is exactly one root to $\mathcal{F}_R$ on this interval. Therefore either $[\arg \mathcal{F}]_{\Gamma_I^+} = -5\pi/4$ and $J = 0$ or $[\arg \mathcal{F}]_{\Gamma_I^+} = 3\pi/4$ and $J = 2$. If $\hat{\tau} = 0$ then from (4.38), $\mathcal{F}(0) < 0$ and $\mathcal{F}'(\lambda) = -\mathcal{G}'(\lambda) < 0$ so there are no roots with positive real part. This should continue to be true for $\hat{\tau} \ll 1$ and therefore $J = 0$ for $\hat{\tau} \ll 1$ on $0 < m < m_{b^-}$. If $\hat{\tau} \gg 1$ then $\mathcal{F}(0) < 0$ and $\mathcal{F} \to -\infty$ as $\lambda \to \beta^-$ but for $\lambda \gg \mathcal{O}(\hat{\tau}^{-1})$, $\mathcal{F} \approx 2\sqrt{\hat{\tau}\lambda} \gg 1$ and since $\mathcal{F}''(\lambda) < 0$ there are exactly two roots with real positive part for $\hat{\tau} \gg 1$. Notice that eigenvalues cannot enter the real plane through $\lambda = 0$

since $\lambda = 0$ is an eigenvalue for all $\hat{\tau}$ and therefore this shows that there must exist a Hopf bifurcation at some $\hat{\tau} = \hat{\tau_m^H}$ when $0 < m < m_{b^-}$. We summarize the eigenvalue conclusions as follows:

Principal Result 4.2.2.1 *Let J denote the number of roots in $Re(\lambda) > 0$ of $\mathcal{F}(\lambda) = 0$ in (4.38). Then, for any $\hat{\tau} > 0$,*

$$\begin{aligned} J =& 0, \qquad m > m_{b^+} \\ J =& 1, \qquad m_{b^-} < m < m_{b^+} \\ J =& 0 \text{ or } J = 2, \qquad 0 < m < m_{b^-}. \end{aligned}$$

On $m_{b^-} < m < m_{b^+}$ the root is on the positive real axis in the interval $0 < \lambda < \beta$ and for $0 < m < m_{b^-}$, there are no roots with positive real part for $\hat{\tau} \ll 1$ and two roots with positive real part when $\tau \gg 1$. This last condition proves the existence of a Hopf bifurcation at some $\hat{\tau} = \hat{\tau_m^H}$.

Explicit Representation for Hopf Bifurcation

We now turn our attention to evaluating $\hat{\tau} = \hat{\tau_m^H}$ and showing it is unique. If a Hopf bifurcation occurs then $i\lambda_I$ is a root to (4.38) and so from (4.40) we need to set $\mathcal{F}_R = \mathcal{F}_I = 0$. If we do this we get

$$\sqrt{2}(\sqrt{a}+1)^{1/2} = d_0 - \frac{d_1\beta}{\theta}, \qquad \sqrt{2}(\sqrt{a}-1)^{1/2} = -\frac{d_1\lambda_I}{\theta};$$
$$a \equiv 1 + \hat{\tau}^2\lambda_I^2, \quad \theta \equiv \beta^2 + \lambda_I^2. \tag{4.43}$$

By dividing these expressions we get

$$\frac{(\sqrt{a}+1)^{1/2}}{(\sqrt{a}-1)^{1/2}} = -\frac{d_0\theta}{d_1\lambda_I} + \frac{\beta}{\lambda_I},$$

which we can simplify to get

$$\frac{\sqrt{a}+1}{\sqrt{a-1}} = \frac{1}{\lambda_I}A, \qquad A = \beta - \frac{d_0\theta}{d_1}. \tag{4.44}$$

Using $\sqrt{a-1} = \hat{\tau}\lambda_I$ and the first expression in (4.43) we have,

$$\hat{\tau} = \frac{d_1^2}{2\theta^2}A. \tag{4.45}$$

Next we determine an equation for θ. To do this we square and subtract the first two expressions of (4.43),

$$2\sqrt{a} + 2 - 2\sqrt{a} + 2 = 4 = \left(d_0 - \frac{d_1\beta^2}{\theta}\right)^2 - \frac{d_1^2\lambda_I^2}{\theta^2}. \tag{4.46}$$

We can use that $\lambda_I^2 = \theta - \beta^2$ in (4.46) to get that θ is the root to the quadratic equation $M(\theta)$ given by

$$M(\theta) = (d_0^2 - 4)\theta^2 - (2\beta d_0 d_1 + d_1^2)\theta + 2d_1^2\beta^2 = 0. \tag{4.47}$$

In order for a solution $\lambda_I = \sqrt{\theta - \beta^2}$ to exist we require $\theta > \beta^2$. A Hopf bifurcation only occurs on $0 < m < m_{b^-}$ and we will only consider this interval for $M(\theta)$. First we notice that,

$$M(\beta^2) = \beta^4\left(d_0^2 - \frac{2d_0d_1}{\beta} + \frac{d_1^2}{\beta^2} - 4\right) = \beta^4(\mathcal{G}(0)^2 - 4) > 0,$$

since by (4.41), $\mathcal{G}(0) > 2$ on this interval. If $d_0 = -2$ then the roots degenerate and we get

$$\theta_1 = \frac{2\beta^2 d_1}{d_1 - 4\beta} \tag{4.48}$$

as the unique root to (4.47). At this root we have from (4.44) that

$$A = \beta + \frac{4\beta^2}{d_1 - 4\beta} = \frac{\beta d_1}{d_1 - 4\beta} > 0$$

since $d_1 < 0$ and therefore in this case there is a unique $\hat{\tau} = \hat{\tau_m^H} > 0$ and unique Hopf-bifurcation eigenvalue $\sqrt{\theta_1 - \beta^2}$. We next consider the two remaining cases $-2 < d_0 < 0$ and $d_0 < -2$. If $-2 < d_0 < 0$ then $M(\theta)$ from (4.47) tends to negative infinity as $\theta \to \pm\infty$ and therefore since $M(\beta^2) > 0$, by the intermediate value theorem, there are two roots to (4.47), one root θ_{2-} in $\beta^2 < \theta_{2-} < \infty$ and another root θ_{2+} in $-\infty < \theta_{2+} < \beta^2$. Only θ_{2-} given by

$$\theta_{2-} = \frac{2\beta d_0 d_1 + d_1^2}{2(d_0^2 - 4)} + \frac{\sqrt{(2\beta d_0 d_1 + d_1^2)^2 - 8d_1^2\beta^2(d_0^2 - 4)}}{2(4 - d_0^2)}, \tag{4.49}$$

is a valid solution to $M(\theta)$ that satisfies $\theta > \beta^2$ and so we discount the second root. We now need to make sure that for this root, $A > 0$ so that $\hat{\tau_m^H} = \hat{\tau} > 0$. First, define $\theta_c = d_1\beta/d_0$ as the unique root to (4.44) when $A = 0$. Since $d_0 < 0$ and $d_1 < 0$ then $\mathrm{d}A/\mathrm{d}\theta < 0$ and so all we need to show to have $A > 0$ when $\theta = \theta_{2-}$ is that $\theta_{2-} < \theta_c$. If we evaluate $M(\theta_c)$ we get

$$M(\theta_c) = \frac{d_1^2\beta^2}{d_0}\left(d_0 - \frac{d_1}{\beta}\right) - \frac{4d_1^2\beta^2}{d_0^2} = \frac{d_1^2\beta^2}{d_0}\left(\mathcal{G}(0) - \frac{4}{d_0}\right) < 0, \tag{4.50}$$

since $\mathcal{G}(0) > 2$. This inequality on $\mathcal{G}$ also implies that

$$\frac{d_1}{d_0} > \beta\left(1 - \frac{2}{d_0}\right) > \beta$$

and therefore that $\theta_c > \beta^2$. This means that $\theta_c \in (\beta^2, \infty)$ and since θ_{2-} is the unique root to $M(\theta)$ in this interval then $M(\theta_c) < 0$ implies $\theta_{2-} < \theta_c$ and therefore $A > 0$ and $\hat{\tau_m^H} > 0$ when $\theta = \theta_{2-}$. Finally we consider the interval $d_0 < -2$. On this interval we still have $M(\beta^2) > 0$ but now $M(\theta) \to +\infty$ as $\theta \to \pm\infty$. We still have from (4.50) that $M(\theta_c) < 0$ and so for $d_0 < -2$ both roots to $M(\theta)$, $\theta_{3\pm}$ exist on $\theta \in (\beta^2, \infty)$. In order to satisfy $A > 0$ we take the smaller root $\theta_{3-} < \theta_c$ also given by (4.49) which leads to the unique Hopf bifurcation $\hat{\tau} = \hat{\tau_m^H} > 0$.

We now briefly consider the case when $s = 0$ and $d_0 = 0$ identically. In this scenario, the roots to (4.47) simplify to

$$\theta_0 = c_0 + \sqrt{c_1}; \qquad c_0 = -\frac{d_1^2}{8}, \quad c_1 = \frac{d_1^4}{64} + \frac{d_1^2\beta^2}{2}.$$

We also have that when $d_0 = 0$ that $A = \beta$ and so we can write

$$\hat{\tau} = \frac{d_1^2\beta}{2}\left(\frac{1}{c_0 + \sqrt{c_1}}\right)^2 = \frac{d_1^2\beta}{2}\frac{c_0^2 - 2c_0\sqrt{c_1} + c_1}{(c_0^2 - c_1)^2}.$$

We can compute that,

$$(c_0^2 - c_1)^2 = \frac{d_1^4\beta^4}{4},$$

and so

$$\begin{aligned}\hat{\tau} =& \frac{d_1^2}{16\beta^3} + \frac{1}{2\beta^3}\sqrt{\frac{d_1^4}{64} + \frac{d_1^2\beta^2}{2}} + \frac{1}{\beta} \\ =& \frac{1}{\beta}\left(1 + \frac{c^2}{2} + c\sqrt{1 + \frac{c^2}{4}}\right), \qquad c = \frac{d_1}{\sqrt{8}\beta} = -\frac{9q}{2\sqrt{2(1+m^2)}(3-\epsilon^2 m^2)}.\end{aligned} \tag{4.51}$$

We now summarize the results for the Hopf bifurcation.

Principal Result 4.2.2.2 *For $0 < m < m_{b^-}$, there exists a unique value $\tau_m^H = (1+m^2)\hat{\tau_m^H} > 0$ for which $\lambda = \lambda_I$ is a root of $\mathcal{F}(i\lambda_I)$ given by (4.38). The Hopf bifurcation point $\hat{\tau_m^H}$ and λ_{IH} are given by*

$$\hat{\tau_m^H} = \frac{d_1^2}{2\theta^2}A, \quad \lambda_{IH} = \sqrt{\theta - \beta^2}, \quad A \equiv \beta - \frac{d_0\theta}{d_1}. \tag{4.52}$$

Here, $\theta > \beta^2$ is the smallest root of (4.47) given by (4.48) if $d_0 = -2$ and (4.49) if $d_0 \neq -2$. When $s = 0$ we can explicitly compute $\hat{\tau_m^H}$ via (4.51).

As with $\tau = 0$, we plot the eigenvalues of largest real part for $\tau \neq 0$ in Figure 4.2 for $l = \infty$, $\epsilon = 0.05$, $\tau = 2$, and $s = 0$ for $q = 1$ and $q = 2$. Comparing Figure 4.2 to Figure 4.1, we have that for $m \gg 1$ the curves have similar behaviour when $\tau = 0$ and $\tau \neq 0$. This is because $\theta_\lambda = \sqrt{1 + m^2 + \tau\lambda} \approx \sqrt{1+m^2}$ for $m \gg 1$ and $\tau = \mathcal{O}(1)$ like in the case $\tau = 2$ chosen here. Therefore changing τ should only have a noticeable affect near the lower threshold $m = m_{b^-}$ given by (4.35a).

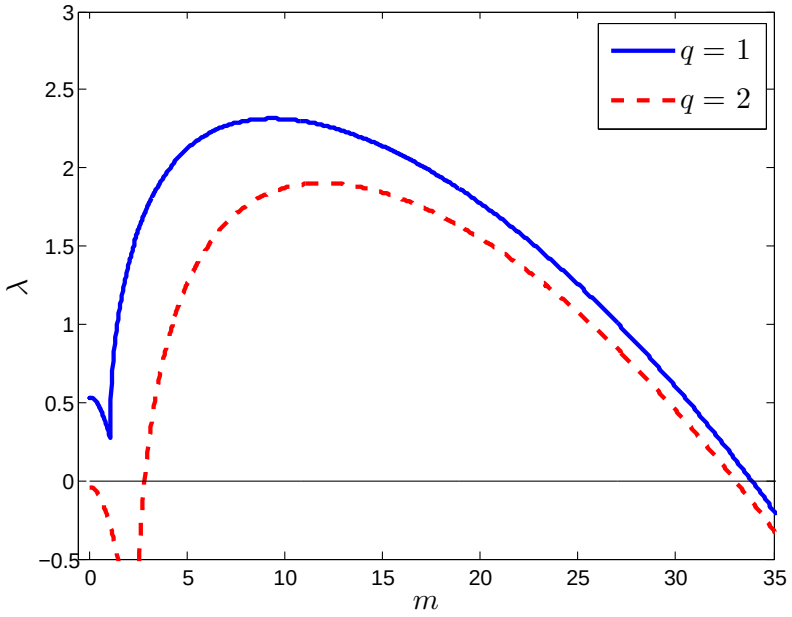

Figure 4.2: Plot of λ versus m for $q = 1$ (solid curve) and $q = 2$ (dashed curve). The parameters here are $s = 0$, $l = \infty$, and $\tau = 2$.

For $q = 2$ in Figure 4.2 we have that $\lambda \to 0$ as $m \to m_{b^-}$ but this is not so for $q = 1$. We can understand this behaviour if we plot τ_m^H and λ_{IH} from (4.52) which is in Figure 4.3.

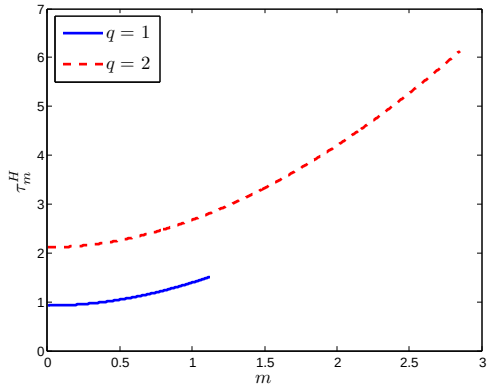

(a)

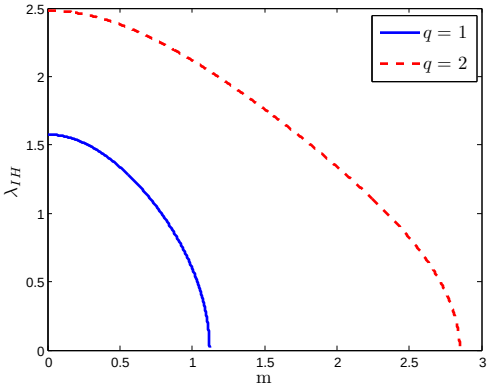

(b)

Figure 4.3: Plot of τ_m^H and λ_{IH} from (4.52) for m in $0 < m < m_{b^-}$ and $l = \infty$. The parameter values are $s = 0$ and $\epsilon = 0.05$ while the solid and dashed curves are for $q = 1$ and $q = 2$ respectively.

For $q = 2$, $\tau_m^H > 2 = \tau$ in Figure 4.3a and so no Hopf bifurcation occurs for $0 < m < m_{b^-}$. Furthermore, since the eigenvalues enter from the $\mathrm{Re}(\lambda) < 0$ complex plane then all of the eigenvalues are stable as evidenced in Figure 4.2. For $q = 1$ however, $\tau > \tau_m^H$ for all m in $0 < m < m_{b^-}$ and so the eigenvalues should have all transitioned through a Hopf bifurcation and entered

the $\mathrm{Re}(\lambda) > 0$ complex plane. As such, all of the eigenvalues are unstable as evidenced in Figure 4.2.

Finite l

We now briefly consider the case where l is finite. In this case, we use (4.26) to replace (4.38) with $\mathcal{F}_l(\lambda)$ and $\mathcal{G}_l(\lambda)$ defined by

$$\mathcal{F}_l \equiv 2\sqrt{1+\hat{\tau}\lambda}\left(\frac{\tanh(l\sqrt{1+m^2}\sqrt{1+\hat{\tau}\lambda})}{\tanh(l\sqrt{1+m^2})}\right) - \mathcal{G}_l(\lambda), \quad \mathcal{G}_l(\lambda) \equiv d_{0l} - \frac{d_{1l}}{\beta-\lambda}, \tag{4.53}$$

with $d_{0l} \leq 0$, $d_{1l} < 0$ defined by

$$d_{0l} = -\frac{2s}{\sqrt{1+m^2}}\frac{\tanh l}{\tanh(l\sqrt{1+m^2})}, \qquad d_{10} = -\frac{9q}{\sqrt{1+m^2}}\frac{\tanh l}{\tanh(l\sqrt{1+m^2})},$$

and β still by (4.37c). We have that $m = m_{b^-}$ defined by (4.28) and $m = m_{b^+}$ defined by (4.30) are the two values of m for which $\lambda = 0$ is a root to $\mathcal{F}_l$ and as such these are the two values for which $\mathcal{G}_l(0) = 2$. Therefore, we can easily extend (4.41) for $\mathcal{G}_l(0)$ with the new values of m_{b^-} and m_{b^+}. To find the roots we can still use (4.39) since $\mathcal{F}_l$ still has a pole at $\lambda = \beta$ and still changes argument by $\pi/2$ over Γ_K. We define $\mathcal{F}_{Rl}(\lambda_I) \equiv \mathrm{Re}(\mathcal{F}_l(i\lambda_i))$ by

$$\mathcal{F}_{Rl} = \mathcal{C}_{Rl}(\lambda_I) - d_{0l} + \frac{d_{1l}\beta}{\beta^2+\lambda_I^2},$$
$$\mathcal{C}_{Rl}(\lambda_I) \equiv \mathrm{Re}\left(2\sqrt{1+i\hat{\tau}\lambda_I}\frac{\tanh(l\sqrt{1+m^2}\sqrt{1+i\hat{\tau}\lambda_I})}{\tanh(l\sqrt{1+m^2})}\right),$$

and similarly,

$$\mathcal{F}_{Il} = \mathcal{C}_{Il}(\lambda_I) + \frac{d_{1l}\lambda_I}{\beta^2 + \lambda_I^2},$$
$$\mathcal{C}_{Il}(\lambda_I) \equiv \mathrm{Im}\left(2\sqrt{1+i\hat{\tau}\lambda_I}\frac{\tanh(l\sqrt{1+m^2}\sqrt{1+i\hat{\tau}\lambda_I})}{\tanh(l\sqrt{1+m^2})}\right).$$

It was shown in section 3 of [79] that $\mathcal{C}_{Rl}(\lambda_I)$ is a monotonic increasing function of λ and therefore, since $d_{1l} < 0$, $\mathrm{d}\mathcal{F}_{Rl}(\lambda_I)/\mathrm{d}\lambda_I > 0$. We can therefore easily retrieve the argument change for each case of m and make the same conclusion for J in (4.39) as we did for $l = \infty$. Because of this we have that Principal Result 4.2.2.1 holds for any l in $0 < l < \infty$. We can compute roots to (4.26) for any l using Newton's method. We plot an example of this for for $q = 1$ and $\tau = 2$ in Figure 4.4.

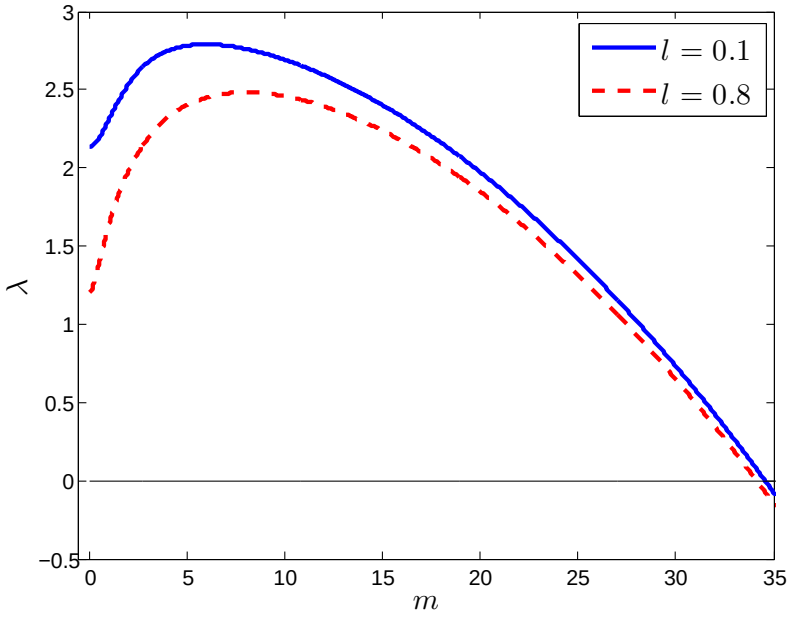

Figure 4.4: Plot of eigenvalues λ versus m for $l = 0.1$ (solid curve) and $l = 0.8$ (dashed curve). The parameter values are $q = 1$, $s = 0$, $\epsilon = 0.05$, and $\tau = 2$.

It is worth mentioning that while Principal Result 4.2.2.1 holds, we cannot guarantee that the Hopf bifurcation for m on $0 < m < m_{b^-}$ is unique and as such that Principal Result 4.2.2.2 holds.

4.3 Explicit Stability Formulation for the Gierer-Meinhardt Model on a Ring

We now consider the unsaturated Gierer-Meinhardt model (4.13) in a radial domain

$$\Omega \equiv \{(r, \theta) | 0 \leq r \leq l, 0 \leq \theta < 2\pi\}, \qquad r = |x|$$

with the activator concentrated on a ring radius $r = r_0$. The solution to this was constructed for $p = 2$ in 2.3.1 and the extension to $p = 3$ is straightforward so the details are omitted here. We have that

$$v = U_0^{\gamma} w\left(\frac{r - r_0}{\epsilon}\right), \qquad u = U_0 \frac{G_l(r; r_0)}{G_l(r_0; r_0)}, \qquad \gamma \equiv q/2,$$

where w is still given by (4.16). Here the Green's function $G_l(r; r_0)$ is given by (2.38) where R is replaced by l and the constant U_0 satisfies

$$U_0^{\zeta} = \left(\frac{1}{r_0\sqrt{2}\pi \mathcal{J}_{0,1}(r_0)\mathcal{J}_{0,2}(r_0)}\right), \qquad \zeta \equiv \frac{3}{2}q - (s+1),$$

with $\mathcal{J}_{0,i}$ defined by (2.39). We have the dynamic condition for r_0 given by (2.43) where

$$\hat{\mathcal{H}} = \frac{\int_{-\infty}^{\infty} w^2 \,\mathrm{d}y}{\int_{-\infty}^{\infty} w_y^2 \,\mathrm{d}y} - 1 = 2, \qquad y = \epsilon^{-1}(r - r_0),$$

and therefore

$$\frac{\mathrm{d}r_0}{\mathrm{d}T} = -\frac{1}{r_0} - \frac{q}{2}\left(\frac{\mathcal{J}'_{0,1}(r_0)}{\mathcal{J}_{0,1}(r_0)} + \frac{\mathcal{J}'_{0,2}(r_0)}{\mathcal{J}_{0,2}(r_0)}\right), \qquad T \equiv \epsilon^{-2} t. \tag{4.54}$$

For the purposes of this section, we will consider the stability around true equilibrium $\mathrm{d}r_0/\mathrm{d}T = 0$ and like section 2.3.1, equilibrium radii will not exist for all values of l and there is a saddle node bifurcation. Figure 4.5 shows the bifurcation diagram for $p = 3$ and $q = 2$.

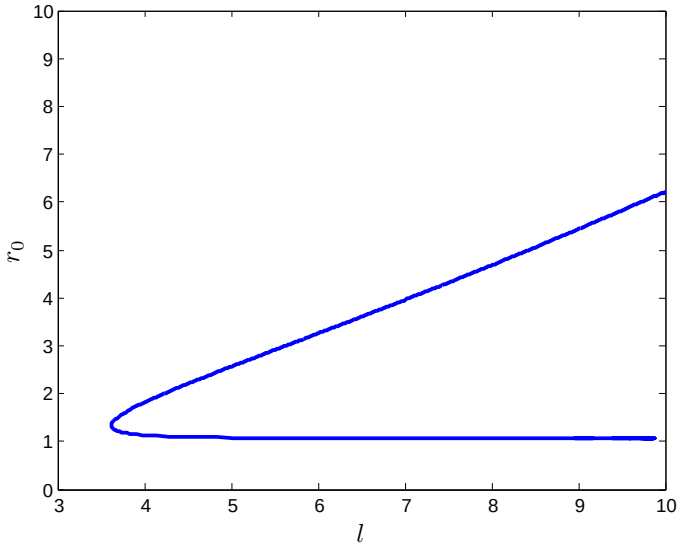

Figure 4.5: Bifurcation diagram for (4.54) for $q = 2$. A saddle-node bifurcation occurs when $l = 3.622$. The larger of the equilibrium r_0 values belong to the stable branch.

Now, unlike Figure 2.6, when $p = 3$ there are no roots to (4.54) when $q = 2$ as evidenced in Figure 4.6 and therefore we will not consider this case.

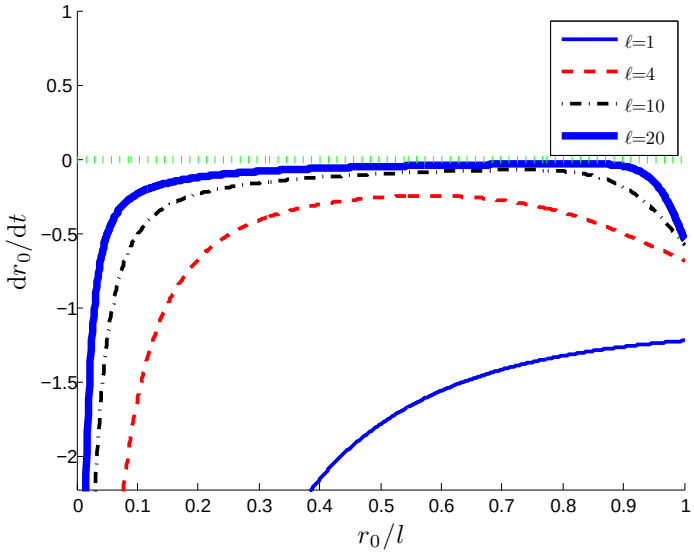

Figure 4.6: Plot of (4.54) for $q = 1$ and various values of l. We always have that $\mathrm{d}r_0/\mathrm{d}T < 0$ and therefore there are no equilibrium ring radii when $q = 1$.

We now turn our attention to the linear stability problem,

$$v = v_e + \Phi\left(\frac{r - r_0}{\epsilon}\right)\exp(im\theta + \lambda t), \quad u = u_e + \eta(r)\exp(im\theta + \lambda t), \qquad m \in \mathbb{N}$$

where we note that since we are considering true equilibrium positions r_0 then we do not have a slow time dependence on the steady-state. As with the stripe we will only consider Φ even for which $\mathrm{Re}(\lambda) > 0$. The details of the derivation of the NLEP for $p = 3$ are similar to the $p = 2$ case in 3.1 and as such we omit the details here. The nonlocal eigenvalue problem (3.16)

becomes

$$L_0\Phi - \chi w^3 \frac{\int_{-\infty}^{\infty} w^2\Phi \,\mathrm{d}y}{\int_{-\infty}^{\infty} w^3 \,\mathrm{d}y} = \left(\lambda + \frac{\epsilon^2 m^2}{r_0^2}\right)\Phi;$$
$$\chi \equiv 3q\left(s + \frac{\mathcal{J}_{0,1}(r_0)\mathcal{J}_{0,2}(r_0)}{\bar{\mathcal{J}}_{m,1}(\theta_\lambda r_0)\bar{\mathcal{J}}_{m,2}(\theta_\lambda r_0)}\right)^{-1}, \quad \theta_\lambda = \sqrt{1+\tau\lambda}, \tag{4.55}$$

where $\mathcal{J}_{0,i}$ is given by (2.39) and $\bar{\mathcal{J}}_{m,i}$ by (3.13). The operator L_0 is given by (4.2) with $f(w) = w^3$. Since the explicitly solveable criteria from section 4.1 is not geometry specific, we still have $L_0 w^2 = 3w^2$ and therefore comparing to (4.7), (4.55) becomes

$$\lambda = 3 - \frac{\epsilon^2 m^2}{r_0^2} - \frac{9q}{2}\left(s + \frac{\mathcal{J}_{0,1}(r_0)\mathcal{J}_{0,2}(r_0)}{\bar{\mathcal{J}}_{m,1}(\theta_\lambda r_0)\bar{\mathcal{J}}_{m,2}(\theta_\lambda r_0)}\right)^{-1}, \tag{4.56}$$

where we have used that $\int_{-\infty}^{\infty} w^5 \,\mathrm{d}y = 3/2\int_{-\infty}^{\infty} w^3 \,\mathrm{d}y$. Once again when $\tau = 0$, we have that (4.56) becomes an explicit expression for λ. We start by finding neutral stability points $\lambda = 0$. When m $\mathcal{O}(1)$ then for $\lambda = 0$ (4.56) becomes

$$\mathcal{M} = \zeta + 1 - \frac{\mathcal{J}_{0,1}(r_0)\mathcal{J}_{0,2}(r_0)}{\bar{\mathcal{J}}_{m,1}(r_0)\bar{\mathcal{J}}_{m,2}(r_0)} = 0. \tag{4.57}$$

$\mathcal{M}(0) = \zeta > 0$ and when $m \gg 1$ we can use (3.31) for larger order asymptotics to the modified Bessel functions to get that

$$\bar{\mathcal{J}}_{1,m}(r_0)\bar{\mathcal{J}}_{2,m}(r_0) \sim \frac{1}{2m}(1 + (r_0/l)^{2m}) \approx \frac{1}{2m}, \quad r_0 > 1 \tag{4.58}$$

and so $\mathcal{M} \to -\infty$ as $m \to \infty$. Furthermore, from section 3.2, $\bar{\mathcal{J}}_{m,1}(r_0)\bar{\mathcal{J}}_{m,2}(r_0)$ is a monotonic decreasing function of m and so therefore $\mathcal{M}$ is a monotonic

decreasing function as well. All of this combines to prove there is a unique root $m = m_{b^-}$ to (4.57) such that $\lambda = 0$ when $\tau = 0$. If $\tau = 0$ then we can rewrite (4.56) as

$$\lambda = -3\mathcal{M}\left(s + \frac{\mathcal{J}_{0,1}(r_0)\mathcal{J}_{0,2}(r_0)}{\bar{\mathcal{J}}_{m,1}(r_0)\bar{\mathcal{J}}_{m,2}(r_0)}\right)^{-1}$$

and if $m < m_{b^-}$, $\mathcal{M} > 0$ and hence $\lambda < 0$ for m in $0 < m < m_{b^-}$. Conversely, $\lambda > 0$ if $m = \mathcal{O}(1)$ in $m > m_{b^-}$. When $m = \epsilon^{-1}\tilde{m}$ with $\tilde{m} = \mathcal{O}(1)$ then using (4.58) we have that (4.56) becomes

$$\begin{aligned} 0 &\approx 3 - \frac{\tilde{m}^2}{r_0^2} - \frac{9q}{2}\left(s + \frac{2\tilde{m}\mathcal{J}_{0,1}(r_0)\mathcal{J}_{0,2}(r_0)}{\epsilon}\right)^{-1} \\ &\sim 3 - \frac{\tilde{m}^2}{r_0^2} - \epsilon\frac{9q}{4\tilde{m}\mathcal{J}_{0,1}(r_0)\mathcal{J}_{0,2}(r_0)} \end{aligned} \tag{4.59}$$

and so if we expand $\tilde{m} = \tilde{m}_0 + \epsilon\tilde{m}_1$ then $\tilde{m}_0 = \sqrt{3}r_0$ and

$$\frac{2\tilde{m}_0\tilde{m}_1}{r_0^2} = -\frac{9q}{4\tilde{m}_0\mathcal{J}_{0,1}(r_0)\mathcal{J}_{0,2}(r_0)}$$

and so

$$\tilde{m}_1 = -\frac{3q}{8\mathcal{J}_{0,1}(r_0)\mathcal{J}_{0,2}(r_0)}.$$

Therefore there exists $m = m_{b^+}$ given by

$$m_{b^+} \sim \frac{1}{\epsilon}\sqrt{3}r_0 - \frac{3q}{8\mathcal{J}_{0,1}(r_0)\mathcal{J}_{0,2}(r_0)},$$

such that $\lambda = 0$ in (4.56). When $\tau = 0$, if $m > m_{b^+}$ then $\lambda < 0$ and if $m = \mathcal{O}(\epsilon^{-1})$ $m < m_{b^+}$ then $\lambda > 0$. Combining this with what we concluded

in $m = \mathcal{O}(1)$, for m in $m_{b^-} < m < m_{b^+}$, $\mathrm{Re}(\lambda) > 0$. We plot the eigenvalues in Figure 4.7 for $\tau = 0$ using (4.56) for $q = 2$ and $l = 5$. We plot the eigenvalues for the two equilibrium radii $r_0 \approx 1.08$ and $r_0 \approx 2.56$ from Figure 4.5.

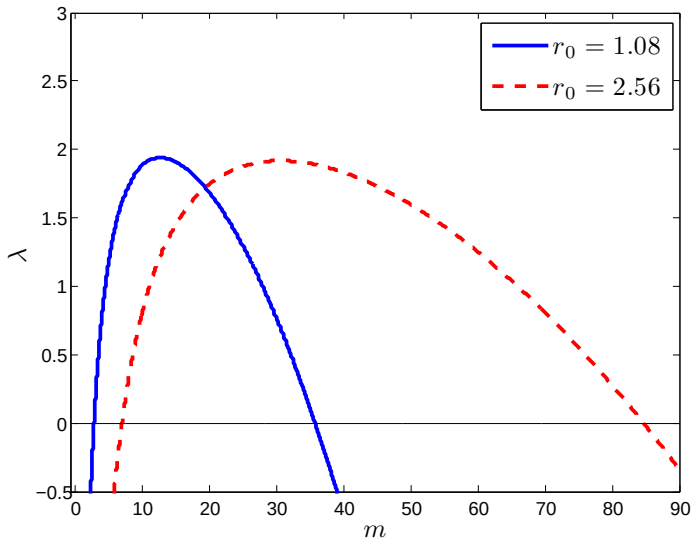

Figure 4.7: Eigenvalues λ versus m for $q = 2$, $s = 0$, $\epsilon = 0.05$, $l = 5$, and $\tau = 0$ using (4.56). The solid curve is for $r_0 = 1.08$ while the dashed curve is for $r_0 = 2.56$.

When $\tau \neq 0$ then similar to section 4.2.2 we can define

$$\mathcal{R}(\lambda) \equiv C_m(\lambda) - f(\mu), \qquad \mu = \lambda + \frac{\epsilon^2 m^2}{r_0^2},$$
$$C_m(\lambda) = \frac{1}{3q}\left(s + \frac{\mathcal{J}_{0,1}(r_0)\mathcal{J}_{0,2}(r_0)}{\bar{\mathcal{J}}_{m,1}(\theta_\lambda r_0)\bar{\mathcal{J}}_{m,2}(\theta_\lambda r_0)}\right), \quad f(\mu) = -\frac{3}{2(\mu - 3)}, \tag{4.60}$$

and then eigenvalues of (4.56) become roots to (4.60). We make the split in this way because then $C_m(\lambda)$ is exactly that given by (3.19a) in section 3.2.

We see then the effect of the explicit formulation is to make $f(\mu)$ an explicit function in terms of λ. From (4.60) we can show directly that

$$\begin{aligned} f'(\mu) > 0, \quad & \mu \in [0, 3) \\ f''(\mu) > 0, \quad & \mu \in [0, 3) \\ f(\mu) < 0, \quad & \mu \in (3, \infty) \end{aligned}$$

and therefore all of the analysis of section (3.2) holds and we can immediately conclude Principal Result 3.2.9.1 holds, i.e. that there exists a range of unstable real eigenvalues for m in $m_{b^-} < m < m_{b^+}$ and that on $0 < m < m_{b^-}$, there exists a Hopf bifurcation as τ is increased from zero. To compute the eigenvalues for $\tau > 0$ we can use the algorithm outlined in section 3.2.10. As an example we plot the eigenvalues for $q = 2$, $s = 0$, $l = 5$, $\epsilon = 0.05$ and $r_0 = 1.08$ and $r_0 = 2.56$ in Figure 4.8 for $\tau = 6$.

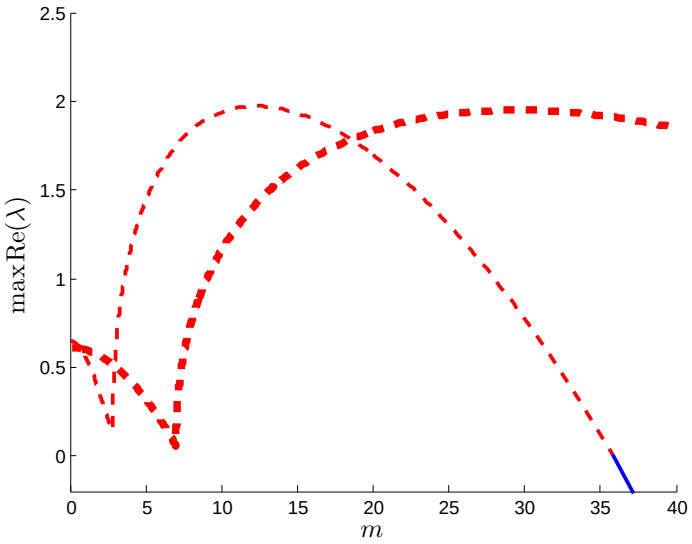

Figure 4.8: Eigenvalues λ versus m for $q = 2$, $s = 0$, $\epsilon = 0.05$, $l = 5$, and $\tau = 6$. The lighter curve is for $r_0 = 1.08$ while the heavy curve is for $r = 2.56$. We plot both for $0 < m < 40$ since large m behaviour is not very impacted by increasing τ and will be represented by Figure 4.7. The positive eigenvalues are in dash while the negative eigenvalues are in solid.

Chapter 5

Full Numerical Simulations of the Gierer-Meinhardt Model

We now wish to verify some of the analysis we predicted by computing full numerical simulations of

$$v_t = \epsilon_0^2 \Delta v - v + \frac{v^p}{u^q g(v)}, \tag{5.1a}$$

$$\tau u_t = D_0 \Delta u - u + \frac{v^o}{u^s} \tag{5.1b}$$

on some domain Ω, where $g(v) = 1$ if saturation is not considered and $g(v) = 1 + \sigma v^2$ with σ the saturation parameter if $p = 2$ and saturation is considered. We want to perform computations on both a stripe and a ring. If we perform computations on a stripe then the domain is

$$\Omega_{\text{stripe}} \equiv \{(x, y) | 0 \leq x \leq 1, 0 \leq y \leq d_0\}$$

subject to Neumann conditions on $\partial\Omega$. If we perform computations on a ring then the domain is

$$\Omega_{\text{ring}} \equiv \{(r, \theta) | 0 \leq r \leq 1, 0 \leq \theta \leq 2\pi\}$$

subject to periodicity in θ, Neumann conditions at $r = 1$ and a compatibility condition $\partial v/\partial r = \partial u/\partial r = 0$ at $r = 0$. For analysis purposes, in other chapters, we often rescaled the diffusion coefficient into the length scale but this is impractical for computations where it is more natural to compute on fixed-length domains. Therefore, for comparison between numerical and analytic work for the stripe we take

$$D = 1, \quad \epsilon = \frac{\epsilon_0}{\sqrt{D_0}}, \quad d = \frac{d_0}{\sqrt{D_0}}, \quad l = \frac{1}{2\sqrt{D_0}}, \tag{5.2a}$$

where these quantities are used in section 4.2. Similarly for the ring we take

$$D = 1, \quad \epsilon = \frac{\epsilon_0}{\sqrt{D_0}}, \quad R = l = \frac{1}{\sqrt{D_0}}, \tag{5.2b}$$

where these quantities are used in Chapter 2, 3, and section 4.3.

For the Laplace operator in each scenario we use a cell-centered discretization on a uniformly spaced 400×400 rectangular grid in both space variables. One of the main advantages of this discretization over a node based discretization in this context is that we avoid evaluating at the singularity $r = 0$ directly. For derivative conditions at the endpoints we use a ghost point formulation [73]. The time-stepping is done via the adaptive step method `ode15s` in Matlab with the Jacobian supplied. For the case of radial coordinates, after computing on an (r, θ) grid we conformal map to the circle via Matlab's `pol2cart` function.

In order to stimulate breakup instabilities we will consider random perturba-

tions sampled uniformly from $[-\delta, \delta]$ with $\delta = 0.001$ from a base homoclinic orbit. In all of the numerical experiments in which we predict spot breakup patterns, we expect that the most dominant Fourier mode will dictate the number of spots that appears in the pattern. However, in both geometries, we concluded that there were neutral stability points at modes $m = m_{b^-}$ and $m = m_{b^+}$ such that there is a range of real unstable eigenvalues (in the absence of saturation) for which $\mathrm{Re}(\lambda) > 0$ on $m_{b^-} < m < m_{b^+}$. Therefore, due to the random nature of the perturbations, modes other than the maximal mode may dominate the stability pattern. On a long enough time-scale, we would still expect the dominant mode to be observed but all of the analysis is based upon linear stability and once a breakup occurs, secondary dynamics may initiate. Furthermore, since random amplitude perturbations do not favour positive or negative amplitudes, this will induce a phase correction. To alleviate these issues, when looking for spot breakup, we will perform a full discrete Fourier transform on the solution and then isolate modes that are within 95% of the maximal mode (which we call *dominant modes*). This is designed to represent the most dominant wavemode interference. We will also plot the maximal mode and compare that to the predicted number of spots. Since we are not concerned with translational effects, we will filter the $m = 0$ mode.

5.1 Stripe Numerical Experiments

We begin by presenting some numerical experiments to coincide with the explicit stripe formulation in 4.2. In this scenario Fourier perturbations are

of the form $\exp(ix_2 k\pi/d)$ with $k \in \mathbb{N}$. We initialize the code with the steady-state (4.15) from section 4.2 subject to the random amplitude perturbation previously discussed. For the first experiment, we consider exponent set $(3, 1, 3, 0)$, $\epsilon_0 = 0.05$, $D_0 = 1$, $\tau = 0.1$, and $d_0 = 2$ which correspond to $\epsilon = 0.05$ $l = 1/2$ in (4.27). We note that this is meant to represent the $\tau = 0$ case but we take τ small and finite to allow full dynamics to occur. We considered this case analytically in Figure 4.1 and in Table 4.1, we computed that $m_{\text{dom}} = 7.42$, which corresponds to $k_{\text{dom}} = 4$, where we have rounded down to the nearest integer. The number of spots is given by

$$N_{\text{spot}} = \frac{m_{\text{dom}} d}{2\pi} = \frac{k_{\text{dom}}}{2}, \tag{5.3}$$

which leads to $N = 2$ spots in this case. Note that the extra factor of 2 comes from the fact that minima do not produce spots. The numerical results of experiment 1 are in Figure 5.1 for times $t = 0$ (a), $t = 2.64$ (b), $t = 3.16$ (c), and $t = 5$ (d). As time progresses it does indeed appear that a two spot pattern is dominant. However we can see this more clearly by looking at the Fourier transform in Figure 5.2 where indeed the most dominant mode produces a two spot pattern.

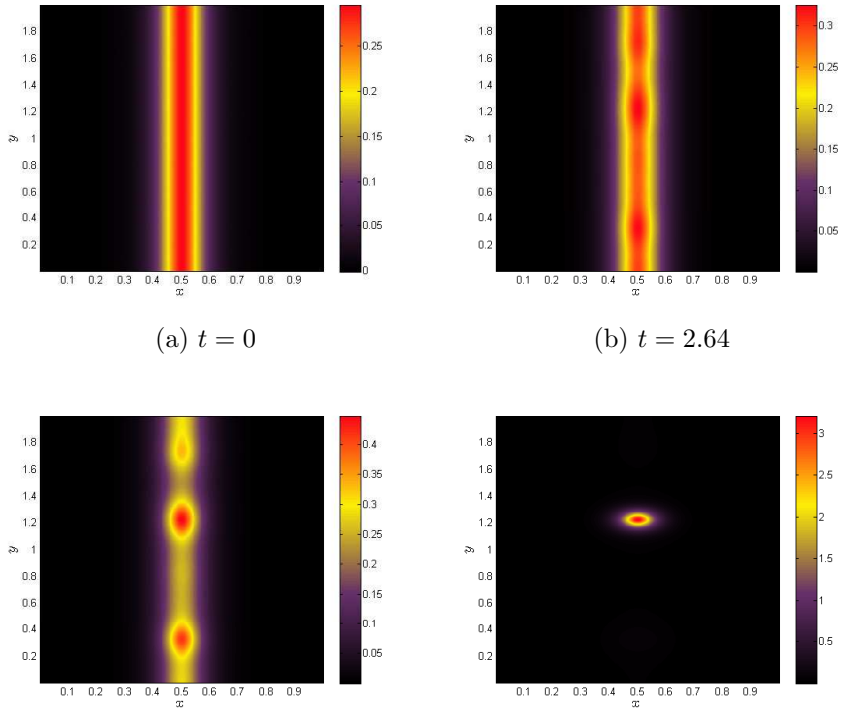

(a) $t = 0$ (b) $t = 2.64$

(c) $t = 3.16$ (d) $t = 5$

Figure 5.1: *Experiment 1:* Contour plot of the solution v to (5.1a) with stripe geometry at four times with with exponent set $(3, 1, 3, 0)$. The parameter values are $\epsilon_0 = 0.05$, $D_0 = 1$, $\tau = 0.1$, and $d_0 = 2$. This corresponds to $\epsilon = 0.05$, $l = 1/2$, $\tau = 0.1$, and $d = 2$ in (4.27) of Chapter 4.

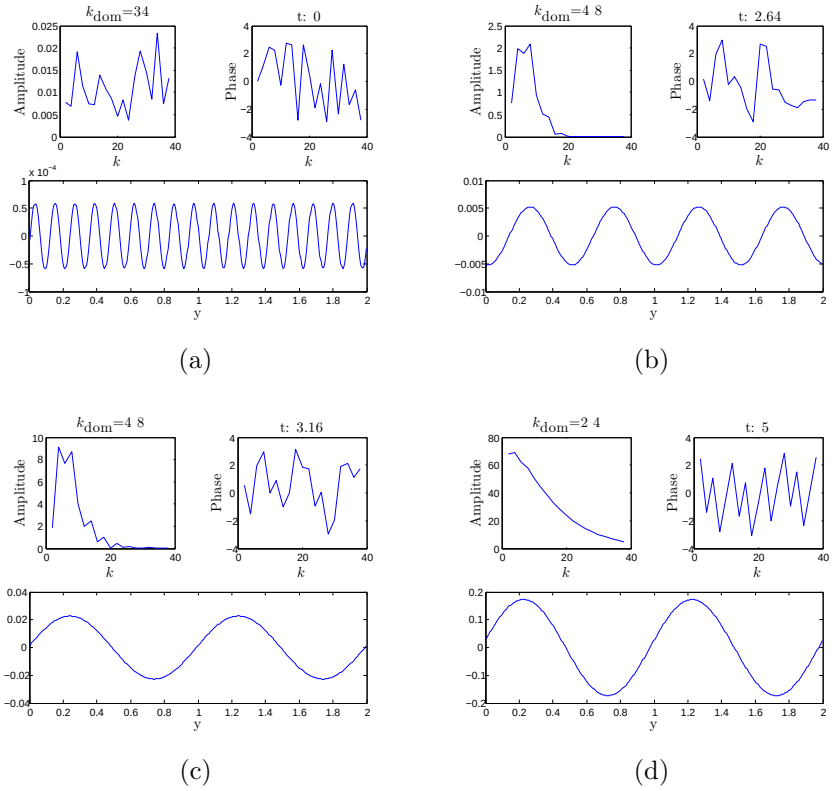

Figure 5.2: *Experiment 1:* Discrete Fourier transform of the solution v to (5.1a) with stripe geometry at four times with with exponent set $(3, 1, 3, 0)$. The parameter values are $\epsilon_0 = 0.05$, $D_0 = 1$, $\tau = 0.1$, and $d_0 = 2$. The upper left plot shows the amplitudes from the Fourier transform while the upper right plot displays the phase. Dominant modes are defined as any modes that have an amplitude within 95% of the largest amplitude mode. The bottom graphic in each panel shows an inverse Fourier transform of a solution comprised of only the most dominant mode.

For experiment 2 we consider the same parameters as experiment 1 but with $d_0 = 3$. This produces the same dominant mode $m_{\text{dom}} = 7.42$ as this is independent of the width of the rectangle but it does affect the number of spots (5.3), where now we predict $N = 3$. The numerical results are in Figure 5.3 for times $t = 0$ (a), $t = 2.42$ (b), $t = 2.64$ (c), and $t = 5$ (d).

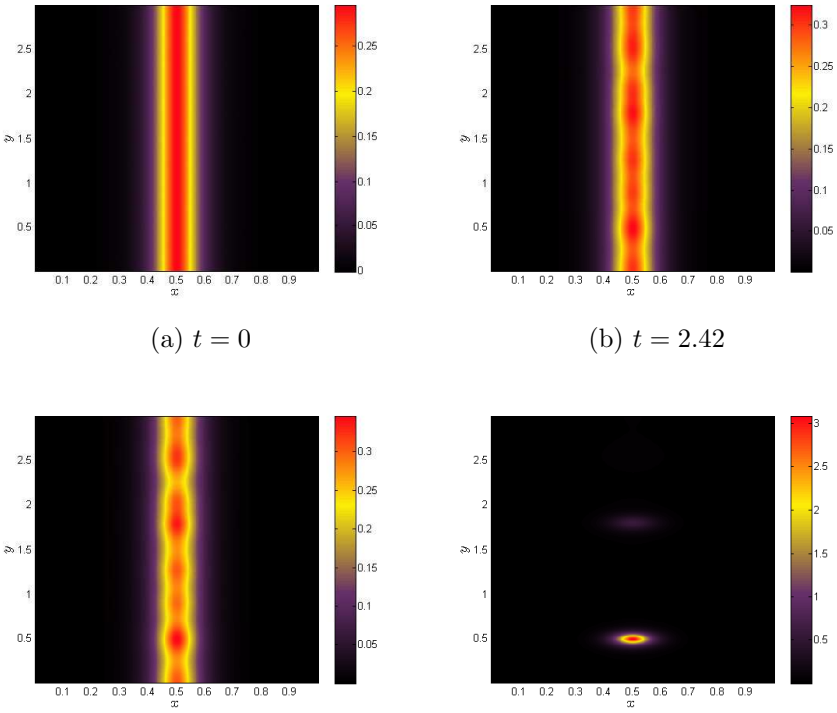

(a) $t = 0$ (b) $t = 2.42$

(c) $t = 2.64$ (d) $t = 5$

Figure 5.3: *Experiment 2:* Contour plot of the solution v to (5.1a) with stripe geometry at four times with with exponent set $(3, 1, 3, 0)$. The parameter values are $\epsilon_0 = 0.05$, $D_0 = 1$, $\tau = 0.1$, and $d_0 = 3$. This corresponds to $\epsilon = 0.05$, $l = 1/2$, $\tau = 0.1$, and $d = 3$ in (4.27) of Chapter 4.

In Figure 5.4 we plot the Fourier transform results of experiment 2 where in fact it is a 4 spot pattern that emerges which is not surprising since in actuality we expect $N = 3.54$ and so anything between a three and four spot pattern matches well. If we compare Figures 5.2 and 5.4 then we see that the dominant modes competing for instability are more spread out in experiment 2 which is a side effect of taking d_0 larger. From Figure 4.1 in 4.2.1, the dominant modes within 95% of the maximum satisfy $5 < m < 14$

which hold for all d but this results in $3 < k < 8$ for experiment 1 and $4 < k < 13$ for experiment 2. Therefore, the clustering of competitive modes is more spread out as d_0 increases and the most dominant mode has a better chance of surviving through most random perturbations.

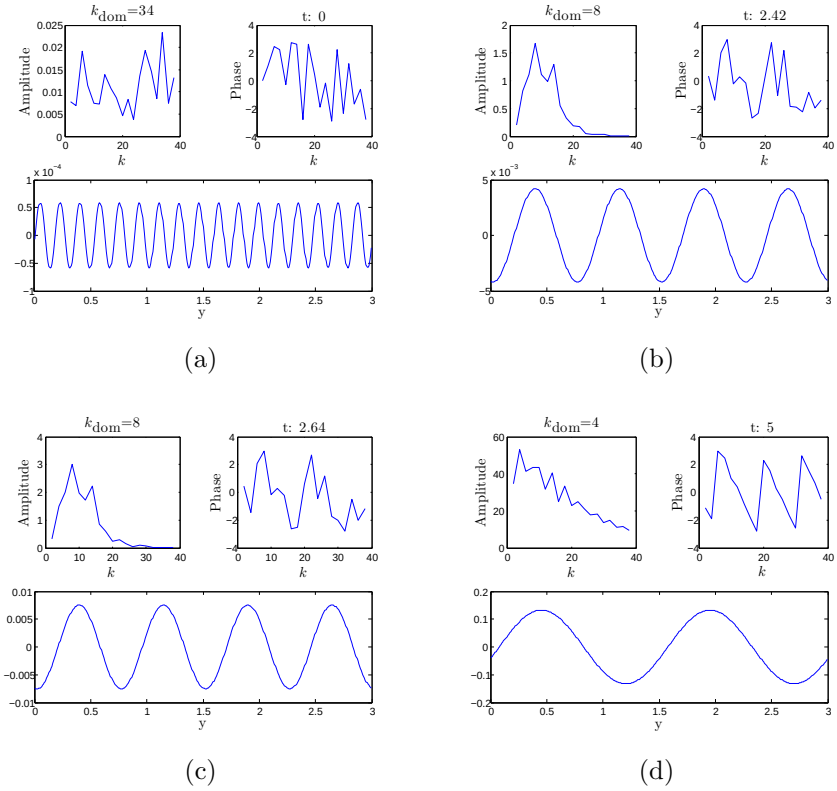

Figure 5.4: *Experiment 2:* Discrete Fourier transform of the solution v to (5.1a) with stripe geometry at four times with with exponent set $(3, 1, 3, 0)$. The parameter values are $\epsilon_0 = 0.05$, $D_0 = 1$, $\tau = 0.1$, and $d_0 = 3$. The upper left plot shows the amplitudes from the Fourier transform while the upper right plot displays the phase. Dominant modes are defined as any modes that have an amplitude within 95% of the largest amplitude mode. The bottom graphic in each panel shows an inverse Fourier transform of a solution comprised of only the most dominant mode.

For experiment 3 we repeat experiment 1 but with $D_0 = 0.1$ which affects

l d, and ϵ via (5.2a). We plot the numerical results of this experiment in Figure 5.5 for times $t = 0$ (a), $t = 2.64$ (b), $t = 4.34$ (c), and $t = 5$ (d). If we compute the eigenvalues using (4.27) from 4.2.1 then we have that $m_{\text{dom}} \approx 4.24$ and therefore from (5.3) with $d = 2\sqrt{10}$, we predict $N = 4$ spots. If we were to plot the eigenvalues for this case, the instability band forms on $1.01 < m < 10.19$ which is much narrower than the band for $l = 1/2$. This narrowed clustering means that the dominant mode should emerge more prominently as there are fewer modes to compete with. Furthermore, as we saw from Figure 4.1 as l increases the magnitude of the largest eigenvalue decreases. This means that for this value of l, the breakup instability should take longer to form compared to experiments 1 and 2. Indeed by looking at Figure 5.6 all of these predictions are verified as the four spot pattern emerges quite distinctly without much competition and the prominence of the pattern is not noticed until $t = 4.34$ which is in contrast to $t = 3.16$ and $t = 2.64$ for experiments 1 and 2 respectively.

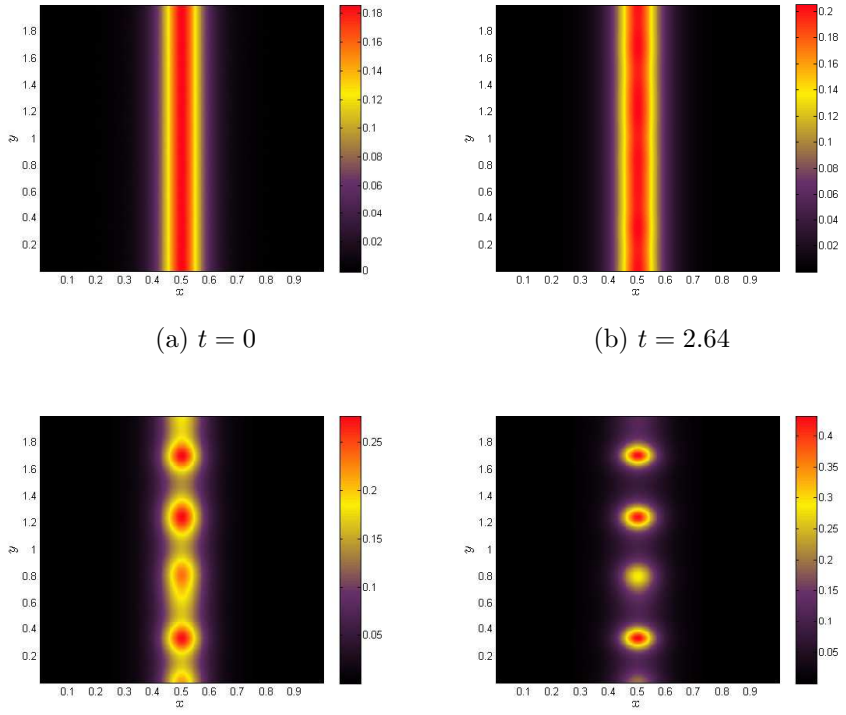

(a) $t = 0$ (b) $t = 2.64$

(c) $t = 4.34$ (d) $t = 5$

Figure 5.5: *Experiment 3:* Contour plot of the solution v to (5.1a) with stripe geometry at four times with with exponent set $(3, 1, 3, 0)$. The parameter values are $\epsilon_0 = 0.05$, $D_0 = 0.1$, $\tau = 0.1$, and $d_0 = 2$. This corresponds to $\epsilon = 0.05\sqrt{10} \approx 0.1581$, $l = \sqrt{10}/2 \approx 1.58$, $\tau = 0.1$, and $d = 2\sqrt{10} \approx 6.32$ in (4.27) of Chapter 4.

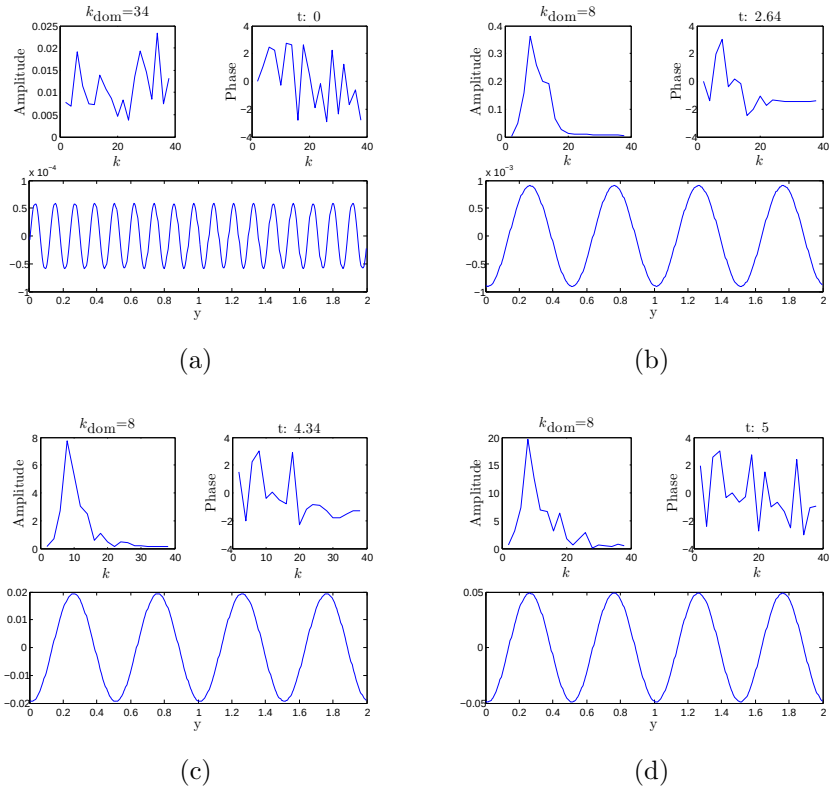

Figure 5.6: *Experiment 3:* Discrete Fourier transform of the solution v to (5.1a) with stripe geometry at four times with with exponent set $(3, 1, 3, 0)$. The parameter values are $\epsilon_0 = 0.05$, $D_0 = 0.1$, $\tau = 0.1$, and $d_0 = 2$. The upper left plot shows the amplitudes from the Fourier transform while the upper right plot displays the phase. Dominant modes are defined as any modes that have an amplitude within 95% of the largest amplitude mode. The bottom graphic in each panel shows an inverse Fourier transform of a solution comprised of only the most dominant mode.

5.2 Ring Numerical Experiments

We will now consider numerical experiments for the ring geometry. With this geometry, Fourier perturbations are of the form $\exp(im\theta)$ for $m \in \mathbb{Z}$ but

we only consider the positive integers keeping in mind the complex conjugate modes also exist. In this case, unlike (5.3), the number of spots $N_{\text{spot}} = m_{\text{dom}}$ exactly.

5.2.1 Explicit Formulation

We will begin by considering the explicit formulation as in section 4.2. Recall from 4.3 that steady-states only exist for $q = 2$ and so we will consider the exponent set $(3, 2, 3, 0)$. We will consider an experiment that corresponds to Figure 4.7 in 4.3 and therefore, we will take $l = 5$, $\epsilon = 0.05$, and $\tau = 0.1$. This corresponds to taking $D_0 = 0.04$ and $\epsilon_0 = 0.01$. We will take r_0 to be the equilibrium values at $l = 5$ which are $r_0 = 1.08$ and $r_0 = 2.56$. When scaled to be on $r \in [0, 1]$, this corresponds to $r_0 = 0.216$ and $r_0 = 0.512$ respectively. Using (4.56) from 4.3, for $r_0 = 0.216$, we expect an instability band on $2 < m < 35$ with a dominant mode $m_{\text{dom}} = 12$, and hence 12 spots. For $r_0 = 0.512$ we expect an instability band $7 < m < 84$ with a dominant mode $m_{\text{dom}} = 30$, and hence 30 spots. The numerical results and discrete Fourier transforms are shown in Figure 5.7 where the computations terminate once the breakup pattern has emerged. For $r_0 = 0.216$ a 14 spot pattern emerges and for $r_0 = 0.512$ a 28 spot pattern emerges. Both results are very close to the predicted dominant spot pattern but are not perfect again owing to the wide range of unstable bands. To ensure the accuracy of the mode prediction we ran several random seed perturbations and saw that the average unstable modes were indeed 12 and 30 spots respectively.

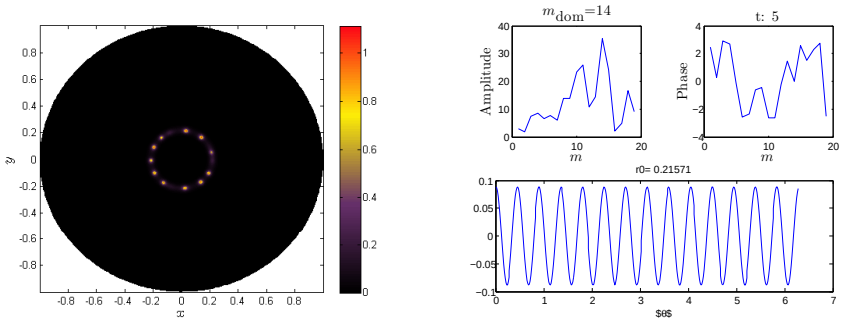

(a) $r_0 = 0.216$ (b) $r_0 = 0.216$

(c) $r_0 = 0.512$ (d) $r_0 = 0.512$

Figure 5.7: *Experiment 4:* Contour and Fourier transform plot of the solution v to (5.1a) with ring geometry with exponent set $(3, 2, 3, 0)$. The parameter values are $\epsilon_0 = 0.01$, $D_0 = 0.04$, and $\tau = 0.1$. This corresponds to $\epsilon = 0.05$, and $l = 5$ in (4.56) of Chapter 4.

5.2.2 Non-Explicit Formulation

We now consider numerical experiments for the non-explicit ring geometry considered in Chapter 2 and Chapter 3. For simplicity we will consider the exponent set $(2, 1, 2, 0)$ moving forward but emphasize that unlike the explicit case, general exponents q, o, and s could be taken and, in fact, we only require $p = 2$ when considering saturation. For these experiments, we will also begin at a radius that is not necessarily the equilibrium radius and as such the ring

radius could change dynamically. We numerically compute the ring radius as the r position which produces the largest value of v when $\theta = 0$. We note that this definition may not be correct for a breakup pattern if the spots separate in non-radially symmetric ways. We will begin by demonstrating the breakup pattern expected in Figure 3.5a of 3.2.10. Here we take $D_0 = 1$ and $\epsilon_0 = 0.025$, which corresponds to $\epsilon = 0.025$ and $R = 1$. We also take $r_0 = 0.5$, which is not the equilibrium radius. However, since we anticipate breakup on an $\mathcal{O}(1)$ timescale versus motion on a $\mathcal{O}(\epsilon^{-2})$ timescale the radius should stay fairly static. Indeed in Figure 5.8 we plot the numerical results for this experiment for times $t = 0$ (a), $t = 5.32$ (b), $t = 6.32$ (c), and $t = 10$ (d) and the numeric ring radius stays essentially static. From Figure 3.5a we predict $m_{\text{dom}} = 4.80$ and hence a four spot breakup pattern which is evidenced in Figure 5.8. Although the $m = 6$ mode is most dominant in the Fourier transform Figure 5.9, it is very balanced with the $m = 4$ mode. In Figure 3.5a, the magnitude of the positive eigenvalues are near and below $\lambda = 1$ which explains the slow breakup instability in Figure 5.8.

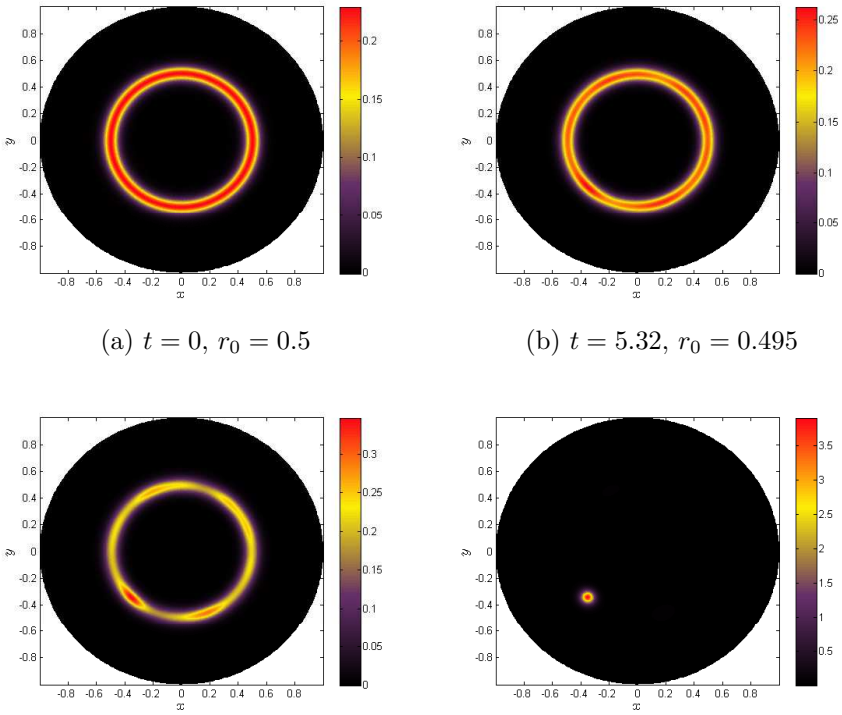

(a) $t = 0$, $r_0 = 0.5$

(b) $t = 5.32$, $r_0 = 0.495$

(c) $t = 6.32$, $r_0 = 0.493$

(d) $t = 10$, $r_0 = 0.493$

Figure 5.8: *Experiment 5:* Contour plot of the solution v to (5.1a) with ring geometry at four times with with exponent set $(2, 1, 2, 0)$. The parameter values are $\epsilon_0 = 0.025$, $D_0 = 1$, and $\tau = 0.1$. This corresponds to $\epsilon = 0.025$, $R = 1$, and $\tau = 0.1$ in the numerical computation of (3.16) of Chapter 3.

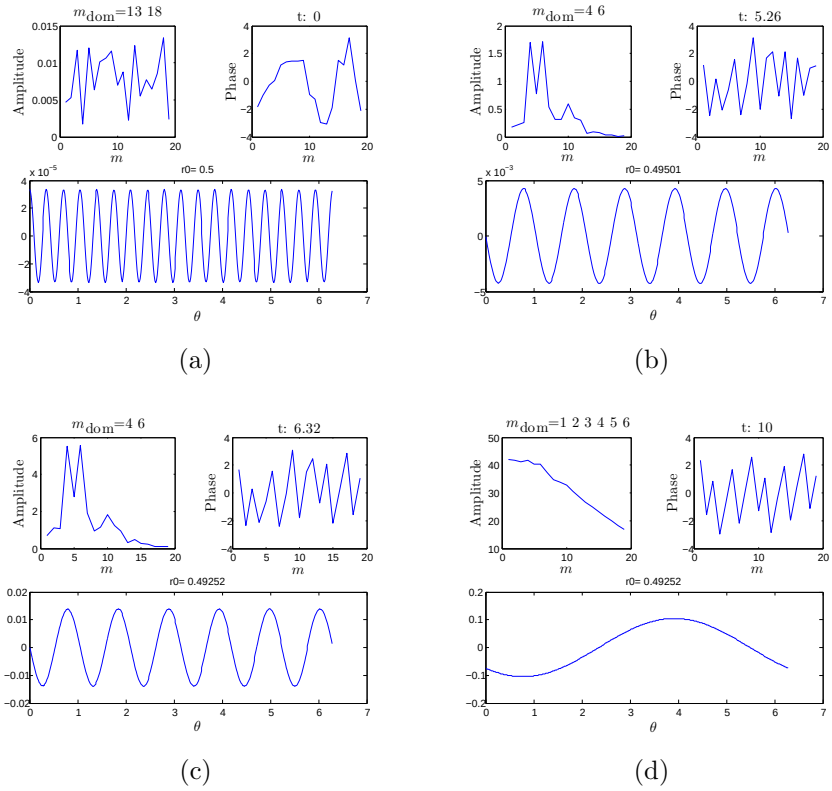

Figure 5.9: *Experiment 5:* Discrete Fourier transform of the solution v to (5.1a) with ring geometry at four times with exponent set $(2, 1, 2, 0)$. The parameter values are $\epsilon_0 = 0.05$, $D_0 = 1$, and $\tau = 0.1$. The upper left plot shows the amplitudes from the Fourier transform while the upper right plot displays the phase. Dominant modes are defined as any modes that have an amplitude within 95% of the largest amplitude mode. The bottom graphic in each panel shows an inverse Fourier transform of a solution comprised of only the most dominant mode.

Adding Saturation

We will now consider the numerical simulations where saturation is included. This has the most significant impact on the dynamics because as we concluded in section 3.2.12, adding saturation can stabilize breakup patterns.

Adding saturation affects the steady-state activator profile but for initializing the code, we still use the steady-state with saturation equal to zero. Therefore, in our simulations where saturation is added, we expect that there will be a transient period where the homoclinic fattens (see Figure 2.2 from section 2.3) before any secondary dynamics occurs. For all numerical experiments unless otherwise stated we are considering $D_0 = 1$, $\epsilon_0 = \epsilon = 0.025$, $R = 1$ and $r_0 = 0.5$. We begin by taking the saturation $\sigma = 25$. From (2.41), this corresponds to $b = 0.1356$ which from Figure 3.10 in section 3.2.12 does not stabilize the pattern. However, it does significantly shrink the instability band and the magnitude of the eigenvalues satisfying $\mathrm{Re}(\lambda) > 0$. We therefore expect that in this scenario, the instability should take longer to form and the dominant mode ($m_{\mathrm{dom}} = 4.68$) should be more pronounced when compared to Figure 5.8 which uses the same parameters but $\sigma = 0$. The results for this experiment are in Figure 5.10 with the Fourier Transform in Figure 5.11 for times $t = 10$ (a), $t = 26.2$ (b), $t = 37.3$ (c), and $t = 50$ (d). In contrast to Figure 5.8 at $t = 10$ when the curve had not only dissociated into spots, but secondary instabilities had reduced it to a single spot, for Figure 5.10, instabilities have not even begun to form at this time. However,the ring is thicker when compared to the zero saturation case, and since the breakup pattern takes longer to occur we see the dynamics of the ring structure since, at $t = 10$, it has shrunk from its original position of $r_0 = 0.5$ to $r_0 = 0.47$. From Figure 2.9, this shrinking behaviour is predicted since r_0 is greater than the equilibrium value.

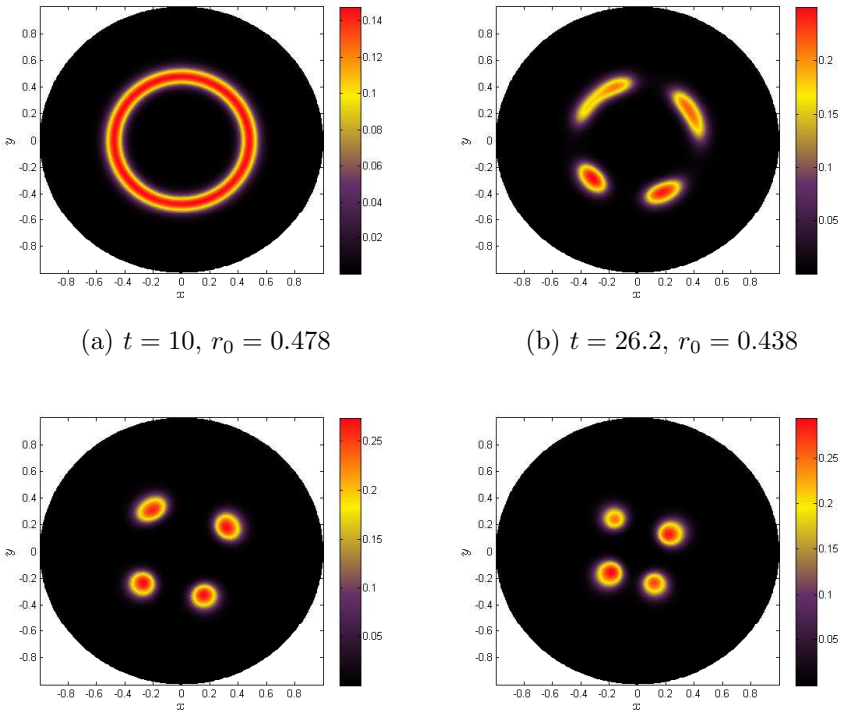

(a) $t = 10$, $r_0 = 0.478$

(b) $t = 26.2$, $r_0 = 0.438$

(c) $t = 37.3$, $r_0 = 0.358$

(d) $t = 50$, $r_0 = 0.243$

Figure 5.10: *Experiment 6:* Contour plot of the solution v to (5.1a) with ring geometry at four times with with exponent set $(2, 1, 2, 0)$. The parameter values are $\epsilon_0 = 0.025$, $D_0 = 1$, $\tau = 0.1$, and $\sigma = 25$. This corresponds to $\epsilon = 0.025$, $R = 1$, and $\tau = 0.1$ in the numerical computation of (3.16) of Chapter 3.

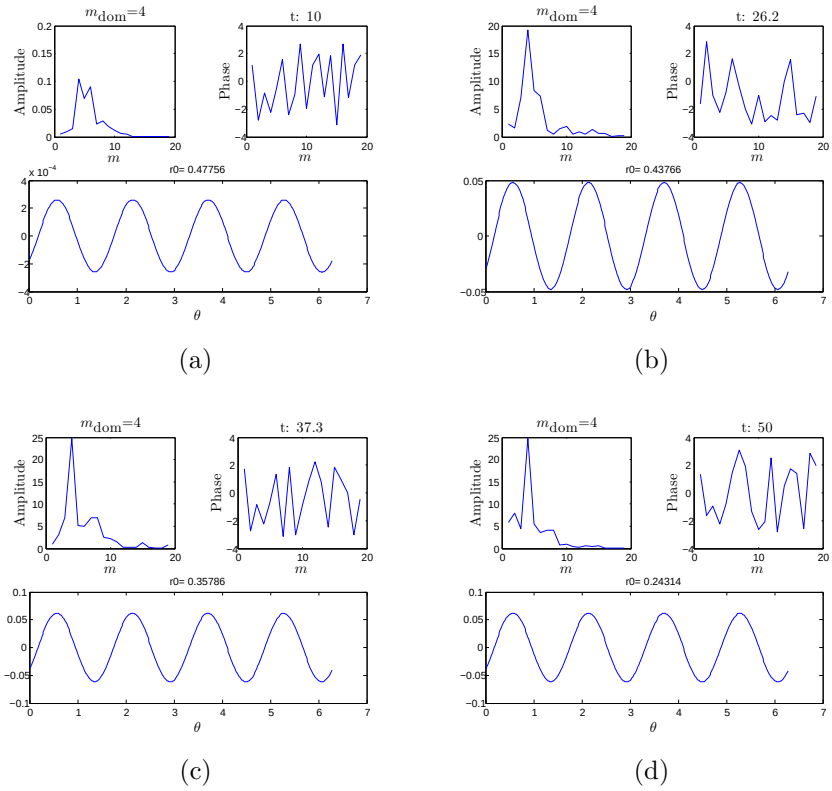

Figure 5.11: *Experiment 6:* Discrete Fourier transform of the solution v to (5.1a) with ring geometry at four times with exponent set $(2, 1, 2, 0)$. The parameter values are $\epsilon_0 = 0.025$, $D_0 = 1$, $\tau = 0.1$, and $\sigma = 25$. The upper left plot shows the amplitudes from the Fourier transform while the upper right plot displays the phase. Dominant modes are defined as any modes that have an amplitude within 95% of the largest amplitude mode. The bottom graphic in each panel shows an inverse Fourier transform of a solution comprised of only the most dominant mode.

As time goes on, eventually the dominant four spot pattern emerges and then the spot structure continues to shrink as a ring. This spot collocation dynamic behaviour was previously observed and analyzed for the Schnakenburg model in [44].

Next we consider the same parameter set but for $\sigma = 950$. For this saturation value and $r_0 = 0.5$ we have that $b = 0.2010$ which by Figure 3.10 does stabilize all of the breakup instability modes. Therefore we expect there to be an initial transient period where the ring fattens from the effect of saturation but where the radius remains relatively static. Afterwards, the ring should remain stable and shrink according to (2.43). During this dynamic process, the width of the ring should also increase because the value of b, even for fixed σ, is intimately tied to r_0 and increases as r_0 decreases. Indeed all of this behaviour is noted in Figure 5.12 for times $t = 0$ (a), $t = 3.48$ (b), $t = 12.2$ (c), and $t = 20$ (d) where the ring does not breakup. By looking at the Fourier transform plot in Figure 5.13 we see that while $m = 4$ remains the dominant integer mode, the amplitudes are decreasing over time and we do truly have a stabilizing pattern. By the end of the simulation, while still stable, the $m = 1$ mode has become dominant and if we look at Figure 5.14 this is exactly what we see is the dominant mode for $r_0 = 0.213$ and $\sigma = 950$ computed using the techniques of section 3.2.10.

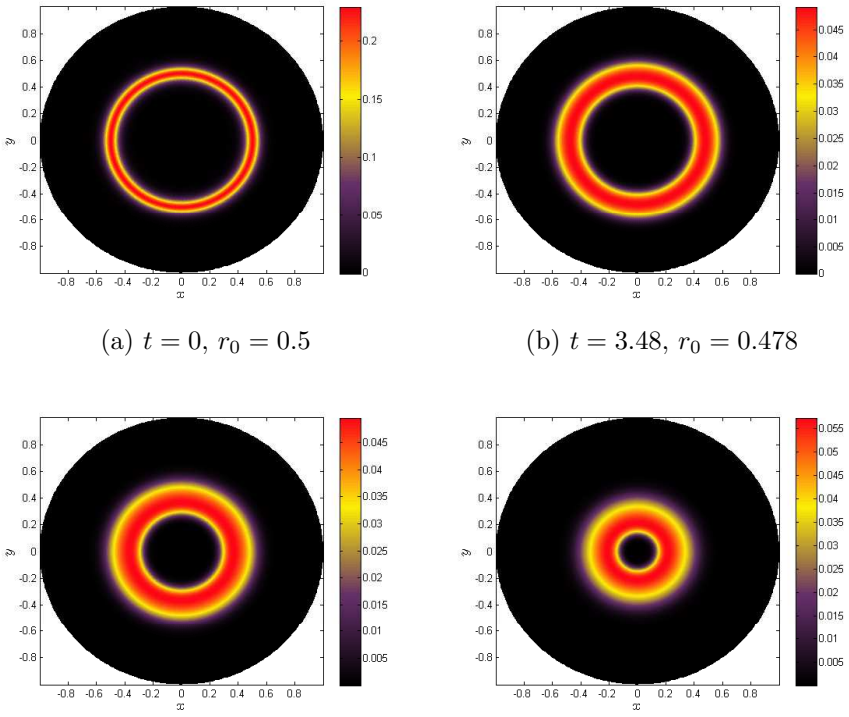

(a) $t = 0$, $r_0 = 0.5$

(b) $t = 3.48$, $r_0 = 0.478$

(c) $t = 12.2$, $r_0 = 0.365$

(d) $t = 20$, $r_0 = 0.213$

Figure 5.12: *Experiment 7:* Contour plot of the solution v to (5.1a) with ring geometry at four times with with exponent set $(2, 1, 2, 0)$. The parameter values are $\epsilon_0 = 0.025$, $D_0 = 1$, $\tau = 0.1$, and $\sigma = 950$. This corresponds to $\epsilon = 0.025$, $R = 1$, and $\tau = 0.1$ in the numerical computation of (3.16) of Chapter 3.

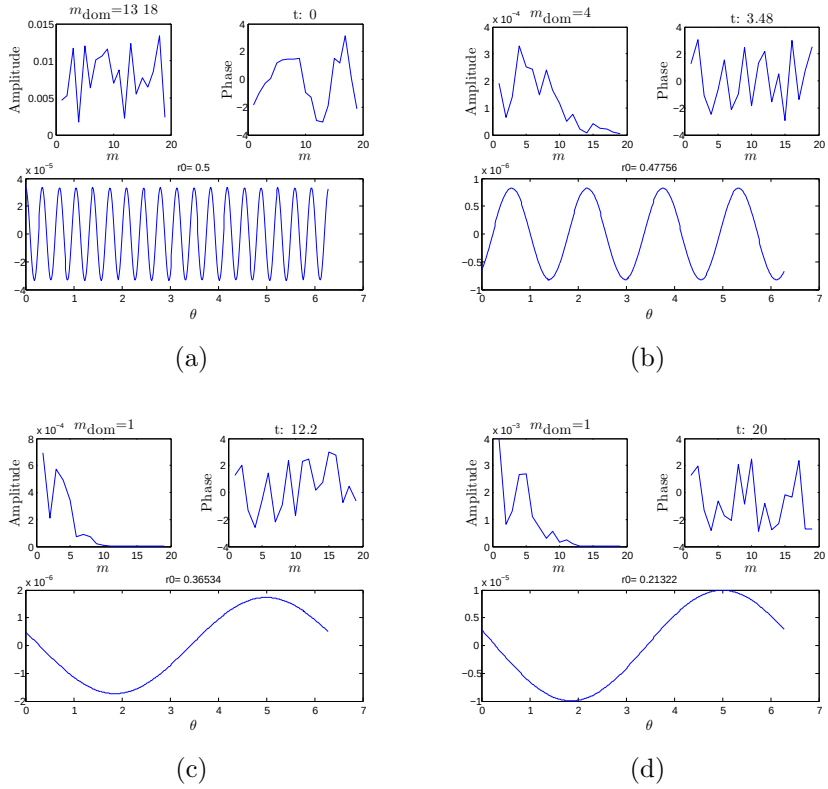

Figure 5.13: *Experiment 7:* Discrete Fourier transform of the solution v to (5.1a) with ring geometry at four times with exponent set $(2, 1, 2, 0)$. The parameter values are $\epsilon_0 = 0.05$, $D_0 = 1$, $\tau = 0.1$, and $\sigma = 950$. The upper left plot shows the amplitudes from the Fourier transform while the upper right plot displays the phase. Dominant modes are defined as any modes that have an amplitude within 95% of the largest amplitude mode. The bottom graphic in each panel shows an inverse Fourier transform of a solution comprised of only the most dominant mode.

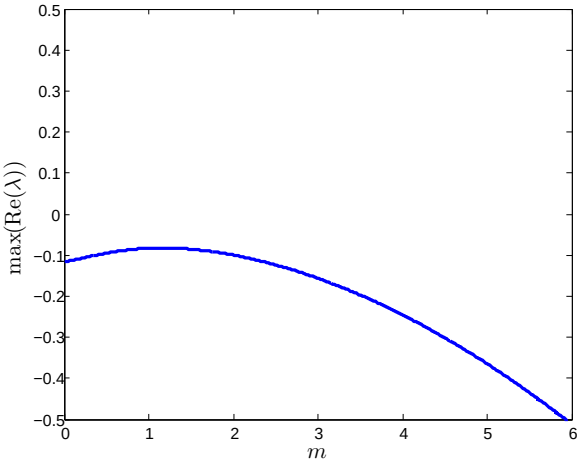

Figure 5.14: Eigenvalues of (3.16) for exponent set $(2, 1, 2, 0)$, $\epsilon = 0.05$, $\tau = 0$, and $R = 1$ with $r_0 = 0.213$ and $\sigma = 950$.

We now consider the perturbations that lead to zig-zag instabilities. In section 2.3.2, we determined that the velocity corrections for a near circular perturbation are in phase with the perturbation itself when r_0 is small enough. Therefore, we expect that given an initial near circular perturbation with $D = \mathcal{O}(1)$, this curve should either grow or shrink by (2.43) and slowly circularize via (2.77). In Figure 5.15, taken at times $t = 0$ (a), $t = 4.92$ (b), $t = 15.76$ (c), and $t = 20$ (d) we take all of the previous parameters except we start with an initial curve radius $r_0 = 0.5 + 0.02\cos(6\theta)$. We still initialize the curve with a homoclinic orbit as if there were no saturation. The homoclinic initially fattens due to the presence of saturation, but as the curve continues to evolve it indeed circularizes.

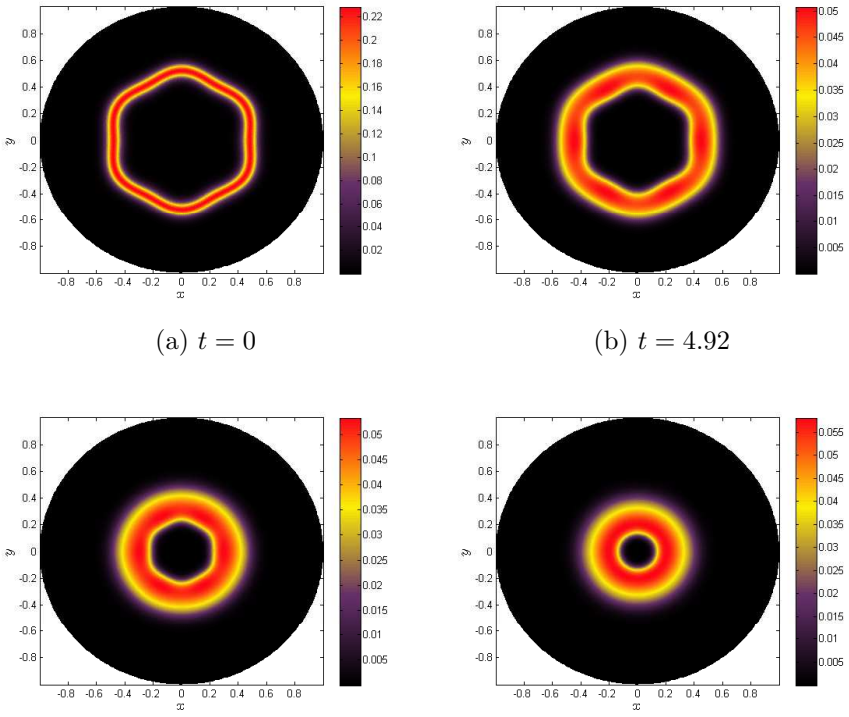

(a) $t = 0$ (b) $t = 4.92$

(c) $t = 15.76$ (d) $t = 20$

Figure 5.15: *Experiment 8:* Contour plot of the solution v to (5.1a) with ring geometry at four times with with exponent set $(2, 1, 2, 0)$. The parameter values are $\epsilon_0 = 0.025$, $D_0 = 1$, $\tau = 0.1$, and $\sigma = 950$. This corresponds to $\epsilon = 0.025$, $R = 1$, and $\tau = 0.1$. We take as an initial radius $r_0 = 0.5 + 0.02\cos(6\theta)$.

Conversely, if $r_0 \gg 1$ then we could no longer guarantee that near circular perturbations would circularize. To demonstrate this, we compute a simulation for $R = 10$ and $r_0 = 5$ in physical space which translates to parameters $D_0 = 0.01$, and $r_0 = 0.5$ in computational space. Furthermore, we take $\epsilon_0 = 0.01$ ($\epsilon = 0.1$) to avoid the weak interaction regime where $D = \mathcal{O}(\epsilon^2)$ and different analysis is required (cf. [39]). While the rescaling in (5.2b) is equivarient in the spatial scales of the problem, it does impact the value

of U_0 on the curve and hence the saturation required to achieve a given b value by (2.41). We wish to use the same b value as in Figure 5.12 and 5.15 which was $b = 0.210$. To achieve this level of saturation for the current parameter set we need to take $\sigma = 5910$. As in Figure 5.15, we initialize the curve with a perturbed radius $r_0 = 0.5 + 0.02\cos(6\theta)$. Figure 5.16 shows the results of this simulation at times $t = 0$ (a), $t = 15$ (b), $t = 31$ (c), and $t = 50$ (d) . We have that the curve initially fattens due to the presence of saturation and then begins to accentuate the small angular perturbations, overall lengthening the curve by the end of the simulation. Even though this curve destabilizes the circular solution it does not itself undergo any breakup instabilities as it evolves.

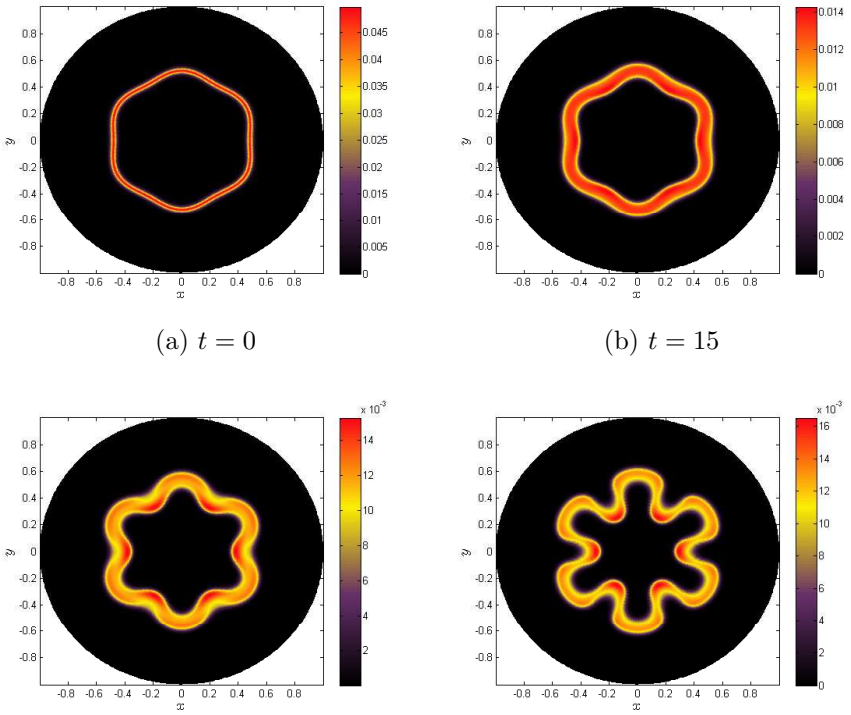

(a) $t = 0$ (b) $t = 15$

(c) $t = 31$ (d) $t = 50$

Figure 5.16: *Experiment 9:* Contour plot of the solution v to (5.1a) with ring geometry at four times with with exponent set $(2, 1, 2, 0)$. The parameter values are $\epsilon_0 = 0.01$, $D_0 = 0.01$, $\tau = 0.1$, and $\sigma = 5910$. This corresponds to $\epsilon = 0.1$, $R = 10$, and $\tau = 0.1$. We take as an initial radius $r_0 = 0.5 + 0.02\cos(6\theta)$.

The delicacy of manipulating ϵ_0 in correspondence with D_0 to avoid the weak interaction regime and the affect of σ increasing for a desired b when the domain length increases, is the side-effect of computing on a fixed domain length. Therefore, it can be difficult to capture some of the rich dynamics that occur on an $\mathcal{O}(\epsilon^{-2})$ timescale for large curves or domains. Fortunately, the techniques developed in Chapter 6 for solving dynamics on arbitrary curves are designed specifically to capture this behaviour and the issues that

arise from full numerical simulations underscores the need for this specialized computational infrastructure.

Chapter 6

Solving the Gierer-Meinhardt Problem for Arbitrary Curves in Two Dimensions

We consider the singular interface limit inhibitor problem (2.19) derived in 2.2.1,

$$\begin{aligned} D\Delta u - u &= 0, \qquad x \in \Omega \\ \frac{\partial u}{\partial n} &= 0, \qquad x \in \partial\Omega \\ u &= U_0(s), \qquad x \in \Gamma \\ \left[\frac{\partial u}{\partial n}\right]_\Gamma &= -\frac{1}{D}\int_{-\infty}^{\infty} f(U_0, \tilde{v}_0)\,\mathrm{d}\hat{\eta}, \qquad x \in \Gamma \end{aligned}$$

subject to

$$V_0 = \kappa_0 + \mathcal{H}\left(\left.\frac{\partial u}{\partial n}\right|_{\eta=0^+} + \left.\frac{\partial u}{\partial n}\right|_{\eta=0^-}\right),$$

with $\mathcal{H}$ given by (2.20).

6.1 Layer Potential Formulation

Before considering the dynamic portion of the curve, we will first look at solving the problem of a static closed curve and then incorporate the velocity condition into the calculation. For either case, we will use the method of Layer potentials [34], which originates in the field of electrostatics. The motivation comes from solving Laplace's equation subject to closed curves and surfaces at fixed potentials or electric fluxes. The electric potential at any point in space is written as an integral of the charge potential difference between a set of delta sources on the curve and the desired point in space. Mathematically, the method is similar to the Green's function formulation. Typically, when solving these problems on non-standard geometries, the method of images is used to modify the Green's function and use the curve data as a source. The method of layer potentials does the opposite of this by using the original free space Green's function (or its derivative) and, instead, considers the source density to be unknown. In order to proceed then, we need the free space Green's function or fundamental solution to the modified Helmholtz equation:

$$D\Delta_q \Psi - \Psi = -\delta(p-q), \qquad p, q \in \mathbb{R}^2$$

where the subscript indicates differentiation with respect to q variables. Imposing that the solution decay at infinity allow us to write the fundamental solution as

$$\Psi(p,q) = \frac{1}{2\pi D} K_0\left(\frac{|p-q|}{\sqrt{D}}\right), \tag{6.1}$$

with K_0 the second modified Bessel function of zeroth order. Using the layer potential formulation we need to find the continuous source density ϕ on Γ such that at any point x in space,

$$u(x) = \int_\Gamma \Psi(x,q)\phi(q)\,\mathrm{d}q_s. \tag{6.2}$$

With the integral in this form, it is often called the single, or monopole, layer potential (as opposed to the double, or dipole, layer potential that uses the derivative of Ψ [34]). The subscript s indicates that the integral is with respect to the arclength of Γ in the q variables. The method of layer potentials, having been created for electrostatic problems, has a rich history of investigation for the Laplace operator (cf. [34], [36], [18]) and so it is useful to exploit those results. The fundamental solution to Laplace's equation,

$$\Delta_q \Phi = -\delta(p-q)$$

is

$$\Phi = -\frac{1}{2\pi}\log|p-q|. \tag{6.3}$$

The following property holds for the Laplace single layer potential with source density ϕ for some curve Γ with Dirichlet boundary conditions $u = f(x), x \in \Gamma$:

$$f(x) = \int_\Gamma \Phi(x,q)\phi(q)\,\mathrm{d}q_s. \qquad x \in \Gamma.$$

Furthermore, the limiting values of the normal derivative with the positive normal on Γ taken as the interior normal of a single curve are

$$\lim_{\alpha\to 0^+} \frac{\partial u}{\partial n_x}(x+\alpha\hat{\mathbf{n}}_{xi}) = \int_\Gamma \frac{\partial \Phi}{\partial n_x}(x,q)\phi(q)\,\mathrm{d}q_s - \frac{\phi(x)}{2}, \tag{6.4a}$$

$$\lim_{\alpha\to 0^+} \frac{\partial u}{\partial n_x}(x-\alpha\hat{\mathbf{n}}_{xi}) = \int_\Gamma \frac{\partial \Phi}{\partial n_x}(x,q)\phi(q)\,\mathrm{d}q_s + \frac{\phi(x)}{2}, \tag{6.4b}$$

where we define normal derivatives with respect to a coordinate system a as,

$$\frac{\partial u}{\partial n_a} = \nabla_a u \cdot \hat{\mathbf{n}}_a.$$

Subtracting (6.4b) from (6.4a) we get

$$\left[\frac{\partial u}{\partial n}\right] = -\left(\hat{\mathbf{n}}\cdot\hat{\mathbf{n}}_i\right)\phi(x), \qquad x\in\Gamma.$$

The subscript i on the normal in (6.4) indicates that we are explicitly considering $\alpha > 0$ to be traversing the inner normal. It is important to make this distinction if Γ has multiple curves since $\hat{\mathbf{n}} = \pm\hat{\mathbf{n}}_i$, depending on curve orientation. For a derivation of the properties of the Laplace operator, see Appendix A. The Dirichlet and Neumann jump properties are inherently tied to the logarithmic singularity as $p \to q$ in $\Phi(p,q)$. If we look at the same limit for the fundamental solution $\Psi(p,q)$ we have [1],

$$\Psi(p,q) \underset{p\to q}{\sim} \frac{1}{D}\Phi(p,q) + R(|p-q|)$$

with R a differentiable function. Therefore the singularity structure between the two problems is the same and we can immediately write down the prop-

erties for the modified Helmholtz problem (2.19):

$$U_0 = \int_\Gamma \Psi(x,q)\phi(q)\,\mathrm{d}q_s, \qquad x \in \Gamma \tag{6.5a}$$

$$\left[\frac{\partial u}{\partial n}\right]\Big|_\Gamma = -(\hat{\mathbf{n}}\cdot\hat{\mathbf{n}}_i)\frac{\phi(x)}{D}, \qquad x \in \Gamma \tag{6.5b}$$

where the extra factor of D comes from the singularity relationship between Φ and Ψ.

6.1.1 Incorporating Neumann Boundary Conditions

We have thus far considered how to solve the problem (2.19) for a closed curve Γ on an unbounded domain. However, the problem we want to ultimately solve has a closed domain with Neumann boundary conditions. This is an easy feature to include in the layer potential formulation since the curve Γ does not have to be a single closed curve, and as such, we can define $\partial\Omega$ to be one of these curves. We can therefore write the new layer potential problem as

$$u(x) = \int_\Gamma \Psi(x,q)\phi(q)\,\mathrm{d}q_s + \int_{\partial\Omega} \Psi(x,q)\phi_b(q)\,\mathrm{d}q_s. \tag{6.6}$$

We introduce a new density ϕ_b here for the integral on the domain boundary and split the integral in this way so that ϕ_b belongs to the, always static, curve $\partial\Omega$ and any dynamic curves belong to the set Γ. By replacing (6.2)

with (6.6), we can define the new jump in normal derivative for $x \in \Gamma$:

$$\lim_{\alpha\to 0^+} \frac{\partial u}{\partial n_x}(x+\alpha\hat{\mathbf{n}}_{xi}) = \int_\Gamma \frac{\partial \Psi}{\partial n_x}(x,q)\phi(q)\,\mathrm{d}q_s - \frac{\phi_(x)}{2D} + \int_{\partial\Omega} \frac{\partial \Psi}{\partial n_x}(x,q)\phi_b(q)\,\mathrm{d}q_s \tag{6.7a}$$

$$\lim_{\alpha\to 0^+} \frac{\partial u}{\partial n_x}(x-\alpha\hat{\mathbf{n}}_{xi}) = \int_\Gamma \frac{\partial \Psi}{\partial n_x}(x,q)\phi(q)\,\mathrm{d}q_s + \frac{\phi_(x)}{2D} + \int_{\partial\Omega} \frac{\partial \Psi}{\partial n_x}(x,q)\phi_b(q)\,\mathrm{d}q_s \tag{6.7b}$$

where we note that substitution is applicable in the last integral for $x \in \Gamma$ and $q \in \partial\Omega$ since then, $\Psi(p,q)$ is no where singular. It is now straightforward to see that (6.5) becomes

$$U_0 = \int_\Gamma \Psi(x,q)\phi(q)\,\mathrm{d}q_s + \int_{\partial\Omega} \Psi(x,q)\phi_b(q)\,\mathrm{d}q_s, \qquad x \in \Gamma \tag{6.8a}$$

$$\left[\frac{\partial u}{\partial n}\right]\Big|_\Gamma = -(\hat{\mathbf{n}}\cdot\hat{\mathbf{n}}_i)\frac{\phi(x)}{D}, \qquad x \in \Gamma. \tag{6.8b}$$

To incorporate the condition $\frac{\partial u}{\partial n} = 0$ on $\partial\Omega$, we once again look at the normal jump formula. This boundary condition states that as we approach the boundary from exterior to Ω, the flux must vanish and therefore

$$\lim_{\alpha\to 0^+} \frac{\partial u}{\partial n}(x+\alpha\hat{\mathbf{n}}_{\Omega e}) = 0, \qquad x \in \partial\Omega,$$

where $\hat{\mathbf{n}}_{\Omega e}$ is the normal from $\partial\Omega$ pointing to the exterior of Ω. Since we are considering the exterior normal and $\hat{\mathbf{n}}_{\Omega e} = -\hat{\mathbf{n}}_{\Omega i}$ then we use (6.4b) and get

$$0 = \int_{\Gamma} \frac{\partial \Psi}{\partial n_{\Omega}}(x,q)\phi(q)\,\mathrm{d}q_s + \frac{\phi_b(x)}{2D} + \int_{\partial\Omega} \frac{\partial \Psi}{\partial n_{\Omega}}(x,q)\phi_b(q)\,\mathrm{d}q_s, \qquad x \in \partial\Omega. \tag{6.9}$$

6.1.2 Scaled Arclength parametrization

In order to compute the integrals, we will use a scaled arclength parametrization. First consider that Γ is composed of M distinct closed curves,

$$\Gamma = \bigcup_{j=1}^{M} \Gamma_j,$$

and write (6.6) as

$$u(x) = \sum_{j=1}^{M} \int_{\Gamma_j} \Psi(x,q_j)\phi(q_j)\,\mathrm{d}q_{js} + \int_{\partial\Omega} \Psi(x,q)\phi_b(q)\,\mathrm{d}q_s, \qquad x \in \Omega \cup \Gamma. \tag{6.10}$$

Define the scaled arclength coordinate as $\sigma = s_j/L_j$, where L_j is the length of curve j. In order to not confuse this with the saturation parameter σ from the previous chapters, we will now reserve $\hat{\sigma}$ for the saturation parameter. Let the parametrization of Γ_j be written as

$$z_j(\sigma) = \langle z_{1j}(\sigma), z_{2j}(\sigma) \rangle,$$

and the parametrization of $\partial\Omega$ as

$$z_b(\sigma) = \langle z_{1b}(\sigma), z_{2b}(\sigma) \rangle.$$

With this in mind, we can write (6.10) for $x \in \Omega \cup \Gamma$ as

$$u(x) = \sum_{j=1}^{M} L_j \int_0^1 \Psi(x, z_j(\sigma)) \phi_j(\sigma) \, \mathrm{d}\sigma + L_{\partial\Omega} \int_0^1 \Psi(x, z_b(\sigma)) \phi_b(\sigma) \, \mathrm{d}\sigma, \quad (6.11)$$

where $\phi_j = \phi(z_j(\sigma))$. We can write the Dirichlet condition (6.8a) as

$$\begin{aligned} U_0(\sigma^*) =& L_m \int_0^1 \Psi(z_m(\sigma^*), z_m(\sigma)) \phi_m(\sigma) \, \mathrm{d}\sigma \\ &+ \sum_{\substack{j=1 \\ j \neq m}}^{M} L_j \int_0^1 \Psi(z_m(\sigma^*), z_j(\sigma)) \phi_j(\sigma) \, \mathrm{d}\sigma \\ &+ L_{\partial\Omega} \int_0^1 \Psi(z_m(\sigma^*), z_b(\sigma)) \phi_b(\sigma) \, \mathrm{d}\sigma, \end{aligned} \quad (6.12)$$

where we have isolated the integral with the singularity separately from the sum. We can write the jump condition (6.8b) as

$$\phi_m(\sigma^*) = (\hat{\mathbf{n}} \cdot \hat{\mathbf{n}}_i) \int_{-\infty}^{\infty} f(U_0(\sigma^*), \tilde{v}_0) \, \mathrm{d}\hat{\eta} \quad (6.13)$$

where we have simplified the jump in the normal derivative using (2.19d). Finally, we can write the Neumann boundary condition (6.9) as

$$\sum_{j=1}^{M} L_j \int_0^1 \frac{\partial \Psi}{\partial n_\Omega}(z_b(\sigma^*), z_j(\sigma))\phi_j(\sigma)\,\mathrm{d}\sigma + \frac{\phi_b(\sigma^*)}{2D} + L_{\partial\Omega} \int_0^1 \frac{\partial \Psi}{\partial n_\Omega}(z_b(\sigma^*), z_b(\sigma))\phi_b(\sigma)\,\mathrm{d}\sigma = 0. \tag{6.14}$$

A Note on Uniqueness

We briefly comment on the uniqueness of the boundary value problem. When the Dirichlet condition U_0 is prescribed then it can be shown that the solution to (6.12) is unique [68]. However, since the Dirichlet value on the curve is an unknown in the system, the guarantee of uniqueness no longer applies and solution bifurcations may occur. We will demonstrate an example of non-unique solutions when we consider the GMS model in section 6.3.

6.1.3 Curve Dynamics

The motion for the curve will be dictated by the normal velocity condition given by (2.19e). However, in using the scaled arclength formulation, if a solution exists then the same solution would exist for any rotation of the curve. To remedy this, we will introduce a tangential velocity but give it zero mean to prevent a rotation from an initial configuration. With these considerations in mind for each $\sigma^* \in [0, 1)$, we have that the motion on curve m is given by

$$\frac{\mathrm{d}z_m}{\mathrm{d}t} = V\hat{\mathbf{n}} + V_t\hat{\mathbf{t}}, \tag{6.15}$$

and that

$$\int_0^1 V_t \, \mathrm{d}\sigma = \int_0^1 \frac{\mathrm{d}z_m}{\mathrm{d}t} \cdot \hat{\mathbf{t}} \, \mathrm{d}\sigma = 0. \tag{6.16}$$

By prescribing the normal velocity and enforcing equal arclength ($|z_{m_\sigma}| = L$) for all time then the mean value condition is sufficient to implicitly impose a tangential velocity [64]. Note that this is in contrast to imposing a tangential velocity that guarantees a given parametrization is equal arclength [84].

6.1.4 Normal Velocity Condition

We now want to incorporate the velocity condition given by (2.19e) into the layer potential formulation. This turns out to be extremely straightforward by using the jump conditions (6.7),

$$\begin{aligned} &\lim_{\alpha \to 0^+} \frac{\partial u}{\partial n_x}(x + \alpha \hat{\mathbf{n}}_{xi}) + \lim_{\alpha \to 0^+} \frac{\partial u}{\partial n_x}(x - \alpha \hat{\mathbf{n}}_{xi}) \\ &= 2 \int_\Gamma \frac{\partial \Psi}{\partial n_x}(x, q) \phi(q) \, \mathrm{d}q_s + 2 \int_{\partial\Omega} \frac{\partial \Psi}{\partial n_x}(x, q) \phi_b(q) \, \mathrm{d}q_s. \end{aligned}$$

In (2.19e) we need to add the derivative contributions of $x + \alpha\hat{\mathbf{n}}$ with $\hat{\mathbf{n}} = \pm\hat{\mathbf{n}}_i$. However, this only affects the sign on the non-integral term in (6.7) and will

always vanish when added. Therefore, we have that

$$V(\sigma^*) = \kappa + 2\mathcal{H}(U_0)\left(L_m \int_0^1 \frac{\partial \Psi}{\partial n_{z_m^*}}(z_m(\sigma^*), z_m(\sigma))\phi_m(\sigma)\,\mathrm{d}\sigma + \sum_{\substack{j=1 \\ j\neq m}}^{M} L_j \int_0^1 \frac{\partial \Psi}{\partial n_{z_m^*}}(z_m(\sigma^*), z_j(\sigma))\phi_j(\sigma)\,\mathrm{d}\sigma + L_{\partial\Omega}\int_0^1 \frac{\partial \Psi}{\partial n_{z_m^*}}(z_m(\sigma^*), z_b(\sigma))\phi_b(\sigma)\,\mathrm{d}\sigma\right), \tag{6.17}$$

where we have defined, $z_m^* = z_m(\sigma^*)$.

6.1.5 Singular Integration

If we attempt to solve (6.12), (6.13), (6.14), and (6.17) using standard numerical techniques, there will be an issue when some of the integrands become singular. First consider the integral

$$\int_0^1 \Psi(z(\sigma^*), z(\sigma))\phi(\sigma)\,\mathrm{d}\sigma = \frac{1}{2\pi D}\int_0^1 K_0\left(\left|\frac{z(\sigma) - z(\sigma^*)}{\sqrt{D}}\right|\right)\phi(\sigma)\,\mathrm{d}\sigma, \tag{6.18}$$

which is singular when $\sigma = \sigma^*$. To determine the nature of the singularity, we perform an asymptotic expansion as $\sigma \approx \sigma^*$,

$$z(\sigma) \sim z(\sigma^*) + L(\sigma - \sigma^*)\hat{\mathbf{t}}_{z^*} + \frac{L^2\kappa}{2}(\sigma - \sigma^*)^2\hat{\mathbf{n}}_{z^*} + \mathcal{O}(\sigma - \sigma^*)^3 \tag{6.19}$$

with $\hat{\mathbf{t}}_{z^*}$ and $\hat{\mathbf{n}}_{z^*}$, the tangent and normal vectors at $z(\sigma^*)$ respectively. Here we have used that

$$\left|\frac{\mathrm{d}z}{\mathrm{d}\sigma}\right| = L, \quad \left|\frac{\mathrm{d}^2 z}{\mathrm{d}\sigma^2}\right| = L^2\kappa,$$

with κ the curvature at $z(\sigma^*)$ and L the length. We can compute that the asymptotic norm is

$$|z(\sigma) - z(\sigma^*)| = L|\sigma - \sigma^*| + \mathcal{O}(\sigma - \sigma^*)^3, \tag{6.20}$$

and therefore have that the Bessel function for $\sigma - \sigma^* \ll 1$ has the form [1],

$$K_0\left(\left|\frac{z(\sigma) - z(\sigma^*)}{\sqrt{D}}\right|\right) \sim \log\left(\frac{2\sqrt{D}}{L}\right) - \gamma - \log|\sigma - \sigma^*| + \mathcal{O}(\sigma - \sigma^*)^2,$$

where γ is the Euler-Mascheroni constant. To alleviate the logarithmic singularity, we will add and subtract the log term to (6.18), to get

$$\begin{aligned}
&\int_0^1 \Psi(z(\sigma^*), z(\sigma))\phi(\sigma)\,\mathrm{d}\sigma \\
=&\frac{1}{2\pi D}\left(\int_0^1 K_0\left(\left|\frac{z(\sigma) - z(\sigma^*)}{\sqrt{D}}\right|\right) + \log|\sigma - \sigma^*|\right)\phi(\sigma)\,\mathrm{d}\sigma \\
&- \frac{1}{2\pi D}\int_0^1 \log|\sigma - \sigma^*|\phi(\sigma)\,\mathrm{d}\sigma,
\end{aligned} \tag{6.21}$$

where the integral with the Bessel function is now non-singular $\forall\sigma \in [0, 1]$. Due to the periodicity of the curve, there is a slight issue with this formulation and that is that $\sigma^* = 0$ also induces a singularity at $\sigma = 1$. Furthermore, as σ^* gets close to zero, it begins to notice the effects of a singularity at $\sigma = -1$

as well, though we classify this as a weak singularity since it is outside of the domain of σ. Since $\sigma^* \in [0,1)$, there is no effect from the weak singularity at $\sigma = 1$. To remedy the effects of the periodicity inducing singularities, we will remove the singularities that are a full period from σ^* on either side and write (6.21) as

$$\begin{aligned}
&\int_0^1 \Psi(z(\sigma^*), z(\sigma))\phi(\sigma)\,\mathrm{d}\sigma = \\
&\frac{1}{2\pi D}\left(\int_0^1 K_0\left(\left|\frac{z(\sigma)-z(\sigma^*)}{\sqrt{D}}\right|\right) + \mathcal{L}(\sigma,\sigma^*)\right)\phi(\sigma)\,\mathrm{d}\sigma \\
&-\frac{1}{2\pi D}\int_0^1 \log|\sigma-\sigma^*|\phi(\sigma)\,\mathrm{d}\sigma - \frac{1}{2\pi D}\int_0^1 \log|\sigma-(\sigma^*+1)|\phi(\sigma)\,\mathrm{d}\sigma \\
&-\frac{1}{2\pi D}\int_0^1 \log|\sigma-(\sigma^*-1)|\phi(\sigma)\,\mathrm{d}\sigma, \qquad (6.22)
\end{aligned}$$

where

$$\mathcal{L}(\sigma,\sigma^*) = \log|\sigma-\sigma^*| + \log|\sigma-(\sigma^*+1)| + \log|\sigma-(\sigma^*-1)|. \qquad (6.23)$$

Considering the singularity properties of the Bessel functions we will avoid evaluating at the singularity directly by defining a function $\mathcal{K}_0$ as

$$\mathcal{K}_0(z(\sigma),z(\sigma^*)) = \begin{cases} K_0\left(\left|\frac{z(\sigma)-z(\sigma^*)}{\sqrt{D}}\right|\right) + \mathcal{L}(\sigma,\sigma^*), & \sigma \neq \sigma^* \\ \log\left|\frac{2\sqrt{D}(\sigma-(\sigma^*+1))(\sigma-(\sigma^*-1))}{L}\right| - \gamma, & \sigma = \sigma^* \neq 0 \\ \log\left|\frac{2\sqrt{D}(\sigma+1)}{L}\right| - \gamma, & \sigma^* = 0, \sigma = 0,1 \end{cases} . \qquad (6.24)$$

Notice that using the asymptotic form is valid at $\sigma = \sigma^*$ because the error terms vanish exactly. Finally, also define

$$\begin{aligned}\mathcal{S} = &\int_0^1 \log|\sigma - \sigma^*|\phi(\sigma)\,\mathrm{d}\sigma + \int_0^1 \log|\sigma - (\sigma^*+1)|\phi(\sigma)\,\mathrm{d}\sigma \\ &+ \int_0^1 \log|\sigma - (\sigma^*-1)|\phi(\sigma)\,\mathrm{d}\sigma,\end{aligned} \tag{6.25}$$

so that (6.22) becomes

$$\int_0^1 \Psi(z(\sigma^*), z(\sigma))\phi(\sigma)\,\mathrm{d}\sigma = \frac{1}{2\pi D}\left(\int_0^1 \mathcal{K}_0(z(\sigma), z(\sigma^*))\phi(\sigma)\,\mathrm{d}\sigma - \mathcal{S}\right). \tag{6.26}$$

Next consider the integral,

$$\begin{aligned}&\int_0^1 \frac{\partial \Psi}{\partial n_{z^*}}(z(\sigma^*), z(\sigma))\phi(\sigma)\,\mathrm{d}\sigma = \\ &\frac{1}{2\pi D^{3/2}}\int_0^1 K_1\left(\left|\frac{z(\sigma)-z(\sigma^*)}{\sqrt{D}}\right|\right)\frac{(z(\sigma)-z(\sigma^*))\cdot\hat{\mathbf{n}}_{z^*}}{|z(\sigma)-z(\sigma^*)|}\phi(\sigma)\,\mathrm{d}\sigma,\end{aligned} \tag{6.27}$$

where K_1 is the second order modified Bessel function of the second kind. Using the expansion for $z(\sigma)$ near σ^* from (6.19) we get,

$$\begin{aligned}K_1\left(\left|\frac{z(\sigma)-z(\sigma^*)}{\sqrt{D}}\right|\right) &\sim \frac{\sqrt{D}}{L}\frac{1}{|\sigma-\sigma^*|} + \mathcal{O}(\sigma-\sigma^*) \\ (z(\sigma)-z(\sigma^*))\cdot\hat{\mathbf{n}}_{z^*} &\sim \frac{L^2\kappa}{2}(\sigma-\sigma^*)^2 + \mathcal{O}(\sigma-\sigma^*)^4,\end{aligned}$$

and along with the expansion of the norm (6.20) we have

$$K_1\left(\left|\frac{z(\sigma)-z(\sigma^*)}{\sqrt{D}}\right|\right)\frac{(z(\sigma)-z(\sigma^*))\cdot\hat{\mathbf{n}}_{z^*}}{|z(\sigma)-z(\sigma^*)|} \sim \sqrt{D}\frac{\kappa}{2} + \mathcal{O}(\sigma-\sigma^*).$$

Therefore, we see that unlike the integral involving the zeroth order Bessel function, K_1 is not singular at $\sigma = \sigma^*$ and so we do not have to alter the integral by removing any singularities. However, to avoid the numerical difficulties of evaluating directly at $\sigma = \sigma^*$, we define the following function

$$\mathcal{K}_1(z(\sigma), z(\sigma^*)) = \begin{cases} \frac{1}{\sqrt{D}} K_1\left(\left|\frac{z(\sigma)-z(\sigma^*)}{\sqrt{D}}\right|\right) \frac{(z(\sigma)-z(\sigma^*))\cdot \hat{\mathbf{n}}_{z^*}}{|z(\sigma)-z(\sigma^*)|}, & \sigma \neq \sigma^* \\ \frac{\kappa}{2}, & \sigma = \sigma^* \end{cases}, \quad (6.28)$$

where we note that if $\sigma^* = 0$ then due to the periodicity we evaluate the second branch if $\sigma = 0$ or $\sigma = 1$. With (6.28) we have that (6.27) becomes

$$\int_0^1 \frac{\partial \Psi}{\partial n_{z^*}}(z(\sigma^*), z(\sigma))\phi(\sigma)\,\mathrm{d}\sigma = \frac{1}{2\pi D}\int_0^1 \mathcal{K}_1(z(\sigma), z(\sigma^*))\phi(\sigma)\,\mathrm{d}\sigma. \quad (6.29)$$

We are now ready to discuss the numerical solution of this problem.

6.2 Numerical Formulation of Curve Motion Problem

Consider a uniform discretization of σ, $\sigma_i = i\Delta\sigma$ with $\Delta\sigma = \frac{1}{N}$ where N are the chosen number of grid points. Define $z_{ij} = z_j(\sigma_i)$ as the discretized curve positions. Using a standard centered difference discretization we have

$$\left.\frac{\mathrm{d}z_j}{\mathrm{d}\sigma}\right|_{\sigma=\sigma_i} = \frac{z_{i+1,j} - z_{i-1,j}}{2\Delta\sigma} + \mathcal{O}(\Delta\sigma^2),$$
$$\left.\frac{\mathrm{d}^2 z_j}{\mathrm{d}\sigma^2}\right|_{\sigma=\sigma_i} = \frac{z_{i+1,j} - 2z_{i,j} + z_{i-1,j}}{\Delta\sigma^2} + \mathcal{O}(\Delta\sigma^2),$$

which we can use to define the unit tangent, normal vectors, and curvature up to $\mathcal{O}(\Delta\sigma^2)$

$$\hat{\mathbf{t}}_{i,j} = \frac{z_{j_\sigma}(\sigma_i)}{L_j} = \frac{z_{i+1,j} - z_{i-1,j}}{2L_j\Delta\sigma}, \tag{6.30}$$

$$\hat{\mathbf{n}}_{i,j} = \langle -\hat{\mathbf{t}}_{i,j_y}, \hat{\mathbf{t}}_{i,j_x} \rangle, \tag{6.31}$$

$$\kappa_{i,j} = \frac{z_{j_{\sigma\sigma}}(\sigma_i) \cdot \hat{\mathbf{n}}_{i,j}}{L_j^2} = \frac{1}{2\Delta\sigma^3 L_j^3} \left(z_{i+1,j} - 2z_{i,j} + z_{i-1,j}\right) \cdot \langle -\hat{\mathbf{t}}_{i,j_y}, \hat{\mathbf{t}}_{i,j_x} \rangle. \tag{6.32}$$

Here the x and y subscripts indicate the first and second components of the vector respectively. For the time discretization with a time step Δt, we will consider the implicit Backward Euler method so that for each curve m, (6.15) becomes

$$(z_m^{k+1} - z_m^k) \cdot \hat{\mathbf{n}}^{k+1} = \Delta t V^{k+1},$$

for the normal component where the subscript k indicates $t = k\Delta t$ and

$$\int_0^1 (z_m^{k+1} - z_m^k) \cdot \hat{\mathbf{t}}^{k+1} \, \mathrm{d}\sigma = 0,$$

for the tangential component where we have used the zero mean condition (6.16). This is closed by prescribing the equal arclength parametrization,

$$\left| \frac{\mathrm{d} z_m^{k+1}}{\mathrm{d}\sigma} \right| = L_m, \tag{6.33}$$

which we can discretize using (6.20) to get

$$|z_{i+1,m}^{k+1} - z_{i,m}^{k+1}| = L_m \Delta\sigma. \tag{6.34}$$

6.2.1 Discretizing Integrals

By doing the integral splitting in section 6.1.5 we are left to discretize regular and singular integrals. The regular integrals can be discretized using any of the standard interpolating methods which will all be of the form,

$$\int_0^1 f(\sigma)\,\mathrm{d}\sigma = \sum_{i=0}^{N} \alpha_i f_i \Delta\sigma,$$

where $f_i = f(\sigma_i)$ and α_i are the quadrature weights. Unless otherwise specified, since our scheme is accurate to $\mathcal{O}(\Delta\sigma^2)$ from the finite difference discretization, we will consider the quadrature weights to be those that come from the trapezoid rule [6],

$$\alpha_i = \begin{cases} \frac{1}{2}, & i = 0, i = N \\ 1, & \text{else} \end{cases}.$$

Generally due to periodicity in z, the integral can be written as a sum over N points however, we generalize because some of the integrals (such as those in (6.24)) depend on σ explicitly and are not periodic.

Discretizing Singular Integrals

It is a slightly more delicate issue to consider the discretization of singular integrals. Fortunately, due to the integral splitting in section 6.1.5, we only have to consider integrals of the form,

$$\int_0^1 f(\sigma)\log|\sigma - (\sigma^* + a)|\,\mathrm{d}\sigma, \tag{6.35}$$

where $\sigma^* \in [0,1)$ is one of the discretized gridpoints ($\sigma^* = j\Delta\sigma$) and $a = -1, 0, 1$ is the shifted singularity being removed. The goal is to develop a discretization so that we can write (6.35) as

$$\int_0^1 f(\sigma) \log|\sigma - (\sigma^* + a)| \, \mathrm{d}\sigma = \sum_{i=0}^{N} w_i f_i \tag{6.36}$$

for some weights w_i. High order quadrature techniques have been developed to handle singularities of logarithmic type [5]. They rely on a weighted trapezoid rule method that adds gridpoints near the singularity as necessary to counterbalance the singular behaviour. This technique will not be employed here and instead we consider product integration [6] which allows us to continue to use our uniform spatial discretization. It is worth noting that the singular integral decomposition means that the singular integrals depend only on σ and not on the specific curves themselves, and therefore higher order quadrature methods could easily be supplemented here if desired without impacting the rest of the formulation significantly. The idea of the product integration is to locally interpolate on $f(\sigma)$ using Lagrange interpolation and analytically perform the polynomial-logarithmic integration that results. We start by writing,

$$\int_0^1 f(\sigma) \log|\sigma - \sigma^*| \, \mathrm{d}\sigma = \sum_{k=1}^{N} \int_{(k-1)\Delta\sigma}^{k\Delta\sigma} f(\sigma) \log|\sigma - j\Delta\sigma| \, \mathrm{d}\sigma,$$

where we are explicitly considering the case $a = 0$ which we will generalize later. In what follows we consider the case of $f(\sigma)$ having a linear interpolation but the mechanism easily extends for higher order interpolants. The

local linear Lagrange interpolation of $f(\sigma)$ on $[(k-1)\Delta\sigma, k\Delta\sigma]$ is

$$f \sim \frac{(\sigma - (k-1)\Delta\sigma)f_k - (\sigma - k\Delta\sigma)f_{k-1}}{\Delta\sigma},$$

and so,

$$\int_0^1 f(\sigma)\log|\sigma-\sigma^*|\,\mathrm{d}\sigma = \sum_{k=1}^{N}\frac{f_k}{\Delta\sigma}\int_{(k-1)\Delta\sigma}^{k\Delta\sigma}(\sigma-(k-1)\Delta\sigma)\log|\sigma-j\Delta\sigma|\,\mathrm{d}\sigma + \frac{f_{k-1}}{\Delta\sigma}\int_{(k-1)\Delta\sigma}^{k\Delta\sigma}(k\Delta\sigma-\sigma)\log|\sigma-j\Delta\sigma|\,\mathrm{d}\sigma. \quad (6.37)$$

Consider evaluating the first integral in this expression by letting $u = (\sigma - (k-1)\Delta\sigma)/\Delta\sigma$,

$$\begin{aligned}
&\frac{1}{\Delta\sigma}\int_{(k-1)\Delta\sigma}^{k\Delta\sigma}(\sigma-(k-1)\Delta\sigma)\log|\sigma-j\Delta\sigma|\,\mathrm{d}\sigma\\
&= \Delta\sigma\left(\log\Delta\sigma\int_0^1 u\,\mathrm{d}u + \int_0^1 u\log|u+(k-1)-j|\,\mathrm{d}u\right)\\
&= \frac{\Delta\sigma\log\Delta\sigma}{2} + \Delta\sigma\psi_{1,j}(k-1),
\end{aligned}$$

where

$$\psi_{1,j}(y) = \int_0^1 u\log|u+y-j|\,\mathrm{d}u,$$

is computed analytically for any y and j. Using the same transformation on the second integral in (6.37) we get

$$\frac{1}{\Delta\sigma}\int_{(k-1)\Delta\sigma}^{k\Delta\sigma}(k\Delta\sigma-\sigma)\log|\sigma-j\Delta\sigma|\,\mathrm{d}\sigma = \frac{\Delta\sigma\log\Delta\sigma}{2} + \Delta\sigma\psi_{2,j}(k-1),$$

where

$$\psi_{2,j}(y) = \int_0^1 (1-u)\log|u+y-j|\,\mathrm{d}u.$$

Using these functions we can define the following weights:

$$\begin{aligned} w_{0,j} &= \frac{\Delta\sigma\log\Delta\sigma}{2} + \Delta\sigma\psi_{2,j}(0), \\ w_{N,j} &= \frac{\Delta\sigma\log\Delta\sigma}{2} + \Delta\sigma\psi_{1,j}(N-1), \\ w_{i,j} &= \Delta\sigma\log\Delta\sigma + \Delta\sigma(\psi_{1,j}(i-1) + \psi_{2,j}(i)), \qquad i \neq 0, N \end{aligned}$$

and can evaluate the discretized integral as a sum using (6.36). Notice that the computational cost for computing (6.35) in this way is not of great significance because the weights can be precomputed and thus, the method has the same local computational cost as integrating a non-singular function. The errors for product integration are of the same order as the equivalent methods for non-singular integrals [6], i.e. the product integration rule using linear interpolation here is $\mathcal{O}(\Delta\sigma^2)$ in line with the Trapezoid rule for regular integrals. If instead of $a = 0$, we have $a = 1$ ($a = -1$) in (6.35) we define the positive (negative) complementary functions:

$$\begin{aligned} \psi^{c\pm}_{1,j}(y) &= \int_0^1 u\log|u+y-j\mp N|\,\mathrm{d}u, \\ \psi^{c\pm}_{2,j}(y) &= \int_0^1 (1-u)\log|u+y-j\mp N|\,\mathrm{d}u, \end{aligned}$$

and the positive (negative) complementary weights:

$$\begin{aligned} w_{0,j}^{c\pm} &= \frac{\Delta\sigma \log \Delta\sigma}{2} + \Delta\sigma \psi_{2,j}^{c\pm}(0), \\ w_{N,j}^{c\pm} &= \frac{\Delta\sigma \log \Delta\sigma}{2} + \Delta\sigma \psi_{1,j}^{c\pm}(N-1), \\ w_{i,j}^{c\pm} &= \Delta\sigma \log \Delta\sigma + \Delta\sigma(\psi_{1,j}^{c\pm}(k-1) + \psi_{2,j}^{c\pm}(k)), \qquad i \neq 0, N. \end{aligned}$$

To demonstrate the error accuracy of the method we will consider the case $\int_0^1 \cos(\sigma) \log|\sigma| \, \mathrm{d}\sigma$. Analytically we can integrate by parts to get that

$$\int_0^1 \cos(\sigma) \log|\sigma| \, \mathrm{d}\sigma = -\int_0^1 \frac{\sin(\sigma)}{\sigma} \, \mathrm{d}\sigma = -\mathrm{Si}(1).$$

From [1] we can write this as a series,

$$-\sum_{k=0}^{\infty} \frac{(-1)^{k-1}}{(2k-1)(2k-1)!} \approx -0.94608307036718301494$$

where we obtained the approximation using 100 terms. We will use this as the numerical value for comparison in our integrals. Table 6.1 shows the results for various values of $\Delta\sigma$ along with the error ratio demonstrating the $\Delta\sigma^2$ convergence.

$\Delta\sigma$	Error	Ratio
0.1	7.73×10^{-4}	—
0.05	1.95×10^{-4}	3.96
0.025	4.90×10^{-5}	3.98
0.0125	1.22×10^{-5}	3.99
0.00625	3.08×10^{-6}	4.00

Table 6.1: Numerical-analytic comparison of integrating $\int_0^1 \cos(\sigma) \log|\sigma| \mathrm{d}\sigma$ using the product integration method with linear interpolation.

Without going through the details of defining the functions, we perform the same integration as in Table 6.1 using quadratic interpolation instead of linear interpolation with the errors and ratios in Table 6.2. Notice that the ratio shows an $\mathcal{O}(\Delta\sigma^4)$ reduction as would be expected with a standard Simpsons integration rule [6].

$\Delta\sigma$	Error	Ratio
0.1	1.70×10^{-6}	—
0.05	1.02×10^{-7}	16.57
0.025	6.27×10^{-9}	16.30
0.0125	3.89×10^{-10}	16.15
0.00625	2.42×10^{-11}	16.04

Table 6.2: Numerical-analytic comparison of integrating $\int_0^1 \cos(\sigma) \log|\sigma| \mathrm{d}\sigma$ using the product integration method with quadratic interpolation.

Finally, to demonstrate the importance of multiple singularity removal in the integral splitting (6.26), consider a unit circle,

$$z = \langle \cos(2\pi\sigma), \sin(2\pi\sigma) \rangle,$$

and integrate

$$\int_0^1 K_0 \left(|z(\sigma) - z(\sigma^*)| \right) \mathrm{d}\sigma \tag{6.38}$$

for a range of $\sigma^* \in [0, 1)$. Though analytic results are not available, the symmetry of the circle indicates that the value of this integral should be the same for any of the singularities. Figure 6.1 shows the value of integrating (6.38) for every $\sigma^* = k\Delta\sigma$, $k \in [0, N-1]$, $\Delta\sigma = 0.02$. The solid line is the result where both of the singularities, a full period away on either side,

are removed and the dashed line is the value when only the actual singular value is removed. While the results are fairly constant in the middle, for the dashed-line, there are errors greater than the quadrature error near the endpoints because the other singularities are being felt due to the periodicity. These artifacts are nearly removed for the solid curve.

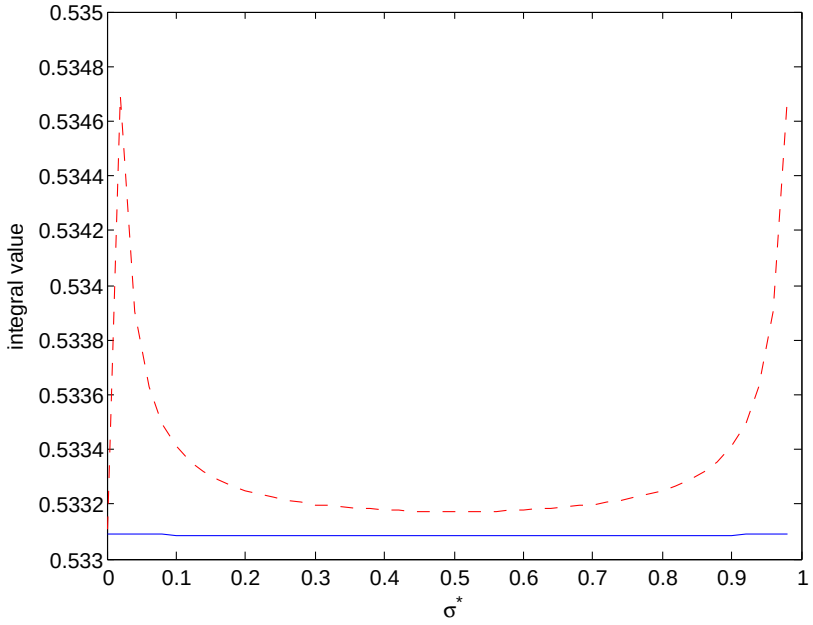

Figure 6.1: This shows the value of integrating (6.38) with $\Delta\sigma = 0.02$ for all the possible discrete values of $\sigma^* \in [0, 1)$. The blue solid curve represents the technique used in the integral splitting (6.26) where singularities within a full period on either side of the true singularity are removed while the red dashed curve represents removing only the true singular value.

It may seem suspicious that we do not recover a constant exactly for the solid curve since splitting the integral should not change its periodicity and, indeed that is the case. However, the sole logarithmic integrals are handled exactly while the logarithmic terms that couple with the Bessel functions are handled

through the trapezoid rule (or some other quadrature rule) and hence will have numeric error. This error is the source of breaking the periodicity in the result. If we look at the asymptotic error expansion for the trapezoid rule through the Euler-Maclaurin formula [6] we have,

$$E_{\Delta\sigma}(\sigma^*) = \int_0^1 \mathcal{K}_0(z(\sigma), z(\sigma^*))\,\mathrm{d}\sigma - T_{\Delta\sigma}(\sigma^*) \sim \frac{\Delta\sigma^2}{12} F(\sigma^*) + \mathcal{O}(\Delta\sigma^4),$$

where $\mathcal{K}_0(z(\sigma), z(\sigma^*))$ is given by (6.24), $T_{\Delta\sigma}$ is the trapezoid approximation to the integral, and

$$F(\sigma^*) = \mathcal{K}_{0_\sigma}(z(0), z(\sigma^*)) - \mathcal{K}_{0_\sigma}(z(1), z(\sigma^*)). \tag{6.39}$$

$F(\sigma^*)$ has an absolute maximum at $\sigma^* = \frac{1}{2}$ and absolute minimum at $\sigma^* = 0$ by recalling that $0 \leq \sigma^* < 1$ (see Figure 6.2).

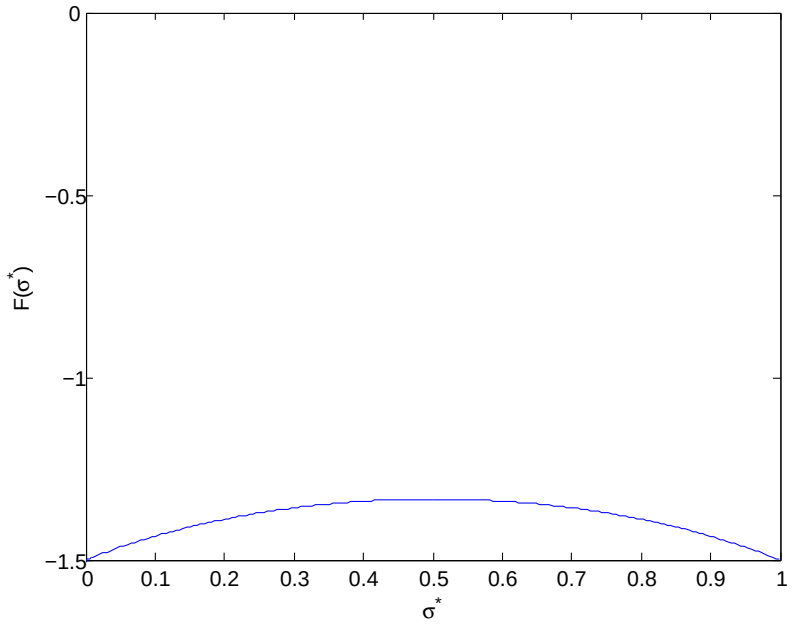

Figure 6.2: The plot of $F(\sigma^*)$ as defined in (6.39). The function has an absolute maximum at $\sigma^* = 0.5$ and and absolute minimum at $\sigma^* = 0$.

If we consider the difference in $F(\sigma^*)$ at its maximum and minimum values we have

$$F_{\max} - F_{\min} = \frac{1}{6},$$

and therefore,

$$\Delta_{\max} E_{\Delta\sigma} = \frac{\Delta\sigma^2}{12}(F_{\max} - F_{\min}) = \frac{\Delta\sigma^2}{72} \ll \Delta\sigma^2.$$

The error introduced by losing the periodicity is smaller than the quadrature error and therefore of little significance. This procedure could be extended using Richardson extrapolation to account for non-periodic errors in higher order quadrature schemes as well.

6.2.2 Numerical Equations

Having discretized the integrals, we can now write the full system of equations that we need to solve numerically. The normal and tangential velocity equations and the equal arclength parametrization are

$$z_{i,m}^{k+1} \cdot \hat{\mathbf{n}}_i^{k+1} = z_{i,m}^{k} \cdot \hat{\mathbf{n}}_i^{k+1} + \Delta t V_{i,m}^{k+1}, \tag{6.40a}$$

$$\sum_{i=0}^{N} \alpha_i (z_{i,m}^{k+1} - z_{i,m}^{k}) \cdot \hat{\mathbf{t}}_i^{k+1} \Delta\sigma = 0, \tag{6.40b}$$

$$|z_{i+1,m}^{k+1} - z_{i,m}^{k+1}| = L_m \Delta\sigma. \tag{6.40c}$$

The equations that prescribe the density ϕ and the value U_0 become,

$$\begin{aligned} U_{0_{i,m}}^{k+1} = {} & \frac{L_m}{2\pi D} \sum_{l=0}^{N} \left(\alpha_l \mathcal{K}_0(z_{l,m}^{k+1}, z_{i,m}^{k+1}) \phi_{l,m}^{k+1} \Delta\sigma - W_{l,i} \phi_{l,m}^{k+1} \right) \\ & + \sum_{\substack{j=1 \\ j \neq m}}^{M} \frac{L_j}{2\pi D} \sum_{l=0}^{N} \alpha_l K_0 \left(\left| \frac{z_{l,j}^{k+1} - z_{i,m}^{k+1}}{\sqrt{D}} \right| \right) \phi_{l,j}^{k+1} \Delta\sigma \\ & + \frac{L_{\partial\Omega}}{2\pi D} \sum_{l=0}^{N} \alpha_l K_0 \left(\left| \frac{z_{b_l} - z_{i,m}^{k+1}}{\sqrt{D}} \right| \right) \phi_{b_l}^{k+1} \Delta\sigma, \end{aligned} \tag{6.40d}$$

$$\phi_{i,m}^{k+1} = (\hat{\mathbf{n}}^0 \cdot \hat{\mathbf{n}}_i^0) \int_{-\infty}^{\infty} f(U_{0_{i,m}}^{k+1}, \tilde{v}_0) \, \mathrm{d}\hat{\eta}, \tag{6.40e}$$

where $W_{i,j} = w_{i,j} + w_{i,j}^{c+} + w_{i,j}^{c-}$. The superscript 0 on the normal vector is used because the relative orientation of curves does not change and so the direction of the normals is set by the initial configuration. Notice that separating the boundary component is convenient here because the boundary curve does not change in time, hence there is no $k+1$ on the z_{bl} term. Also,

we leave the integral in (6.40e) undiscretized because it is an integration over $\hat{\eta}$ and not over the curve where the unknown values are specified. Finally, we can write the Neumann boundary and velocity condition as

$$0 = \sum_{j=1}^{M} \frac{L_j}{2\pi D} \sum_{l=0}^{N} \alpha_l \mathcal{K}_1(z_{l,j}^{k+1}, z_{b_l}) \phi_{l,j}^{k+1} \Delta\sigma + \frac{\phi_{b_i}^{k+1}}{2} + \frac{L_{\partial\Omega}}{2\pi D} \sum_{l=0}^{N} \alpha_l \mathcal{K}_1(z_{b_l}, z_{b_i}) \phi_{b_l}^{k+1} \Delta\sigma, \tag{6.40f}$$

$$V_{i,m}^{k+1} = \kappa_{i,m}^{k+1} + 2\mathcal{H}(U_{0_{i,m}}^{k+1}) \left(\sum_{j=1}^{M} \frac{L_j}{2\pi D} \sum_{l=0}^{N} \alpha_l \mathcal{K}_1(z_{l,j}^{k+1}, z_{i,m}^{k+1}) \phi_{l,j}^{k+1} \Delta\sigma + \frac{L_{\partial\Omega}}{2\pi D} \sum_{l=0}^{N} \alpha_l \mathcal{K}_1(z_{b_l}, z_{i,m}^{k+1}) \phi_{b_l}^{k+1} \Delta\sigma \right). \tag{6.40g}$$

While we will consider integrals accurate up to $\mathcal{O}(\Delta\sigma^2)$, one can easily extend this to higher order methods by using the appropriate weights α and W. Given an initial curve we can compute the solution at the next time step using Newton's method. When forming the Jacobian for Newton's method, notice that we indeed have enough equations (the system (6.40)) to solve for the unknown vector $\mathbf{u} = [\mathbf{z}, \mathbf{V}, \mathbf{L}, \mathbf{U_0}, \phi, \phi_\mathbf{b}]$, where the components are the discrete values on the curve. Due to the possibility of non-uniqueness of the U_0 problem, we cannot guarantee that solution bifurcations will not occur (i.e. we cannot guarantee the Jacobian to have full rank).

To initialize a curve, we need a parametrization of some curve in $\mathbb{R}^2$, $z_0 =$

$\langle x(\theta), y(\theta) \rangle$ with $\theta \in [0, \Theta]$. Write the unit arclength parametrization as

$$\sigma = \frac{\int_0^\theta \sqrt{\frac{\mathrm{d}x}{\mathrm{d}v}^2 + \frac{\mathrm{d}y}{\mathrm{d}v}^2}\,\mathrm{d}v}{\int_0^\Theta \sqrt{\frac{\mathrm{d}x}{\mathrm{d}\theta}^2 + \frac{\mathrm{d}y}{\mathrm{d}\theta}^2}\,\mathrm{d}\theta},$$

which we can interpolate for discrete values of $\sigma \in [0, 1]$. We can pre-compute values to arbitrary accuracy by refining in θ along with higher order quadrature and interpolation. Having an initial unit arclength curve, we can determine the initial values of U_0 and ϕ for the static curve by using Newton's method to solve (6.40d) and (6.40e). Again, due to the possible non-uniqueness of solutions, it can be difficult to find an initial guess which will allow Newton's method to converge. Assuming this problem converges an initial vector $\mathbf{u}_0$ can be used in the dynamic Newton's method for the full problem.

Validating Numerical Formulation with the Mullins Sekerka Problem

Before solving the problem using the GMS model, we will validate our code with a different curve motion problem, the Mullins-Sekerka (MS) problem formulated in [55]. This problem is a singular perturbation limit of the Cahn-Hilliard problem [4] and it (along with similar problems) has been studied analytically (cf. [65], [78], [60], [3]) and numerically (cf. [84], [77], [2]). The differential equation for motion is still (6.15) with the tangential velocity condition (6.16) and equal arclength (6.33) as this is problem independent.

However, the Dirichlet (6.5a), and jump conditions (6.5b) get replaced with

$$\kappa = \int_\Gamma \Phi(x,q)V(q)\,\mathrm{d}q_s + C(t), \tag{6.41a}$$

$$\left[\frac{\partial u}{\partial n}\right] = -V, \tag{6.41b}$$

where here the fundamental solution for Laplace's problem is used because the MS problem solves Laplace's equation away form the interface instead of the modified Helmholtz equation. Notice in these new boundary conditions that the integral density so happens to be the normal velocity exactly, and so there is no secondary velocity expression required. Furthermore, the Neumann boundary conditions do not apply to this problem since the only requirement is that the solution is bounded in the far-field. This boundedness requirement is the reason for $C(t)$ appearing in (6.41a) as otherwise the solution will be logarithmic there (cf. [34],[84]). However, introducing this unknown, time dependent, constant also requires a closure condition which is ([34]),

$$\int_\Gamma V(q)\,\mathrm{d}q_s = 0.$$

This condition is analogous to the zero net-flux Fredholm condition required for Neumann problems of the Laplace operator on bounded domains. We omit the details for the numerical formulation as they are nearly identical to the equations for the reaction diffusion models in section 6.2.2. For comparison reference we note that if Γ is a multiconnected domain of two concentric circles in free-space with radius R_1 and R_2 ($R_2 > R_1$) then we can find a

radially symmetric exact solution [84],

$$u(r) = \begin{cases} -\frac{1}{R_1}, & 0 \le r \le R_1 \\ -\frac{1}{R_1} + \left(\frac{1}{R_1} + \frac{1}{R_2}\right) \frac{\log\left(\frac{r}{R_1}\right)}{\log\left(\frac{R_2}{R_1}\right)}, & R_1 \le r \le R_2 \\ \frac{1}{R_2}, & r \ge R_2 \end{cases}, \tag{6.42}$$

with equations for the radii given by,

$$\frac{\mathrm{d}R_1}{\mathrm{d}t} = -\frac{1}{R_1} \frac{\left(\frac{1}{R_1} + \frac{1}{R_2}\right)}{\log\left(\frac{R_2}{R_1}\right)},$$
$$\frac{\mathrm{d}R_2}{\mathrm{d}t} = -\frac{1}{R_2} \frac{\left(\frac{1}{R_1} + \frac{1}{R_2}\right)}{\log\left(\frac{R_2}{R_1}\right)}.$$

Notice that

$$\frac{\mathrm{d}}{\mathrm{d}t}(R_1^2 + R_2^2) = 0,$$

and so,

$$R_2 = \sqrt{A^2 + R_1^2},$$

where $A^2 = R_{10}^2 + R_{20}^2$ is the sum of the initial values for each radius. We can therefore write the problem for $R_1(t)$ as,

$$t = -\frac{1}{2} \int_{R_{10}}^{R_1(t)} \frac{x^2 \sqrt{x^2 + A^2}}{x + \sqrt{x^2 + A^2}} \log\left(\frac{x^2 + A^2}{x^2}\right) \mathrm{d}x. \tag{6.43}$$

We can solve this numerically and invert to get $R_1(t)$ (and hence $R_2(t)$) for any time t and thus have the analytic solution. Figure 6.3 shows the analytic solution (6.42) as well as the numerical solution from the integral

equation technique for two times $t = 0$ and $t = 0.2$. The outer radius is taken to be $R_2 = 2$ while the inner radius is $R_1 = 1$. The lines represent the numeric solution while the circles represent the analytic solution. Here we chose $N = 50$ points on each curve with a time step of $\Delta t = 1 \times 10^{-3}$. The figure shows an excellent agreement between the numerical formulation and the analytic solution.

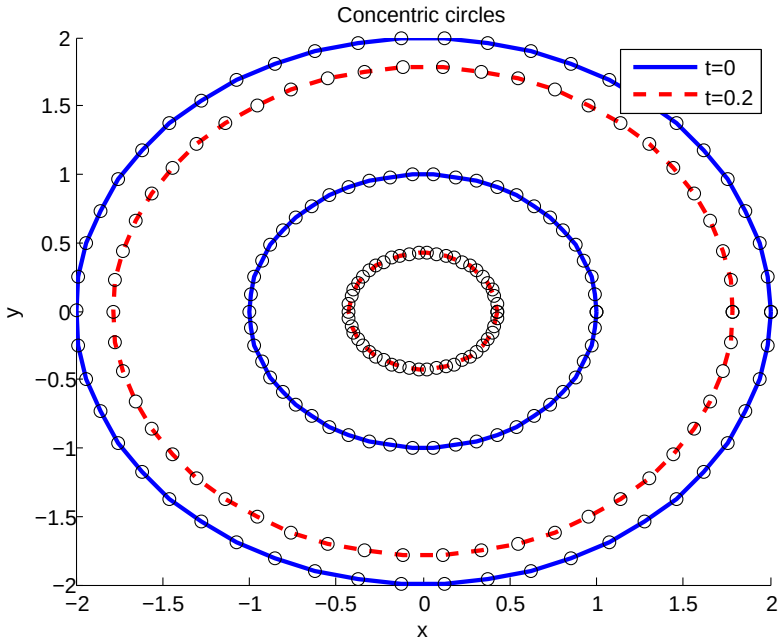

Figure 6.3: The solution to the Mullins-Sekerka problem for concentric circles with an outer radius $R_2 = 2$ and inner radius $R_1 = 1$. The solid blue curve is the numeric solution at $t = 0$ and the red dashed curve is the numeric solution at $t = 0.2$. The hollow circles are the analytic solution as computed with (6.42) and (6.43)

,

In a more technical comparison, we consider the global truncation errors for the same concentric circles with $R_1 = 1$ and $R_2 = 2$ compared to the analytic

solution (6.42). Standard backward Euler global truncation analysis would predict an error on the order of Δt but since the source term for the equation of motion has a spatial error $\Delta\sigma^2 \log \Delta\sigma$ then we actually predict a global error of $\mathcal{O}(\Delta\sigma^2 \log \Delta\sigma + \Delta t)$. In Table 6.3 we take $\Delta t = \Delta\sigma^2$ for a variety of N values so that the overall convergence should be $\Delta\sigma^2 \log \Delta\sigma$ and indeed that is observed.

N	xerr	xrat	Verr	Vrat	Lerr	Lrat	CPU Time
8	2.90E-03	—	1.45E-01	—	1.61E-01	—	0.189
16	7.96E-04	3.64	3.42E-02	3.93	4.11E-02	3.93	0.520
32	2.12E-04	3.75	8.22E-03	3.96	1.04E-02	3.96	2.43
64	5.49E-05	3.87	2.01E-03	3.98	2.61E-03	3.98	21.4
128	1.40E-05	3.93	4.98E-04	3.99	6.53E-04	3.99	352

N	xerr	xrat	Verr	Vrat	Lerr	Lrat	CPU Time
8	5.38E-04	—	7.00E-02	—	3.16E-01	—	0.189
16	1.76E-04	3.05	1.66E-02	4.21	7.97E-02	3.96	0.520
32	5.10E-05	3.45	4.01E-03	4.14	2.00E-02	3.99	2.43
64	1.36E-05	3.74	9.86E-04	4.07	5.01E-03	3.99	21.4
128	3.52E-06	3.88	2.44E-04	4.04	1.25E-03	4.00	352

Table 6.3: The global truncation error for solving the MS problem with concentric circles $R_1 = 1$ (top table), $R_2 = 2$ (bottom table) solving to $T = 0.0469$. We define *xerr* as the error in the x-component of the curve position. The error in the y-component is the same and omitted. *Verr* and *Lerr* are the errors in the normal velocity and curve length respectively. The *rat* suffix for each indicates the ratio of successive errors to the previous one. The convergence is $\mathcal{O}(\Delta\sigma^2 \log \Delta\sigma)$ as expected. The CPU timings reflect the computation of both curves and does not included anything that can be precomputed such as the singular scalar logarithmic integrals.

Next, we demonstrate some of the other qualitative results of the MS problem obtained in [84], such as non-concentric circles favouring growth of the larger circle at the expense of the smaller one (Figure 6.4) and the tendency of

non-circular curves to become circular (Figure 6.5).

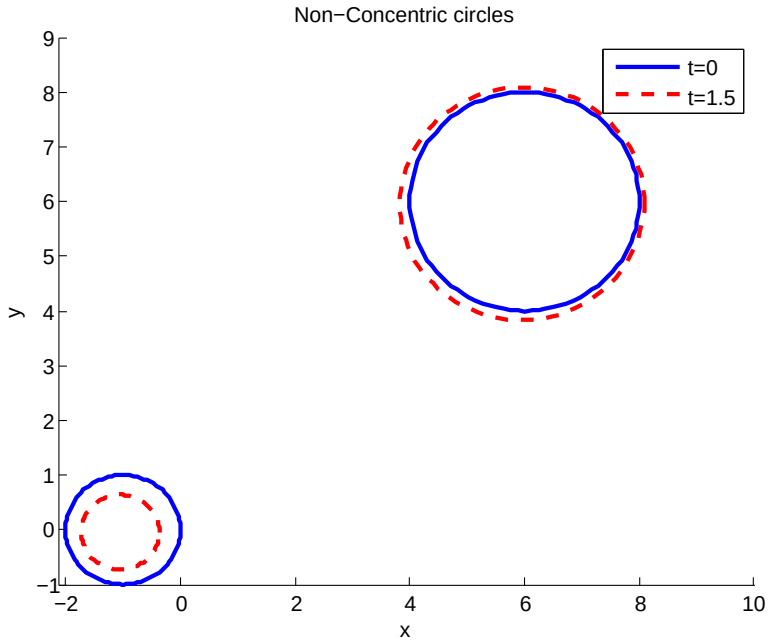

Figure 6.4: Evolution of non concentric circles with MS. The first circle is centered at $(-1, 0)$ with radius $R_1 = 1$ and the second circle is centered at $(6, 6)$ with radius $R_2 = 2$. The initial curve is in a blue solid line while the final curve at time $t = 1.5$ ($\Delta t = 1 \times 10^{-2}$) is in a red dashed line. As time evolves, an effect known as Ostwald ripening occurs [62] which favours growth of larger objects at the expense of shrinking small objects.

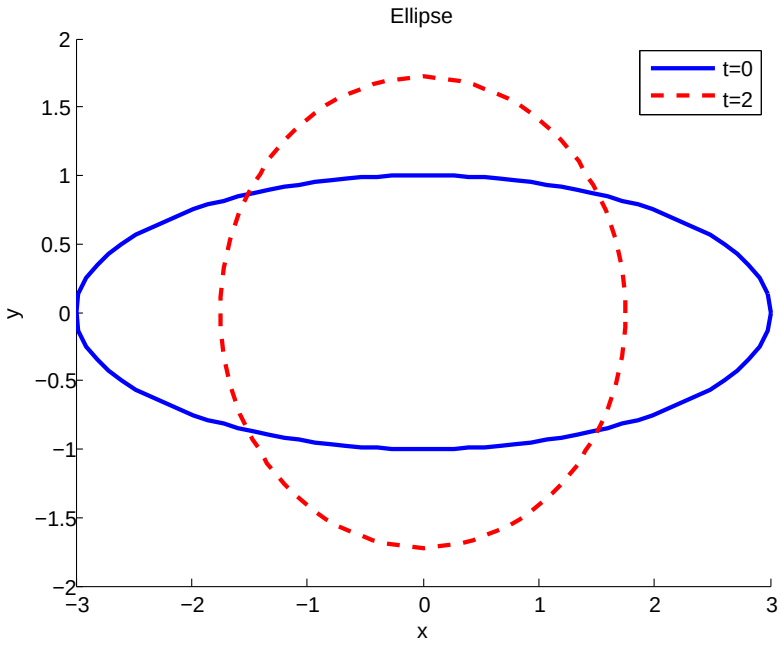

Figure 6.5: Evolution of an ellipse to MS with major axis 3 and minor axis 1. The initial curve is in a blue solid line while the final curve at time $t = 2$ ($\Delta t = 1 \times 10^{-2}$) is in a red dashed line. The curve becomes more circular as time evolves which is a consequence of the area preserving and length shrinking property of the MS model [84].

We emphasize that our aim in comparing results is not to demonstrate the superiority of our technique over the proposed method in [84]. However, we indicate a few significant comparisons between our two methods. Firstly, the formulation of solving (6.15) in [84] is based on looking at the tangent angle and does an implicit-explicit (IMEX) splitting so that only stiff terms are solved implicitly resulting in a diagonal Jacobian of the discretization of the differential equation. However, ultimately they are still forced into solving integral equations to update the velocity which results in the same dense Jacobian that we have implemented. While not using the same splitting

technique for (6.15), we will have a sparse Jacobian for the differential equation. Furthermore, by using an IMEX splitting, the scheme in [84] requires a lower bound that the time step not be larger than 2.5×10^{-3}. However, our method, being fully implicit allows us to take larger time steps due to the general stronger stability of fully implicit schemes (as noted in Figures 6.4 and 6.5). Finally, by not using the tangent angle formulation, we do not have to consider curve reconstruction and the full curve update happens within the Newton method solver.

6.3 Solving the GMS Model

We will now solve the saturated Gierer-Meinhardt model with saturation parameter $\hat{\sigma}$, (2.32) discussed in 2.3, which introduced the saturation criteria for which homoclinic orbit solutions w existed. We will now discuss how to incorporate the limiting saturation into solving the full model.

6.3.1 Including Saturation and Computing Homoclinic Orbits

Having chosen the GMS model we can write (6.13) as

$$\phi_m(\sigma^*) = (\hat{\mathbf{n}} \cdot \hat{\mathbf{n}}_i) U_0^{\beta} \int_{-\infty}^{\infty} w^o \, \mathrm{d}\hat{\eta}, \quad \beta = qo - s.$$

We can also write (2.20) as $\mathcal{H} = -\frac{q}{4U_0}\hat{\mathcal{H}}$ with $\hat{\mathcal{H}}$ defined in (2.31). As we iterate a solution using Newton's method, the value of b is not being controlled but rather is subject to an update on U_0. Therefore, it is possible

that U_0 could be computed such that $b > b_c$ which is invalid. To remedy the possibility of exceeding the critical b value, we consider a mapping of a variable $c \in (-\infty, \infty)$ to $b \in [0, b_c]$ via,

$$b = \frac{b_c}{2}(\cos(c) + 1).$$

This form is chosen since there are not any steep gradients in the function for Newton's method to overshoot and diverge like there are for exponential functions. If the critical b value is reached exactly, the tangent is horizontal but a homoclinic cannot exist precisely at this value so this case can be ignored. Similarly there is a horizontal tangent issue at $b = 0$ but this will not be a problem for $\hat{\sigma} > 0$ as long as we do not initialize near $b = 0$. If $\hat{\sigma} = 0$ then $b = 0$ is a solution for all vectors $\mathbf{u}$ and time t. One notorious issue with a trigonometric function in Newton's method is the convergence to a single root, however since any period maps to the set of b values we are interested, we are not concerned with the particular value of c that converges. We will supplement the addition of a new variable to the system via the equation (2.23),

$$b - U_0^{2q}\hat{\sigma} = 0.$$

Another advantage of considering b as a separate variable is that the homoclinic only depends on b and can therefore be precomputed. Otherwise, we would have to consider the dependence of the homoclinic on U_0 and thus there would need to be an ODE computation at each iteration significantly slowing down the formulation. In the current form, the time required for a Newton solve is equivalent whether $b = 0$ or $b \neq 0$. While computing deriva-

tives for the Newton solve, almost all of the terms appear algebraically except for b (or c) which has a dependence in the numerically computed homoclinic solution. Computing the c derivatives we get

$$\frac{\mathrm{d}\phi_m}{\mathrm{d}c} = (\hat{\mathbf{n}}\cdot\hat{\mathbf{n}}_i)U_0^\beta \int_{-\infty}^{\infty} r w^{o-1} w_b \,\mathrm{d}\hat{\eta}\left(-\frac{b_c}{2}\sin(c)\right),$$
$$\frac{\mathrm{d}\mathcal{H}}{\mathrm{d}c} = -\frac{q}{4U_0}\left(\frac{\int_{-\infty}^{\infty} 2ww_b\,\mathrm{d}\hat{\eta}}{\int_{-\infty}^{\infty} w_{\hat{\eta}}^2\,\mathrm{d}\hat{\eta}} - \frac{\int_{-\infty}^{\infty} w^2\,\mathrm{d}\hat{\eta}\int_{-\infty}^{\infty} 2w_{\hat{\eta}}w_{b_{\hat{\eta}}}\,\mathrm{d}\hat{\eta}}{\left(\int_{-\infty}^{\infty} w_{\hat{\eta}}^2\,\mathrm{d}\hat{\eta}\right)^2}\right)\left(-\frac{b_c}{2}\sin(c)\right).$$

In this expression we consider the c derivative using chain rule since the b dependence on the homoclinic is more natural. To actually compute the homoclinic we consider (2.22) along with the same expression differentiated with respect to b,

$$w_{b_{\hat{\eta}\hat{\eta}}} - w_b + \frac{2ww_b}{(1+bw^2)^2} - \frac{w^4}{(1+bw^2)^2} = 0.$$

We then write these two second order differential equations as a first order system and solve them using a standard boundary value solver such as `bvp4c` in MATLAB. We supplement this system with the boundary conditions $w_{\hat{\eta}}(0) = 0$ and $w_{b_{\hat{\eta}}} = 0$ and to appropriately capture the exponential decay in the far-field, we prescribe a mixed boundary condition

$$w_{\hat{\eta}}(\hat{L}) = -w(\hat{L}),$$

where $\hat{L} \gg 1$ is chosen to sufficiently represent infinity. Note that since w is even (see Lemma 2.2.0.1), we only solve the system on the domain $\hat{\eta} \geq 0$ and recast the necessary integrals, which are also of even functions, to be on the

same interval. Plots of various homoclinic orbits are in Figure 2.2 in section 2.3.

6.3.2 GMS Results

We are now in a position to solve (6.40) subject to the choice of f and $\mathcal{H}$ in section 6.3.1. We will start by comparing to analytic results for radially symmetric solutions on a circular domain of radius R. For this problem, it is easier to consider a polar coordinate system ($r \in [0, R]$ and $\theta \in [0, 2\pi]$) with a localization on some circle $r = r_0$. In this case then, the normal coordinate η would be $\eta = r_0 - r$. When $b = 0$ and $p = 2$ we have that the homoclinic orbit that solves (2.22) is

$$w(\rho) = \frac{3}{2}\operatorname{sech}^2\left(\frac{\rho}{2}\right),$$

where $\rho = \frac{r-r_0}{\epsilon}$ is the inner region radial coordinate (i.e. $\rho = -\hat{\eta}$). Using this homoclinic orbit we can write the problem (2.19) as

$$\Delta u - \frac{u}{D} = 0, \qquad 0 \leq r \leq R \setminus r_0 \tag{6.44a}$$

$$\frac{\mathrm{d}u}{\mathrm{d}r} = 0, \qquad r = R \tag{6.44b}$$

$$u = U_0, \qquad r = r_0 \tag{6.44c}$$

$$\left[\frac{\mathrm{d}u}{\mathrm{d}r}\right] = -\frac{1}{D}U_0^{\beta}\int_{-\infty}^{\infty} w^o \,\mathrm{d}\rho, \qquad r = r_0, \tag{6.44d}$$

where we are seeking radially symmetric solutions and so we take the Laplace operator to have only a radial dependence. This is subject to the velocity

condition (2.43,

$$\frac{\mathrm{d}r_0}{\mathrm{d}t} = -\frac{1}{r_0} - \frac{q}{U_0}\left(\left.\frac{\mathrm{d}u}{\mathrm{d}r}\right|_{r=r_0^+} + \left.\frac{\mathrm{d}u}{\mathrm{d}r}\right|_{r=r_0^-}\right)$$

where we have computed $\mathcal{H}$ explicitly since the homoclinic orbit is known analytically. The solution to this is given by (2.42),

$$u(r) = U_0 \frac{G_0(r; r_0)}{G_0(r_0; r_0)},$$

with U_0 given by (2.40) and G_0 by (2.38). Figure 6.6 shows a comparison with this analytic solution and the numerical scheme for exponent set $(2, q, o, s) = (2, 1, 2, 0)$ and for parameters $R = 1$, $r_0 = 1/2$ and $D = 1$. Figure 6.7 shows the value of U_0 computed numerically and analytically using (2.42) for $t = 0$ and $t = 0.119$.

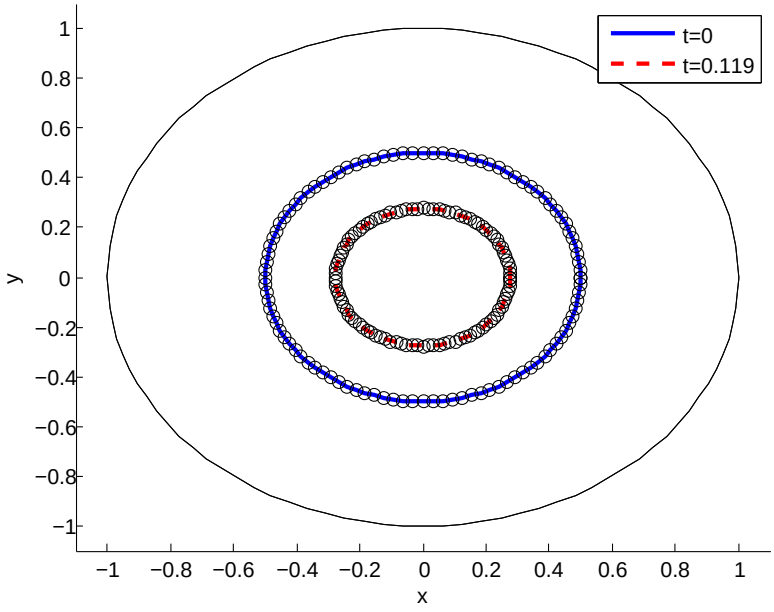

Figure 6.6: Circle evolution under the GMS model with $\hat{\sigma} = 0$, $R = 1$, $r_0 = 1/2$, $D = 1$, exponent set $(2, 1, 2, 0)$ and time step 1×10^{-3}. The lines represent the numerical solution while the circles represent the analytic solution computed using (2.42). The outer black line represents the boundary curve $r = R = 1$.

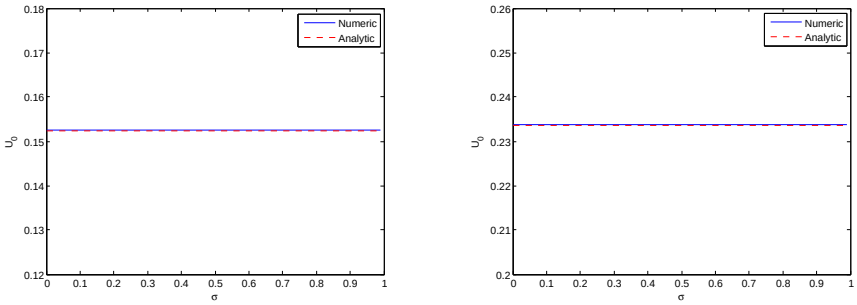

(a) $t = 0$, exact value $U_0 = 0.1525$ (b) $t = 0.119$, exact value $U_0 = 0.2336$

Figure 6.7: U_0 values computed numerically (solid line) and analytically (dashed-line) using (2.40) for the GMS model with $\hat{\sigma} = 0$, $R = 1$, $r_0 = 1/2$, $D = 1$, and exponent set $(2, 1, 2, 0)$.

We can also showcase the existence of equilibrium discussed in 2.3.1 which we can verify analytically using the velocity expression (2.43). One such plot of (2.43), for the exponent set $(2, 2, 2, 0)$, $R = 4$, and $D = 1$ is in Figure 6.8 which shows a stable equilibrium at $r_0 \approx 2.76$. We demonstrate this is found qualitatively in Figure 6.9 where an initial circle with radius $r_0 < 2.76$ grows (Figure 6.9a) while one with initial radius $r_0 > 2.76$ shrinks (Figure 6.9b).

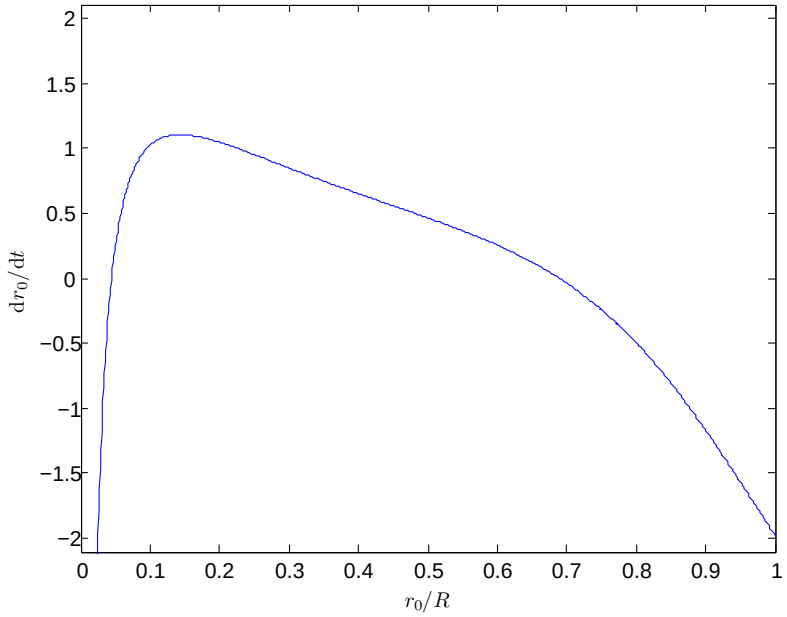

Figure 6.8: Slope-field for circle evolution using the GMS model with $R = 4$, $D = 1$, exponent set $(2, 2, 2, 0)$ and $\hat{\sigma} = 0$. There is an unstable equilibrium at $r_0/R \approx 0.044$ ($r_0 \approx 0.176$) and a stable equilibrium at $r_0/R \approx 0.69$ ($r_0 \approx 2.76$).

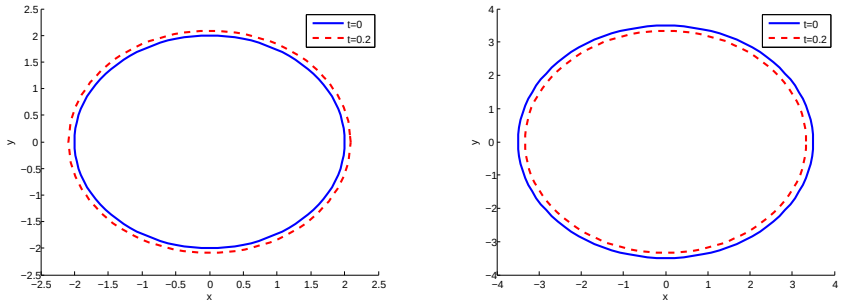

(a) Circle with radius $r_0 = 2$.

(b) Circle with radius $r_0 = 3$.

Figure 6.9: Circle evolution using the GMS model with $R = 4$, $D = 1$, exponent set $(2, 2, 2, 0)$, and $\hat{\sigma} = 0$. The boundary curve at $R = 4$ has been omitted.

When $b \neq 0$, the equations (2.42) still hold for the radially symmetric solution except now (2.40) is a nonlinear equation since the homoclinic orbit w depends on b which ultimately depends on U_0 via (2.23). We therefore call the radially symmetric results for the $b \neq 0$ case pseudo-analytic because we require a Newton's method solver for U_0. The results for this case are presented in Figure 6.10 with the same parameter regime as for Figure 6.6 but with the addition of saturation $\hat{\sigma} = 10$. Figure 6.11 shows the value of U_0 computed numerically and using (2.40). Notice the effect of the saturation drastically alters the curve inhibitor U_0 value and that the values without saturation in Figure 6.7 would lead to $b > b_c$ with $\hat{\sigma} = 10$.

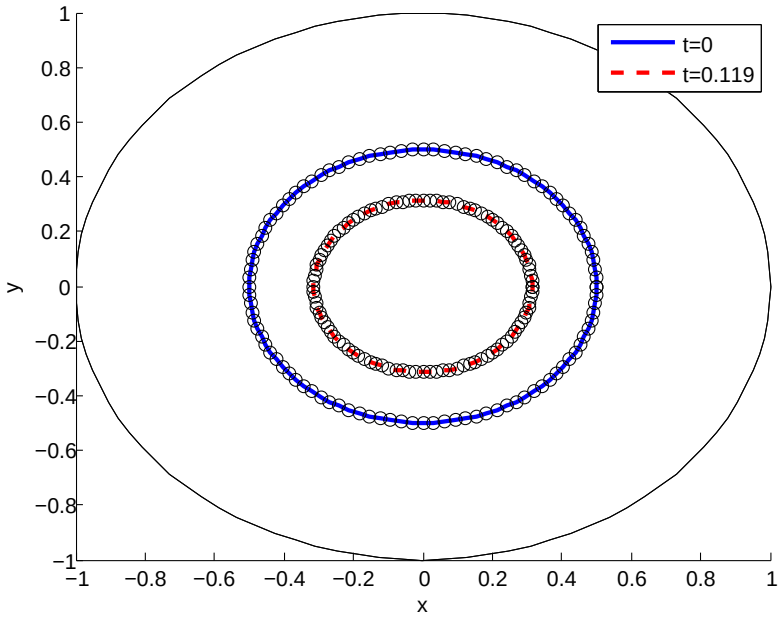

Figure 6.10: Circle evolution under the GMS model with $\hat{\sigma} = 10$, $R = 1$, $r_0 = 1/2$, $D = 1$, exponent set $(2, 1, 2, 0)$ and time step 1×10^{-3}. The lines represent the numerical solution while the circles represent the analytic solution computed using (2.42). The outer black line represents the boundary curve $r = R = 1$.

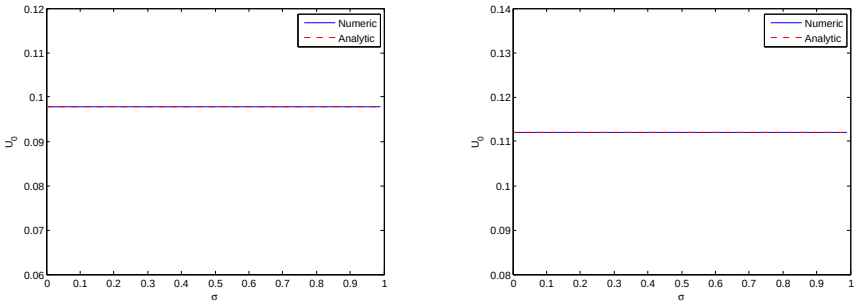

(a) $t = 0$, exact value $U_0 = 0.0977$. (b) $t = 0.119$, exact value $U_0 = 0.1120$

Figure 6.11: U_0 values computed numerically (solid line) and analytically (dashed-line) using (2.40) for the GMS model with $\hat{\sigma} = 10$, $R = 1$, $r_0 = 1/2$, $D = 1$, and exponent set $(2, 1, 2, 0)$. Since $\hat{\sigma} \neq 0$ a Newton's method was used to solve the analytic value.

To see the effect on the motion and U_0 values as $\hat{\sigma}$ is varied, we plot the curves in Figure 6.12a and U_0 values in Figure 6.12b at $t = 0.1$ for different values of the saturation parameter. The effect is such that the velocity and U_0 decreases for increasing saturation.

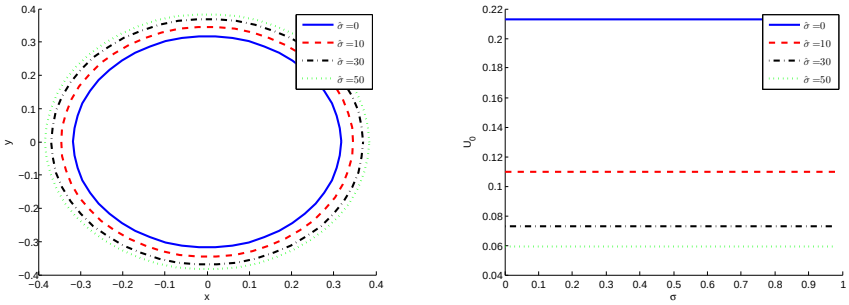

(a) Circle curves. (b) U_0 values.

Figure 6.12: Circle evolution under the GMS model with $R = 1$, $r_0 = 1/2$, $D = 1$, exponent set $(2, 1, 2, 0)$ and time step 1×10^{-2}. The lines represent the numerical solution for different values of the saturation parameter $\hat{\sigma}$ (0,10,30,50) at $t = 0.1$. The boundary curve $R = 1$ has been omitted to more clearly show the separate curves.

We now showcase the correct convergence behaviour as in section 6.2.2. Table 6.4 takes $\Delta t = \Delta\sigma^2$ for a variety of N values with the GMS model for a circle of radius $r_0 = 0.5$ with parameters $R = 1$, $r_0 = 1/2$, $D = 1$, exponent set $(2, 1, 2, 0)$ and saturation $\hat{\sigma} = 10$. We see once again that the predicted $\mathcal{O}(\Delta\sigma^2 \log \Delta\sigma)$ error appears. While omitted, the errors for U_0, and ϕ also converge to the appropriate order.

N	xerr	xrat	Verr	Vrat	Lerr	Lrat	CPU Time
8	3.66E-03	—	2.40E-01	—	4.53E-02	—	0.8
16	1.04E-03	3.51	6.45E-02	3.73	1.05E-02	4.31	3.1
32	2.58E-04	4.04	1.63E-02	3.97	2.64E-03	3.98	14.1
64	6.30E-05	4.10	4.06E-03	4.00	6.71E-04	3.94	125.5
128	1.45E-05	4.34	1.01E-03	4.01	1.75E-04	3.82	1572

Table 6.4: The global truncation error for solving the GMS problem on a circle of radius $r_0 = 0.5$ with $R = 1$, $r_0 = 1/2$, $D = 1$, exponent set $(2, 1, 2, 0)$ and saturation $\hat{\sigma} = 10$ solving to $T = 0.0469$. We define *xerr* as the error in the x-component of the curve position. The error in the y-component is the same and omitted. *Verr* and *Lerr* are the errors in the normal velocity and curve length respectively. The *rat* suffix for each indicates the ratio of successive errors to the previous one. The convergence is $\mathcal{O}(\Delta\sigma^2 \log \Delta\sigma)$ as expected. The CPU timings reflect the computation of both curves and does not included anything that can be precomputed such as the singular scalar logarithmic integrals.

Non-radially Symmetric Solutions and Non-Uniqueness

It was mentioned in section 6.3.2 that the standard uniqueness theorems for the modified Helmholtz equation with Dirichlet or Neumann conditions fail for this problem because the boundary conditions are unknowns in the problem. Furthermore in section 2.3.1, we constructed non-radially symmetric solutions (2.51) using Fourier techniques. We also noted that computing so-

lutions to (2.51) for arbitrary initial data converged quite consistently to the radially symmetric case. We will instead use these solutions as a verification that non-radially symmetric solutions found from the numerical curve motion problem indeed satisfy the analytic problem. For example, if we attempt to compute U_0 using the numerical curve formulation for an initial U_0 configuration $U_{00}(\sigma) = \cos(3\sigma)$ then we converge to a non radially symmetric solution (solid curve in Figure 6.13). If we use this computed U_0 solution as an initial guess for the non-radially symmetric Newton's method on (2.51) then it is also a solution to this problem (dashed curve in Figure 6.13). The agreement shows that indeed the non-radially symmetric solution found is a true one and not an artifact of the system such as by numerical discretization.

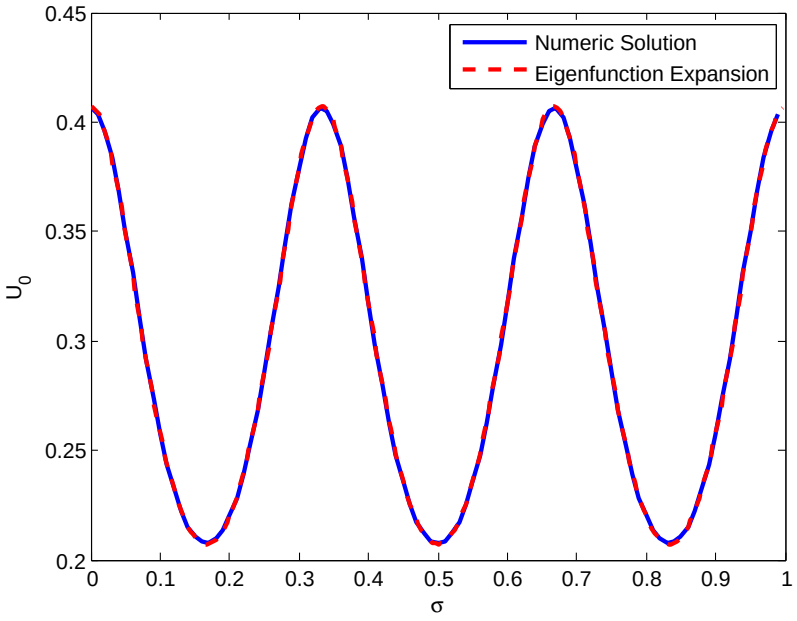

Figure 6.13: Initial circle U_0 formulation under the GMS model with $R = 4$, $r_0 = 2$, $D = 1$, and exponent set $(2, 1, 2, 0)$. The blue solid curve is the computed U_0 solution from the numerical interface problem with an initial guess of $\cos(3\sigma)$ while the red dashed curve is the convergent solution to (2.51) by using the computed solution as an initial guess.

Having demonstrated the existence of multiple solutions to this geometry, we are clearly able to violate the uniqueness which can not only lead to different initial U_0 and velocity configurations but also to solution bifurcations in the dynamic problem. This is currently beyond the scope of this work but is something of interest to pursue in further analysis.

Other Examples

We will now showcase examples beyond circular solutions concentric with the origin of which analytic work is limited or has not been considered. Figure

6.14 shows a angular dependent radius in a "flower-pedal" pattern. Very quickly it can be seen that the dynamic tendency is to circularize and then shrink. Since we start with an initial unperturbed radius that is quite small, we predicted this circularization in section 2.3.2. However, this behaviour generally is in stark contrast to what has been observed in weak diffusion limits of a stripe [39] and in energy minimizing space filling curves [22]. Figure 6.15 also has an angular perturbation in the radius forming a lobe structure, but the dynamic effect is to become an ellipse before shrinking. As the curve shrinks, the ratio of major and minor axes of the ellipse tend to 1 but it is not clear if the curve ever fully circularizes. It is interesting to note that typically this perturbation leads to splitting into two distinct structures [39] as opposed to the behaviour here.

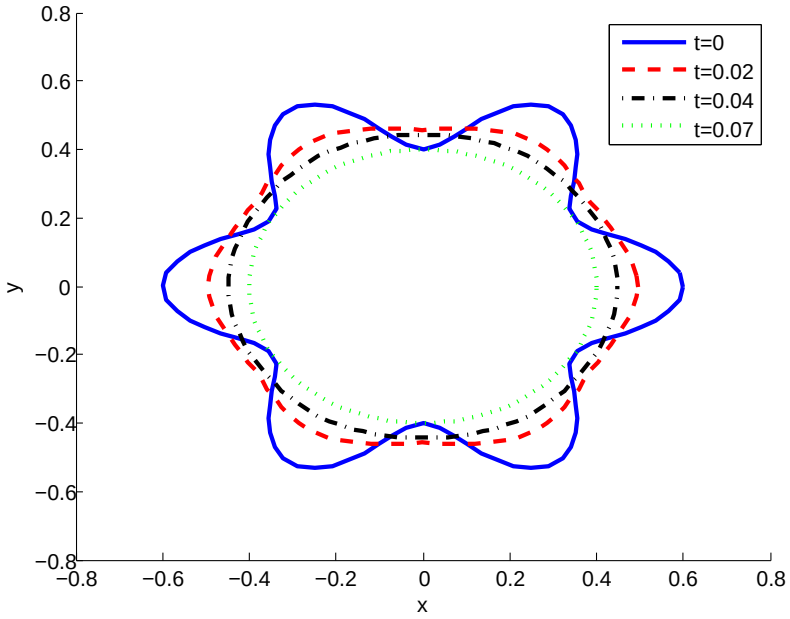

Figure 6.14: Perturbation of a circle with perturbed radius $r = 1/2 + 0.1\cos(6\theta)$ using the GMS model with $R = 1$, $D = 1$, exponent set $(2, 1, 2, 0)$, and $\hat{\sigma} = 10$. The boundary curve at $R = 1$ has been omitted.

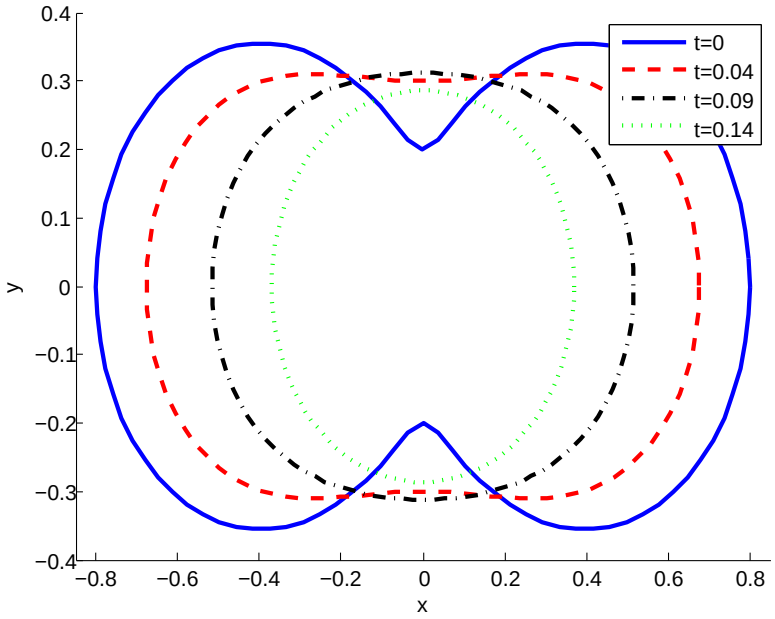

Figure 6.15: Perturbation of a circle with perturbed radius $r = 1/2 + 0.3\cos(2\theta)$ using the GMS model with $R = 1$, $D = 1$, exponent set $(2, 1, 2, 0)$, and $\hat{\sigma} = 10$. The boundary curve at $R = 1$ has been omitted.

Figure 6.16 shows the evolution under the GMS model starting from an elliptical configuration. As with the perturbation in Figure 6.15 it is not immediately clear if the curve completely circularizes as it shrinks to the origin or if the ratio of the major and minor axes just tends to 1.

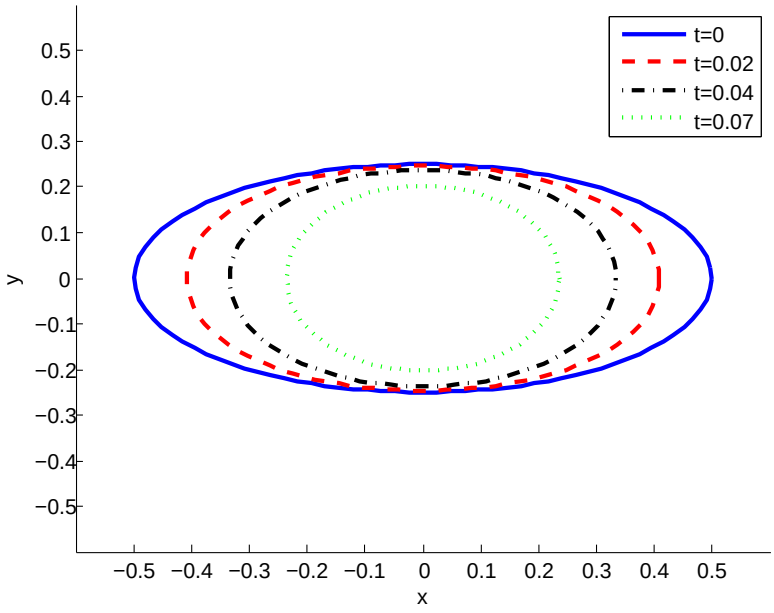

Figure 6.16: Ellipse with major axis $a = 1/2$ and minor axis $b = 1/4$ using the GMS model with $R = 1$, $D = 1$, exponent set $(2, 1, 2, 0)$, and $\hat{\sigma} = 10$. The boundary curve at $R = 1$ has been omitted.

Next, we consider non-concentric circles such as in Figure 6.17. Figure 6.17a shows a non-concentric initial circle placed on the x-axis at $[1, 0]$ with radius $r_0 = 1/2$ while Figure 6.17b shows the same initial circle but placed at the origin. The dynamics of the two models look very similar.

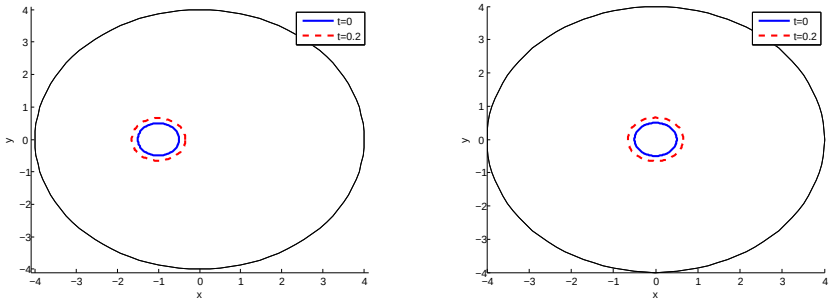

(a) Circle with centre $(-1, 0)$ and radius $r_0 = 1/2$.

(b) Circle with centre $(0, 0)$ and radius $r_0 = 1/2$.

Figure 6.17: Circle evolution using the GMS model with $R = 4$, $D = 1$, exponent set $(2, 1, 2, 0)$, and $\hat{\sigma} = 10$.

However, in Figure 6.18a, we place a circle of radius $r_0 = 1/2$ off the axes entirely and centre it at $[-1, 2]$ with saturation $\hat{\sigma} = 10$. The interesting phenomena here is that, as the curve grows, the circle becomes elliptical and the major axis rotates in the counter-clockwise direction. When the saturation is set to zero (Figure 6.18b), the curve remains a circle and furthermore actually shrinks instead of grows. This demonstrates the effect the saturation can have on the qualitative curve structure.

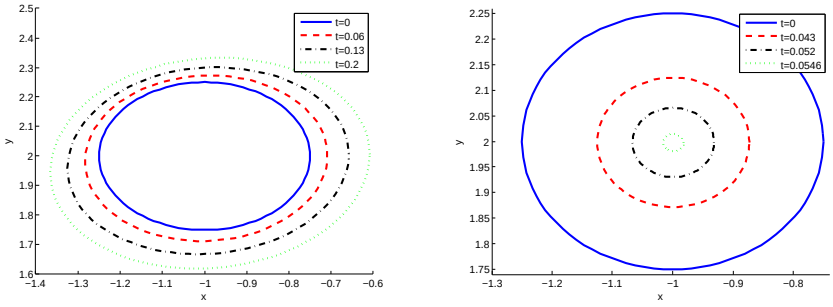

(a) Circle with saturation $\hat{\sigma} = 10$. (b) Circle with saturation $\hat{\sigma} = 0$.

Figure 6.18: Non-concentric circle evolution with centre $[-1, 2]$ and radius $r_0 = 1/2$ using the GMS model with $R = 4$, $D = 1$, and exponent set $(2, 1, 2, 0)$. The boundary curve at $R = 4$ has been omitted.

Finally, we consider the case of curve buckling. In Figure 5.16 of section 5.2.2 we saw a scenario where a perturbed circle elongated into a buckling type pattern. Furthermore, we discussed in section 2.3.2 that if this type of phenomenon were to occur it must be such that r_0 is not small as otherwise the curvature was a stabilizing mechanism. Therefore, we consider a case with a perturbed circle $r = 5 + 0.2\cos(6\theta)$ in a larger circular domain $R = 10$ with exponent set $(2, 1, 2, 0)$ and saturation $\hat{\sigma} = 5$. As can be seen in Figure 6.19, indeed a buckling pattern forms in this instance. However, it is worth noting that it is unclear if this curve pattern is stable to breakup. In Figure 5.16, the parameter regime was approaching the weak interaction regime where curve buckling and curve splitting is known to occur for stripes. As such, it is an open problem to investigate stable curve buckling in the semi-strong regime.

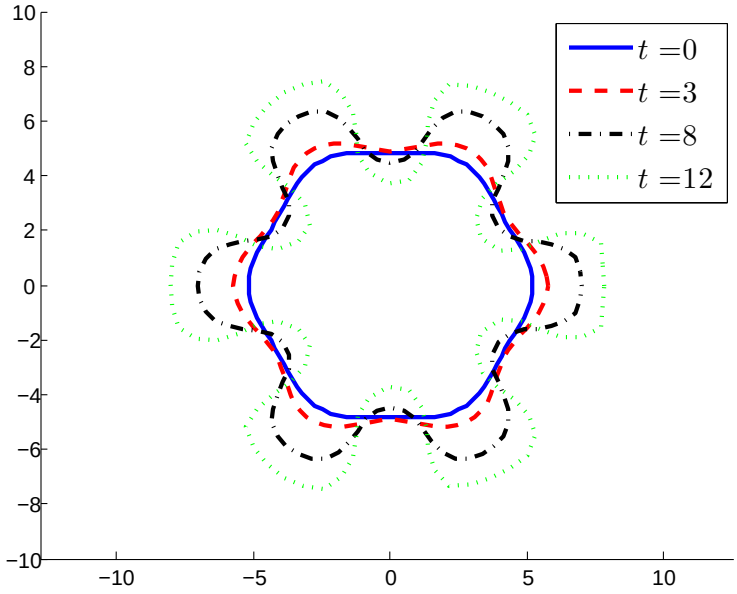

Figure 6.19: Perturbation of a circle with perturbed radius $r = 5+0.2\cos(6\theta)$ using the GMS model with $R = 10$, $D = 1$, exponent set $(2, 1, 2, 0)$, and $\hat{\sigma} = 5$. The boundary curve at $R = 10$ has been omitted.

Not only have we demonstrated agreement with analytically obtained results in the GMS, we have shown that our numerical method can easily extend to curves for which analytical work is limited or unavailable. Furthermore, the generality of the method can easily be extended to other models with different reaction terms $f(u, v)$ and $g(u, v)$. As was stated in Chapter 5, the computations using this method have already been scaled to the $\mathcal{O}(\epsilon^{-2})$ time-scale and therefore avoids the long computation time required for full model simulations. Since there is a limiting value of b for the GMS model, one could expect that curve rupturing may occur. However, in our computations it seems that U_0 always compensates with the saturation parameter $\hat{\sigma}$ in

such a way to prevent this rupturing. We therefore conjecture that, in the semi-strong regime, as long as $U_0(s)$ is defined at $t = 0$ it will continue to be defined for all points along the curve and therefore curve rupturing cannot happen.

Chapter 7

Conclusions

We have presented a variety of techniques and results to better understand general reaction diffusion equations of the form

$$v_t = \epsilon^2 \Delta v - v + g(u, v)$$
$$\tau u_t = D\Delta u - u + \frac{1}{\epsilon} f(u, v)$$

localized on closed curves in $\mathbb{R}^2$. Particularly we have focused our attention on the saturated Gierer-Meinhardt model,

$$g(u, v) = \frac{v^2}{u^q(1 + \sigma v^2)}, \qquad f(u, v) = \frac{v^o}{u^s}.$$

Firstly, in Chapter 2, we derived a singular limit problem for the inhibitor u given by (2.19) for arbitrary curves using a boundary fitted coordinate system. This involved asymptotically translating information from the localized activator v as jump and normal velocity conditions. Taking this formulation, we derived results in 2.3.1 for a ring where the saturation parameter σ was zero and concluded that a saddle-node bifurcation occurred in terms of the outer domain radius R for which two equilibrium ring solutions existed. These results were similar to those derived in [45] but when we included saturation, there was not an equivalent analysis in the same work. As

soon as $\sigma > 0$, at least one equilibrium solution existed for all R and instead a hysteresis bifurcation occurred. This is demonstrated best in Figure 2.11 where we see that as R increases from zero there are regions where there are one, two, and three equilibrium radii r_0. This demonstrates hysteresis because if one were to start on the lower branch of solutions where r_0 has the smallest equilibrium value and increase R then eventually the steady-state solution transitions to the branch where r_0 is the largest. If R is then decreased, the equilibrium will transition back to the lower r_0 branch but at a different value of R than the first upper branch transition. Hysteresis has a potentially significant impact on the biological aspect of pattern formation. Recall that with scaling, R can change by physically altering the circular domain radius or by altering the diffusion coefficient. Both of these could have biological applications where patterns on an organism change as a result of maturity (domain growth) of the organism or in the presence of chemicals which could affect the diffusion coefficient. Specifically in [67], it is noted that patterns on a freshwater snail, *Theodoxus fluviatilis*, change because of concentrations of salt in the water they are exposed to. While the specific pattern transitions for this snail are more complex than growing or shrinking ring structures, a diffusion dependent steady-state bifurcation could help generally explain environmental impact on pattern formation. In [66], it was noted that the size and shape of patterns on a variety of fish can change in a matter of seconds and spots can have drastically different diameters. This qualitative change over a fast time scale can be described with a hysteresis like feedback loop. The saturation parameter appears to play an important role in biological self-regulation, something that previous

models which excluded the effect could not sufficiently explain.

Next we showed that since the boundary data for the inhibitor is not prescribed a priori, but rather is an unknown of the curve, standard uniqueness results do not apply. As such, we showed the existence of ring solutions where the inhibitor is not radially symmetric. These solutions were verified to exist numerically in Chapter 6. While the ring solutions provided interesting results, they did not rely on the general boundary coordinate model derivation as they could easily be constructed using polar coordinates. Therefore, we next considered a problem of a near circle $r = r_0 + \varepsilon h(\theta)$ where $\varepsilon \ll 1$. While this could also be studied using a polar coordinate formulation, it would require carefully tracking the asymptotic consistency of both ϵ and ε, where as the singular boundary coordinate framework is valid on any curve. One of the key requirements in the near-circle formulation was that when saturation was considered, the effective saturation parameter b given by (2.23) is perturbed by the changing geometry and was a function of the arclength of the curve. After resolving the continuity, jump, and normal velocity conditions we solve the problem up to $\mathcal{O}(\varepsilon^2)$. It was necessary to consider the expansion up to this order because as was evidenced in section 2.3.2, the first order correction only accounted for introducing sinusoidal perturbations from the Fourier series of $h(\theta)$. However, polynomial representations $h(\theta)^\alpha$ for $\alpha > 1$ occurred at $\mathcal{O}(\epsilon^2)$ and introduced $n = 0$ Fourier modes which overall caused a shift in each of the boundary inhibitor value, U_0, modified saturation parameter, b, and normal velocity V respectively. This was evidenced in Figures 2.12 and 2.13. By analyzing the normal velocity correction we saw that when r_0 was

small enough, the velocity was dominated entirely by the curvature which circularized the curve. However, for r_0 large (or equivalently, D small), this could not be guaranteed to be satisfied and indeed we saw growing curves in Chapter 5.

Following the formulation of various solutions, we returned to the radially symmetric ring solution in Chapter 3 and performed a linear stability analysis. When formulating the stability problem, we could not use standard $\exp(\lambda t)$ eigenfunctions since the steady-state was slowly evolving with timescale $T = \epsilon^{-2}t$. Because of this, we needed to use a WKB formulation (3.4) which resulted in the eigenfunction being the evolution of the eigenvalue over time given by (3.9). The form of the operator used with the activator eigenfunctions admitted even and odd solutions which we analyzed separately. For the even solutions, in Lemma 3.1.0.1, we saw that only solutions which were of a single sign could lead to instabilities and in section 3.2, using the global inhibitor problem we derived a non-local eigenvalue problem for the activator eigenfunctions (3.16). Splitting this eigenvalue problem using functions $C_m(\lambda)$ and $f(\mu)$ defined by (3.19), we were able to transform this into a root finding problem (3.20). We then studied the roots of this problem on the real axis and in the complex plane after setting saturation $b = 0$. This lead to Principal Result 3.2.9.1 which has two very key conclusions. Firstly, there exist neutral stability Fourier modes $m = m_{b^-}$ and $m = m_{b^+}$ such that a real unstable eigenvalue always exists on $m_{b^-} < m < m_{b^+}$. This is an important result because it states that ring solutions will always go unstable to breakup instabilities for some range of modes when $b = 0$. A second interesting result

was that on $0 < m < m_{b^-}$ there were no unstable eigenvalues for τ small enough which, as τ increased, transitioned via a Hopf bifurcation to become unstable.

In order to verify the conclusions from Principal Result 3.2.9.1, we derived an algorithm for computing eigenvalues in 3.2.10. In Figures 3.5 and 3.6, we confirmed the range of unstable eigenvalues existed. In Table 3.1 we performed a series of comparisons to the asymptotic and numerically computed neutral stability points which showed excellent agreement with one another. Next we added saturation and showed via Figure 3.9 that the largest eigenvalue tended to zero as b tended to its critical value. This had the effect of stabilizing the ring solution as was seen in Figures 3.10 and 3.11. Full numerical simulations in Chapter 5 confirmed the stabilizing effect of saturation to breakup instabilities.

In section 3.3, we showed the odd eigenfunctions produced eigenvalues of $\mathcal{O}(\epsilon^2)$, called small eigenvalues, which means they would only become relevant on the long time-scale $T = \mathcal{O}(\epsilon^{-2})$. Unlike previous work, such as [39], we were not able to classify these eigenvalues using the outer region away from the curve since the derivative did not commute through the operator, having extra terms due to r^{-1}. Therefore, we approached the small eigenvalues via the inner region only. We concluded that the small eigenvalues given by (3.99) turned out to precisely be the normal velocity condition for a near circle from section 2.3.2. We showed via (3.101) how this conclusion could be predicted a priori. This is significant because it means that assuming ring

solutions are stable to breakup then the full dynamics are captured by the near circular problems discussed in section 2.3.2.

In Chapter 4 we considered a general framework for which the non-local eigenvalue analysis of section 3.2 could be made explicit. Indeed we showed that under a special class of eigenfunctions $g(w)$ to the linearized operator of the homoclinic orbit defined in Lemma 3.1.0.1, we could formulate the NLEP explicitly via (4.7). Assuming a form for $g(w)$, we derived a condition (4.11) relating $g(w)$ to $f(w)$ in the problem $w_{yy} - w + f(w) = 0$. If this $f(w)$ was such that a homoclinic orbit existed then we could obtain the explicit formulation (4.7). This allowed us to gain analytic insight into the stability of stripe solutions (section 4.2) and circle solutions (section 4.3). The significance of the explicit formulation for these geometries was that we were able to derive Principal Result 4.2.2.1 which allowed us to extend stability results for parameter regimes not previously explored. Furthermore, in an infinite stripe domain, we were able to analytically obtain the unique value of $\tau = \tau_m^H$ for which a Hopf bifurcation occurred and presented this in Principal Result 4.2.2.2. Such an analytic treatment of the Hopf bifurcation had never previously been considered. We validated the Hopf bifurcation analysis in Figures 4.2 and 4.3 where we showed that for a fixed value of τ, and two exponent values q that complex eigenvalues with positive real part did or did not exist based on the comparison with the analytically determined Hopf bifurcation value τ_m^H. The results generalized for finite and infinite domains but for finite domains we could not classify the unique Hopf bifurcation value.

Full numerical simulations in Chapter 5 verified breakup instability patterns for both the stripe and ring in the explicit and implicit formulations. This was done by randomly adding data to steady-state solutions and looking at the discrete Fourier transform during the curve evolution. In all instances the predicted instability modes or bands persisted until secondary instabilities of spot dynamics occurred. We define secondary instabilities to be anything which that occurs after the breakup pattern has emerged. Some types of observed secondary instabilities were spot collocation motion where spots continued to move as a ring and spot annihilation where spots were destroyed until a single spot remained. We tested stability to zig-zag modes by giving a perturbed circle as initial data and allowing it to evolve. We demonstrated parameter regimes for which the curve was both stable and unstable to zig-zag modes.

Finally in Chapter 6 we derived a general numerical framework for solving quasi-steady solutions in $\mathbb{R}^2$. We used a layer potential formulation for solving any problem of the form (2.19) subject to general conditions,

$$\begin{aligned}\left[\frac{\mathrm{d}u}{\mathrm{d}n}\right]_\Gamma &= F(U_0, V),\\ \left\langle\frac{\mathrm{d}u}{\mathrm{d}n}\right\rangle_\Gamma &= G(U_0, V)\end{aligned}$$

where U_0 was the inhibitor value on the curve and V, the normal velocity. We showed the universality of this formulation by verifying our numerical method with the Mullins-Sekerka problem in 6.2.2. One of the intricate details about a layer potential formulation is that it involves the evaluation of singular

integrals with logarithmic strength. We extract the logarithmic integrals and evaluate them analytically using a Lagrange polynomial interpolation for any density functions. Since we are dealing with closed curves, in order to avoid the effects of near-singularities arising from periodicity we also remove logarithmic singularities that are within one period from the true singularity. In 6.2.1 we show that this introduces an error that has the same order as the overall numerical quadrature error. We treat the curve evolution entirely implicitly which allows us to take relatively large time steps. This is in contrast to work such as [84] where an implicit-explicit splitting technique is used. In 6.3 we use the numerical method for solving the saturated Gierer-Meinhardt model and verify many of the analytically determined conclusions such as the r_0 equilibrium radii and the circularization of near circular curves with $r_0 \ll 1$. However, we then extend results beyond what is currently understood analytically in 6.3.2. We use an elliptical geometry and show that it also tends to a circular curve. We also consider the evolution of non-concentric circles and interesting behaviour such as that which occurs in Figure 6.18 happens whereby a curve that is an initial circle evolves into a rotating ellipse.

7.1 Future Work and Open Problems

The completion of this work has stimulated some new key results in the pattern formation community, specifically attributed to the introduction of the saturation parameter in the Gierer-Meinhardt model. As such, there are several open problems that have arisen which warrant some future investi-

gation. Firstly, the general curve tracking framework developed in Chapter 6 will hopefully stimulate analytic investigation into other geometries that have not been previously considered. Of specific interest is the non-concentric circle problem which dynamically transitioned to an ellipse. Since this dynamic event can occur with a single non-concentric circle, then perhaps this could be recast, using a conformal mapping argument, to a concentric geometry which is more available to analysis. In terms of the numerical tracking method itself, the dynamic transition of non-concentric circles may demonstrate the existence of solution bifurcations and we are interested in using techniques such as pseudo-arclength continuation to search for these bifurcation diagrams as a function of the saturation parameter. Another interesting case study would be the further investigation of buckling states such as those evidence in Figure 6.19 and whether the saturation can be chosen such that both a buckling pattern forms and that it is stable to breakup.

One of the limitations of the curve tracking method implementation is that if disjoint curves approach each other, there are convergence issues due to near singular integration of neighbouring logarithmic functions. As such, we are interested in adapting the method to handle near singular integration. A method outlined in [68] presents some promising ideas for how we could implement this feature. We are also interested in finding a level set formulation for this problem to compare and contrast the advantages of each method. In section 2.3.1 we commented that non-radially symmetric inhibitor solutions exist on a ring but that they are difficult to compute using a standard Newton algorithm because of the persistence of the constant solution. We are

therefore interested in using a regularized optimization approach where we penalize the constant solution to find non-radially symmetric solutions.

For the explicit eigenvalue formulation in Chapter 4, we discussed that Principal Result 4.2.2.2 proves the existence of a unique Hopf bifurcation value $\tau = \tau_m^H$ for stripe solutions in an infinite domain. However, no such result exists for stripe solutions in a finite domain and as such, this remains an open problem. For the implicit formulation in Chapters 2 and 3, we showed that including saturation not only changes the bifurcation curve from saddle-node to one producing hysteresis but also that saturation can stabilize breakup instability modes. It is likely that the bifurcation diagram transformation and stability analysis are related and it is an open problem to determine the effect of introducing a second set of stable solutions in Figure 2.11 to the overall linear stability to breakup modes. In terms of saturation, we have considered the exponent set $p = 2$, but there would be an equivalent saturated solution for other values of p and it is an open problem to investigate these under the homoclinic existence criteria of Lemma 2.2.0.1.

On the topic of stability, throughout this thesis we have only considered pattern formation problems in the semi-strong regime where $D_v = \epsilon^2 \ll 1$ and $D_u = D = \mathcal{O}(1)$. In contrast to this, there is also a weak interaction regime where $D_u = \mathcal{O}(\epsilon^2)$ as well. In this regime we expect that stability results for the Gierer-Meinhardt model without saturation as computed for stripes in [39] generalize to arbitrary curves since the underlying differential equations are identical. One of the insights of [39] is that there exists a fold

point of a saddle-node bifurcation $D_u = D_c$ such that solutions do not exist for $D_u < D_c$. It has been shown (cf. [45], [42], [56]) that this saddle-node bifurcation fold point transitions to solutions which admit spot or stripe splitting. In the presence of saturation, one can show using full numerical simulations such as those in Chapter 5 that the saturation parameter itself can cause curve splitting even when $D_u > D_c$, i.e. well within the existence range. It is currently an open problem to classify the conditions for such curve splitting.

Bibliography

[1] M. Abramowitz, I. A. Stegun, et al. *Handbook of mathematical functions*, volume 1. Dover New York, 1972.

[2] N. Akaiwa and D. Meiron. Two-dimensional late-stage coarsening for nucleation and growth at high-area fractions. *Physical Review E*, 54(1):R13, 1996.

[3] N. Alikakos, P. W. Bates, and G. Fusco. Slow motion for the cahn-hilliard equation in one space dimension. *Journal of differential equations*, 90(1):81–135, 1991.

[4] S. M. Allen and J. W. Cahn. Ground state structures in ordered binary alloys with second neighbor interactions. *Acta Metallurgica*, 20(3):423–433, 1972.

[5] B. K. Alpert. Hybrid gauss-trapezoidal quadrature rules. *SIAM Journal on Scientific Computing*, 20(5):1551–1584, 1999.

[6] K. E. Atkinson. *An introduction to numerical analysis*. John Wiley & Sons, 1989.

[7] P. W. Bates and J. Shi. Existence and instability of spike layer solu-

tions to singular perturbation problems. *Journal of Functional Analysis*, 196(2):211–264, 2002.

[8] B. P. Belousov. A periodic reaction and its mechanism. *Compilation of Abstracts on Radiation Medicine*, 147(1), 1959.

[9] C. M. Bender and S. A. Orszag. *Advanced mathematical methods for scientists and engineers I: Asymptotic methods and perturbation theory*, volume 1. Springer, 1999.

[10] W. C. Bray. A periodic reaction in homogeneous solution and its relation to catalysis. *Journal of the American Chemical Society*, 43(6):1262–1267, 1921.

[11] V. Breña-Medina, D. Avitabile, A. Champneys, and M. Ward. Stripe to spot transition in a plant root hair initiation model. *submitted, SIAM Journal of Applied Math*, 2014.

[12] P.-L. Buono and R. Eftimie. Analysis of hopf/hopf bifurcations in non-local hyperbolic models of self organised aggregations. *Mathematical Models and Methods in Applied Sciences*, 24(02):327–357, 2014.

[13] S. Chandrasekhar. *Hydrodynamic and hydromagnetic stability*. Courier Corporation, 2013.

[14] A. Doelman, R. A. Gardner, and T. J. Kaper. Large stable pulse solutions in reactiondiffusion equations. In *Indiana Univ. Math. J*, 2000.

[15] A. Doelman and H. van der Ploeg. Homoclinic stripe patterns. *SIAM Journal on Applied Dynamical Systems*, 1(1):65–104, 2002.

[16] L. Edelstein-Keshet. *Mathematical models in biology*, volume 46. Siam, 1988.

[17] R. A. Fisher. The wave of advance of advantageous genes. *Annals of Eugenics*, 7(4):355–369, 1937.

[18] G. B. Folland. *Introduction to partial differential equations*. Princeton University Press, 1995.

[19] A. C. Fowler. *Mathematical models in the applied sciences*, volume 17. Cambridge University Press, 1997.

[20] A. Gierer and H. Meinhardt. A theory of biological pattern formation. *Kybernetik*, 12(1):30–39, 1972.

[21] P. Glandsdorf and I. Prigogine. Thermodynamic theory of structure, stability andfluctuations, 1971.

[22] K. B. Glasner and A. E. Lindsay. The stability and evolution of curved domains arising from one-dimensional localized patterns. *SIAM Journal on Applied Dynamical Systems*, 12(2):650–673, 2013.

[23] R. E. Goldstein, D. J. Muraki, and D. M. Petrich. Interface proliferation and the growth of labyrinths in a reaction-diffusion system. *Physical Review E*, 53(4):3933, 1996.

[24] M. Granero, A. Porati, and D. Zanacca. Bifurcation Analysis of Pattern Formation in a Diffusion Governed Morphoetic Field. *Journal of Mathematical Biology*, 4(1):21–27, 1977.

[25] A. Gray, E. Abbena, and S. Salamon. Modern differential geometry of curves and surfaces with mathematica. *Boca Raton, FL*, pages 373–380, 1997.

[26] C. Gui and J. Wei. Multiple interior peak solutions for some singularly perturbed neumann problems. *Journal of differential equations*, 158(1):1–27, 1999.

[27] M. Hennessy. *Mathematical problems relating to the fabrication of organic photovoltaic devices*. PhD thesis, University of Oxford, 2014.

[28] L. Holden and T. Erneux. Slow passage through a hopf bifurcation: from oscillatory to steady state solutions. *SIAM Journal on Applied Mathematics*, 53(4):1045–1058, 1993.

[29] D. Holloway and L. Harrison. Order and localization in reaction-diffusion pattern. *Physica A-Statistical Mechanics and its Applications*, 222(1-4):210–233, DEC 15 1995.

[30] E. Ince. Ordinary differential equations, 1956, 1962.

[31] D. Iron and M. J. Ward. A metastable spike solution for a nonlocal reaction-diffusion model. *SIAM Journal on Applied Mathematics*, 60(3):778–802, 2000.

[32] D. Iron and M. J. Ward. The dynamics of multispike solutions to the one-dimensional gierer–meinhardt model. *SIAM Journal on Applied Mathematics*, 62(6):1924–1951, 2002.

[33] D. Iron, M. J. Ward, and J. Wei. The stability of spike solutions to the one-dimensional gierer–meinhardt model. *Physica D: Nonlinear Phenomena*, 150(1):25–62, 2001.

[34] M. A. Jaswon and G. T. Symm. *Integral equation methods in potential theory and elastostatics*, volume 132. Oxford Univ Press, 1977.

[35] E. Kavanagh. Interface motion in the ostwald ripening and chemotaxis systems. Master's thesis, University of British Columbia, 2014.

[36] O. D. Kellogg et al. *Foundations of potential theory*. New York., 1929.

[37] A. Kolmogorofl, I. Petrovsky, and N. Piscounofl. Study of the diffusion equation with growth of the quantity of matter and its application to a biology problem. *Dynamics of Curved Fronts*, page 105, 2012.

[38] T. Kolokolnikov. *Pattern formation in reaction-diffusion models far from the Turing regime*. PhD thesis, University of British Columbia, 2004.

[39] T. Kolokolnikov, W. Sun, M. Ward, and J. Wei. The stability of a stripe for the gierer-meinhardt model and the effect of saturation. *SIAM Journal of Applied Dynamical Systems*, 5(2):313–363, 2006.

[40] T. Kolokolnikov, M. Ward, and J. Wei. Zigzag and breakup instabilities of stripes and rings in the two-dimensional gray-scott model. *Studies in Applied Mathematics*, 16(1):35–95, 2006.

[41] T. Kolokolnikov, M. Ward, and J. Wei. The stability of steady-state hot-spot patterns for a reaction-diffusion model of urban crime. *Discrete and Continuous Dynamical Systems - Series B*, 19(5):1373–1410, 2014.

[42] T. Kolokolnikov, M. J. Ward, and J. Wei. The existence and stability of spike equilibria in the one-dimensional gray–scott model: the pulse-splitting regime. *Physica D: Nonlinear Phenomena*, 202(3):258–293, 2005.

[43] T. Kolokolnikov, M. J. Ward, and J. Wei. Pulse-splitting for some reaction-diffusion systems in one-space dimension. *Studies in Applied Mathematics*, 114(2):115–165, 2005.

[44] T. Kolokolnikov, M. J. Ward, and J. Wei. Spot self-replication and dynamics for the schnakenburg model in a two-dimensional domain. *Journal of nonlinear science*, 19(1):1–56, 2009.

[45] T. Kolokolnikov and J. Wei. On ring-like solutions for the gray–scott model: existence, instability and self-replicating rings. *European Journal of Applied Mathematics*, 16(02):201–237, 2005.

[46] T. Kolokolnikov, J. Wei, and M. Winter. Existence and stability analysis of spiky solutions for the gierer–meinhardt system with large reaction rates. *Physica D: Nonlinear Phenomena*, 238(16):1695–1710, 2009.

[47] C.-S. Lin, W.-M. Ni, and I. Takagi. Large amplitude stationary solutions to a chemotaxis system. *Journal of Differential Equations*, 72(1):1–27, 1988.

[48] A. J. Lotka. Contribution to the theory of periodic reactions. *The Journal of Physical Chemistry*, 14(3):271–274, 1910.

[49] A. J. Lotka. Analytical note on certain rhythmic relations in organic

systems. *Proceedings of the National Academy of Sciences of the United States of America*, 6(7):410, 1920.

[50] P. Mandel and T. Erneux. The slow passage through a steady bifurcation: delay and memory effects. *Journal of statistical physics*, 48(5-6):1059–1070, 1987.

[51] H. Meinhardt. From observations to paradigms; the importance of theories and models. an interview with hans meinhardt by richard gordon and lev beloussov. *The International journal of developmental biology*, 50(2-3):103–111, 2005.

[52] D. S. Morgan and T. J. Kaper. Axisymmetric ring solutions of the 2d gray–scott model and their destabilization into spots. *Physica D: Nonlinear Phenomena*, 192(1):33–62, 2004.

[53] I. Moyles, W. H. Tse, and M. J. Ward. Explicitly solvable nonlocal eigenvalue problems and the stability of localized stripes in reaction-diffusion systems. *Submitted.*, 2015.

[54] I. Moyles and B. Wetton. A numerical framework for singular limits of a class of reaction diffusion problems. *Submitted.*

[55] W. W. Mullins and R. F. Sekerka. Morphological stability of a particle growing by diffusion or heat flow. *Journal of applied physics*, 34(2):323–329, 1963.

[56] C. Muratov and V. Osipov. Static spike autosolitons in the gray-scott model. *Journal of Physics A: Mathematical and General*, 33(48):8893, 2000.

[57] Y. Nec and M. J. Ward. An explicitly solvable nonlocal eigenvalue problem and the stability of a spike for a sub-diffusive reaction-diffusion system. *Mathematical Modelling of Natural Phenomena*, 8(02):55–87, 2013.

[58] W.-M. Ni and J. Wei. On positive solutions concentrating on spheres for the gierer–meinhardt system. *Journal of Differential Equations*, 221(1):158–189, 2006.

[59] Y. Nishiura. Global structure of bifurcating solutions of some reaction-diffusion systems. *SIAM Journal on Mathematical Analysis*, 13(4):555–593, 1982.

[60] T. Nose. Kinetics of phase separation in polymer mixtures. *Phase Transitions*, 8(3):245–260, 1987.

[61] R. M. Noyes and S. D. Furrow. The oscillatory briggs-rauscher reaction. 3. a skeleton mechanism for oscillations. *Journal of the American Chemical Society*, 104(1):45–48, 1982.

[62] W. Ostwald. Studien uber die umwandlung und bildung fester korper. *Eitschrift Phys. Chem*, 22:289, 1897.

[63] K. Painter, P. Maini, and H. Othmer. Complex spatial patterns in a hybrid chemotaxis reaction-diffusion model. *J. Math. Biol*, 41(4):285–314, 2000.

[64] Z. Pan and B. Wetton. A numerical method for coupled surface and grain boundary motion. *European Journal of Applied Mathematics*, 19(03):311–327, 2008.

[65] R. L. Pego. Front migration in the nonlinear cahn-hilliard equation. *Proceedings of the Royal Society of London. A. Mathematical and Physical Sciences*, 422(1863):261–278, 1989.

[66] A. C. Price, C. J. Weadick, J. Shim, and F. H. Rodd. Pigments, patterns, and fish behavior. *Zebrafish*, 5(4):297–307, 2008.

[67] P. Prusinkiewicz, D. R. Fowler, and H. Meinhardt. *The algorithmic beauty of sea shells*. Springer Science & Business Media, 2009.

[68] B. D. Quaife. *Fast integral equation methods for the modified Helmholtz equation*. PhD thesis, Simon Fraser University, 2011.

[69] S. Roth. Mathematics and biology: a kantian view on the history of pattern formation theory. *Development genes and evolution*, 221(5-6):255–279, 2011.

[70] E. B. Saff and A. D. Snider. *Fundamentals of complex analysis for mathematics, science, and engineering*. Prentice-Hall, 1976.

[71] J. Schnakenberg. Simple chemical reaction systems with limit cycle behaviour. *Journal of theoretical biology*, 81(3):389–400, 1979.

[72] L. A. Segel and J. L. Jackson. Dissipative structure: an explanation and an ecological example. *Journal of Theoretical Biology*, 37(3):545–559, 1972.

[73] J. W. Thomas. *Numerical partial differential equations: finite difference methods*, volume 22. Springer Science & Business Media, 1995.

[74] A. M. Turing. The chemical basis of morphogenesis. *Philosophical Transactions of the Royal Society of London. Series B, Biological Sciences*, 237(641):37–72, 1952.

[75] J. J. Tyson. Some further studies of nonlinear oscillations in chemical systems. *The Journal of Chemical Physics*, 58(9):3919–3930, 1973.

[76] J. Tzou, M. Ward, and T. Kolokolnikov. Slowly varying control parameters, delayed bifurcations, and the stability of spikes in reactiondiffusion systems. *Physica D: Nonlinear Phenomena*, 290(0):24 – 43, 2015.

[77] P. W. Voorhees, G. McFadden, R. Boisvert, and D. Meiron. Numerical simulation of morphological development during ostwald ripening. *Acta Metallurgica*, 36(1):207–222, 1988.

[78] M. J. Ward. Metastable bubble solutions for the allen-cahn equation with mass conservation. *SIAM Journal on Applied Mathematics*, 56(5):1247–1279, 1996.

[79] M. J. Ward and J. Wei. Hopf bifurcations and oscillatory instabilities of spike solutions for the one-dimensional gierer-meinhardt model. *Journal of Nonlinear Science*, 13(2):209–264, 2003.

[80] J. Wei and M. Winter. *Mathematical Aspects of Pattern Formation in Biological Systems*. Springer-Verlag.

[81] J. Wei and M. Winter. A nonlocal eigenvalue problem and the stability of spikes for reaction–diffusion systems with fractional reaction rates. *International Journal of Bifurcation and Chaos*, 13(06):1529–1543, 2003.

[82] J. Wei and M. Winter. On the gierer–meinhardt system with saturation. *Communications in Contemporary Mathematics*, 6(02):259–277, 2004.

[83] A. M. Zhabotinsky. Periodical oxidation of malonic acid in solution (a study of the belousov reaction kinetics). *Biofizika*, 9:306–311, 1964.

[84] J. Zhu, X. Chen, and T. Y. Hou. An efficient boundary integral method for the mullins–sekerka problem. *Journal of Computational Physics*, 127(2):246–267, 1996.

Appendix A

Derivation of Boundary Properties for Single Layered Potentials

The properties of layered potentials for Laplace's equation have appeared in a variety of manners and texts (cf. [18], [34], [36]). In this appendix, we will derive the Dirichlet and Neumann jump conditions for the single layer potential of Laplace's problem with the fundamental solution (6.3) in a more systematic way. The connection to the fundamental solution of the Helmholtz problem (6.1) is described in section 6.1. Consider solving the following Dirichlet Laplace problem

$$\begin{aligned} \Delta u &= 0, \qquad x \in \mathbb{R}^2 \setminus \Gamma \\ u &= f(x), \qquad x \in \Gamma \end{aligned}$$

with Γ a closed curve in $\mathbb{R}^2$. The single layer potential for some continuous density ϕ is then

$$u(x) = \int_\Gamma \Phi(x,q)\phi(q)\,\mathrm{d}q,$$

for all x. To evaluate the Dirichlet condition, we need to understand what happens as x approaches x_0 along its normal direction. Consider some point x_0 on Γ and define the portion of the curve Γ_ϵ,

$$\Gamma_\epsilon : \{q \in \Gamma || x_0 - q| < \epsilon\}, \qquad \epsilon \ll 1.$$

Let, $x = x_0 + \alpha \hat{\mathbf{n}}_i$, where the subscript indicates that $\alpha > 0$ traverses the inward pointing normal. As we near Γ,

$$\begin{aligned} &\lim_{\alpha \to 0^+} u(x_0 + \alpha \hat{\mathbf{n}}_i) \\ &= \lim_{\alpha \to 0} \left(\int_{\Gamma \setminus \Gamma_\epsilon} \Phi(x_0 + \alpha \hat{\mathbf{n}}_i, q) \phi(q) \, \mathrm{d}q + \int_{\Gamma_\epsilon} \Phi(x_0 + \alpha \hat{\mathbf{n}}_i, q) \phi(q) \, \mathrm{d}q \right) = f(x_0^+), \end{aligned}$$

where we have used the Dirichlet condition. Now, since the fundamental solution is not singular on $\Gamma \setminus \Gamma_\epsilon$ then we have that

$$f(x_0^+) = \int_{\Gamma \setminus \Gamma_\epsilon} \Phi(x_0, q) \phi(q) \, \mathrm{d}q + \int_{\Gamma_\epsilon} \lim_{\alpha \to 0^+} \Phi(x_0 + \alpha \hat{\mathbf{n}}_i, q) \phi(q) \, \mathrm{d}q, \qquad \text{(A.1)}$$

where we have carried the limit inside the integral since we are not directly evaluating at the singularity. On Γ_ϵ, we have that $q = x_0 + \beta \hat{\mathbf{t}}$ with $-\epsilon < \beta < \epsilon$ and so on this portion of the curve,

$$\Phi(x_0 + \alpha \hat{\mathbf{n}}_i, q) = -\frac{1}{2\pi} \log \left| \sqrt{\alpha^2 + \beta^2} \right| \underset{\alpha \ll 1}{\sim} -\frac{1}{2\pi} \log |\beta| + \mathcal{O}(\alpha^2),$$

and

$$\phi(q) \approx \phi(x_0),$$

since it is continuous. The second integral in (A.1) then becomes,

$$\begin{aligned}\int_{\Gamma_\epsilon} \lim_{\alpha\to 0^+} \Phi(x_0+\alpha\hat{\mathbf{n}}_i, q)\phi(q)\,\mathrm{d}q &= -\frac{\phi(x_0)}{2\pi}\int_{-\epsilon}^{\epsilon} \lim_{\alpha\to 0^+} \left(\log|\beta| + \mathcal{O}(\alpha^2)\right)\mathrm{d}\beta \\ &= -\frac{\phi(x_0)}{\pi}\left(\epsilon\log\epsilon - \epsilon\right) \\ &\underset{\epsilon\to 0}{=} 0,\end{aligned}$$

and therefore the singularity contributes nothing to the integral and as $\epsilon \to 0$,

$$f(x_0^+) = \int_\Gamma \Phi(x_0^+, q)\phi(q)\,\mathrm{d}q.$$

Similarly, if we approach from below the curve, we have

$$f(x_0^-) = \int_\Gamma \Phi(x_0^-, q)\phi(q)\,\mathrm{d}q$$

and so we have that $[u] = 0$ and the Dirichlet condition is

$$f(x) = \int_\Gamma \Phi(x, q)\phi(q)\,\mathrm{d}q, \qquad x \in \Gamma. \tag{A.2}$$

Now consider what happens to the normal derivative of u as we approach the curve from above,

$$\begin{aligned}\lim_{\alpha\to 0^+} \frac{\partial u}{\partial n_x}(x_0+\alpha\hat{\mathbf{n}}_i) = &\int_{\Gamma\setminus\Gamma_\epsilon} \frac{\partial \Phi}{\partial n_x}(x_0, q)\phi(q)\,\mathrm{d}q \\ &+ \int_{\Gamma_\epsilon} \lim_{\alpha\to 0^+} \frac{\partial \Phi}{\partial n_x}(x_0+\alpha\hat{\mathbf{n}}_i, q)\phi(q)\,\mathrm{d}q,\end{aligned} \tag{A.3}$$

where once again we have interchanged derivatives, limits, and integrals by avoiding evaluating the singularity directly. Now,

$$\frac{\partial \Phi}{\partial n_x}(x,q) = -\frac{1}{2\pi}\frac{x-q}{|x-q|^2}\cdot \hat{\mathbf{n}}_x, \tag{A.4}$$

where $\hat{\mathbf{n}}_x$ is the positively oriented normal at x_0. Note that $\hat{\mathbf{n}}_x = \pm\hat{\mathbf{n}}_i$ depending on the orientation and we will proceed with $\hat{\mathbf{n}}_x = \hat{\mathbf{n}}_i$ noting that there is a minus sign difference if $\hat{\mathbf{n}}_x$ is the external norm. Substituting x and q on Γ_ϵ into (A.4),

$$\frac{\partial \Phi}{\partial n_x}(x_0 + \alpha\hat{\mathbf{n}}_i, x_0 + \beta\hat{\mathbf{t}}) = -\frac{1}{2\pi}\frac{\alpha}{\alpha^2+\beta^2}.$$

Now if $\beta \neq 0$ then for $\alpha \ll 1$,

$$\frac{\alpha}{\alpha^2+\beta^2} \sim \frac{\alpha}{\beta^2} \to 0.$$

However, if $\beta = 0$ then

$$\frac{\alpha}{\alpha^2+\beta^2} = \frac{1}{\alpha} \underset{\alpha\ll 1}{\to} \operatorname{sgn}(\alpha)\infty.$$

Therefore,

$$-\frac{1}{2\pi}\frac{\alpha}{\alpha^2+\beta^2} = A\delta(\beta).$$

To find A we integrate around $\beta = 0$,

$$\int_{0^-}^{0^+} \frac{\alpha}{\alpha^2+\beta^2}\,\mathrm{d}\beta = -2\pi A.$$

To track the singularity at $\beta = 0$, take $\beta = \alpha b$ and let $\alpha \to 0$. Since $\alpha > 0$, the integral becomes

$$\int_{-\infty}^{\infty} \frac{1}{1+b^2}\,\mathrm{d}b = \pi = -2\pi A. \tag{A.5}$$

Therefore we have that

$$\frac{\partial \Phi}{\partial n_x}(x_0 + \alpha \hat{\mathbf{n}}_i, x_0 + \beta \hat{\mathbf{t}}) = -\frac{1}{2}\delta(\beta).$$

Substituting this into (A.3) we get

$$\begin{aligned}\lim_{\alpha \to 0^+} \frac{\partial u}{\partial n_x}(x_0 + \alpha \hat{\mathbf{n}}_i) &= \int_{\Gamma \setminus \Gamma_\epsilon} \frac{\partial \Phi}{\partial n_x}(x_0, q)\phi(q)\,\mathrm{d}q - \phi(x_0)\int_{-\epsilon}^{\epsilon} \frac{1}{2}\delta(\beta)\,\mathrm{d}\beta \\ &\underset{\epsilon \to 0}{=} \int_{\Gamma} \frac{\partial \Phi}{\partial n_x}(x_0, q)\phi(q)\,\mathrm{d}q - \frac{\phi(x_0)}{2}.\end{aligned}$$

Now if we instead approach the curve from below then the only difference is that the scaling in (A.5) satisfies $\alpha < 0$ and so the integral becomes

$$\int_{\infty}^{-\infty} \frac{1}{1+b^2}\,\mathrm{d}b = -\pi = -2\pi A,$$

and instead we get

$$\lim_{\alpha \to 0^-} \frac{\partial u}{\partial n_x}(x_0 + \alpha \hat{\mathbf{n}}_i) = \int_{\Gamma} \frac{\partial \Phi}{\partial n_x}(x_0, q)\phi(q)\,\mathrm{d}q + \frac{\phi(x_0)}{2}.$$

Therefore we have the jump condition

$$\lim_{\alpha\to 0^+} \frac{\partial u}{\partial n_x}(x+\alpha\hat{\mathbf{n}}_i) = \int_\Gamma \frac{\partial \Phi}{\partial n_x}(x,q)\phi(q)\,\mathrm{d}q - \frac{\phi(x)}{2} \qquad x\in\Gamma, \tag{A.6a}$$

$$\lim_{\alpha\to 0^-} \frac{\partial u}{\partial n_x}(x+\alpha\hat{\mathbf{n}}_i) = \int_\Gamma \frac{\partial \Phi}{\partial n_x}(x,q)\phi(q)\,\mathrm{d}q + \frac{\phi(x)}{2} \qquad x\in\Gamma. \tag{A.6b}$$

Notice that indeed as was stated in section 6.1,

$$\begin{aligned}\left[\frac{\partial u}{\partial n}\right]_\Gamma &= \lim_{\alpha\to 0^+} \frac{\partial u}{\partial n_x}(x_0+\alpha\hat{\mathbf{n}}_x) - \lim_{\alpha\to 0^-} \frac{\partial u}{\partial n_x}(x_0+\alpha\hat{\mathbf{n}}_x),\\ &= \begin{cases} \lim\limits_{\alpha\to 0^+} \frac{\partial u}{\partial n_x}(x_0+\alpha\hat{\mathbf{n}}_i) - \lim\limits_{\alpha\to 0^-} \frac{\partial u}{\partial n_x}(x_0+\alpha\hat{\mathbf{n}}_i) = -\phi(x), & \hat{\mathbf{n}}_x = \hat{\mathbf{n}}_i \\ \lim\limits_{\alpha\to 0^+} \frac{\partial u}{\partial n_x}(x_0-\alpha\hat{\mathbf{n}}_i) - \lim\limits_{\alpha\to 0^-} \frac{\partial u}{\partial n_x}(x_0-\alpha\hat{\mathbf{n}}_i) = \phi(x), & \hat{\mathbf{n}}_x = -\hat{\mathbf{n}}_i \end{cases},\\ &= -(\hat{\mathbf{n}}_x\cdot\hat{\mathbf{n}}_i)\phi(x).\end{aligned}$$

We will now finish off by looking at the tangential derivative for completeness,

$$\begin{aligned}\lim_{\alpha\to 0^+} \frac{\partial u}{\partial t_x}(x_0+\alpha\hat{\mathbf{n}}_i) = &\int_{\Gamma\setminus\Gamma_\epsilon} \frac{\partial \Phi}{\partial t_x}(x_0,q)\phi(q)\,\mathrm{d}q\\ &+ \int_{\Gamma_\epsilon} \lim_{\alpha\to 0^+} \frac{\partial \Phi}{\partial t_x}(x_0+\alpha\hat{\mathbf{n}}_i,q)\phi(q)\,\mathrm{d}q.\end{aligned} \tag{A.7}$$

Looking at the derivative on Γ_ϵ,

$$\frac{\partial \Phi}{\partial t_x}(x_0+\alpha\hat{\mathbf{n}}_i, x_0+\beta\hat{\mathbf{t}}) = -\frac{1}{2\pi}\frac{\beta}{\alpha^2+\beta^2} \underset{\alpha\ll 1}{\sim} -\frac{1}{2\pi\beta}.$$

Using the Cauchy Principal Value for the integration,

$$\int_{-\epsilon}^{\epsilon} \frac{1}{\beta}\,\mathrm{d}\beta = 0$$

and there is no contribution on Γ_ϵ. Therefore,

$$\lim_{\alpha\to 0^+} \frac{\partial u}{\partial t_x}(x+\alpha\hat{\mathbf{n}}_i) = \int_\Gamma \frac{\partial \Phi}{\partial n_x}(x,q)\phi(q)\,\mathrm{d}q \qquad x\in\Gamma, \tag{A.8a}$$

$$\lim_{\alpha\to 0^-} \frac{\partial u}{\partial n_x}(x+\alpha\hat{\mathbf{n}}_i) = \int_\Gamma \frac{\partial \Phi}{\partial n_x}(x,q)\phi(q)\,\mathrm{d}q \qquad x\in\Gamma, \tag{A.8b}$$

and we get

$$\left[\frac{\partial u}{\partial t_x}\right]_\Gamma = 0,$$

showing that the tangential derivative is continuous.